

**DOE-ER-0313/54
Distribution
Categories
UC-423, -424**

**FUSION MATERIALS
SEMIANNUAL PROGRESS REPORT
FOR THE PERIOD ENDING**

June 30, 2013

**Prepared for
DOE Office of Fusion Energy Sciences
(AT 60 20 10 0)**

DATE PUBLISHED: September 2013

**Prepared by
OAK RIDGE NATIONAL LABORATORY
Oak Ridge, Tennessee 37831
Managed by
UT-Battelle, LLC
For the
U.S. DEPARTMENT OF ENERGY**

FOREWORD

This is the fifty-fourth in a series of semiannual technical progress reports on fusion materials science activity supported by the Fusion Energy Sciences Program of the U.S. Department of Energy. It covers the period ending June 30, 2013. This report focuses on research addressing the effects on materials properties and performance of exposure to the neutronic, thermal and chemical environments anticipated in the chambers of fusion experiments and energy systems. This research is a major element of the national effort to establish the materials knowledge base for an economically and environmentally attractive fusion energy source. Research activities on issues related to the interaction of materials with plasmas are reported separately.

The results reported are the products of a national effort involving a number of national laboratories and universities. A large fraction of this work, particularly in relation to fission reactor irradiations, is carried out collaboratively with partners in Japan, Russia, and the European Union. The purpose of this series of reports is to provide a working technical record for the use of program participants, and to provide a means of communicating the efforts of fusion materials scientists to the broader fusion community, both nationally and worldwide.

This report has been compiled under the guidance of F. W. (Bill) Wiffen and Betty Waddell, Oak Ridge National Laboratory. Their efforts, and the efforts of the many persons who made technical contributions, are gratefully acknowledged.

Peter J. Pappano
Research Division
Office of Fusion Energy Sciences

TABLE OF CONTENTS

1. FERRITIC/MARTENSITIC STEEL DEVELOPMENT

See also Sections 2.5, 8.4, and 8.5.

1.1 Stability of Nanoprecipitates in Fe-Base Model Alloys —

1

L. Tan, Y. Katoh, and L. L. Snead (Oak Ridge National Laboratory)

The radiation resistance of TaC, TaN, and VN MX-type nanoprecipitates is being evaluated using Fe²⁺ ion irradiation at 500°C for nominal doses of ~20 and ~200 dpa. A parallel study using neutron irradiation at 300, 500, and 650°C for up to about 20 dpa is also in progress. The characterization and analyses of the low dose (~20 dpa) Fe²⁺ ion irradiated samples have been completed. The results indicate that the irradiation did not alter the crystalline nature of the nanoprecipitates. Particle dissolution, growth, and reprecipitation in different levels were observed after the irradiation. The radiation resistance of the carbide was much stronger than the nitrides in declined order TaC, VN, and TaN. TaC nanoprecipitates were observed to be much more resistant to irradiation than reported for a study using similar irradiation conditions. Post-irradiation examination of the high dose (~200 dpa) Fe²⁺ ion-irradiated and neutron-irradiated samples will be conducted and compared to the current observations.

1.2 Recent Observations of Helium Effects on Cavity Evolution in Tempered Martensitic Steels —

6

T. Yamamoto, Y. Wu, G. R. Odette, (University of California, Santa Barbara); S. Kondo, and A. Kimura (Kyoto University)

New dual ion (Fe³⁺ and He⁺) beam irradiations (DII) were performed at 500°C on a group of ferritic alloys up to nominal dpa and He levels of 26 dpa and 390 appm, respectively, at a He (appm)/dpa ratio of ≈ 15 using the DuET facility at Kyoto University in Japan. The actual dpa, He and He/dpa vary with depth in the sample. The alloys studied include normalized and tempered martensitic steels, (TMS) F82H IEA in as-tempered and cold-worked conditions as well as F82H mod.3, and a nanostructured ferritic alloy (NFA), MA957. To date, TEM observations have been performed for F82H mod.3 at depths from 0.1 to 1.7 mm. In the F82H mod.3, the number density of the cavities (N) ranged from 1 to 9 x 10²¹/m³ while average diameter (<d>) of all the cavities ranged from 2.4 to 5.5 nm. The N are significantly smaller than that for higher ≈ 47 appm He/dpa in previous study, while the <d> are similar.

2. ODS AND NANOCOMPOSITED ALLOY DEVELOPMENT

See also Sections 7.3 and 7.4.

TABLE OF CONTENTS

- 2.1 Characterization of a Larger Best Practice Heat of 14YWT in Annealed Powder, HIP Consolidated and Extruded Forms — 15**
 N. J. Cunningham, Y. Wu, G. R. Odette, (University of California, Santa Barbara);
 D. T. Hoelzer, (Oak Ridge National Laboratory); and S. A. Maloy (Los Alamos National Laboratory)
- We describe the characterization of new 14YWT heats from gas atomized and mechanically alloyed powder using an alternative processing method that incorporates Y during the gas atomization process. Post mechanically alloying processes included annealing the powder at 850°C and 1150°C, HIP consolidation at 850°C and 1150°C, and consolidation by hot extrusion at 850°C, annealing for 1 h at 1000°C, and then cross-rolling to 50% thickness at 1000°C; the latter has been dubbed FCRD-NFA1. In all cases a high number density of nm-sized features were observed using a combination of atom probe tomography, transmission electron microscopy, and small angle neutron scattering. The 850°C lower temperature annealing and HIP consolidation resulted in smaller precipitates compared to the 1150°C processing temperature. However, after annealing at 1200°C for 48 h the precipitate size and number density were similar in the two cases. The FCRD-NFA1 had a microstructure and NF distribution similar to a previously reported alloy, PM2. However, the extruded samples also had a large number of large (>20 nm) Ti-rich precipitates. These larger precipitates may affect the mechanical properties, which are currently under investigation.
- 2.2 Development of ODS FeCrAl for Fusion Reactor Applications — 27**
 B. A. Pint, D. T. Hoelzer, and K. A. Unocic (Oak Ridge National Laboratory)
- Several additional isothermal Pb-Li capsule tests of cast FeCrAlY specimens were completed at 700°C in order to further guide alloy selection. Characterization of specimens after exposure indicated that the Cr and Al contents remain relatively constant near the exposed surface and that LiAlO₂ formed on the surface of all of the exposed alloys. In general, the results suggest that the Al content needs to be near 5 wt.% for excellent Pb-Li compatibility. Based on this information, several powder compositions were procured and have now been received and analyzed. These powders are now being milled to produce the first batches of ODS FeCrAl for evaluation.
- 2.3 TEM Characterization of a Simultaneously Neutron-Irradiated and Helium-Injected PM2000 ODS Alloy — 31**
 H. J. Jung, D. J. Edwards, R. J. Kurtz, (Pacific Northwest National Laboratory);
 G. R. Odette, and T. Yamamoto (University of California, Santa Barbara)
- TEM examination of a simultaneously neutron-irradiated and He-injected PM2000 ODS alloy was performed. The He implanted region had a high density of <2 nm He bubbles largely associated with matrix dislocation loops. Nearly all ODS particles had a single faceted void attached to them that was from 5 to 15 nm. On the non-implanted side, no He bubbles were seen, and faceted voids were found on ~10% of the ODS particles. The He-implanted side has both <100>{100} and ½<111>{111} dislocation loops and a low density of line dislocations, while the un-implanted side has mostly line dislocations and a lower

TABLE OF CONTENTS

density of dislocation loops. In both regions, nanoscale fcc precipitates having a cube-on-cube orientation relationship with the matrix were observed. EDS measurements indicate this phase is rich in Al and Ti. Substantial Cr segregation occurs around the dislocation loops, concurrent with Fe depletion. The precipitates do not appear to be associated with the loops or line dislocations. The ODS particles, which are all amorphous, contain >20 at% Al, and show Cr segregation/Fe-depletion at their periphery.

- 2.4 The Association Relationships Among Bubbles, Precipitates, and Grain Boundaries in Dual Beam Irradiated Nano-Structured Ferritic Alloys — 42**
 Y. Wu, T. Yamamoto, N. Cunningham, G. R. Odette, (University of California, Santa Barbara); S. Kondo, and A. Kimura (University of Kyoto, Japan)

Transmission electron microscopy (TEM) was used to characterize the associations between various microstructural features, including helium bubbles, in nanostructured ferritic alloys, following dual ion irradiations at 650°C. Almost all of the nm-scale oxide precipitates are associated with one and, in some cases a few, interface bubbles. The distribution of precipitates and bubbles along dislocations and small angle grain boundaries are not significantly different than in the matrix. However, the precipitates on large angle grain boundaries are larger and often associated with more bubbles.

- 2.5 Friction Stir Welding of ODS Steels and Advanced Ferritic Structural Steels — 51**
 Z. Feng, Z. Yu, D. Hoelzer, M. A. Sokolov, and L. T. Tan (Oak Ridge National Laboratory)

Initial friction stir trial welds were made on ODS alloy MA965, RAFM steels EUROFER97 and F82H, and between MA956 and EUROFER97 (dissimilar weld). Defect-free similar and dissimilar welds were obtained. The microstructure of the welded region was characterized using optical microscopy (OM) and small-angle neutron scattering (SANS). OM examination showed that the microstructures in the stir zone (SZ), thermo-mechanically affected zone (TMAZ) and heat affect zone (HAZ) were significantly different from these in the base metal (BM). Small angle neutron scattering measurements were performed in the base metal and welded region to characterize the changes in nano-scale oxide features. Aggregation of the fine nano-scale particles was observed in the SZ. Micro-hardness mapping on the cross section of welds clearly revealed the effects of FSW.

3. CERAMIC COMPOSITE STRUCTURAL MATERIAL DEVELOPMENT

See also Sections 8.2 and 8.3.

TABLE OF CONTENTS

- 3.1 Swelling and X-Ray Peak Broadening of High Dose Neutron Irradiated SiC Composites — 61**
 C. Shih, R. Meisner, Y. Katoh, and L. L. Snead (Oak Ridge National Laboratory)
- The lattice parameter changes in high dose (up to ~70 dpa) neutron irradiated nuclear grade SiC/SiC composites were studied with room temperature powder XRD and compared with macroscopic dimensional changes at nominal irradiation temperatures of 300, 500 and 800°C. The results show no lattice parameter change for all high dose neutron irradiated SiC/SiC composites while macroscopic volume swelling is observed. This observation agrees with the very limited literature data on XRD studies of high dose CVD SiC and high dose hot pressed SiC. The lattice parameter changes disagree with macroscopic dimensional changes, suggesting progressive evolution of microstructures involving transition of ultra-fine interstitial clusters into larger interstitial loops as the very high irradiation doses are achieved. However, the errors in lattice parameter measurements caused by high surface roughness of the unpolished composites remains an issue and need to be further studied.
- 3.2 Properties of Defects and Implants in Mg⁺ Implanted Silicon Carbide — 70**
 W. Jiang, Z. Zhu, T. Varga, M. E. Bowden, S. Manandhar, T. Roosendaal, S. Y. Hu, C. H. Henager, Jr., R. J. Kurtz, (Pacific Northwest National Laboratory); and Y. Wang (Los Alamos National Laboratory)
- Implantation of 3C-SiC, 6H-SiC and CVD-SiC has been performed with 200 keV Mg⁺ ions to fluences up to 3.2×10^{16} ions/cm² at 773 K. Rutherford backscattering analyses of the as-produced damage states along multiaxial channeling directions indicate that there are interstitial-type defect configurations that are well aligned with the <100> axis, such as Si-Si <100> interstitial splits. The depth profile of the as-implanted Mg exhibits a Gaussian-like distribution without evidence of considerable diffusion-driven mass transport during implantation. A post implantation thermal annealing study shows that there is a significant recovery of the structural defects with essentially immobile Mg in SiC up to 1473 K. Further annealing at higher temperatures is currently in progress with intent to recover implantation damage to the maximum extent possible while retaining Mg implants in the sample. Characterizations will follow using spectroscopy and microscopy to study microstructure and Mg behavior in SiC.
- 3.3 EMTA Thermal Conductivity Predictions for Unirradiated and Irradiated SiC/SiC Composites — 76**
 B. N. Nguyen, C. H. Henager, Jr., and R. J. Kurtz (Pacific Northwest National Laboratory)
- This study first applied an Eshelby-Mori-Tanaka approach implemented in PNNL's EMTA software to predict thermal conductivities of unirradiated 2D SiC/SiC composites. The EMTA homogenization method is structured in three steps to capture the effects of the constituent materials including the pyrolytic carbon (PyC) fiber coating on the thermal conductivities of as-formed composites. EMTA also applies an iterative reverse engineering procedure to identify an unknown constituent material thermal conductivity.

TABLE OF CONTENTS

EMTA reverse engineering was shown to be efficient and accurate to compute the thermal conductivities of the SiC matrix and of the fiber coating as functions of temperature, and consequently, to achieve better agreement between the predicted and experimental thermal conductivities for the composites. Next, a new method that builds on EMTA to estimate the thermal conductivity of SiC/SiC composites subjected to neutron irradiation at elevated temperature up to a dose of 10 dpa was developed. This method considers the irradiation-induced conductivity degradation behavior of chemical vapor deposited (CVD) SiC and defines an equivalent CVD-SiC material with an equivalent pore content to estimate the thermal conductivity of a SiC/isothermal-chemical-vapor-infiltration (ICVI)-SiC composite. It was shown that the proposed method effectively mimics the irradiation effect that induces the reduction of composite thermal conductivity.

3.4 Process Development and Optimization for Silicon Carbide Joining and Irradiation Studies-II —

T. Koyanagi, J. O. Kiggans, T. Cheng, and Y. Katoh (Oak Ridge National Laboratory)

The candidate joining methods for SiC ceramics and composites in the ongoing work to develop and optimize performance in neutron irradiation environments include chemically vapor-deposited (CVD) SiC bonded by the NITE (nano-infiltration and transient eutectic-phase) – like processes, diffusion bonding utilizing active titanium or molybdenum inserts, and transient eutectic-phase-assisted bonding with yttria-alumina-garnet (YAG) solder. In previous work the optimal processing conditions for Ti foil joining have been established. During the present reporting period, joint specimens with high shear strength were successfully produced through the active Mo metal insert methods, and then evaluated for as-fabricated properties.

3.5 Low Activation Joining of SiC/SiC Composites for Fusion Applications: Tape Casting TiC+Si Powders —

C. H. Henager, Jr., R. J. Kurtz, N. L. Canfield, Y. Shin, W. G. Luscher, J. T. Mansurov, T. J. Roosendaal, and B. A. Borlaug (Pacific Northwest National Laboratory)

The use of SiC composites in fusion environments likely requires joining of plates using reactive joining or brazing. One promising reactive joining method uses solid-state displacement reactions between Si and TiC to produce $Ti_3SiC_2 + SiC$. We continue to explore the processing envelope for this joint for the TITAN collaboration in order to produce optimal joints to undergo irradiation studies in HFIR. One noted feature of the joints produced using tape-calendared powders of TiC+Si has been the large void regions that have been apparently unavoidable. Although the produced joints are very strong, these voids are undesirable. In addition, the tapes that were made for this joining was produced about 20 years ago and was aging. Therefore, we embarked on an effort to produce some new tape cast powders of TiC and Si that could replace our aging tape calendared materials.

4.0 HIGH HEAT FLUX MATERIALS AND COMPONENT TESTING

See also Sections 8.6, 8.7, and 8.8.

TABLE OF CONTENTS

- 4.1 Recent Progress in the Development of Ductile-Phase Toughened Tungsten for Plasma-Facing Materials — 95**
 K. H. Cunningham, K. Fields, D. Gragg, F. W. Zok, (University of California, Santa Barbara); C. Henager, R. Kurtz, and T. Roosendaal (Pacific Northwest National Laboratory)
- Fracture testing was performed on notched and pre-cracked specimens of a W - 28w% Cu plate at room temperature and at 679K, as a follow-up to previous work. An order-of-magnitude toughness increase from that of monolithic tungsten was observed as a result of ductile Cu bridging. Pure W samples were consolidated from elemental powder using spark plasma sintering, achieving a maximum of 95.2% of the theoretical density. Commercially available tungsten wire was tested in tension, showing significant ductility and strength. The tungsten wire was plated with copper using electrodeposition, and continuing research will investigate methods of incorporating the Cu-coated W wire into a consolidated W matrix using spark plasma sintering. We expect the addition of ductile W wire to provide significant toughening compared to monolithic W, with the Cu coating preventing the wire from strongly bonding to the matrix.
- 4.2 Effect of Green Density and Fast Sintering on Grain Growth of Nano W — 108**
 X. Wang and Z. Z. Fang (University of Utah)
- Two novel processing techniques were developed for inhibiting the grain growth of W during sintering of nano W and W alloy powders; one of which is a hot-pressing green compaction technique for increasing the relative density of green compacts of the nano powders. The second is a fast sintering technique for applying a combination of rapid heating and high pressure during sintering. Nano W and W-TiC powders were used to investigate the effect of green density and fast sintering on grain growth. The following preliminary results were obtained:
- (1) The maximum obtainable green density of cold-pressed samples was 38% of the theoretical full density at 800 MPa, while the hot-pressed sample exhibited an 18% increase in green density (56% TD).
 - (2) Higher green density enabled the samples to be fully sintered at lower temperature.
 - (3) Near fully dense bodies with a grain size smaller than 300 nm were obtained via fast sintering.
- 4.3 Electron –Beam Additive Manufacturing of Tungsten Materials for Fusion — 114**
 E. K. Ohriner, R. Dehoff, and L. L. Snead (Oak Ridge National Laboratory)
- Initial experiments were performed with the ARCAM A2 electron beam additive manufacturing unit using standard beam deflection conditions. Local regions were observed with the desired microstructure of a solid tungsten surface layer and a liquid phase sintered boundary layer of tungsten particles in a steel matrix. A new ARCAM unit is currently being installed for use in future experiments.

TABLE OF CONTENTS

- 4.4 High-Heat Flux Testing of Low-Level Irradiated Materials Using Plasma Arc Lamps — 117**
 A. S. Sabau, E. K. Ohriner, Y. Katoh and L. L. Snead (Oak Ridge National Laboratory)
- The Research Safety Summary (RSS) was approved for high-heat flux testing of irradiated specimens. The radiation safety during high-heat flux testing was enhanced by the installation of a digital flow meter on the outlet part of the rod cooling circuit in order to monitor the flow rate during high-heat flux testing. One of the most difficult tasks is the measurement of sample temperature. The best data on sample temperature was obtained using a thermocouple welded to the sample during the high-heat flux testing. A pyrometer was used to measure the surface temperatures on either the specimen holder or the specimen. It was found that at high IR energies the pyrometer data is affected by the infrared energy from the PAL. Thus calibration runs are needed in order to enhance the accuracy of the pyrometer data.
- 5. MAGNET AND DIAGNOSTIC SYSTEM MATERIALS**
- 5.1 Irradiation Response of Next Generation High Temperature Superconducting Rare-Earth and Nanoparticle-Doped $\text{YBa}_2\text{Cu}_3\text{O}_{7-x}$ Coated Conductors for Fusion Energy Applications — 125**
 K. J. Leonard, T. Aytug, F. A. List III, (Oak Ridge National Laboratory); A. Perez-Bergquist, W. J. Weber, (University of Tennessee); and A. Gapud (University of South Alabama)
- The irradiated superconducting properties of Zr-doped $(\text{Y,Gd})\text{Ba}_2\text{Cu}_3\text{O}_{7-x}$, $(\text{Dy,Y})\text{Ba}_2\text{Cu}_3\text{O}_{7-x}$ and $\text{Gd}_2\text{Ba}_2\text{Cu}_3\text{O}_{7-x}$ are being evaluated for 5 MeV Ni, and 25 MeV Au irradiations to fluences between 10^{11} and 10^{12} ions/cm². For low fluence irradiations, small decreases were observed in the critical current for a-b pinning in both the $\text{GdBa}_2\text{Cu}_3\text{O}_{7-x}$ and $(\text{Dy,Y})\text{Ba}_2\text{Cu}_3\text{O}_{7-x}$ conductors, but increased pinning at other angular orientations, decreasing angular field isotropy. The 10^{12} cm⁻² 25 MeV Au irradiated $(\text{Dy,Y})\text{Ba}_2\text{Cu}_3\text{O}_{7-x}$ did show a reduction in critical current, J_c , for externally applied magnetic fields of less than 7 Tesla for tests conducted at 77 K. However, at higher field strengths the irradiated J_c values exceed that of the unirradiated material. Properties of the Zr-doped $(\text{Y,Gd})\text{Ba}_2\text{Cu}_3\text{O}_{7-x}$ conductor also show positive results following low fluence 5 MeV Ni and 25 MeV Au irradiation, where increases in a-b pinning are observed over the control samples.
- 5.2 High Neutron Dose Irradiation of Dielectric Mirrors — 135**
 K. L. Leonard, G. E. Jellison, Jr., N. A. P. Kiran Kumar, and L. L. Snead (Oak Ridge National Laboratory)
- $\text{HfO}_2/\text{SiO}_2$ and $\text{Al}_2\text{O}_3/\text{SiO}_2$ dielectric mirrors show impressive resistance to neutron irradiation to 0.1 dpa. However, for the $\text{HfO}_2/\text{SiO}_2$ mirror the neutron dose causes crystallinity changes in the film layers of the mirrors and substrate resulting in decreases in reflectivity of the $\text{HfO}_2/\text{SiO}_2$ mirror following post irradiation annealing. Cooling following annealing resulted in delamination. $\text{Al}_2\text{O}_3/\text{SiO}_2$ mirrors appear to have added stability with little microstructural and optical property changes in samples irradiated up to 0.1 dpa and

TABLE OF CONTENTS

annealed to 673 K. However significant Si and Al interdiffusion cause compositional variation that will eventually result in the formation of aluminum-silicate structures on the layer interface, disrupting the optical properties.

Optical tests of samples irradiated to 1 and 4 dpa during the first half of 2013 confirmed that both the $\text{HfO}_2/\text{SiO}_2$ and $\text{Al}_2\text{O}_3/\text{SiO}_2$ do not survive exposure to 4 dpa, resulting in film delamination. Microstructural evaluations of the 4-dpa samples are now being performed to verify and build upon the low dose results.

6. FUSION CORROSION AND COMPATIBILITY SCIENCE

See also Section 2.2.

6.1 Liquid Metal Compatibility – A Thermal Convection Loop for Pb-Li Compatibility Testing — 142

S. J. Pawel, A. W. Willoughby, M. S. Stephens, Z. M. Burns, B. A. Pint, and J. D. McNabb (Oak Ridge National Laboratory)

Fabrication of the first Pb-Li thermal convection loop has been completed. The loop was fabricated using dispersion strengthened FeCrAl (Kanthal APMT) tubing. This alloy is known for high strength and creep resistance at elevated temperature, and based on capsule testing, it is also anticipated to have excellent resistance to Pb-Li.

7. MECHANISMS AND ANALYSIS

7.1 Ion Irradiation Effects on High Entropy Alloy— 145

N. A. P. Kiran Kumar^{1,2*}, K. J. Leonard¹, H. Bei¹, T. S. Byun¹, Y. Zhang^{1,2}, and S. J. Zinkle¹ (Oak Ridge National Laboratory¹, University of Tennessee²)

Preliminary microstructural and nanoindentation examinations have been performed on Fe-28%Ni-27%Mn-18%Cr high entropy alloy specimens irradiated with 3 MeV Ni ions at room temperature to 0.1 and 1 dpa and at 500°C to 1 and 10 dpa. The hardness in the ion irradiated region of the crystalline face centered cubic HEA samples increased rapidly with increasing dose at room temperature, from ~40% higher than the unirradiated value at 0.1 dpa to approximately double the unirradiated hardness at 1 dpa. The increase in the irradiated hardness was less pronounced for irradiations at 500°C, with values of 15-20% increase at 1 dpa and ~20% increase at 10 dpa. Microstructural characterization of the irradiated HEA specimens found small defect clusters after room temperature irradiation and larger defect clusters after 500°C irradiation; voids were not observed at any irradiation condition in the preliminary examination. After irradiation at 500°C, evidence of significant solute segregation was observed at grain boundaries and discrete precipitates were observed; precipitation was not observed in the room temperature irradiated samples. The grain boundary precipitates were highly enriched in Cr and Mn. Overall, the behavior of the high entropy alloy following irradiation at 500°C appears to be significantly different from the behavior observed in irradiated Fe-Cr-Ni austenitic alloys.

TABLE OF CONTENTS

- 7.2 Effects of Ion Irradiation on BAM-11 Bulk Metallic Glass — 154**
 A. G. Perez-Bergquist^{1,2}, H. Bei¹, Y. Zhang^{1,2}, and S. J. Zinkle¹ (¹*Oak Ridge National Laboratory*, ²*University of Tennessee*)
- Preliminary microstructural and nanoindentation examinations have been performed on BAM-11 (Zr-17.9%Cu-14.6%Ni-10%Al-5%Ti) bulk metallic glass (BMG) irradiated with 3 MeV Ni⁺ ions to 0.1 and 1 dpa at room temperature and 200°C. Transmission electron microscopy (TEM) examination indicated the unirradiated and irradiated BMG samples were all fully amorphous with no evidence of nanoscale crystals. The hardness in the ion irradiated region of the BMG samples decreased by nearly 20% after irradiation at room temperature to 0.1 and 1 dpa, and decreased by ~25% and ~10%, respectively after irradiation at 200°C to 0.1 and 1 dpa. The elastic modulus of the irradiated samples decreased by ~10% after irradiation at room temperature to 0.1 and 1 dpa, and increased by ~10% and ~5%, respectively after irradiation at 200°C to 0.1 and 1 dpa. These results suggest that the BAM-11 bulk metallic glass may not have high intrinsic resistance to radiation-induced atomic rearrangements, i.e., the glass may not be in an optimized short-range order configuration for radiation damage stability.
- 7.3 The Effect of Deposition Rate, Miscut Angle and Orientation on FeY₂Ti₂O₇ Interfaces: Implications to the Development and Optimization of Nanostructured Ferritic Alloys — 162**
 T. Stan, Y. Wu, and G. R. Odette (University of California, Santa Barbara)
- The smallest 2-3 nm features in nanostructured ferritic alloys (NFA) are Y₂Ti₂O₇ complex oxide cubic pyrochlore phase. The interface between the bcc Fe-Cr ferrite matrix and the fcc Y₂Ti₂O₇ plays a critical role in the stability, strength and damage tolerance of NFA. To complement other characterization studies of the actual nano-features, mesoscopic interfaces were created by electron beam deposition of a thin Fe layer onto {111} and {100} Y₂Ti₂O₇ bulk single crystal surfaces. Cross-section high resolution TEM was used to characterize details of the interfaces, which ranged from being atomically sharp to more diffuse interface zones that, in some cases, included a thin metallic oxide MO_x layer. The fast deposited polycrystalline Fe layer on the 5 degree miscut {111} Y₂Ti₂O₇ sample has the Nishiyama-Wasserman orientation relationship: {110}_{Fe}||{111}_{Y₂Ti₂O₇} and <001>_{Fe}||<110>_{Y₂Ti₂O₇}. Fe grains on the well-oriented {111} Y₂Ti₂O₇ sample have nano-grains at the interface. The grains on the {100} Y₂Ti₂O₇ sample were {110} textured but had no in-plane orientation relationship with the sample. We recognize that the mesoscopic interfaces may differ from those of the embedded NF, but the former will facilitate characterization and investigations of the functionality of controlled interfaces, such as interactions with point defects and helium.

TABLE OF CONTENTS

- 7.4 An Electron Energy Loss Spectroscopy Study of Helium Bubbles in Nanostructured Ferritic Alloys — 172**
 Y. Wu, R. G. Odette, T. Yamamoto, (University of California, Santa Barbara); J. Ciston, (Lawrence Berkeley National Laboratory); and P. Hosemann (University of California, Berkeley)
- Here we compare a measurement of the helium content in bubbles with a model based on the capillary approximation and a high-pressure equation of state. Electron Energy-Loss Spectroscopy (EELS) measurements on bubbles were carried out using the TEAM 0.5 microscope at the National Center for Electron Microscopy and Lawrence Berkeley Laboratory (LBL). The EELS energy shift can be related to the helium atom density. The best estimate of the helium density was $\approx 61 \pm 2.8$ He atoms/nm³ for bubbles with radii of $\approx 1.36 \pm 0.3$ nm. These results are reasonably consistent with a high pressure EOS assuming a simple capillary model and surface energy of 1.8 J/m².
- 8. MODELING PROCESSES IN FUSION SYSTEM MATERIALS**
- 8.1 Object Kinetic Monte Carlo Simulations of Microstructure Evolution — 179**
 G. Nandipati, W. Setyawan, H. L. Heinisch K. J. Roche, R. J. Kurtz, (Pacific Northwest National Laboratory); and B. D. Wirth (University of Tennessee)
- We have developed a flexible lattice-based object KMC code, *KSOME*, to simulate the evolution of point defects in metals created by particle irradiation. In principle, *KSOME* deals with the migration, emission, creation, transformation and recombination of all types of intrinsic point defects and their complexes. In addition, the interaction of these point defects with sinks such as dislocations, grain boundaries and free surfaces is also treated. *KSOME* is designed such that all the necessary information regarding the properties of defects such as type, size, location, orientation etc., and their diffusion-reaction processes, along with simulation parameters regarding the size, temperature and properties of the simulation cell, are provided via text-based input files. This gives *KSOME* the capability to simulate complex systems involving complex processes that have not been possible with previously developed OKMC codes.
- 8.2 Molecular Dynamics Modeling of Atomic Displacement Cascades in 3C-SiC — 184**
 G. D. Samolyuk, Y. N. Osetskiy, and R. E. Stoller (Oak Ridge National Laboratory)
- A set of atomic displacement cascades was simulated using the Tersoff and Gao-Weber [1] interatomic potentials for SiC. The types of created defects and their dynamics were analyzed. The validity of existing interatomic potentials was investigated by comparing typical point defect formation energies with first principles results.

TABLE OF CONTENTS

- 8.3 First-Principles Calculations of Intrinsic Defects and Mg Transmutants in 3C-SiC — 188**
 S. Y. Hu, W. Setyawan, R. M. Van Ginhoven, W. Jiang, C. H. Henager, Jr., and R. J. Kurtz
 (Pacific Northwest National Laboratory)
- This is an extended abstract for a paper submitted for publication in the Journal of Nuclear Materials [1].
- 8.4 Molecular Dynamics Investigation of Helium Bubble Equation of State — 190**
 Y. N. Osetskiy and R. E. Stoller (Oak Ridge National Laboratory)
- An extensive modeling program was launched earlier to model He-filled bubbles in Fe. We are studying bubbles of radius from 0.25 to 5.0nm with He-to-vacancy ratio from 0.1 to 2.0 over the temperature range 300-1000K. An unexpectedly long simulation time was found to be necessary to accurately determine the equilibrium properties of small bubbles.
- 8.5 Dynamics of Defect-Loaded Grain Boundaries Under Shear Deformation in α -Fe — 193**
 L. Yang, F. Gao, H. L. Heinisch, and R. J. Kurtz (Pacific Northwest National Laboratory)
- The defects produced in collision cascades will interact with microstructural features in materials, such as GBs and dislocations. The coupled motion of GBs under stress has been widely observed in simulations and experiments. Two symmetric tilt GBs with a common $\langle 110 \rangle$ tilt axis ($\Sigma 3$ and $\Sigma 11$) in bcc iron are used to investigate the coupled motion of GBs under shear deformation. Also, we have explored the effect of self-interstitial atoms (SIAs) loading on the GB motion, with different concentrations of interstitials randomly inserted around the GB plane. The simulation results show that the interstitial loading reduces the critical stress of the GB coupled motion for the $\Sigma 3$ GB. Furthermore, the interstitials and vacancies are inserted randomly at the GB plane and at a distance of 1 nm away from the GB plane, respectively, to understand the self-healing mechanism of GBs under stress. The behavior of the defect-loaded GBs depends on the GB structure. The loaded interstitials in the $\Sigma 3$ GB easily form $\langle 111 \rangle$ interstitial clusters that do not move along with the GB. The vacancies in the $\Sigma 3$ GB impede the GB motion. However, the interstitials move along with the $\Sigma 11$ GB and annihilate with vacancies when the GB moves into the vacancy-rich region, leading to the self-healing and damage recovery of the $\Sigma 11$ GB.
- 8.6 Displacement Cascade Simulation in Tungsten at 1025 K — 200**
 G. Nandipati, K. Roche, H. Heinisch, R. J. Kurtz, (Pacific Northwest National Laboratory);
 and B. D. Wirth (University of Tennessee, Knoxville)
- Molecular dynamics simulation was employed to investigate the irradiation damage properties of bulk tungsten at 1025 K (0.25 melting temperature). A comprehensive data set of primary cascade damage was generated up to primary knock-on atom (PKA) energies 100 keV. The dependence of the number of surviving Frenkel pairs (N_{FP}) on the PKA energy (E) exhibits three different characteristic domains presumably related to the different cascade morphologies that form. The low-energy regime < 0.2 keV is

TABLE OF CONTENTS

characterized by a hit-or-miss type of Frenkel pair (FP) production near the displacement threshold energy of 128 eV. The middle regime 0.3 – 30 keV exhibits a sublinear dependence of $\log(N_{FP})$ vs $\log(E)$ associated with compact cascade morphology with a slope of 0.73. Above 30 keV, the cascade morphology consists of complex branches or interconnected damage regions. In this extended morphology, large interstitial clusters form from superposition of interstitials from nearby damage regions. Strong clustering above 30 keV results in a superlinear dependence of $\log(N_{FP})$ vs $\log(E)$ with a slope of 1.365. At 100 keV, an interstitial cluster of size 92 and a vacancy cluster of size 114 were observed.

- 8.7 A Semi-Phenomenological Model for Dislocation Mobility in Tungsten — 205**
D. Rivera, G. Po, T. Crosby, and N. Ghoniem (University of California at Los Angeles, UCLA)

The dependence of dislocation velocity in tungsten on the applied stress and temperature is investigated. A brief theoretical overview of the mechanisms of kink pair formation and the relationship to dislocation motion under stress is given. We then discuss the theory of phonon scattering and its influence on damping dislocation motion at stresses higher than a transition value, where kink nucleation ceases to control dislocation mobility. A general phenomenological framework is formulated, where semi-empirical equations for the dislocation velocity in tungsten are given.

- 8.8 Helium Effects on Displacement Cascades in Tungsten — 223**
W. Setyawan, G. Nandipati, K. Roche, H. Heinisch, R. J. Kurtz, (Pacific Northwest National Laboratory); and B. D. Wirth (University of Tennessee)

Molecular dynamics (MD) simulations were performed to investigate He effects on displacement cascades in W. Helium content, proportion of interstitial and substitutional He and temperature were varied to reveal the various effects. The effect of interstitial He on the number of self-interstitial atoms (SIAs) produced during cascade damage appears to be insignificant. However, interstitial He tends to fill a vacancy (V). Nevertheless, this process is less favorable than SIA-V recombination particularly when excess SIAs are present before a cascade. The efficiency of He filling and SIA-V recombination increases as temperature increases due to increased point defect mobility. Likewise, substitutional He is more susceptible to displacement during a collision cascade than W. This susceptibility increases towards higher temperatures. Consequently, the number of surviving V is governed by the interplay between displaced substitutional He and SIA-V recombination. The temperature dependence of these processes results in a minimum number of V reached at an intermediate temperature.

9. IRRADIATION METHODS, EXPERIMENTS, AND SCHEDULES

- 9.1 HFIR Irradiation Experiments — 228**
Y. Katoh and J. L. McDuffee (Oak Ridge National Laboratory)

1.1 STABILITY OF NANOPRECIPITATES IN FE-BASE MODEL ALLOYS — L. Tan, Y. Katoh, and L. L. Snead (Oak Ridge National Laboratory)

OBJECTIVE

The objective of this work is to determine the stability of MX-type nanoprecipitates in reduced-activation ferritic (RAF) steels using Fe-base model alloys under thermal, stress, and radiation conditions. This will help understand the failure mechanisms of RAF steels and identify promising strengthening particles for advanced RAF steel development.

SUMMARY

The radiation resistance of TaC, TaN, and VN MX-type nanoprecipitates is being evaluated using Fe²⁺ ion irradiation at 500°C for nominal doses of ~20 and ~200 dpa. A parallel study using neutron irradiation at 300, 500, and 650°C for up to about 20 dpa is also in progress. The characterization and analyses of the low dose (~20 dpa) Fe²⁺ ion irradiated samples have been completed. The results indicate that the irradiation did not alter the crystalline nature of the nanoprecipitates. Particle dissolution, growth, and reprecipitation in different levels were observed after the irradiation. The radiation resistance of the carbide was much stronger than the nitrides in declined order TaC, VN, and TaN. TaC nanoprecipitates were observed to be much more resistant to irradiation than reported for a study using similar irradiation conditions. Post-irradiation examination of the high dose (~200 dpa) Fe²⁺ ion-irradiated and neutron-irradiated samples will be conducted and compared to the current observations.

PROGRESS AND STATUS

Introduction

MX-type precipitates have shown excellent coarsening resistance compared to Laves phase and chromium-rich M₂₃C₆ in 9-12% Cr ferritic-martensitic steels as well as RAF steels. They are critical for high temperature strength of this class of steels. Recently, however, limited data have shown the instability of MX, e.g., VN, TaC, and TaN, at elevated temperatures and irradiation conditions [1-4]. Three model alloys, favoring the formation of TaC, TaN, and VN nanoprecipitates, had been prepared to investigate the stability of these nanoprecipitates under thermal, stress, and irradiation conditions [5]. Thermal aging experiments at 600 and 700°C h for up to 5000 h had shown different levels of growth or dissolution for these nanoprecipitates [6]. The experimental progress assessing the radiation resistance of these nanoprecipitates is reported here.

Experimental Procedure

Mini-bars (2 x 2 x 20 mm³) of the three model alloys Fe-1WVN, Fe-1WTaC, and Fe-1WTaN were machined using electro-discharge machining (EDM) with one of the longitudinal surfaces polished to mirror-finish for Fe²⁺ ion irradiation. The center region of the polished surfaces was irradiated using 5 MeV Fe²⁺ ions at 500°C for a nominal dose of ~20 dpa with a dose rate on the order of 10⁻⁴ s⁻¹, using the ion beam facility at University of Michigan through ATR National Science User Facility (ATR-NSUF).

The microstructures of the samples were characterized using transmission electron microscopy (TEM) in both conventional and scanning modes (STEM) on a FEI CM200 field-emission-gun TEM/STEM equipped with an EDAX energy dispersive X-ray spectroscopy (EDS) detector. TEM specimens, perpendicular to the polished surfaces, were lifted out and thinned to electron-transparent using focused ion beam (FIB) on a Hitachi NB5000. Specimen thickness of the characterized regions was estimated using convergent beam electron diffraction (CBED) technique.

Results

The ion irradiation damage to the alloy samples was simulated using the stopping and range of ions in matter software SRIM-2013 [7]. According to Stoller et al. [8], the “quick” Kinchin-Pease option, recommended displacement threshold energies, and zero lattice binding energy for each alloy element were used in the calculation. Figure 1 shows the calculated results with irradiation dose (dpa) as a function of depth into the TaC/TaN/VN samples. The depth distributions of the irradiation doped Fe concentration in atomic percentage (at.%) in respective alloys are also included. The Fe ion irradiation produces approximately the same displacement damage to the three alloy samples with damages gradually increasing from ~7.8 dpa at surface to a peak of ~48.8 dpa at a depth of 1.3 μm , and then quickly decreasing to 0 (unirradiated condition) at ~1.9 μm . The nominal dose of ~20 dpa is corresponding to the dose at half depth to the peak, which is schematically marked with a solid arrow. The irradiation doped Fe concentrations follow pseudo-Gaussian distributions with peaks, occurring behind the damage peak, at a depth of ~1.48 μm in the alloy samples. Slightly different amounts of doped Fe are shown in Fig. 1. It is expected that the amounts of doped Fe, <0.013 at.%, would not influence the microstructure and property of the alloy samples.

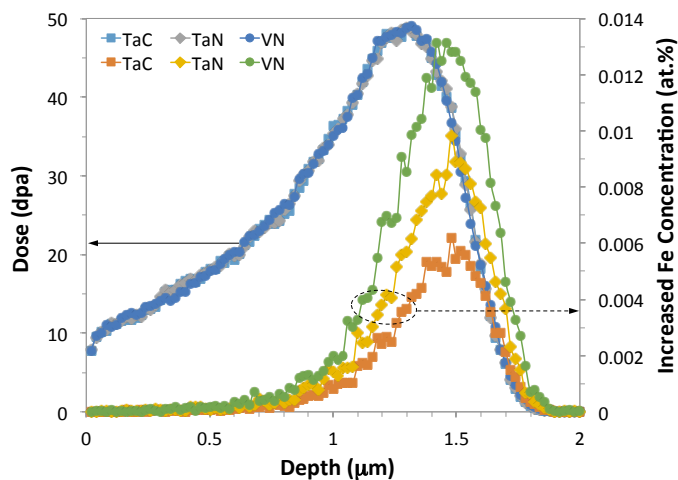


Figure 1. Simulated depth distribution of Fe ion irradiation damage dose (dpa) and doped Fe concentrations (at.%) in the model alloys TaC, TaN, and VN.

The microstructures of the model alloy samples prior to the Fe^{2+} ion irradiation are shown with the bright-field (BF) images in Figure 2. Many nanoprecipitates are uniformly distributed in the alloys. According to the selected area diffraction patterns (SADPs) and equilibrium phase calculation of the alloys, these nanoprecipitates are TaC, TaN, and VN in respective alloys.

Unlike the oval shape of the TaC nanoprecipitates, the TaN and VN nanoprecipitates were found to be in disk shape despite their spherical appearance resulted from their adjacent strain field. The longest side of the nanoprecipitates was used in the statistical particle size measurement. The CBED estimated specimen thickness was assumed to be uniform within the characterized regions. The volumetric number density and size of the nanoprecipitates were analyzed and plotted in Figure 4.

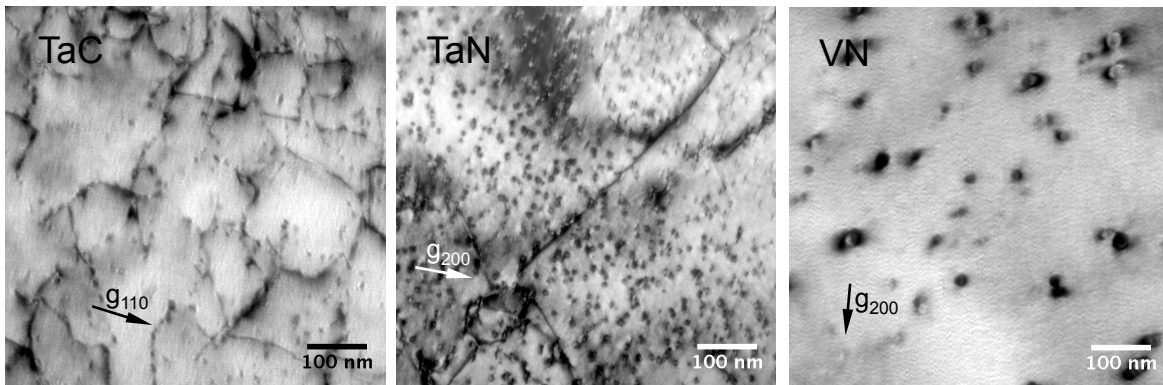


Figure 2. BF images of the unirradiated model alloys showing the distribution of the TaC, TaN, and VN nanoprecipitates.

High-angle annular dark field (HAADF) STEM was used to characterize the TaC nanoprecipitates. The Z-contrast imaging technique was found to be suitable for TaC, which captured the TaC distribution throughout the irradiated depth. Figure 3a shows a HAADF-STEM image of TaC irradiated to ~20 dpa at half-depth to the damage peak. The black arrow denotes the irradiation direction. The HAADF-STEM contrast of TaN was not as good as TaC, which was even worse for VN because of the lower weight (or Z) of V compared to Ta. Therefore, dark-field (DF) imaging using the beam condition as shown in Fig. 3 was employed to characterize TaN and VN. Figures 3b and 3c exhibit the DF images of TaN and VN, respectively, irradiated for ~20 dpa at half-depth to the damage peak. The white particles of TaN and VN are approximately parallel to the irradiation direction. This orientation relationship was not a result of the irradiation because other orientation relationship, e.g., approximately perpendicular to the irradiation direction, was also observed in other grains.

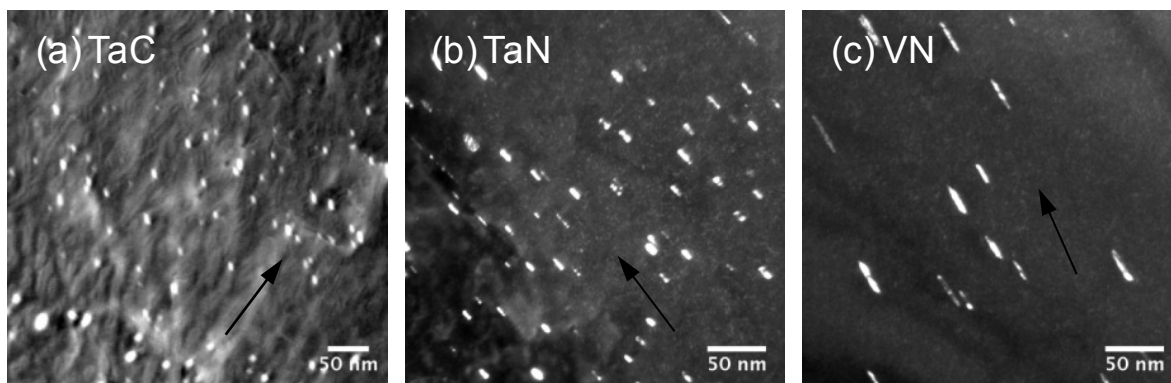


Figure 3. (a) HAADF (STEM) and (b-c) DF (TEM) images of the TaC, TaN, and VN irradiated to ~20 dpa. The arrow on each image indicates the irradiation direction.

The density and average size of the TaC, TaN, and VN nanoprecipitates after ~20 dpa irradiation are plotted in Figure 4 in solid symbols, comparing to the data in the unirradiated condition in open symbols. Slight dissolution (smaller size) with some reprecipitation (larger density) were observed for the TaC nanoprecipitates after the irradiation. In contrast, the irradiation resulted in some increase in density with significant growth in size of VN. The large standard deviation of size may also suggest the coexistence of particle growth and reprecipitation. However, TaN had slightly decreased size, together with significantly decreased density, suggesting primary dissolution of TaN after the irradiation.

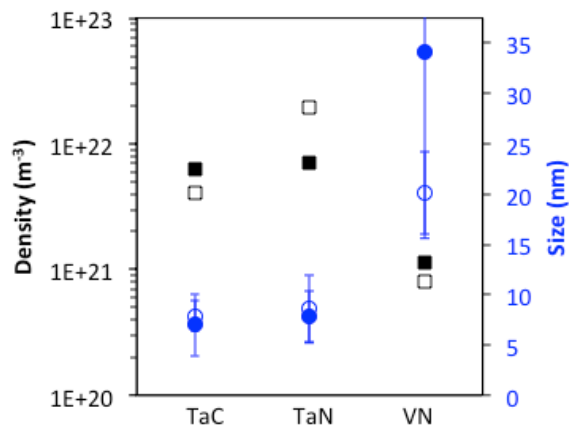


Figure 4. Particle density (black squares) and size (blue circles) after ~20 dpa irradiation (solid symbols) compared to the initial unirradiated condition (open symbols) of TaC, TaN, and VN nanoprecipitates.

The relatively good radiation resistance of TaC nanoprecipitates was inconsistent with the literature reported predominant dissolution of TaC after Fe^{3+} ion irradiation of Fe-0.2Ta-0.015C alloy at 500° for ~20 dpa [3,4] and neutron irradiation of ORNL9Cr-2WVTa and JLF-1 RAF steels at 300°C for ~5 dpa [3,4]. The predominant dissolution of TaC in the neutron-irradiated RAF steels may be attributable to the lower irradiation temperature, lower particle volume fraction, and more likely to be the nature of Ta(C,N) rather than TaC, due to the presence of relatively

high nitrogen content in the steels, as suggested in this study that the radiation resistance of nitride is inferior to carbide. The slightly lower particle volume fraction in Fe-0.2Ta-0.015C alloy may have favored the greater dissolution of TaC compared to the observations in this work. However, the lower volume fraction should not result in the dominant dissolution of TaC. Other factors, e.g., irradiation temperature, displacement rate, etc., may have also played roles.

Fe²⁺ ion irradiation of the alloy samples for a nominal dose of ~200 dpa has been completed recently. The microstructural characterization and analysis will be conducted in the same way to have a clear picture regarding the radiation resistance of these MX-type nanoprecipitates. Neutron irradiation of the alloy samples will be finished soon. The effect of dose, dose rate, and irradiation temperature on particle stability will be explored.

REFERENCES

- [1] M. Tamura, H. Sakasegawa, A. Kohyama, H. Esaka, and K. Shinozuka, *J. Nucl. Mater.* **329**, 328 (2004).
- [2] A. Kabadwal, M. Tamura, K. Shinozuka, and H. Esaka, *Metall. Mater. Trans. A* **41**, 364 (2010).
- [3] H. Tanigawa, H. Sakasegawa, and R. L. Klueh, "Irradiation Effects on Precipitation in Reduced-Activation Ferritic/Martensitic Steels," *Mater. Trans.* **46**, 469-474 (2005).
- [4] H. Tanigawa, H. Sakasegawa, H. Ogiwara, H. Kishimoto, and A. Kohyama, "Radiation Induced Phase Instability of Precipitates in Reduced-Activation Ferritic/Martensitic Steels," *J. Nucl. Mater.* **367-370**, 132-136 (2007).
- [5] L. Tan, "Stability of Strengthening Precipitates in Model Ferritic Steels," Semiannual Progress Report, DOE/ER-0313/52, June 30, 2012.
- [6] L. Tan, Y. Katoh, and L. L. Snead, "Stability of Nanoprecipitates in Fe-Base Model Alloys," Semiannual Progress Report, DOE/ER-0313/53, December 31, 2012.
- [7] The Stopping and Range of Ions in Matter (SRIM) (<http://www.srim.org>).
- [8] R. E. Stoller, M. B. Toloczko, G. S. Was, A. G. Certain, S. Dwaraknath, and F. A. Garner, "On the Use of SRIM for Computing Radiation Damage Exposure," *Nucl. Instrum. Methods Phys. Res. B* **310**, 75-80 (2013).

1.2 RECENT OBSERVATIONS OF HELIUM EFFECTS ON CAVITY EVOLUTION IN TEMPERED MARTENSITIC STEELS — T. Yamamoto, Y. Wu, G. R. Odette, (University of California, Santa Barbara); S. Kondo, and A. Kimura (Kyoto University)

OBJECTIVE

The objective of this work is to characterize the effects of He/dpa ratio on cavity evolution under Fe^{3+} and He^+ dual ion beam irradiation in a normalized and tempered martensitic steel (TMS) F82H mod.3.

SUMMARY

New dual ion (Fe^{3+} and He^+) beam irradiations (DII) were performed at 500°C on a group of ferritic alloys up to nominal dpa and He levels of 26 dpa and 390 appm, respectively, at a He (appm)/dpa ratio of ≈ 15 using the DuET facility at Kyoto University in Japan. The actual dpa, He and He/dpa vary with depth in the sample. The alloys studied include normalized and tempered martensitic steels, (TMS) F82H IEA in as-tempered and cold-worked conditions as well as F82H mod.3, and a nanostructured ferritic alloy (NFA), MA957. To date, TEM observations have been performed for F82H mod.3 at depths from 0.1 to 1.7 mm. In the F82H mod.3, the number density of the cavities (N) ranged from 1 to $9 \times 10^{21}/\text{m}^3$ while average diameter ($\langle d \rangle$) of all the cavities ranged from 2.4 to 5.5 nm. The N are significantly smaller than that for higher ≈ 47 appm He/dpa in previous study, while the $\langle d \rangle$ are similar.

BACKGROUND

Predicting and mitigating the effects of a combination of large levels of transmutant He and displacement damage (dpa), produced by high energy neutrons, on the dimensional stability and mechanical properties of structural materials is one of the key challenges in the development of fusion energy [1]. The fundamental overriding questions about He-dpa synergisms include: a) what are the basic interacting mechanisms controlling He and defect transport, fate and consequences, and how are they influenced by the starting microstructure and irradiation variables (dpa rate, He/dpa ratio, temperature and applied stress) and, b) how can the detrimental effects of He-dpa synergisms be mitigated and managed by proper microstructural design? In the absence of a fusion neutron source, we have been utilizing various alternative experimental techniques to study the He-dpa synergisms, that includes: a) in situ He implantation (ISHI) in mixed spectrum fission reactors, HFIR at ORNL and ATR at INL; b) spallation proton irradiation (SPI) in STIP (spallation target irradiation projects) at Paul Scherr Institute in Switzerland; and, c) multiple ion beams to simultaneously implant He and create displacement damage with heavy ions. In this work we specifically use the dual ion beam irradiation (DII) facility, DuET, at Kyoto University, Japan. The DII produces a broad range of dpa and He up to very high levels in short periods of time. However, great caution is required in applying DII data to neutron irradiation conditions due to a host of differences including dpa rates, the proximity of a free surface and injected interstitials and impurities in some cases. Nevertheless, DII are useful for mechanism studies and it is important to compare and contrast DII microstructural evolutions with the corresponding effects of neutron irradiations. Here we report the results of DII up to ≈ 45 dpa at He/dpa ratio of ≈ 15 appm/dpa compared with our earlier results for He/dpa ≈ 47 appm/dpa [2].

PROGRESS AND STATUS

Experimental Procedure

Table 1 summarizes the irradiation conditions of our new and previous DII experiments performed on ferritic materials at 500 °C. The new irradiation was aimed to achieve the same nominal displacement damage level of 26 dpa as in a previous study, but at a lower, 15 versus 47, appm He/dpa ratio. The alloys included were F82H IEA in as tempered as well as in 20% or 50% cold-worked conditions, F82H mod.3 and MA957. The latter two alloys are common to all irradiation conditions and permit single variable comparisons. The irradiated specimens, with mechanically and electrically polished surfaces, were in the form of coupons approximately 1 mm wide and 20 mm long extracted from 0.5 mm thick wafers. The DII was performed in DuET facility at the Institute of Advanced Energy, Kyoto University (Kyoto, Japan). The Fe^{3+} ions were accelerated to 6.4MeV by a tandem accelerator and the He^+ ions were accelerated to 1MeV by a single end accelerator. The specimens were positioned in a temperature-monitored/controlled stage. The He^+ ion beam passed through a rotating energy degrader creating four ion implantation energy bands that result in a broader and more uniform He deposition profile up to the maximum depth of ≈ 1.5 mm. Figure 1a shows dpa and He profiles estimated using TRIM 2008 code for ion currents that were monitored and re-adjusted hourly. The damage calculations are based on Kinchin-Pease model with displacement energies of 40 eV for Fe and Cr as recommended in ASTM E521-96 (2009) [3]. The displacement damage increases with depth to peak at ≈ 1.5 mm deep and tails off at ≈ 2 mm deep. The overall He profile created by four energy bands has a slightly smaller range. The He deposition increases within the range from ≈ 400 appm at 0.4 mm to ≈ 670 appm at 1.1 mm deep, roughly tracking the corresponding dpa. Thus the resulting He/dpa ratio is relatively constant at 16.3 ± 2.4 appm/dpa over a wide depth interval. Figure 1b shows the corresponding estimates for the previous irradiation that had ≈ 3 times more He with almost identical dpa damage levels.

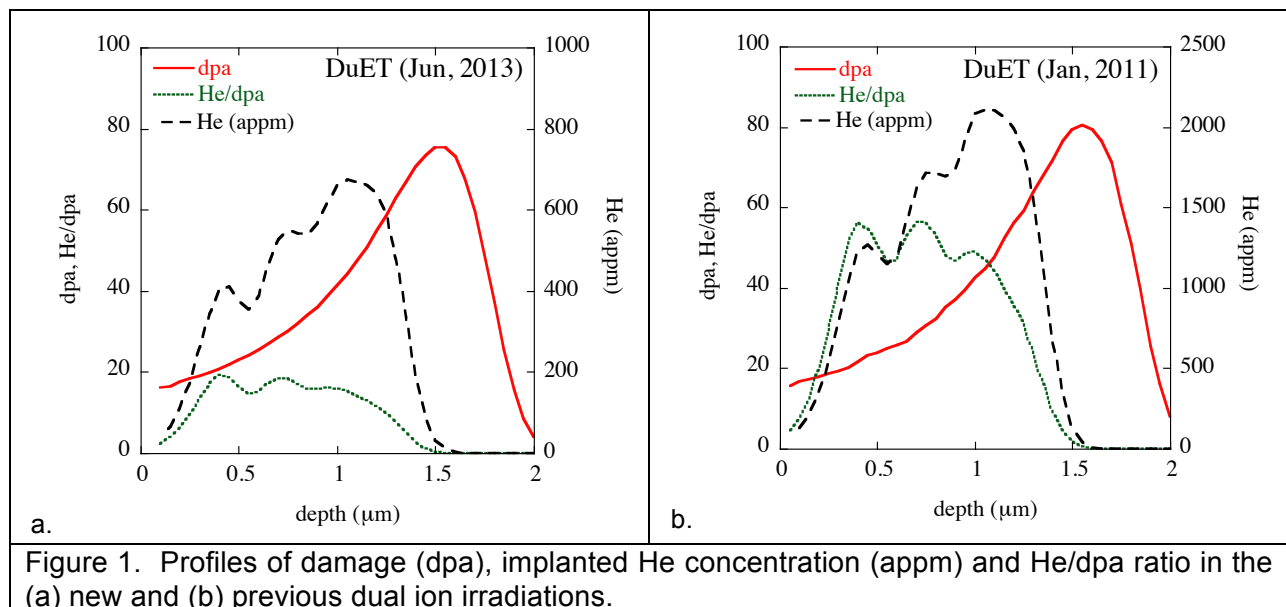


Figure 1. Profiles of damage (dpa), implanted He concentration (appm) and He/dpa ratio in the (a) new and (b) previous dual ion irradiations.

A FEI HELIOS Focused Ion Beam (FIB) tool was used to micro-machine < 100 nm thick electron transparent $\approx 5 \mu\text{m}$ wide and $5 \mu\text{m}$ deep lift-outs that included both damaged-implanted and undamaged regions. TEM was performed on the FEI 200 keV Technai T20 and 300 KeV Titan instruments in the UCSB Microstructure and Microanalysis Facility. Through focus series images were analyzed to identify and quantify the average diameter ($\langle d \rangle$), number density (N) and volume fraction (f_v) of cavities at various depths.

Table 1. Summary of DuET experimental conditions.

Exp ID	Materials	T (°C)	Nominal Condition (@550-650nm)				Peak He (@1000-1100nm)		
			dpa	He (appm)	He/dpa	dpa/s	dpa	He (appm)	He/dpa
DI10B1	F82H mod.3, MA957	500	26	1210	47	5.0×10^{-4}	45	2100	47
DI10B3			10	480	47	5.1×10^{-4}	18	840	47
DI13A1	F82H mod.3, F82H IEA (AT, 20%CW or 80%CW), MA957	500	26	390	15	5.1×10^{-4}	44	670	15

Results

Cavity Microstructures After DII at 500°C

Figure 2 compares low magnification overviews of representative cavity microstructure over the depth range from 0 to $2 \mu\text{m}$ for a) 15 appm He/dpa and b) 47 appm He /dpa, in the images taken at -1500 nm underfocus condition. The cavity formation peaks near the highest He concentration at the depth around $1.1 \mu\text{m}$ in both cases. Cavity formation can also be seen near the surface at a depth as shallow as $\approx 0.02 \mu\text{m}$ at corresponding damage level of $\approx 5 \text{ dpa}$ and He levels of $\approx 10 \text{ appm}$ and $\approx 30 \text{ appm}$, respectively. Cavity formation is also observed up to a depth of $\approx 1.75 \mu\text{m}$ in 15 appm He/dpa case and up to $1.63 \mu\text{m}$ in 47 appm He/dpa case. This corresponds to the maximum He energy/range in the DII irradiation. These general trends are consistent to the evaluation of implanted He concentrations shown in Figs 1.

Figure 3 compares higher magnification cavity images in the peak He region for both He/dpa conditions. The depth increases from top to bottom and the estimated dpa levels are $\approx 45 \text{ dpa}$ at the center of the images; the corresponding He concentrations are 670 (Figure 3a) appm and 2100 (Figure 3b) appm, respectively. Clearly the higher He creates significantly more visible cavities. However, even in the lower He case most of the cavities appear to have transformed to growing faceted voids with a peak at sizes that are similar to those in the higher He case. Figure 4 shows the size distribution of cavities, including data from other locations at the same depth. Three quarters of cavities are around 6.5 nm in diameter in the lower He case, with a peak that is shifted to a larger size than for the higher He/dpa case, at $\approx 4 \text{ nm}$ in the latter case; however voids as large as $\approx 20 \text{ nm}$ in diameter are observed in higher He condition. Note, due to the small N, from ≈ 0.7 to $8.6 \times 10^{21}/\text{m}^3$, at lower He, far fewer cavities sampled, even though the same total area of the sample was imaged. We will continue to analyze the lower He/dpa case to get a better statistics on the cavity size distributions.

Figure 5a shows the $\langle d \rangle$ of cavities obtained in 100 nm sections over the entire implantation depth range from 0.1 to 1.6 μm in the sample DII at both appm He/dpa. Figures 5b and 5c shows the corresponding cavity N and f, respectively. The N is fewer in at the lower He/dpa, but the $\langle d \rangle$ are remarkably similar. The corresponding f_v is much lower than in the higher He case, due to the large difference in N.

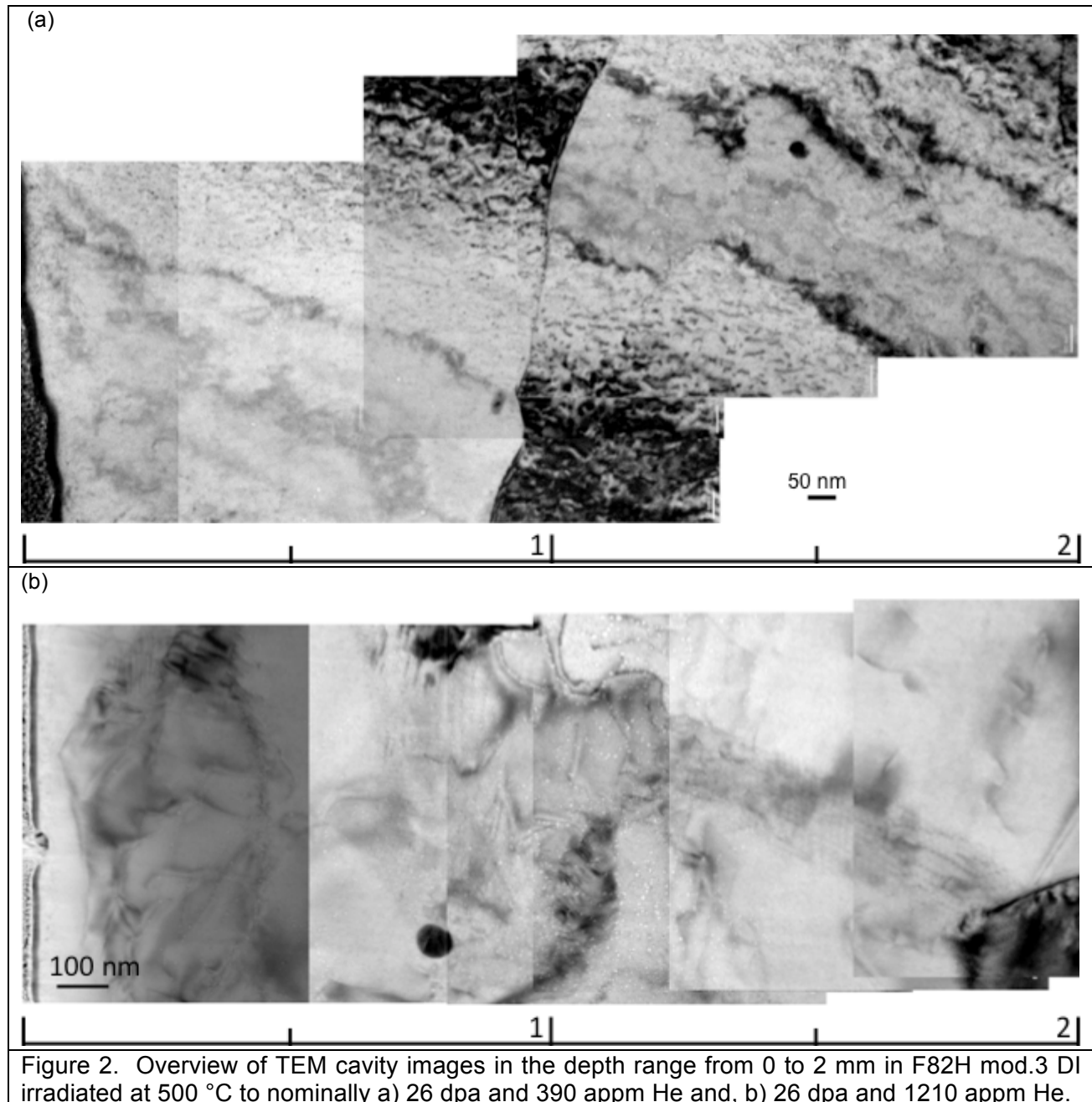


Figure 2. Overview of TEM cavity images in the depth range from 0 to 2 mm in F82H mod.3 DI irradiated at 500 °C to nominally a) 26 dpa and 390 appm He and, b) 26 dpa and 1210 appm He.

Discussion

In our previous analyses of DuET and HFIR in-situ helium implantation (ISHI) experiments, He^*dpa was used as an add-hoc but useful parameter to view data trends in the various He and dpa conditions. Figures 6 show the updated plots of $\langle d \rangle$, N and f_v as a function of He^*dpa for most of the data obtained in our DuET and ISHI experiments in the TMS alloys including Eurofer 97 and F82H mod.3 in cold-worked condition. Note that the cavity statistics are very sensitive to the local microstructure, which varies significantly from place to place. Thus the variability in comparing small regions of irradiated volume is very large. Since the ISHI regions are order 25 or larger than for the DII, the variability in the latter case is especially significant. Thus the shaded regions in Figure 6 are meant to draw attention to general trends that have been observed. Additional TEM studies that cross-correlate local microstructure characteristics with cavity statistics will be needed for further quantification. The average cavity size, $\langle d \rangle$, increases with He^*dpa and is similar for the ISHI and DII conditions. The cavity number density, N , appears to peak in both cases and on average is much higher for the ISHI case, especially compared to the lower He DII condition. The cavity volume fraction, f_v , increases more rapidly for the ISHI, beginning at a lower He^*dpa .

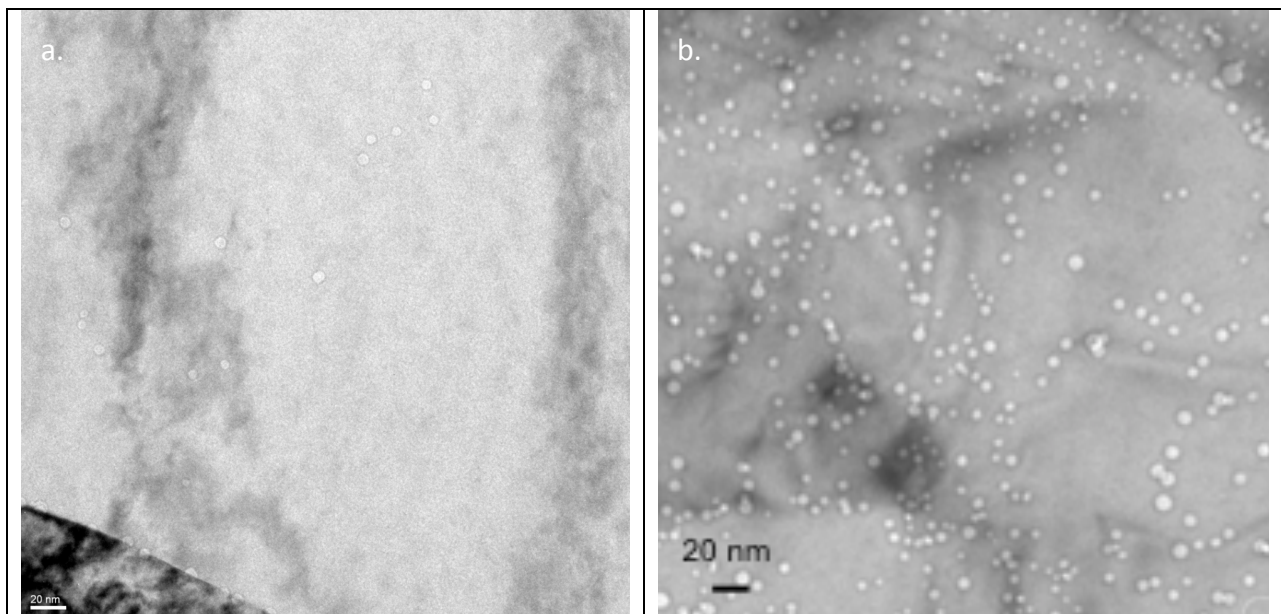


Figure 3. Underfocus cavity images of F82H mod.3 DI irradiated at 500 °C to the damage level of ≈ 45 dpa and He levels of (a) 670 appm and (b) 2100 appm. The damage and He levels are estimated for the vertically center location in the images.

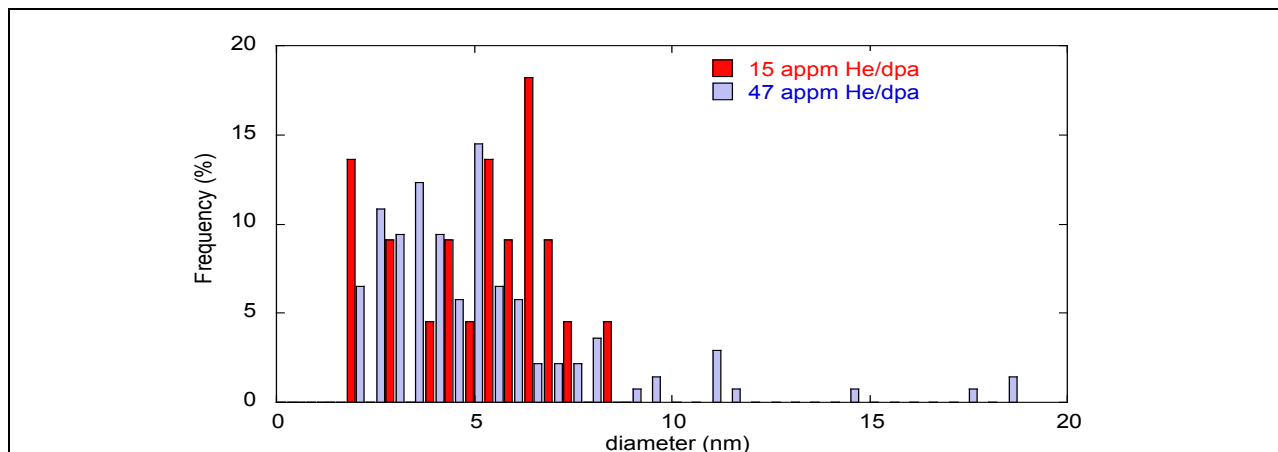
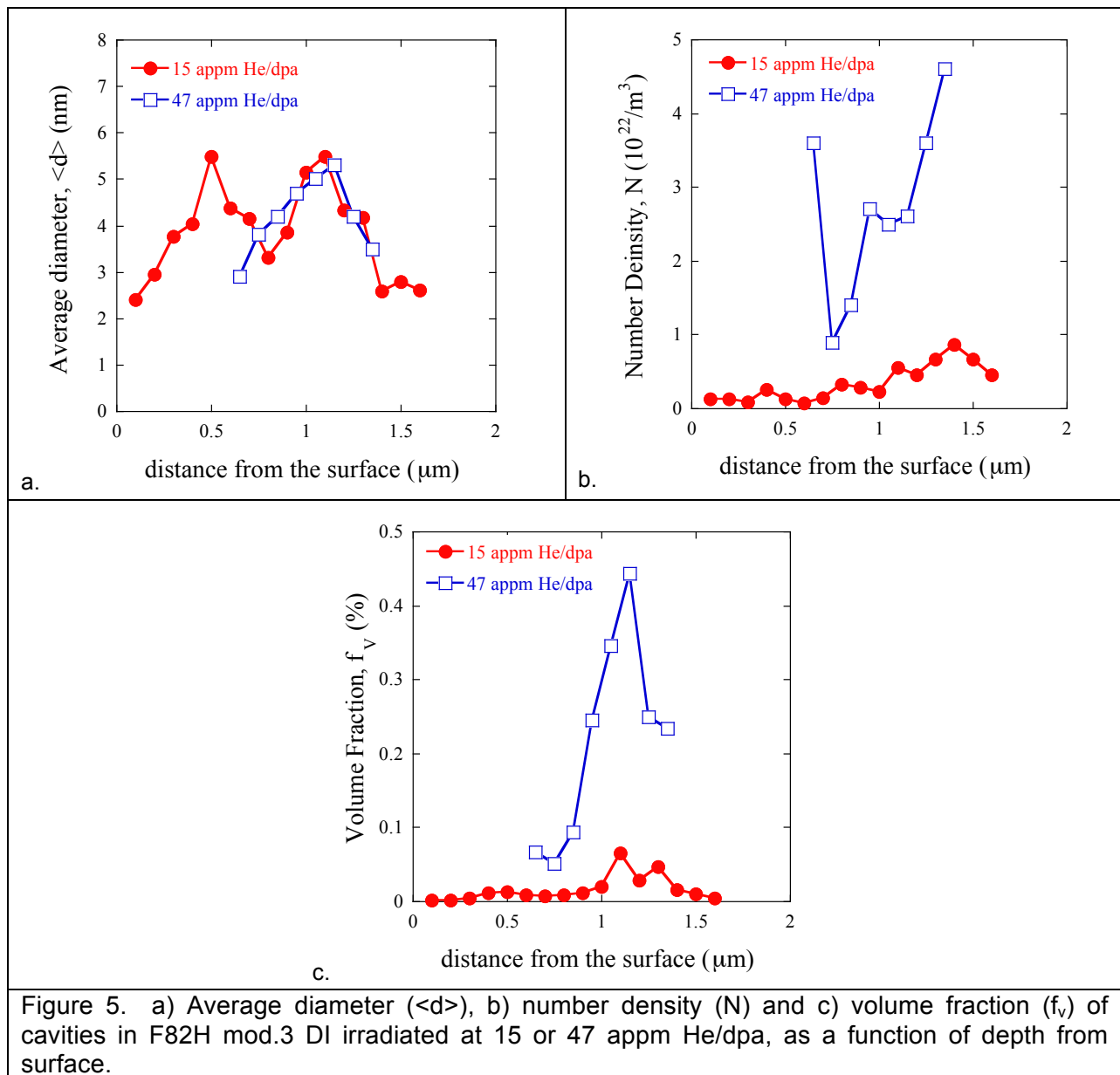
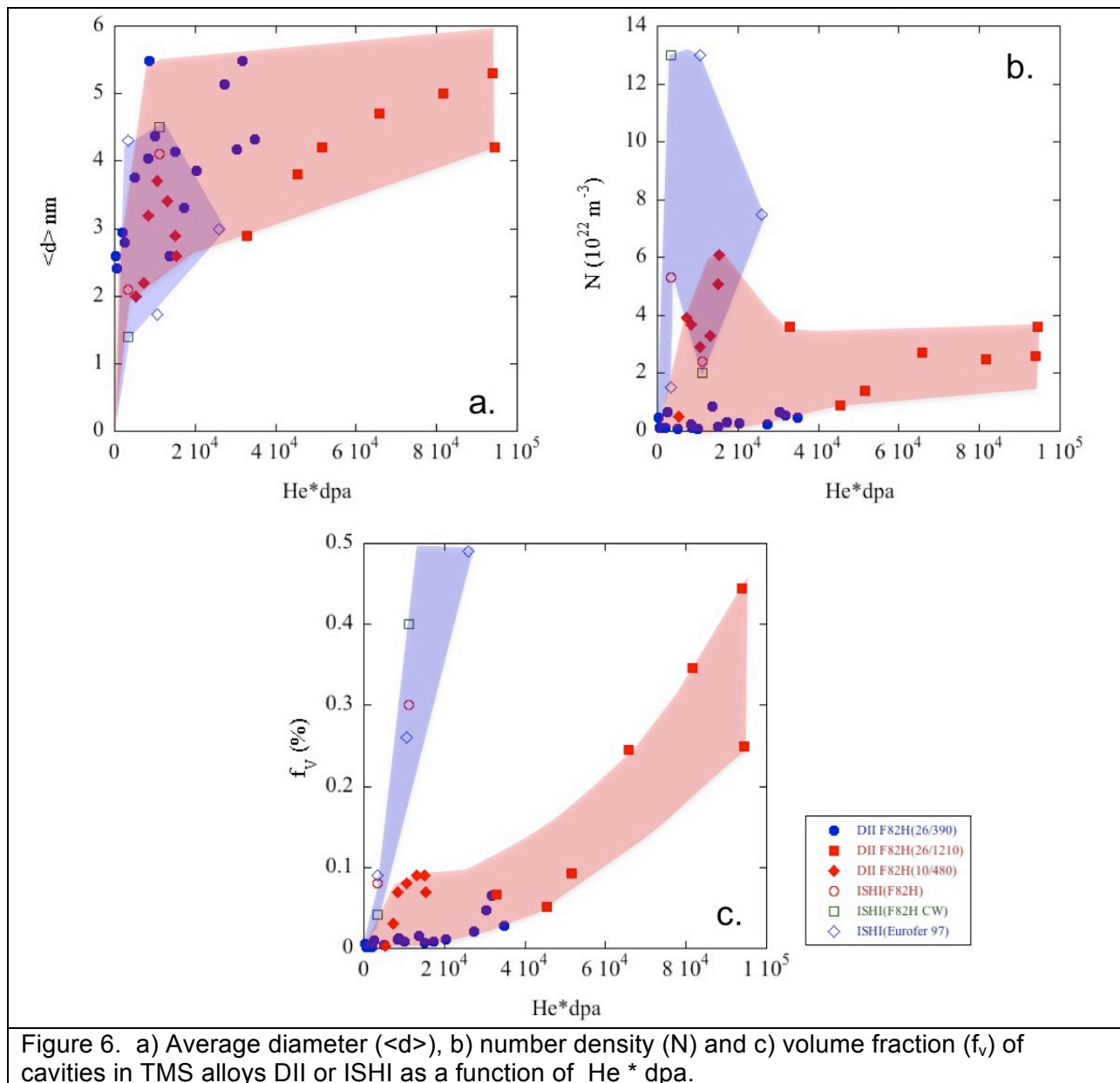


Figure 4. Size distributions of cavities in F82H mod.3 DI irradiated at 500 °C to the damage level of ≈ 45 dpa and He levels of 670 appm and 2100 appm. The damage and He levels are estimated at the center depth location of the images.





FUTURE WORK

We will continue to analyze microstructures from previous a new DII experiments.

ACKNOWLEDGEMENTS

The work performed at UCSB was supported by the U. S. Department of Energy, Office of Fusion Energy Sciences, under contract DE-FG03-94ER54275. The DuET experiments are supported by the Joint Usage/Research Program on Zero-Emission Energy Research, Institute

of Advanced Energy, Kyoto University. We acknowledge the contributions of the NSF sponsored UCSB Microstructure and Microanalysis Facility.

REFERENCES

- [1] Y. Dai, G. R. Odette, and T. Yamamoto, “*The Effects of helium on irradiated structural alloys,*” in *Comprehensive Nuclear Materials*, R. Konings, T. R. Allen, R. E. Stoller, and S. Yamanaka Eds. (2012) Elsevier.
- [2] T. Yamamoto, Y. Wu, G. R. Odette, K. Yabuchi, S. Kondo, and A. Kimura, *Fusion Materials Semiannual Report 12/31/2010* DOE/ER-313/52 (2011) 8.
- [3] ASTM Standards E521-96 (2009), ASTM International (2009).

2.1 CHARACTERIZATION OF A LARGER BEST PRACTICE HEAT OF 14YWT IN ANNEALED POWDER, HIP CONSOLIDATED AND EXTRUDED FORMS —

N. J. Cunningham, Y. Wu, G. R. Odette, (University of California, Santa Barbara); D. T. Hoelzer, (Oak Ridge National Laboratory); and S. A. Maloy (Los Alamos National Laboratory)

OBJECTIVES

The objective is to characterize a set of 14YWT alloys made from a large heat of gas atomized and mechanically alloyed powder using an alternative processing method that incorporates Y during the gas atomization process.

SUMMARY

We describe the characterization of new 14YWT heats from gas atomized and mechanically alloyed powder using an alternative processing method that incorporates Y during the gas atomization process. Post mechanically alloying processes included annealing the powder at 850°C and 1150°C, HIP consolidation at 850°C and 1150°C, and consolidation by hot extrusion at 850°C, annealing for 1 h at 1000°C, and then cross-rolling to 50% thickness at 1000°C; the latter has been dubbed FCRD-NFA1. In all cases a high number density of nm-sized features were observed using a combination of atom probe tomography, transmission electron microscopy, and small angle neutron scattering. The 850°C lower temperature annealing and HIP consolidation resulted in smaller precipitates compared to the 1150°C processing temperature. However, after annealing at 1200°C for 48 h the precipitate size and number density were similar in the two cases. The FCRD-NFA1 had a microstructure and NF distribution similar to a previously reported alloy, PM2. However, the extruded samples also had a large number of large (>20 nm) Ti-rich precipitates. These larger precipitates may affect the mechanical properties, which are currently under investigation.

BACKGROUND

Nanostructured ferritic alloys (NFAs) have outstanding properties for applications in advanced fission and fusion reactors. NFAs are strengthened and made irradiation tolerant by a high number density of thermally stable Y-Ti-O nanofeatures (NFs). The conventional NFA processing path uses ball milling to mechanically alloy Y_2O_3 in the Fe-Cr matrix, which is an expensive process and often leads to heterogeneous distributions of NFs. To overcome these challenges an alternative processing path in which Y is included in the melt prior to gas atomization and rapid solidification was developed in collaboration with partner institutions including Oak Ridge National and Los Alamos National Laboratory, ATI Powder Metals, UC Berkeley and South Dakota School of Mines. Many small lab heats of NFA were prepared using this alternative processing method and analyzed in a program primarily funded by the DOE Office of Nuclear Energy [1]. The results of this extensive effort were used to identify the best processing practices. A previous report detailed the production, characterization, and mechanical property testing of the final extruded and hot cross-rolled heat known as 14YWT-PM2 (PM2) for the small-batch studies [2]. This report describes a larger heat of gas atomized and ball milled powder that was produced using the “best practices” knowledge gained by the smaller scale testing.

ATI Powder Metals Laboratory (Pittsburgh, PA) produced the 14YWT-atomized powders in its Laboratory Gas Atomizer (LGA) vacuum induction melting (VIM) furnace. Details of the atomization process are described elsewhere [2]. After atomization the Y is phase separated

and requires ball milling. A total of 15 kg of nominal 14wt.%Cr-3wt.%W-0.35wt.%Ti-0.25wt.%Y iron alloy powder was ball milled by Zoz, GmbH (Wenden, Germany) with 52.5 g of FeO powder for 40 h in a CM100b attritor mill with a ball mass-to-charge ratio of 10:1 and ball size of 5 mm. The canister was evacuated and backfilled with Ar three times to remove any atmosphere contamination and milled in Ar at an overpressure of 100 mbar. The milling speed alternated between 256 (2 minutes) and 150 rpm (10 minutes). FeO was added to increase the O content to ≈ 0.08 wt.%.

This milled powder (V540) was analyzed in several conditions, including as annealed powder, after HIP consolidation and after hot extrusion. After outgassing at 400°C under vacuum the powder was annealed at both 850 and 1150°C for 3 h at 15°C/min ramp and cooling rates. Atom probe tomography (APT) was performed on both conditions and TEM was performed on the 1150°C-annealed powder. Two HIP consolidated alloys were produced from the outgassed samples using a pressure of 200 MPa for 3 h also at both 850 and 1150°C. The HIP consolidated alloys were subsequently aged at 1200°C for times of 48, 96, 144, and 228 h. Both small angle neutron scattering (SANS) and Vicker's micro-hardness (μH) measurements were performed on the as-HIPed and aged specimens. A final alloy designated FCRD-NFA1 was consolidated at ORNL. The powders were first canned and degassed at 400°C then hot extruded at 850°. After extrusion the alloy was annealed for 1 h at 1000°C and hot cross-rolled to a $\approx 50\%$ thickness of ≈ 10 mm. A full microscopic analysis was performed on this alloy including SANS, μH , APT, and TEM. Mechanical testing including fracture, creep, and tensile testing is currently underway.

TEM was performed on FIB lift-out specimens using both FEI Titan 300 kV and FEI T20 200 kV instruments. Grain size measurements and NF size and number density measurements typically used bright field imaging. The NFs were manually counted and the size distribution and number density was measured using image J. The convergent beam techniques were used to measure the foil thickness. Atom probe tomography was performed using a LEAP 3000X HR instrument. All samples were prepared using an FEI Helios FIB using the lift-out method outlined by Thompson [3]. Samples were primarily run in voltage mode, with one sample run in laser mode. All voltage mode samples were at temperatures between 35 and 55 K, 1% evaporation rate, 20-25% voltage pulse, and 200 kHz pulse frequency. The normal green laser energy was ≈ 0.2 nJ, but a test on one sample was performed to assess the effects of very high laser energy of 0.7 nJ. All analysis was performed using the IVAS software. SANS was performed at the NIST Center for Neutron Research in Gaithersburg, MD on the NG-7 30m SANS beamline. A collimated neutron beam with 5 ± 0.3 Å wavelength was scattered by 1 mm x 10 mm x 10 mm samples in a 1.7 ± 0.1 T horizontal magnetic field. The raw SANS data consists of an intensity map, $I(x,y) = I(q,\varphi)$, of the neutron counts on a two-dimensional ^3He detector. Here φ is the angle with respect to the magnetic field and q is the scattering vector, which is a function of the scattering half angle, θ , and the neutron wavelength, λ . The 64 cm x 64 cm detector with 0.5 cm X 0.5 cm pixel size was located 1.55 m from the sample and offset by ≈ 20 cm in the horizontal direction to give a higher q range of ≈ 0.05 to 4 nm⁻¹, corresponding to a feature size length scale of 12.6 to 1.6 nm ($d \approx 2\pi/\lambda$). Scattering from a control (Fe-14wt.%Cr-3wt.%W-0.4wt.%Ti), that does not contain Y, was subtracted from the alloy of interest to isolate the NF scattering and the resulting signal was fit to determine average diameter ($\langle d \rangle$), number density (N), and volume fraction (f) from the sample using the method given by Alinger et al. [4].

STATUS AND PROGRESS

Milled and annealed powders

The TEM micrograph in Figures 1a shows a bimodal grain structure in the 1150°C-annealed powder, with a mixture of small grains, <math><0.5 \mu\text{m}</math>, and larger grains, several μm in size. The FIBed sample was too small for an accurate overall grain size measurement. Figure 1b shows the NF distribution, shown by the small dark spots, with an average diameter ($\langle d \rangle$) $\approx 1.5 \text{ nm}$, a number density (N) of $\approx 6.5 \times 10^{23} \text{ m}^{-3}$, and a nominal volume fraction (f) of 0.18%.

Three APT tips from the 850°C annealed powder were analyzed (≈ 10 million ions) and five tips were analyzed from the 1150°C annealed powder (≈ 34.5 million ions). In all cases, a high NF number density was observed. The average bulk composition for both annealing temperatures is shown in Table 1. The bulk composition for the various annealing temperature were generally similar, except that the 1150°C anneal had a Y content of 0.044 at.% while the 850°C anneal was 0.076 at.%. Although the Y was lower in the 1150°C anneal, the range from 0.044 to 0.076 at.% Y is not unexpected and is consistent with previous studies. The low value of Y may be due to the inhomogeneity of the NF distribution or larger Y precipitates that are not observed by APT due to their small number density and the small sample size. There is also a possibility of undercounting Y ions that are undetected in the atom probe analysis. A small amount of N was observed and indicates that the milling procedure minimized contamination compared to some previous alloys.

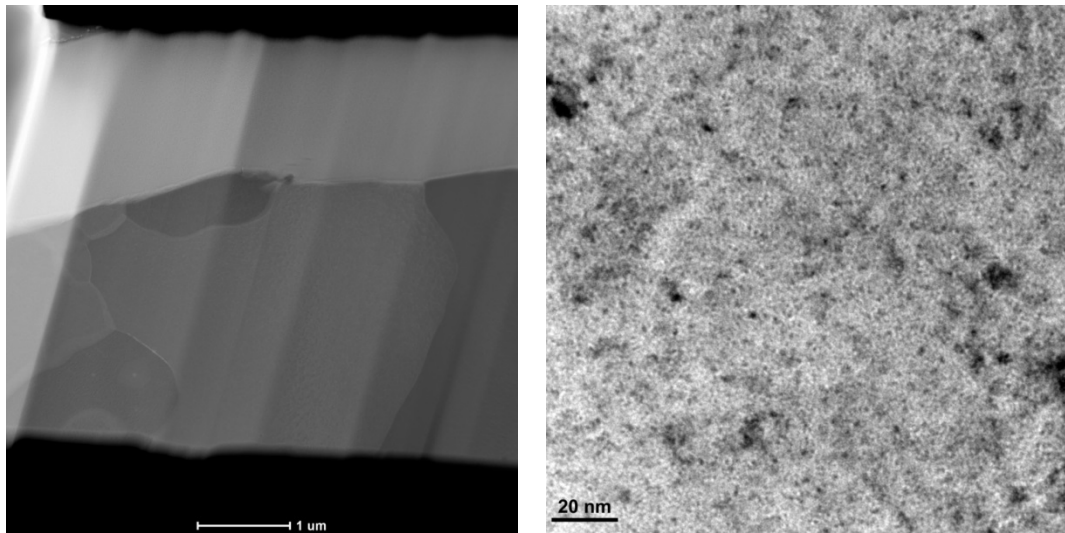


Figure 1. TEM images of 1150°C annealed powder showing a) bimodal grain size and b) fine dispersion of NF.

Table 1. The average APT bulk composition (at.%) in the V540 850 and 1150°C annealed powders.

	Fe	Cr	W	Ti	Y	O	C	Si	N
850°C Anneal	82.61	15.41	0.998	0.381	0.076	0.263	0.064	0.073	0.002
1150°C Anneal	83.10	15.13	0.980	0.361	0.044	0.225	0.017	0.063	0.002

Table 2 shows the matrix composition, excluding NFs, for the two samples. Again the composition is similar for the two aging temperatures. Except for large reductions in the Ti, Y, and O that are associated with the NFs there is little change between the bulk and matrix compositions. The Ti and O are reduced by $\approx 50\%$ while the Y is reduced by more than 70%.

Table 2. The average APT matrix composition (at.%) in the V540 850 and 1150°C annealed powders.

	Fe	Cr	W	Ti	Y	O	C	Si	N
850°C Anneal	83.07	15.38	0.996	0.185	0.018	0.131	0.052	0.066	0.001
1150°C Anneal	83.482	14.988	0.975	0.241	0.012	0.156	0.013	0.060	0.002

Table 3 shows the average composition of the clusters after correcting for iron and other matrix atoms. Again both alloys show similar average NF composition. There is significant Cr content in the NF of $\approx 20\%$ and the Y/Ti ratio is ≈ 0.36 , typical of other NFAs.

Table 3. The average APT NF composition (at.%) in the V540 850 and 1150°C annealed powders after removing matrix atoms.

	Cr	W	Ti	Y	O
850°C Anneal	21.76	0.77	29.24	10.71	34.97
1150°C Anneal	19.91	0.24	28.99	10.20	38.27

Although the overall average NF composition was similar for the 850°C and 1150°C anneals, one 850°C annealed APT tip showed a population of NFs with Y/Ti ratios > 1 . In this particular case, the upper portion of the tip had many NFs that were mostly Y and O as shown in Figure 2. In the bottom 1/3 of the tip, below a possible grain boundary, most of the NF had lower Y/Ti ratios more typical of those found in other NFAs. Since the NFs with higher Y/Ti ratios were only observed in one sample, it is difficult to draw broad conclusions; however, since this alloy was annealed at a lower temperature the NFs may suggest that the Y and O features are present before annealing or cluster first, before reacting with Ti.

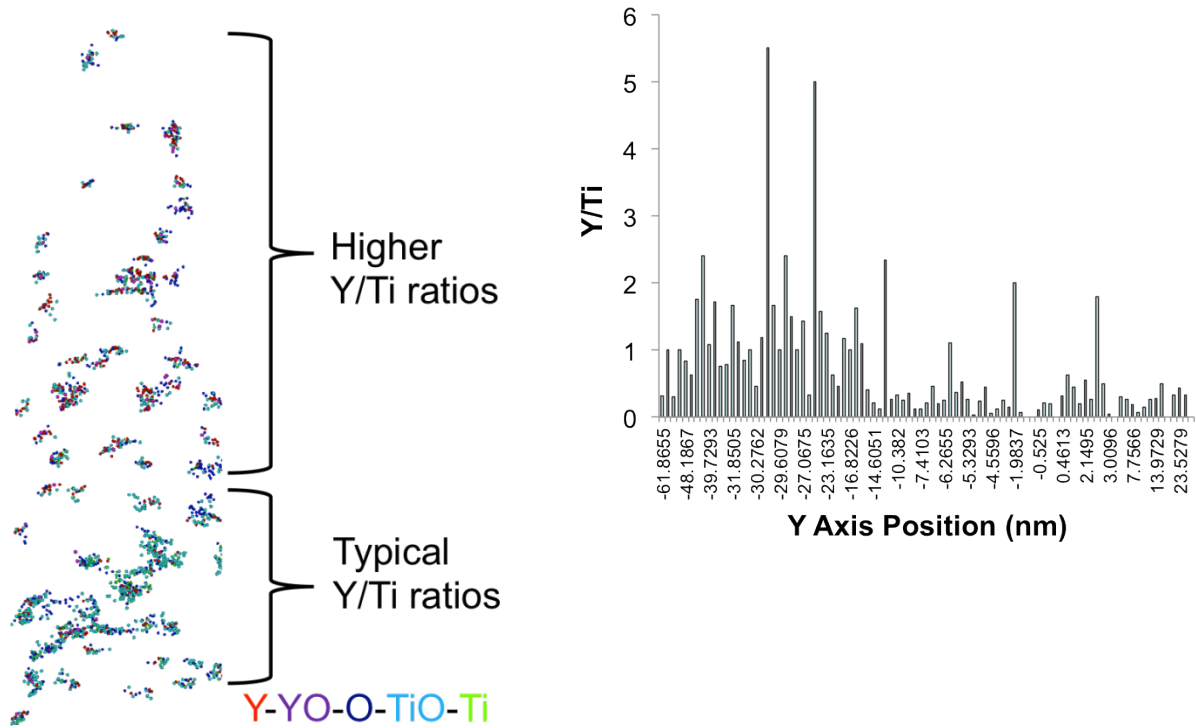


Figure 2. APT analysis on 850°C sample showing two populations of NF with one set having Y/Ti ratios > 1.

The average NF size ($\langle d \rangle$), number density (N), and clustered solute fraction (f_{solute}) for the two powders anneals are shown in Table 4. As expected, the 850°C anneal had a higher number density and smaller size than the 1150°C condition. Despite the high Y/Ti ratio found in some NF, in one 850°C APT tips the overall NF Y/Ti/O ratio was nearly identical.

Table 4. The average NF $\langle d \rangle$, N, f and Y/Ti/O ratio measured by APT.

	$\langle d \rangle$ (nm)	N (10^{23} m^{-3})	f_{solute} (%)	Y/Ti/O
850°C Anneal	1.8	10.0	0.51	14/39/47
1150°C Anneal	2.1	4.8	0.38	14/38/48

Figure 3 shows atoms maps of one large precipitate that was found on a grain boundary in the 850°C annealed powder. This precipitate was composed mainly of Ti, Si, and C with trace amounts of N in the center. No other larger precipitates were observed in either the 850 or 1150°C tips.

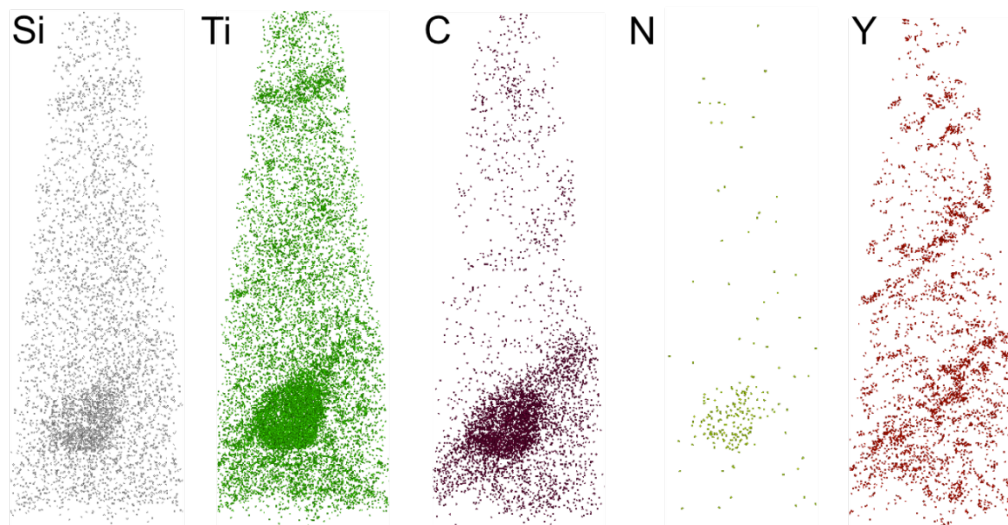


Figure 3. Atom map showing large Ti-Si-C-N precipitate on possible grain boundary in 850°C annealed powder.

Extruded alloy FCRD-NFA1

The FCRD-NFA1 alloy consolidated by extruding at 850°C and subsequently cross-rolled to 50% thickness after annealing for 1 h at 1000°C was analyzed by TEM, APT, and SANS. The microstructure is shown in the TEM images in Figure 4. This alloy showed a unimodal grain size distribution with the average size of $\approx 0.5 \mu\text{m}$. This is similar to the previous extruded alloy, PM2 [2].

EDX analysis on some of the larger precipitates showed that they were mainly composed of Ti and N, indicating some contamination may have occurred. An example TEM image showing the larger precipitates on grain boundaries is shown in Figure 5. TEM also showed the presence of the smaller Y-Ti-O NF and measured the $\langle d \rangle$, N and f to be $2.1 \pm 1.3 \text{ nm}$, $1.6 \times 10^{23} \text{ m}^{-3}$, and 0.25%, respectively. EDX was performed on larger NF from 5 to 20 nm in diameter. The measured Y/Ti ratio in these larger NF ranged from 0.5 to 1.3. SANS analysis was also performed on the FCRD-NFA1 and showed slightly larger NF (3 nm) with higher number density ($6.0 \times 10^{23} \text{ m}^{-3}$) and volume fraction (0.82%) compared to the TEM results. Figure 6 compares the $45 \pm 15^\circ$ scattering curves of the FCRD-NFA1 alloy with NFA alloy MA957 and a Fe14Cr control. Overall, the scattering is slightly higher in the FCRD-NFA1 but still comparable to that for MA957.

Almost all the tips FCRD-NFA1 atom probe tips fractured early when encountering large Ti rich precipitates. Figure 7 shows atom maps from one sample with two large precipitates composed mainly of Ti, O, C, and N. Smaller Y-Ti-O NF were found in the rest of the sample. The NF Y/Ti/O ratio for FCRD-NFA1 is 14/42/45 with slightly higher, but still similar compared to the milled and annealed powders. The Y/Ti/Cr/O was 11/32/24/34, again showing high 20% Cr in the NFs. This alloy included a processing step at 1000°C between the powder temperatures annealing temperature, and the N and $\langle d \rangle$ fell between the annealed powders at $6.9 \times 10^{23} \text{ m}^{-3}$ and 2.02 ± 0.78 , respectively. The f was $\approx 0.74\%$.

The APT bulk and matrix composition from the FCRD-NFA1 sample without large Ti-rich precipitates is shown in Table 5. Again the majority of Y, Ti, and O are found in the precipitates and not in the matrix. This tip also has higher C content compared to the annealed powders

(0.138 at.% vs 0.064 at.%). Part of this C contamination may come from the can used during extrusion, since the APT tip was taken near the sample/can interface.

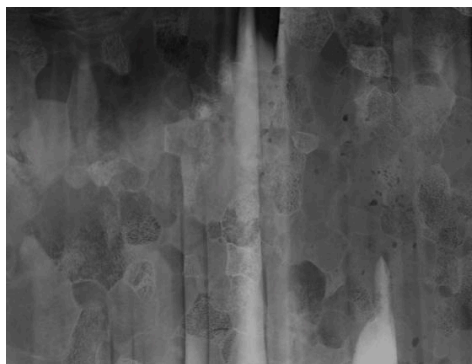


Figure 4. TEM image showing grain structure in FCRD-NFA1 alloy.

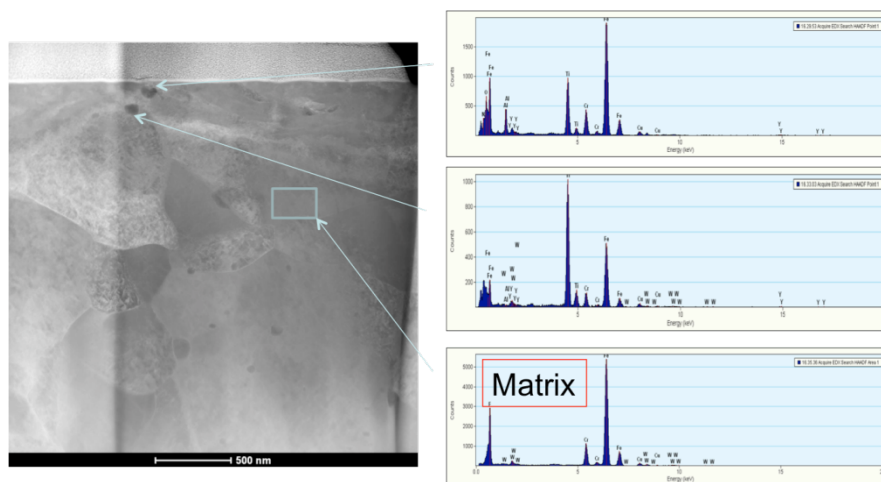


Figure 5. TEM image of the FCRD-NFA1 alloy showing the presence of larger precipitates on grain boundaries that are mainly composed of Ti and N.

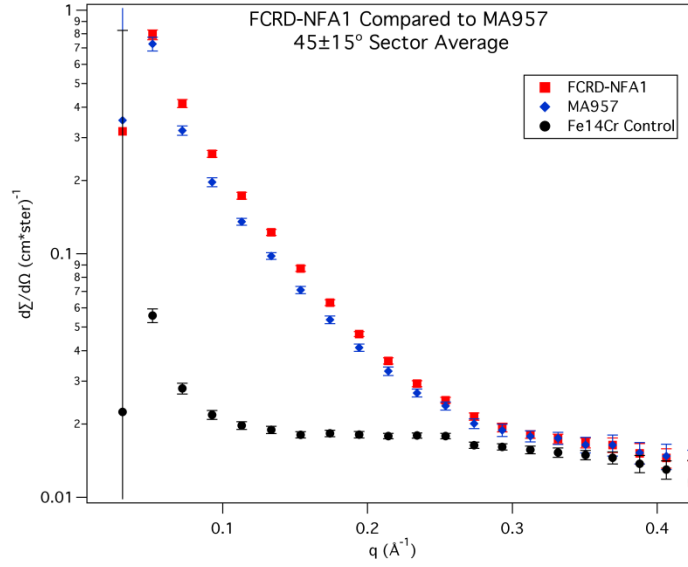


Figure 6. SANS 45° scattering curves comparing FCRD-NFA1, MA957, and Fe14Cr control.

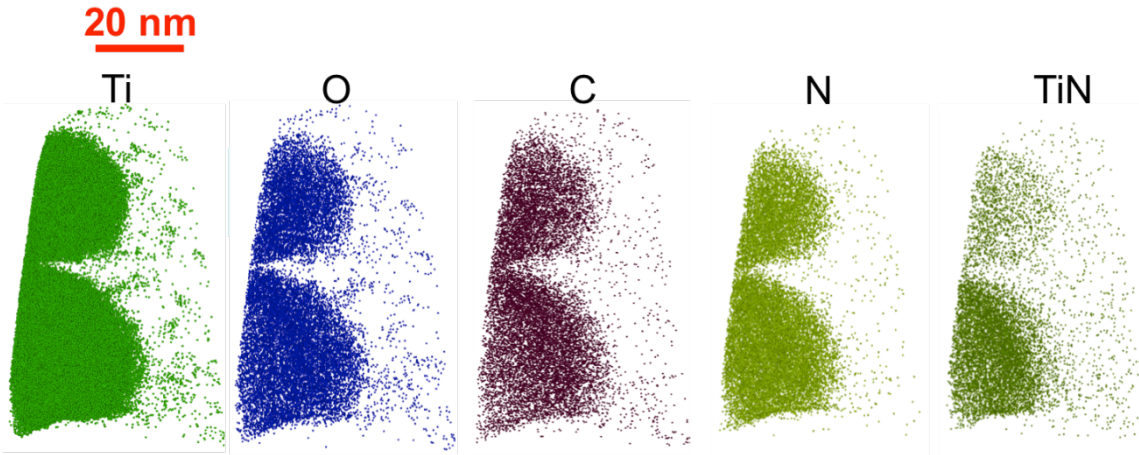


Figure 7. Atom maps showing large precipitates in FCRD-NFA1 composed of Ti, O, C, and N.

Table 5. The APT bulk and matrix composition (at.%) in the FCRD-NFA1 extruded alloy.

	Fe	Cr	W	Ti	Y	O	C	Si	N
Bulk	82.94	15.05	0.967	0.283	0.090	0.366	0.138	0.076	0.006
Matrix	83.57	14.97	0.969	0.056	0.016	0.125	0.127	0.073	0.005

Table 6 compares two previously characterized NFAs with the newest FCRD-NFA1 alloy. Alloy PM2 was the smaller batch precursor to FCRD-NFA1 and MA957 is an older NFA that has been extensively studied. The results from different characterization methods are shown along with the corresponding average $\langle d \rangle$, N and f . The APT Y/Ti/O ratio, μH , and grain size are also given. The newer 14YWT NFAs have slightly smaller NFs compared to MA957, but similar number densities and compositions. The microhardness is slightly higher in the newer 14YWT alloys and they have a smaller average grain size. The grains are only slightly elongated in the newer extrusions compared to MA957.

High temperature aging

SANS was performed on the 850 and 1150°C HIP consolidated alloys as well as aged specimens. All the HIP condition were aged at 1200°C for 48, 96, 144, and 228 h. Currently only the 48 h aging SANS data has been analyzed. Results from the longer aging times will be reported in the future and will be compared to previous aging performed on MA957. As noted above, the 850°C HIP baseline alloy had the smallest NF and highest number density at $\langle d \rangle = 2.1$ nm and $N = 2.93 \times 10^{24} \text{ m}^{-3}$. This corresponded to a nominal NF volume fraction of 1.5% and resulted in a μH of 495 ± 16 . The 1150°C HIP had a $\langle d \rangle = 3.0$ nm, $N = 7.2 \times 10^{23} \text{ m}^{-3}$, and $f = 1.0\%$ resulting in a μH of 357 ± 17 . After aging at 1200°C for 48 h the NF populations in the two conditions were nearly identical. The aged 850°C HIP had a $\langle d \rangle = 3.6$ nm, $N = 3.6 \times 10^{23} \text{ m}^{-3}$, and $f = 0.90\%$. The aged 1150°C HIP had a $\langle d \rangle = 3.7$ nm, $N = 3.3 \times 10^{23} \text{ m}^{-3}$, and $f = 0.9\%$. The microhardness in the 850 and 1150°C HIPs after aging were 304 ± 36 and 308 ± 34 , respectively. The magnetic to nuclear scattering ratio (M/N) was similar in both alloys at 1.2 for the HIP at 850°C and 1.1 for the 1150°C HIP consolidation. This is slightly below the expected value of 1.4 for a population of $\text{Y}_2\text{Ti}_2\text{O}_7$ NF. The M/N in the un-aged alloys is similar to the FCRD-NFA1 alloy with $M/N = 1.2$. After aging the M/N increased to 1.5 and 1.6 in both cases.

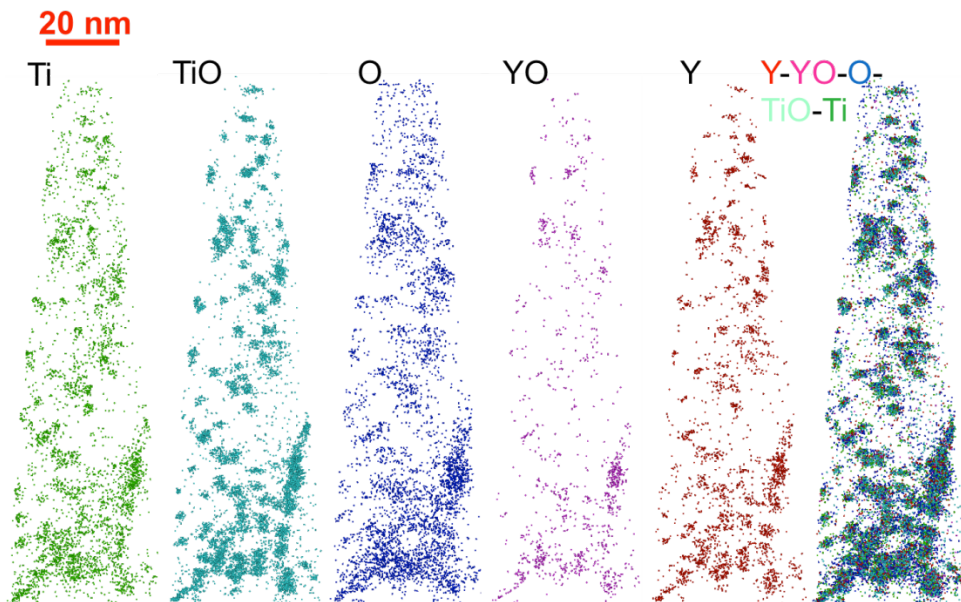


Figure 8. Atom maps showing high number density of Y-Ti-O NF in FCRD-NFA1.

Table 6. Comparison of 14YWT alloys FCRD-NFA1 and PM2 with MA957.

Technique	NFA1	PM2	MA957
TEM <d> (nm)	2.1	1.4	2.8
APT <d> (nm)	2.0	2.1	2.7
SANS <d> (nm)	3.0	2.8	2.7
Average (nm)	2.4	2.1	2.7
TEM N (10^{23} m^{-3})	1.6	5.8	2.6
APT N (10^{23} m^{-3})	6.9	11.0	5.1
SANS N (10^{23} m^{-3})	6.0	8.9	9.0
Average (10^{23} m^{-3})	4.8	8.6	5.6
TEM f (%)	0.25	-	0.40
APT f (%)	0.74	-	0.51
SANS f (%)	0.82	1.00	0.90
Average (%)	0.60	1.00	0.60
APT Y/Ti/O	14/42/45	12/43/40	14/46/40
μH	359 \pm 18	401 \pm 15	336 \pm 8
Grain Size (μm)	454	424	1.47x0.63

Conclusions and future work

The new extruded and cross-rolled FCRD-NFA1 larger heat has a similar microstructure and NF distribution to the previously processed, smaller precursor batch PM2 alloy. In both cases high number densities of Y-Ti-O NFs were observed with a similar character. One notable exception is that there appears to be a greater number of larger, Ti-rich precipitates in the FCRD-NFA1. These larger precipitates were observed both in TEM and APT.

Further comparison between PM2 and FCRD-NFA1 will evaluate the mechanical properties. Limited mechanical property data from PM2 showed promising creep resistance as well as acceptable fracture toughness. The larger volume of FCRD-NFA1 material will allow for a more comprehensive mechanical property investigation. Figure 9 shows the type of samples and orientations that are currently being tested. Fracture testing will occur using one-half-1/3 bend bar specimens in four orientations: L-T, T-L, T-S and L-S. The first letter corresponds to the direction normal to the crack plane in the directions of the length of the specimen, and the second letter corresponds to the crack propagation direction. Two types of tensile specimens were produced. The flat, 0.5 mm thick specimens will be used for tensile testing both at room temperature and at elevated temperature. The round gauge length specimens will be used for creep testing by performing strain-rate jump tests.

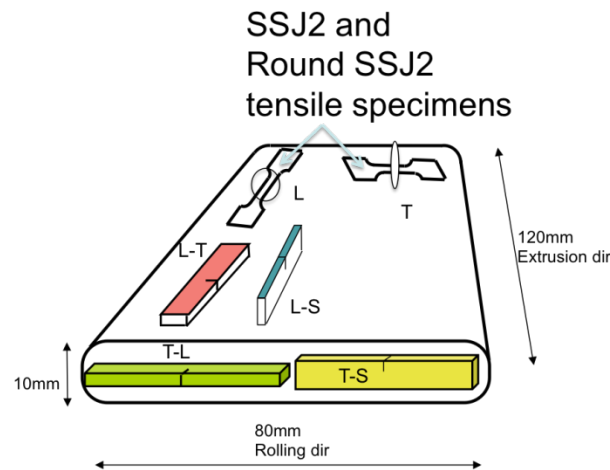


Figure 9. Mechanical test specimen layout in extruded and cross-rolled FCRD-NFA1.

ACKNOWLEDGMENT

This work is part of a multi-laboratory collaboration between LANL, UCSB and ORNL. The research was supported by the DOE Office of Fusion Energy FusMat program, as well as the DOE Office of Nuclear Energy under NEUP grants and by a subcontract from the LANL FCRD program. We acknowledge the support of the National Institute of Standards and Technology, U.S. Department of Commerce, in providing the neutron research facilities used in this work. This work was made possible through use of the Microscopy and Microanalysis facility located at the California Nanosystems Institute (CNSI) at UCSB.

REFERENCES

- [1] N. J. Cunningham, “Study of the Structure, Composition, and Stability of Y-Ti-O nm-Scale Features in Nano-Structured Ferritic Alloys,” Ph.D. Thesis, University of California, Santa Barbara, Santa Barbara CA (2012).
- [2] N. J. Cunningham, Y. Wu, G. R. Odette, D. Gragg, K. Fields, D. T. Hoelzer, and S. A. Maloy, “Characterization of the Final Precursor Alloy to a Larger Best Practice Heat of 14YWT,” DOE Fusion Reactor Materials Program Semiannual Progress Report for the Period Ending December 31, 2012, DOE/ER-0313/53.
- [3] K. Thompson, D. Lawrence, D. J. Larson, J. D. Olson, T. F. Kelly, and B. Gorman, “In Situ Site-Specific Specimen Preparation for Atom Probe Tomography,” *Ultramicroscopy* **107**, 2007, 131.
- [4] M. J. Alinger, G. R. Odette, and D. T. Hoelzer, “On the Role of Alloy Composition and Processing Parameters in Nanocluster Formation and Dispersion Strengthening in Nanostructured Ferritic Alloys,” *Acta Mater.* **57**, 2009, 392-406.

2.2 DEVELOPMENT OF ODS FeCrAl FOR FUSION REACTOR APPLICATIONS – B. A. Pint, D. T. Hoelzer and K. A. Unocic (Oak Ridge National Laboratory, USA)

OBJECTIVE

The dual coolant lead-lithium (DCLL) blanket concept requires improved Pb-Li compatibility with ferritic steels in order to demonstrate viable blanket operation in a DEMO-type fusion reactor. The goal of this work is to develop an oxide dispersion strengthened (ODS) alloy with improved compatibility with Pb-Li and excellent mechanical properties. The current focus is determining the desired Cr and Al contents in the alloy by evaluating the Pb-Li compatibility of model cast FeCrAl alloys.

SUMMARY

Several additional isothermal Pb-Li capsule tests of cast FeCrAlY specimens were completed at 700°C in order to further guide alloy selection. Characterization of specimens after exposure indicated that the Cr and Al contents remain relatively constant near the exposed surface and that LiAlO₂ formed on the surface of all of the exposed alloys. In general, the results suggest that the Al content needs to be near 5 wt.% for excellent Pb-Li compatibility. Based on this information, several powder compositions were procured and have now been received and analyzed. These powders are now being milled to produce the first batches of ODS FeCrAl for evaluation.

PROGRESS AND STATUS

Introduction

The DCLL blanket concept (Pb-Li and He coolants) is the leading U.S. design for a test blanket module (TBM) for ITER and for a DEMO-type fusion reactor.[1] With reduced activation ferritic-martensitic (FM) steel as the structural material, the DCLL is limited to ~475°C metal temperature because Fe and Cr readily dissolve in Pb-Li above 500°C and Eurofer 97 plugged a Pb-Li loop at 550°C.[2-3] For a higher temperature blanket for DEMO, structural materials with enhanced creep and compatibility are needed. ODS FeCrAl alloys are one possibility to meet this objective and considerable research on ODS FeCr alloys has shown an excellent combination of creep strength and radiation resistance.[4-7] Isothermal compatibility tests have shown low mass losses at up to 800°C.[8] Therefore, a materials development effort is underway, specific to this application. Previously, initial results were provided on the Pb-Li compatibility of six FeCrAl alloys with 10-20%Cr and 3-5%Al and the stability of various potential oxide dispersions in a FeCrAl matrix [9].

Experimental Procedure

Static capsule tests were performed using Mo (inert to Pb-Li) inner capsules and type 304 stainless steel (SS) outer capsules to protect the inner capsule from oxidation. The uncoated cast FeCrAlY specimens were ~1.5 mm thick and 4-5 cm² in surface area with a 600 grit surface finish and were held with 1 mm diameter Mo wire. The capsules were loaded with 125g of Pb-Li in an Ar-filled glove box. The Pb-Li was melted and cast at ORNL and had Li contents of 15.4-15.6 at%. The Mo and SS capsules were welded shut to prevent the uptake of impurities during the isothermal exposure. After exposure, residual Pb-Li on the specimen surface was removed by soaking in a 1:1:1 mixture of acetic acid, hydrogen peroxide and ethanol for up to 72 h. Mass change was measured with a Mettler-Toledo balance with an accuracy of 0.01 mg/cm². Post-test specimen surfaces were examined using x-ray diffraction (XRD) and secondary electron microscopy (SEM) equipped with energy dispersive x-ray (EDX) analysis. After surface characterization, the specimens were metallographically sectioned and polished and examined by light microscopy and electron probe microanalysis (EPMA) using wavelength dispersive x-ray analysis.

Results and Discussion

Figure 1 shows the mass change data for the first 6 FeCrAlY experiments (3 and 5%Al) and 5 of the 6 new experiments as a function of the actual Cr and Al contents of the cast alloys. In general, the goal is to develop an ODS FeCrAl with the lowest necessary Al and Cr levels as lower Al contents make the alloy easier to process and weld and lower Cr contents are desired to avoid issues with embrittlement,[10,11] especially under irradiation. The new results for alloys with 4-5%Al are mostly consistent with the previous results. However, the alloys with 3 and 5%Al showed little effect of Cr on the mass change, the 4%Al alloys showed less mass loss with higher Cr contents between 10 and 15%. For the Fe-12Cr-4.5Al+Y specimen, the 0.3mg/cm² mass loss was almost as low as the alloys with 5%Al. One of the capsules leaked with a specimen with ~13Cr-4Al and no Y (marked “in progress” in Figure 1). A more extended procedure is being used to remove this specimen from the capsules and remove residual Pb-Li. The mass change for this alloy will be provided in the next report. This specimen was exposed to identify the effect of Y on compatibility. Historically, Y and other rare earth elements or oxides are added to alumina-forming high temperature alloys like FeCrAl to improve the adhesion of the thermally grown alumina scale, especially at $\geq 1000^{\circ}\text{C}$ [12,13]. For this application in Pb-Li at $\leq 700^{\circ}\text{C}$, it is not certain if Y provides any benefit. An additional specimen with ~10Cr-5Al but no Y was also exposed to study the effect of Y. Compared to the specimen with Y and similar Cr and Al contents, the mass change was very similar but slightly less without Y. Since Y has very low solubility in FeCrAl, one benefit of Y may be in stabilizing a finer grain size in these cast alloys by the formation of FeY_x precipitates. Grain size of ODS alloys is determined by the processing and heat treatment and will be less of an issue.

In order to better understand the mass change data in Figure 1, the reaction products were analyzed and the composition profile of sectioned specimens were determined. Consistent with prior observations [8,14], the reaction products on the most recently exposed specimens were identified as LiAlO₂ by XRD.

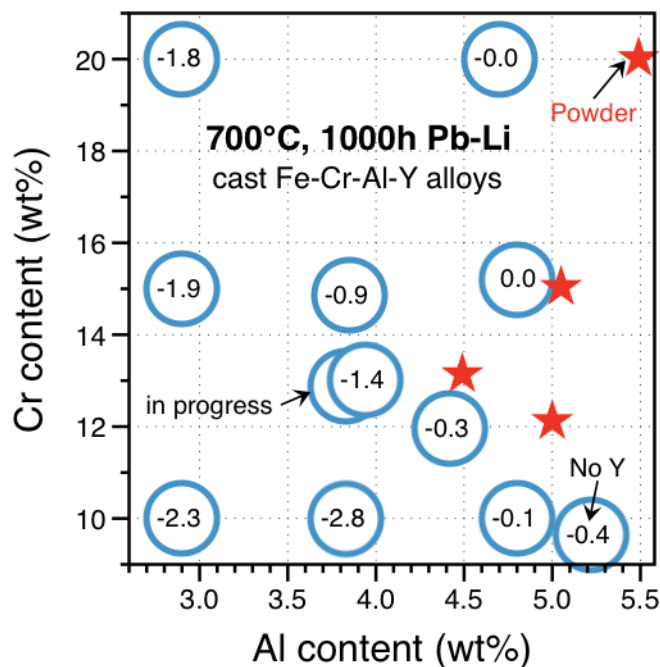


Figure 1. Specimen mass change of case FeCrAlY alloy coupons after exposure to Pb-Li for 1,000h at 700°C as a function of the Cr and Al contents. The stars mark the composition of four powder batches.

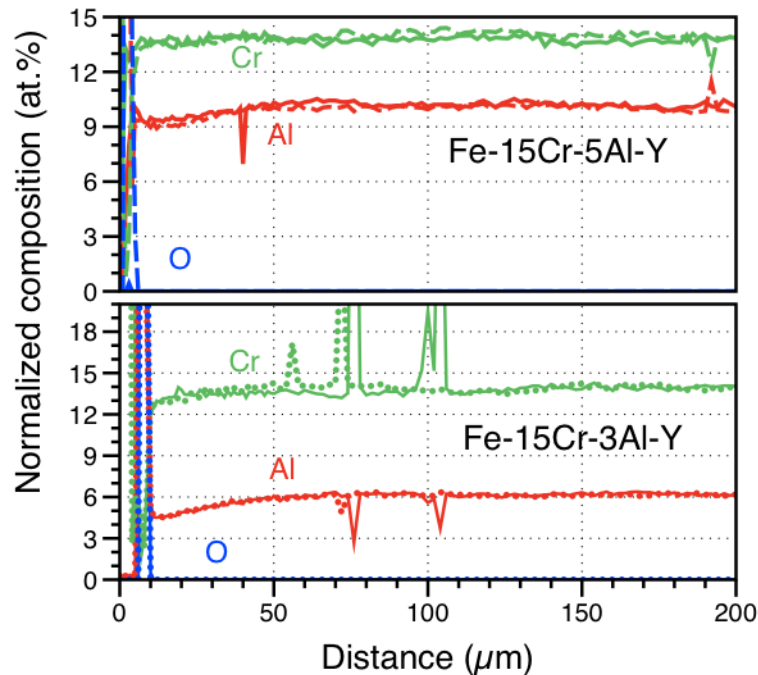


Figure 2. EPMA line profiles from polished sections of two FeCrAl specimens after exposure in Pb-Li for 1,000h at 700°C. In both cases, two line profiles were taken in different locations.

Figure 2 shows normalized composition profiles from two specimens analyzed by EPMA. Two profiles are shown for each specimen one with a dashed line and the other solid. In at.%, the 5 and 3 wt.% Al alloys contain ~10 and 6 at.%Al. The O profiles are shown to mark the substrate surface. Some Al depletion was apparent to a depth of ~40μm from the surface. For the alloy with 6at%Al in the matrix, the surface content has dropped to ~4.6%Al, while the other alloy had dropped to ~9%. Some amount of Cr depletion also was observed but not as significant. The disruptions in the Cr and Al profiles are where the line scan intersected a Y-rich precipitate, which is depleted in Al. The Cr and Al profiles do not fit the inductively coupled plasma (ICP) chemical analysis of these two alloys. That difference is currently being investigated.

Based on the results in Figure 1, several FeCrAl powder compositions were selected to fabricate ODS alloys. The compositions of the as-received powders are shown as stars in Figure 1. These powders will be ball milled with Y₂O₃ and then extruded to consolidate. The resulting ODS FeCrAl will then be evaluated in mechanical and compatibility experiments.

References

- [1] M. Abdou, D. Sze, C. Wong, M. Sawan, A. Ying, N. B. Morley and S. Malang, *Fus. Sci. Tech.*, 47 (2005) 475.
- [2] O. K. Chopra, D. L. Smith, P. F. Tortorelli, J. H. DeVan and D. K. Sze, *Fusion Technol.*, 8 (1985) 1956.
- [3] J. Konys, W. Krauss, J. Novotny, H. Steiner, Z. Voss and O. Wedemeyer, *J. Nucl. Mater.* 386-88 (2009) 678.
- [4] S. Ukai and M. Fujiwara, *J. Nucl. Mater.* 307 (2002) 749.
- [5] G. R. Romanowski, L. L. Snead, R. L. Klueh, D. T. Hoelzer, *J. Nucl. Mater.*, 283-287 (2000) 642.

- [6] R. L. Klueh, J. P Shingledecker, R. W. Swindeman, D. T. Hoelzer, J. Nucl. Mater. 341 (2005) 103.
- [7] D. A. McClintock, M. A. Sokolov, D. T. Hoelzer and R. K. Nanstad, J. Nucl. Mater., 392 (2009) 353.
- [8] B. A. Pint, L. R. Walker and K. A. Unocic, Mater. High Temp. 29 (2012) 129.
- [9] B. A. Pint, D. T. Hoelzer, D. Shin, J. O. Kiggans, Jr., K. A. Unocic, DOE/ER-0313/53 (2012) 10.
- [10] P. J. Grobner, Metal. Trans. 4 (1973) 251.
- [11] S. Kobayashia and T. Takasugi, Scr. Mater. 63 (2010) 1104.
- [12] F. A. Golightly, F. H. Stott and G. C. Wood, Oxid. Met. 10 (1976) 163.
- [13] B. A. Pint, Oxid. Met. 45 (1996) 1.
- [14] B. A. Pint and K. L. More, J. Nucl. Mater. 376 (2008) 108.

2.3 TEM CHARACTERIZATION OF A SIMULTANEOUSLY NEUTRON-IRRADIATED AND HELIUM-INJECTED PM2000 ODS ALLOY — H. J. Jung, D. J. Edwards, R. J. Kurtz, (Pacific Northwest National Laboratory); G. R. Odette, and T. Yamamoto (University of California, Santa Barbara)

OBJECTIVE

To investigate the irradiated microstructure of PM2000, a Y-Al-O dispersion-strengthened (ODS) iron-based alloy irradiated to a fast neutron dose of 21.2 dpa with simultaneous helium injection at 500°C in the High Flux Isotope Reactor (HFIR).

SUMMARY

Transmission electron microscopy (TEM) discs of PM2000 were coated on one side with a ~4 μm thick NiAl film and irradiated in HFIR to a neutron displacement damage dose of 21.2 dpa at 500°C. The dpa are primarily produced by fast neutrons, while the *in situ* He injection (ISHI) to 1230 appm derives from the thermal neutron two-step $^{59}\text{Ni}(n,\alpha)$ reaction. A uniform He injection profile extends up to about 8 μm below the NiAl coating, hence the remaining material experiences only dpa damage (21.2 dpa at 500°C). This report summarizes analytical TEM analyses to compare the two different regions, i.e., simultaneous He-injection/displacement damage versus displacement damage only, or high and very low He/dpa ratios, respectively. TEM analyses of the He implanted region reveals a high density of small (<2 nm) He bubbles predominantly associated with dislocation loops in the matrix. Because of a very large grain size, no grain or subgrain boundaries were observed in the samples prepared by focused ion beam (FIB) micromachining. The only voids formed were associated with large ODS particles, all of which were amorphous, irrespective of particle size and level of He. The ODS particles range in size from 15-30 nm, and most particles have a single faceted void attached to it that ranges in size from 5 to 15 nm. On the non-implanted side of the sample, no He bubbles could be detected, and faceted voids were found on ~10% of the ODS particles. The He-implanted side contains both <100>{100} and $\frac{1}{2}$ <111>{111} dislocation loops and a low density of line dislocations, whereas the un-implanted side possesses predominantly line dislocations with a lower density of dislocation loops. In both regions, nanoscale fcc precipitates exhibiting a cube-on-cube orientation relationship with the bcc matrix were observed. Chemical analysis using energy dispersive x-ray spectroscopy (EDS) indicates this phase is rich in Al and Ti. It was also noted that substantial Cr segregation occurs around the dislocation loops, concurrent with Fe depletion. The clusters of fcc precipitates that do not appear to be associated with the existing loop or line dislocations. The amorphous Y-Al-O particles contain a high Al concentration (>20 at%) and Cr segregation/Fe-depletion at the periphery.

PROGRESS AND STATUS

Introduction

The first-wall and blanket structural materials of future nuclear reactors demand tolerance to a harsh combination of neutron irradiation that produces displacement damage (dpa) and large inventories of transmutation product He. Fusion structures also experience high and time varying mechanical stresses and potentially corrosive chemical environments [1]. Oxide-dispersed strengthened (ODS) ferritic-based alloys are promising candidates to meet these

severe service challenges owing to excellent high-temperature mechanical properties and remarkable radiation tolerance [2,3].

Due to negligible solubility of He in metals and alloys, it precipitates as gas bubbles in the matrix, at dislocations, and at interfaces such as grain boundaries, martensite lath boundaries, and secondary-phase particle-matrix interfaces [4]. While a high density of small He bubbles may hinder dislocation movement, promoting radiation hardening, the development of significant levels of void swelling is of greater concern. This arises because He bubbles that reach a critical size transform into unstable growing voids, potentially causing significant swelling in an otherwise swelling resistant class of alloys [5]. Furthermore, high concentrations at grain boundaries may degrade creep properties and fracture toughness.

Because the alloy composition is fixed to achieve desired material performance, the formation of He in a fusion environment cannot be prevented, only controlled and managed. Thus to realize the potential of ferritic-based alloys for fusion applications, controlling the distribution of He is of critical importance. The most viable path to achieve this goal involves developing alloy microstructures that can hinder the accumulation of He in large bubbles. Minimizing the migration of He to boundaries while preventing the He from accumulating into damaging bubbles can be accomplished by dispersing the He at the interfaces of a very high density of nano-oxide particles. This approach has led to the development of nanostructured ferritic alloys (NFA) such as 14YWT and MA957. PM2000 is another ferritic based ODS alloy, possessing a much coarser distribution of Y-Al-O particles, as well as a significantly higher levels of Cr and Al to promote better corrosion resistance.

Due to the absence of a neutron irradiation environment producing conditions relevant to fusion reactors, a novel approach, the *in situ* He injection (ISHI) technique, was used to investigate the effects of simultaneous displacement damage and He accumulation on microstructural evolution of candidate alloys, as described in detail by Yamamoto et al. in [7]. Here we present analytical TEM characterization of PM2000 discs irradiated in the High Flux Isotope Reactor (HFIR) using the ISHI approach to produce the He during neutron irradiation.

Specimen Preparation and TEM Characterization Methods

TEM discs of PM2000, coated on one surface with a 4 μm thick NiAl layer, were irradiated as part of the JP27 irradiation experiment in HFIR to a dose of 21.2 dpa at 500°C, with 1230 appm He being injected over the duration of the irradiation. Cross-sectional TEM foils were prepared to characterize features such as He bubbles/voids, dislocation loops, line dislocations, secondary-phase precipitates, and the ODS particles. The cross-sectional foils were prepared using an FEI Quanta 3D FIB/SEM by milling through the NiAl coating to the underlying steel. The foils were finished with low-energy surface cleaning (2 keV Ga⁺ ion) at $\pm 3^\circ$ tilt angles to remove the damaged layer, then further cleaned to remove any remaining FIB artifacts using a Fischione Model 1040 NanoMill. The parameters for the nanomilling are listed in Table 1.

Table 1. Nanomilling cleaning condition

High tension (eV)	Beam current (nA)	Time (min)	Milling size (μm)	Tilt angle ($^\circ$)	Temperature ($^\circ\text{C}$)
900	165	20 (each side)	40 \times 20	± 10	-165

Sample composition was investigated using a JEOL 7600 FEG-SEM equipped with an Oxford Instruments AZtec EDS system. TEM characterization was performed using a JEOL 2010F microscope, operating at 200 keV, and equipped with an Oxford Instruments Link EDS detector.

Table 2. Composition of PM2000 (ODS alloy)

Alloy	Composition (wt.%) with Fe balance									
	Cr	Ti	Y(Y ₂ O ₃)	C	Al	W	Mn	Si	Ni	V
PM2000	19.00	0.5	0.5	-	5.5	-	-	-	-	-
PM2000 (EDS)	18.53	0.47	0.29 as Y	-	6.02			0.96	0.14	0.32

Bright-field TEM/STEM images of dislocation loops were acquired using multiple diffraction vectors at two-beam conditions near [001] and [110] zone axes. An approach based on both crystallographic projection and $g \cdot b = 0$ contrast was adopted for loop analysis [8]. Dark-field TEM images were obtained to investigate a second phase fcc precipitate. Energy-Filtered TEM images for elemental mapping were taken using Gatan EELS spectrometer (776 Enfina 1000). Also, STEM-EDS mapping was conducted to visualize the elemental distribution within the analyzed regions.

The nominal composition of PM2000 is listed in Table 2, along with the overall composition measured using energy dispersive x-ray spectroscopy on the non-coated side of the TEM disc.

Results and Discussion

Initial analyses indicated the entire FIB sample is a single grain. An interaction zone between the NiAl coating and the underlying PM2000 alloy was observed and serves as a reference for evaluation of the depth from the sample surface. Elemental mapping revealed this interaction zone essentially involves the diffusion of Ni, and lower levels of Al, into the PM2000 to a depth of ~500 nm. Redistribution of the Cr and Fe also occur to offset the interdiffusion of Ni and Al. Beyond a micron from the interface, the Ni levels approach levels of 0.2 wt.% or less. All analyses were conducted at regions several microns from the NiAl interface, but still well within the uniformly He-implanted layer.

Fig. 1 presents an elemental map that provides an overview of Cr, Fe, Y, Al, and Ti distributions for both the neutron-only irradiated side (top purple box) and ISHI sides (bottom blue box). The first observation concerns regions of Cr-segregation/Fe-depletion independent of the dislocation structure in the neutron-only irradiated side (top purple box). This Cr-segregation is also present in the He-injected side, but differs significantly in that the segregation is closely associated with edge-on dislocation loops (bottom blue box). The Cr and Fe contents appear to be inversely related throughout the foils. The second observation is that Al and Ti show coupled segregation, nominally independent of the Cr-segregation. The segregation of Al and Ti appears to be related to second phase precipitation, as will be discussed later in this report. The third observation is the Cr-rich shell that forms around the periphery of the yttrium-oxide nanoparticles, accompanied with simultaneous Fe-depletion, an observation reported previously by de Castro et al [9], who conducted thermal annealing of an Fe-12Cr ODS alloy at 750 °C for 4, 24 and 96 hours. The thickness of the Cr shell around the particles in the HFIR-irradiated

TEM discs is 10 to 15 nm thicker than that observed in the case of the unirradiated heat-treated ODS alloy, suggesting this Cr-rich shell is kinetically enhanced at the matrix-particle interface during neutron irradiation. The fourth observation is that a high concentration of Al (around 20 at%) is measured within the oxide nanoparticles, which matches the reports by Capdevila et al [10] and Klimiankou et al. [11], at least with respect to the presence of Al in the particles.

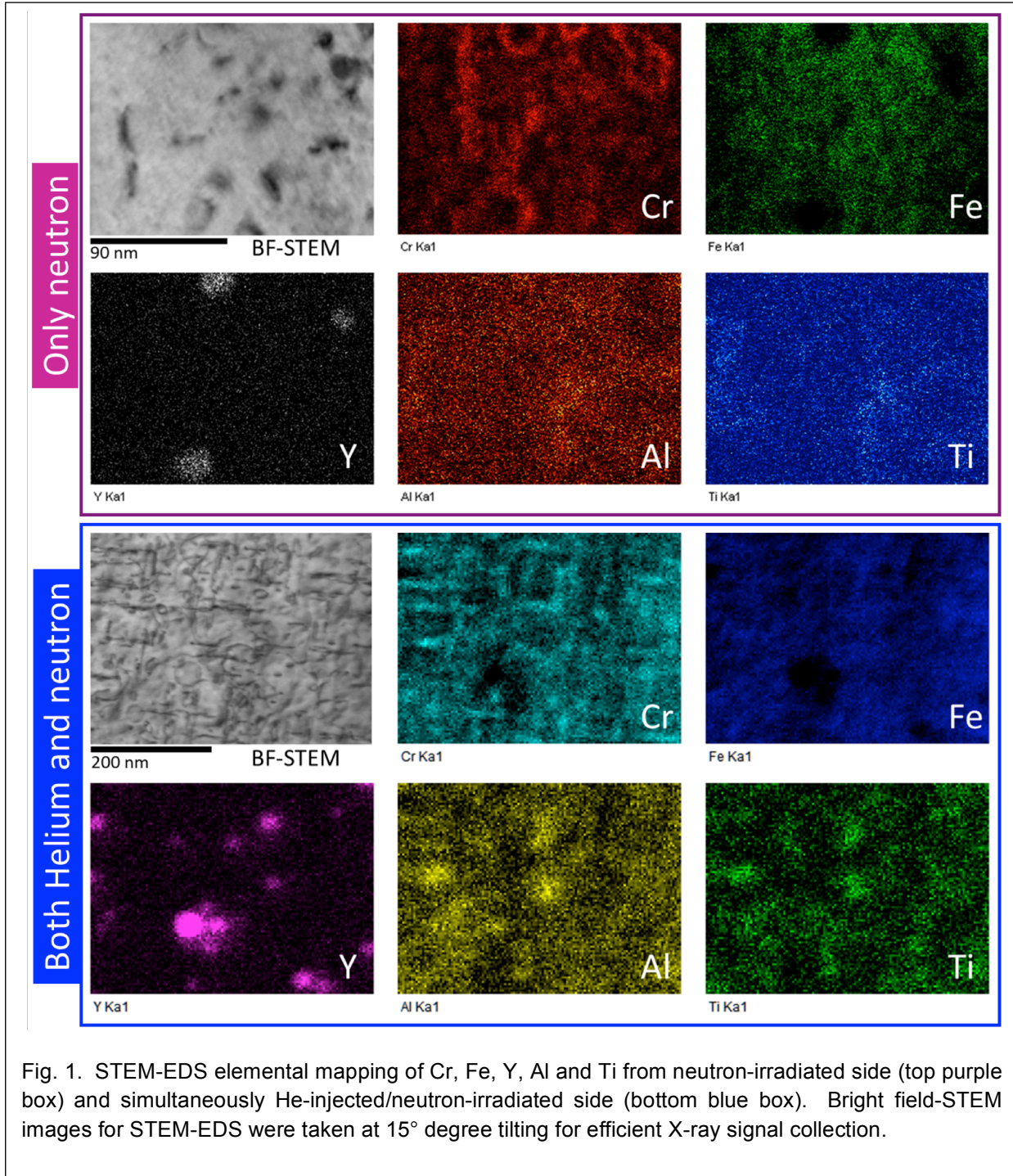


Fig. 1. STEM-EDS elemental mapping of Cr, Fe, Y, Al and Ti from neutron-irradiated side (top purple box) and simultaneously He-injected/neutron-irradiated side (bottom blue box). Bright field-STEM images for STEM-EDS were taken at 15° degree tilting for efficient X-ray signal collection.

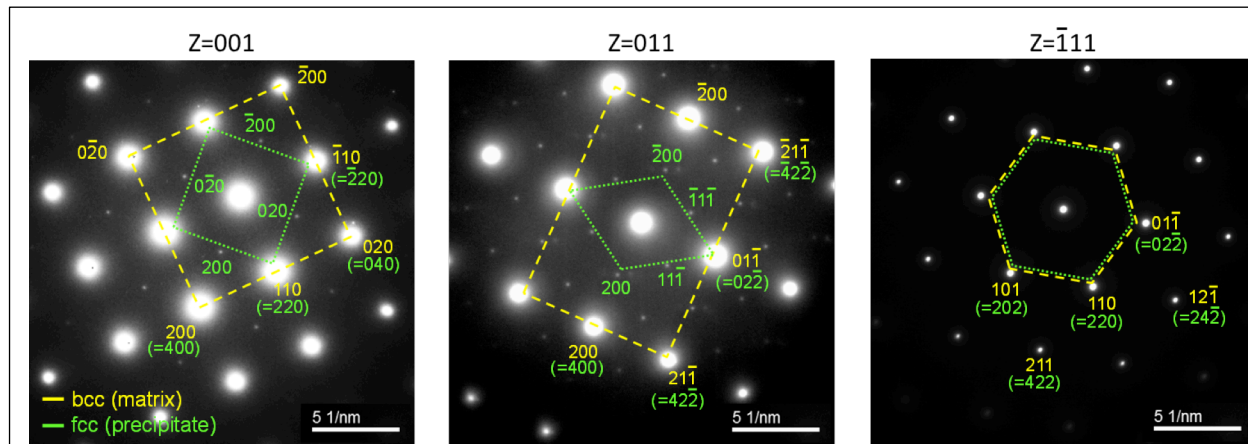


Fig. 2. Selected area diffraction (SAD) patterns of [001], [011], and [111] zones that are representative of the matrix and 2nd phase precipitation common to both sides of the sample. While Fe-based bcc matrix spots are indicated as yellow dot line, 2nd phase fcc precipitate spots are denoted as green dotted line. The 2nd fcc phase has a cube-on-cube orientation relationship to the matrix with a lattice parameter twice that of the bcc matrix.

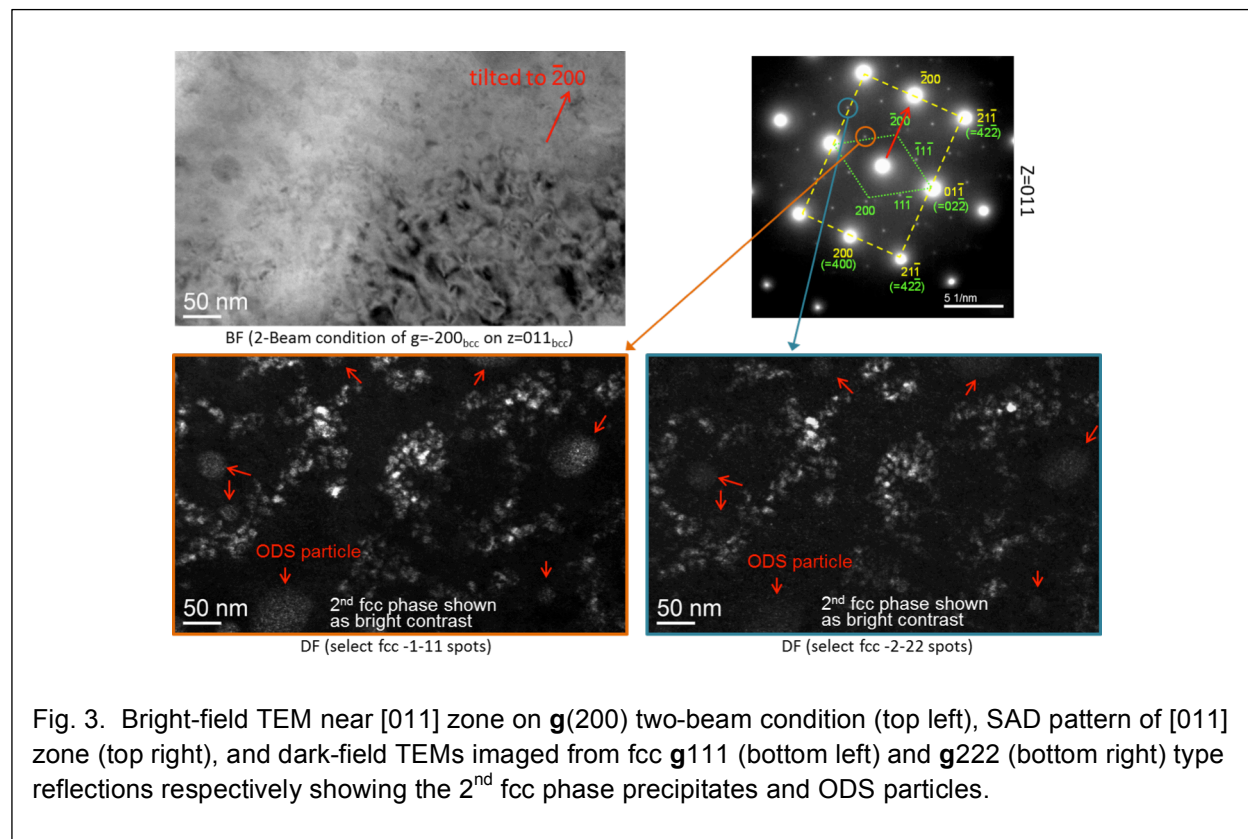


Fig. 3. Bright-field TEM near [011] zone on $g(200)$ two-beam condition (top left), SAD pattern of [011] zone (top right), and dark-field TEMs imaged from fcc $g111$ (bottom left) and $g222$ (bottom right) type reflections respectively showing the 2nd fcc phase precipitates and ODS particles.

In order to verify the presence of second phase precipitates suggested from the elemental mapping in Fig. 1, selected area diffraction (SAD) patterns and images were taken at different zone axes such as [001], [110] and [111] as can be seen in Figs. 2 and 3. Note that the diffraction patterns from the two different sides of the sample yielded the same spots, so the He-injection and difference in dislocation structure doesn't appear to impact second phase formation. The diffraction patterns in Fig. 2 reveal less intense, extra reflections that do not correspond to the ferritic bcc lattice; instead, careful examination revealed they belong to an fcc lattice. Alignment of the two crystal structures indicates a cube-on-cube orientation relationship between the precipitates and the matrix. The lattice parameter of the second phase is approximately twice that of the matrix, and may correspond to an ordered DO₃ phase identified by Wittmann et al [12] in an investigation of Fe-Cr-Al alloys. Dark-field TEM (DFTEM) images were taken from corresponding fcc **g**₁₁₁ and **g**₂₂₂-type precipitate reflections, revealing precipitate clusters that form independent of the ODS particles and dislocation structures (see Fig. 3). The location of the second phase precipitates corresponds with Al/Ti-enrichment. Capadevila et al [10] also presented evidence of nanoscale regions enriched in Al and Ti, but not Cr, suggesting they were formed during thermomechanical processing alone.

In this irradiated condition, all of the ODS particles on both neutron-only and ISHI regions were found to be completely amorphous based on both the images and the diffraction patterns. High-resolution (HR) TEM from an ODS particle was taken with Fast Fourier Transform (FFT) as seen in Fig. 4. HRTEM shows an amorphous region at the center of an ODS particle with bcc matrix fringes from the overlapping bcc matrix oriented to the [001] zone axis. The FFTs of these images reveal a diffuse amorphous halo from the center of the ODS particle and periodic [001] type arrangement from the bcc matrix. Lattice fringes from the bcc matrix are visible within the ODS particle, but this arises because the amorphous ODS particle is only partially

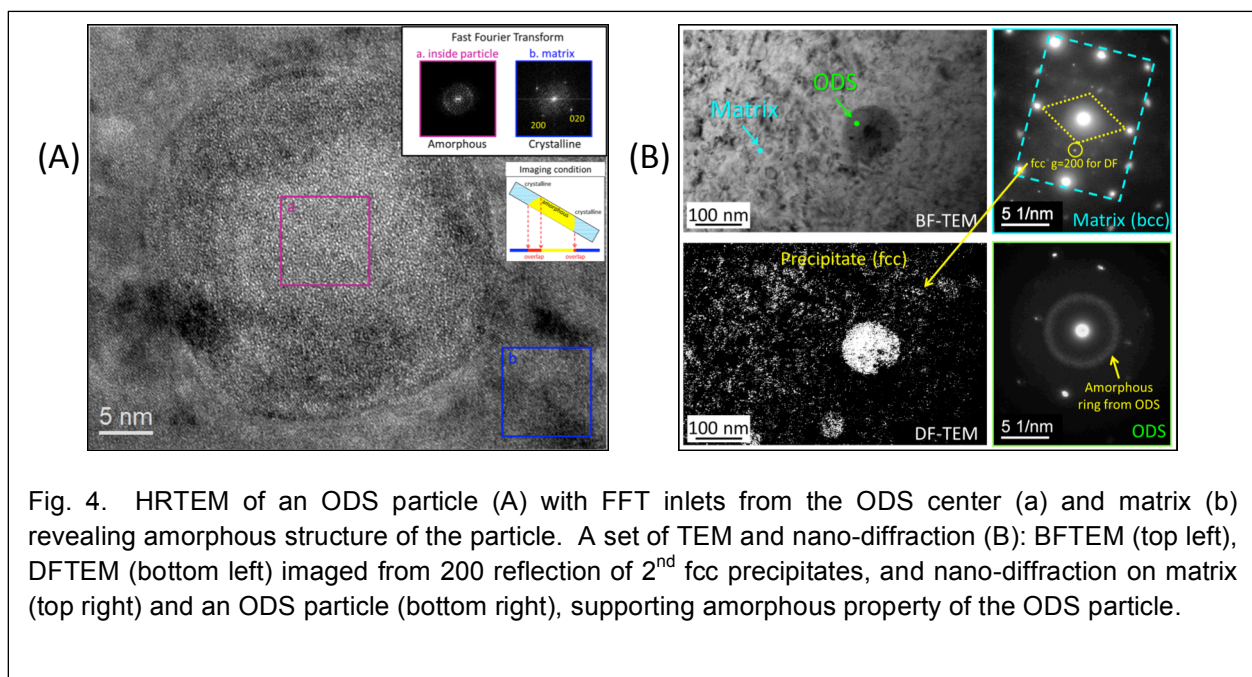


Fig. 4. HRTEM of an ODS particle (A) with FFT inlets from the ODS center (a) and matrix (b) revealing amorphous structure of the particle. A set of TEM and nano-diffraction (B): BFTEM (top left), DFTEM (bottom left) imaged from 200 reflection of 2nd fcc precipitates, and nano-diffraction on matrix (top right) and an ODS particle (bottom right), supporting amorphous property of the ODS particle.

embedded within the foil. The lack of any Moiré fringes in the overlapping regions between the particle and matrix further confirms that the ODS particles are no longer crystalline after irradiation to 21.2 dpa. Further investigation was conducted using a pseudo-parallel electron beam probe of 2~3 nm diameter to acquire nanodiffraction patterns (ND) from the matrix and the ODS particle regions in Fig. 4b. ND on the center of an ODS particle reveals the expected diffuse halo-like ring corresponding to an amorphous structure (bottom left in Fig. 4b) while ND on the matrix shows strong a [110] type-zone bcc pattern and weak [110] type-zone fcc precipitate reflections without the amorphous ring. DFTEM images obtained from an fcc g_{200} spot reveals both the amorphous ODS particles and fcc precipitates because the amorphous halo lies at similar d-spacing with the fcc g_{200} reflection.

Fig. 5 illustrates elemental maps of Cr and Fe taken on the He-injected side of the sample using energy-filtered TEM (EFTEM), which filters only electrons corresponding to a specific atom and images the atomic distribution using the filtered electrons. The EFTEM map can provide a better spatial resolution than that of the STEM EDS maps. The Cr and Fe EFTEMs maps were taken using energy windows of 590 ± 10 eV (Cr $L_{2,3}$ edge) and 720 ± 10 eV (Fe $L_{2,3}$ edge). The Cr is readily segregated around the dislocation loops and Fe is depleted correspondingly in region 1 (red box) of Fig. 5, confirming the trend noticed in the initial elemental mapping presented in Fig 1.

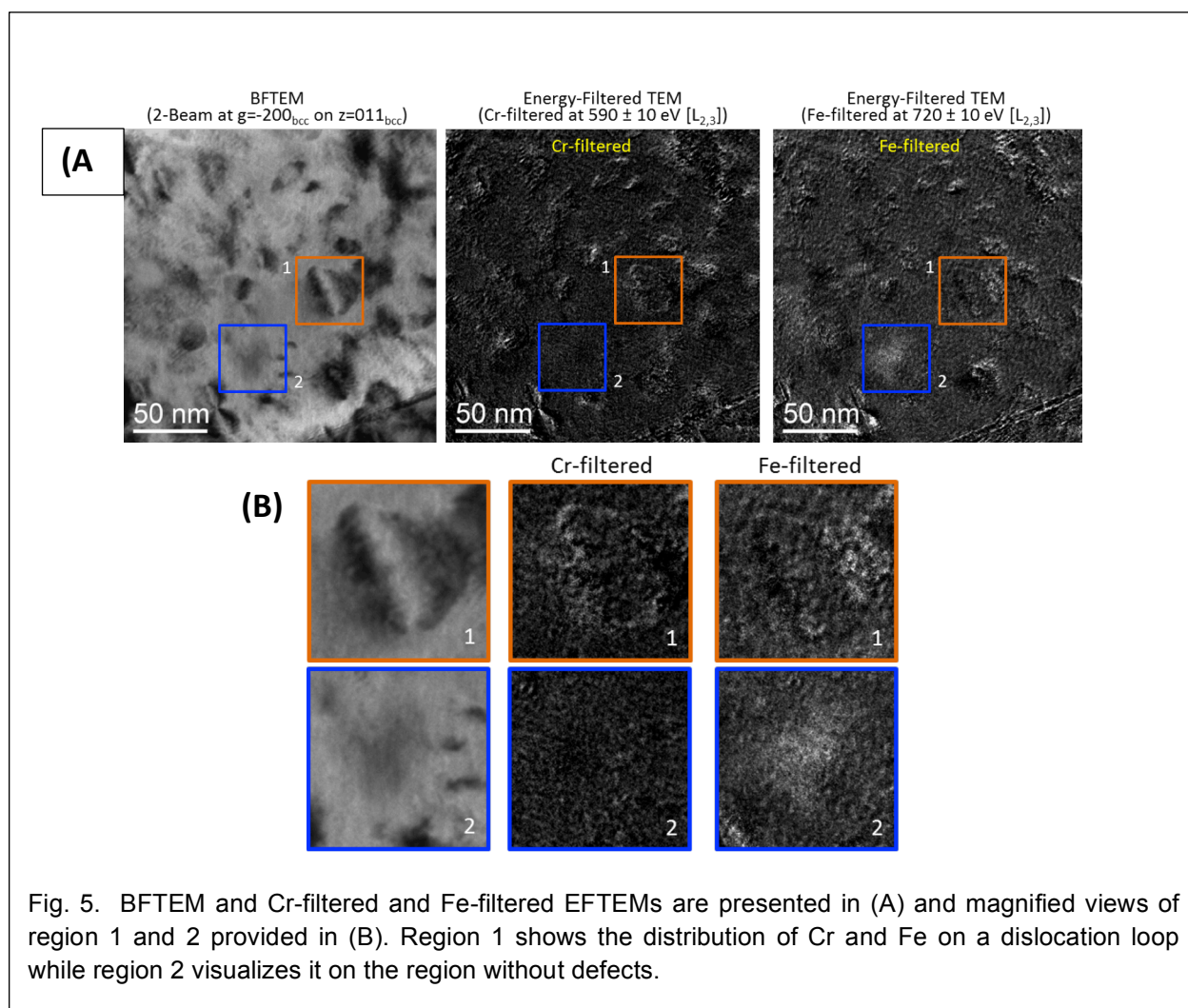


Fig. 5. BFTEM and Cr-filtered and Fe-filtered EFTEMs are presented in (A) and magnified views of region 1 and 2 provided in (B). Region 1 shows the distribution of Cr and Fe on a dislocation loop while region 2 visualizes it on the region without defects.

Having established that significant segregation occurs in irradiated PM2000, we performed initial examinations of the dislocation and He bubble evolution. Figure 6 presents examples of the dislocation structure present in both the He-implanted and He free sides. Both $\langle 100 \rangle$ and $\frac{1}{2}\langle 111 \rangle$ dislocation loops are the dominant dislocation defect observed in the He-implanted side, with a low density of line dislocations present throughout the implanted region. The average size of the $\langle 100 \rangle$ loops is approximately 30 ± 9.8 nm, and 18.5 ± 5.3 nm for the $\frac{1}{2}\langle 111 \rangle$ type loops, with some of the $\langle 100 \rangle$ loops extending to over 100 nm in diameter [14]. In the FIB sample taken from the non-implanted side this ratio of loops to line dislocations shifts somewhat in favor of the line dislocations, and the initial impression is that the loops are smaller in diameter compared to those measured in the He-implanted side. The $\langle 100 \rangle$ -type loops were found to be consistently enriched with Cr based on the elemental mapping, but this hasn't been confirmed with the $\frac{1}{2}\langle 111 \rangle$ type loops.

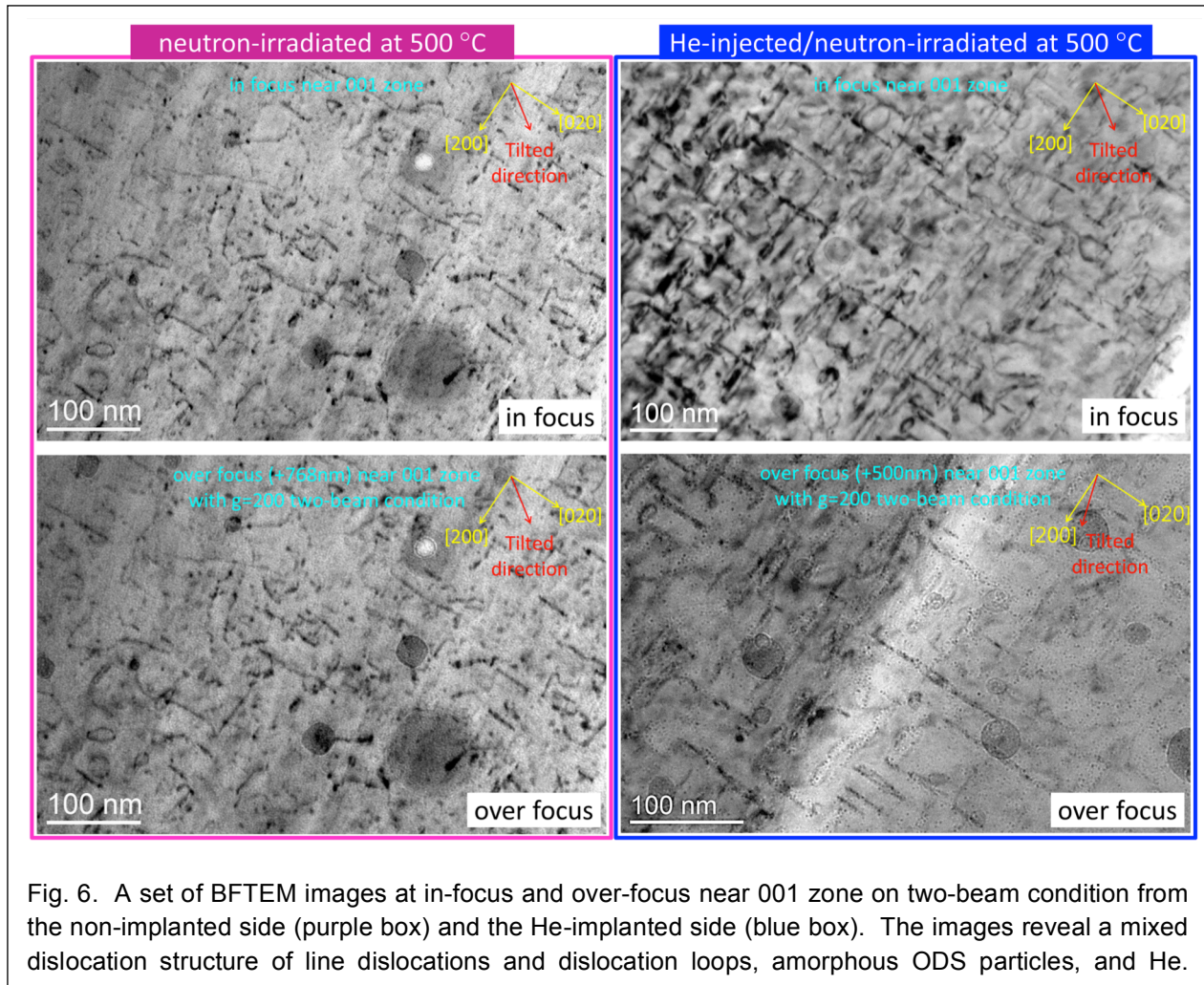


Fig. 6. A set of BFTEM images at in-focus and over-focus near 001 zone on two-beam condition from the non-implanted side (purple box) and the He-implanted side (blue box). The images reveal a mixed dislocation structure of line dislocations and dislocation loops, amorphous ODS particles, and He.

The second observation is that small He bubbles are associated with both the $\langle 100 \rangle$ type loops and $\frac{1}{2}\langle 111 \rangle$ loops, but not necessarily with the line dislocations. The only voids observed in this alloy were formed on the oxide particles, as shown in Figs. 7 and 8. Interestingly, on the non-implanted side less than 10% of the ODS particles possess faceted voids; whereas on the He-injected side of the foil, all of the observed ODS particles were associated with a single faceted void. No He bubbles were observed around the ODS particles.

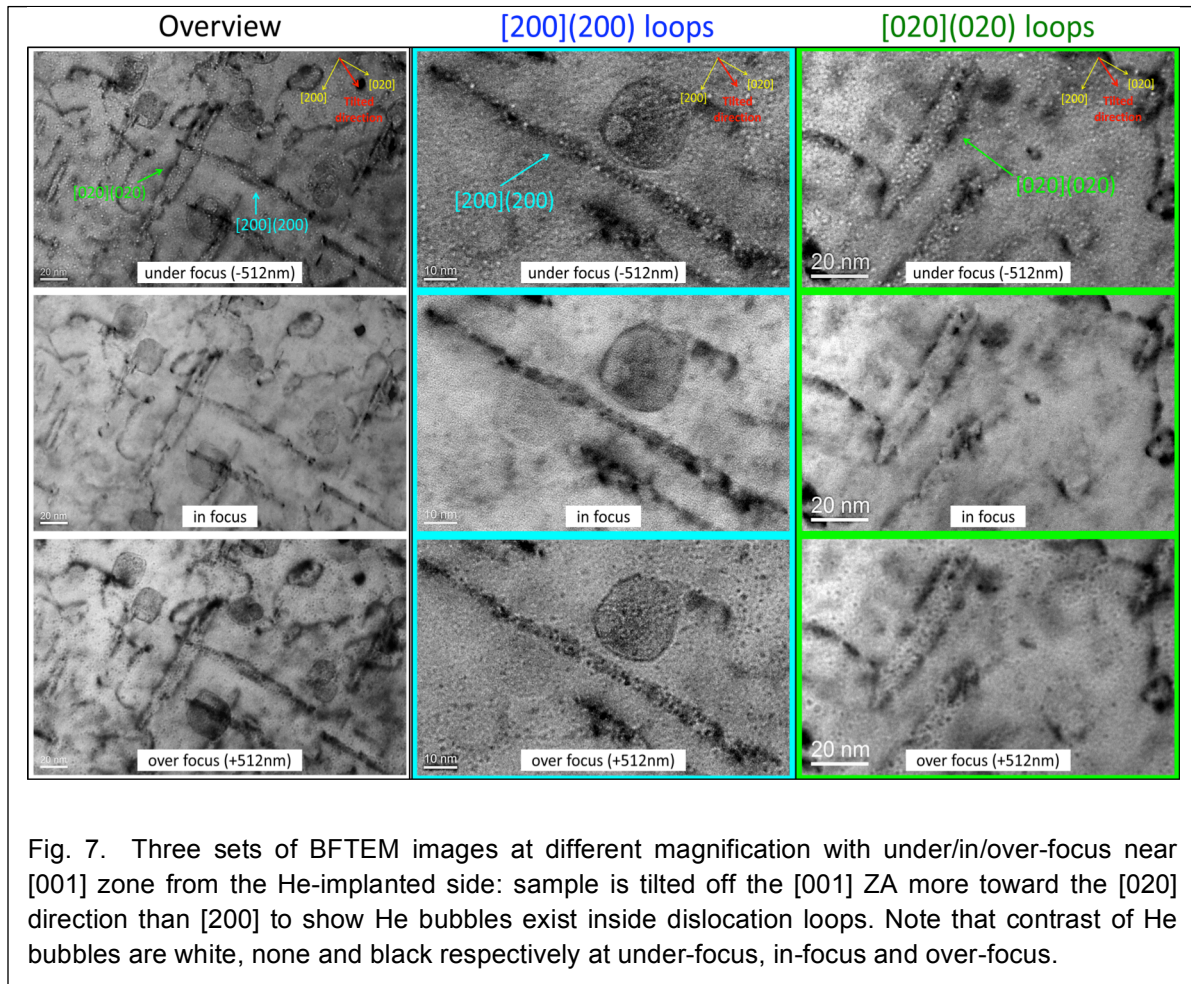
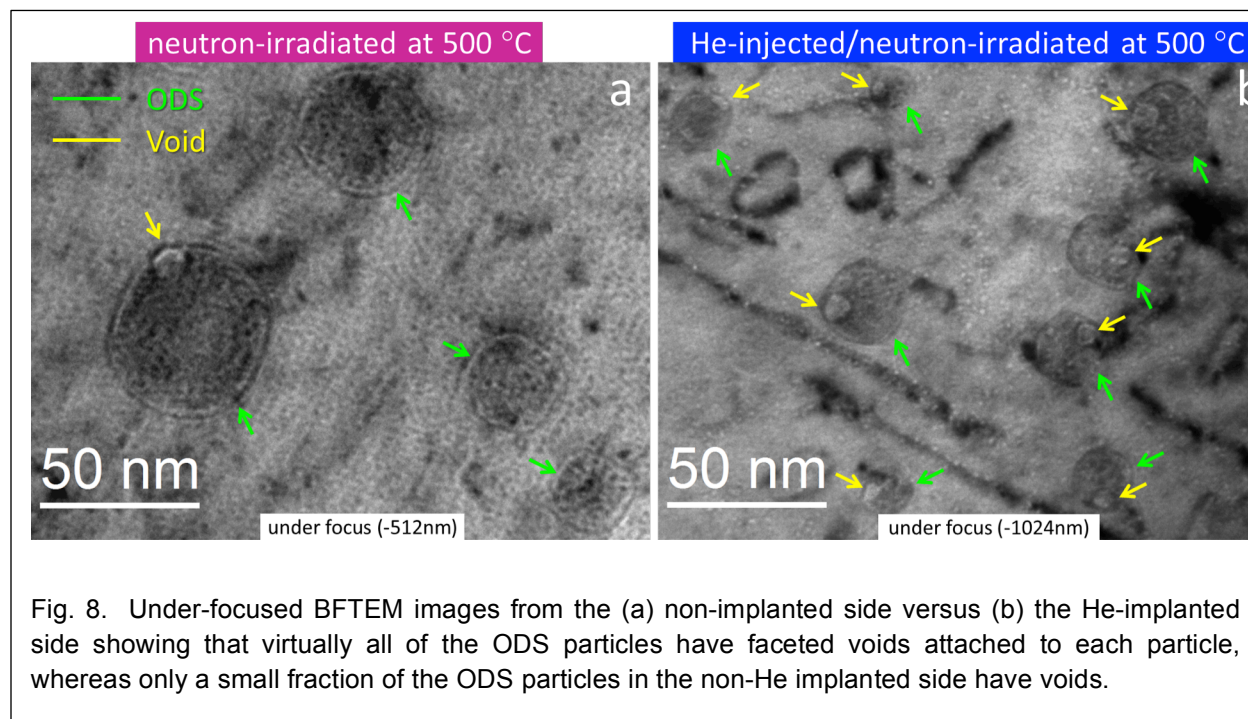


Fig. 7. Three sets of BFTEM images at different magnification with under/in/over-focus near [001] zone from the He-implanted side: sample is tilted off the [001] ZA more toward the [020] direction than [200] to show He bubbles exist inside dislocation loops. Note that contrast of He bubbles are white, none and black respectively at under-focus, in-focus and over-focus.



A higher magnification view of the loops and bubbles is provided in Figure 7, demonstrating more clearly the association between the two features. In some cases bubbles were visibly arranged in a manner that suggested nucleation and growth around an existing dislocation loop, but the loop itself was invisible because it did not satisfy the $\mathbf{g} \cdot \mathbf{b}$ criterion. Our results suggest that He bubbles are forming on the habit plane of the dislocation loops, but in limited cases we find examples of bubbles that appear to follow the periphery of a loop, so further work is needed to understand the relationship between the different loop types and He bubbles. No voids were found other than those associated with amorphous ODS particles, so the presence of large $\langle 100 \rangle$ type loops appears to provide sufficient sites to effectively capture the He and nucleate a high density of small bubbles, limiting their ability to reach bubbles of the critical size to form voids.

Future Work

Subsequent analysis is planned to elucidate the nature of the loops and their association with the bubbles. A critical point is to compare the dislocation character between the He-implanted region versus the non-implanted region, and to elucidate the synergism between the He bubbles, dislocation loops, line dislocations and radiation-induced segregation that leads to a relatively stable and low void swelling microstructure.

ACKNOWLEDGEMENTS

This research was supported by the US Department of Energy, Office of Fusion Energy Sciences, under contracts DE-AC06-76RLO1830 and DE-333 FG03-94ER54275. The authors

wish to thank Ruby Ermi and Alan Schemer-Kohrn for their assistance in preparing the samples for TEM analysis.

REFERENCES

- [1] N. Baluc, K. Abe, J. L. Boutard, V. M. Chernov, E. Diegele, S. Jitsukawa, A. Kimura, R. L. Klueh, A. Kohyama, R. J. Kurtz, R. Lässer, H. Matsui, A. Möslang, T. Muroga, G. R. Odette, M. Q. Tran, B. van der Schaaf, Y. Wu, J. Yu, and S.J. Zinkle, *Nucl. Fusion* **47** (2007) S696.
- [2] G. R. Odette, M. J. Alinger, and B. D. Wirth, *Annu. Rev. Mater. Res.* **38** (2008) 471.
- [3] R. J. Kurtz, A. Alamo, E. Lucon, Q. Huang, S. Jitsukawa, A. Kimura, R. L. Klueh, G. R. Odette, C. Petersen, M. A. Sokolov, P. Spätig, J. W. Rensman, *J. Nucl. Mater.* **386-388** (2009) 411.
- [4] H. Ullmaier, *Nucl. Fusion*. **24** (1984) 1039.
- [5] R. E. Stoller and G. R. Odette, *J. Nucl. Mater.* **131** (1985) 118.
- [6] R. Schäeublin and Y. L. Chiu, *J. Nucl. Mater.* **362** (2007) 152.
- [7] T. Yamamoto, G. R. Odette, P. Miao, D. T. Hoelzer, J. Bentley, N. Hashimoto, H. Tanigawa, and R. J. Kurtz, *J. Nucl. Mater.* **367-370** (2007) 399.
- [8] B. Yao, D. J. Edwards, and R. J. Kurtz, *J. Nucl. Mater.* **434**, 1-3, (2013) 402.
- [9] V. de Castro, E. A. Marquis, S. Lozano-Perez, R. Pareja, and M. L. Jenkins, *Acta Materialia* **59**, 10 (2011), 3927.
- [10] J. Ribis and S. Lozano-Perez, *Mater. Lett.* **74** (2012) 143.
- [11] C. Capdevila, M. K. Miller, K. F. Russell, J. Chao and J. L. González-Carrasco, *Mater. Sci. Eng. A* **490** 1-2, (2008) 277-288.
- [12] M. Klimiankou, R. Lindau, A. Moslang, and J. Schroder, *Powder Metall.* **48** (2005) 277-287.
- [13] R. Wittmann, S. Spindler, B. Fischer, H. Wagner, D. Gerthsen, J. Lange, M. Brede, J. Klöwer, P. Schunk, and T. Schimmel, *J. Mater. Sci.* **34** (1999) 1791.
- [14] B. Yao, D. J. Edwards, R. J. Kurtz, G. R. Odette and T. Yamamoto, Semiannual Progress Report on Fusion Reactors Materials, DOE/ER-0313/52, June 30, 2012.

2.4 THE ASSOCIATION RELATIONSHIPS AMONG BUBBLES, PRECIPITATES, AND GRAIN BOUNDARIES IN DUAL BEAM IRRADIATED NANO-STRUCTURED FERRITIC ALLOYS — Y. Wu, T. Yamamoto, N. Cunningham, G. R. Odette, (University of California, Santa Barbara); S. Kondo, and A. Kimura (University of Kyoto, Japan)

OBJECTIVE

The objective of this work is to characterize the relationship between start-of-life alloy and irradiation-induced features in nano-structured ferritic alloys, with emphasis on bubbles and bubble associations, as a foundation for microstructurally informed helium transport, fate and consequence models.

SUMMARY

Transmission electron microscopy (TEM) was used to characterize the associations between various microstructural features, including helium bubbles, in nanostructured ferritic alloys, following dual ion irradiations at 650°C. Almost all of the nm-scale oxide precipitates are associated with one and, in some cases a few, interface bubbles. The distribution of precipitates and bubbles along dislocations and small angle grain boundaries are not significantly different than in the matrix. However, the precipitates on large angle grain boundaries are larger and often associated with more bubbles.

PROGRESS AND STATUS

Introduction

Nano-structured ferritic alloys (NFA) are dispersion strengthened by nm-scale Y-Ti-O oxide features (NF), resulting in outstanding high temperature creep strength and remarkable radiation damage tolerance [1-3]. Therefore, NFA are good candidates advanced fission and fusion energy applications. In particular, NFA manage low solubility helium by trapping it in the form of small bubbles at the interface between NF and the Fe-Cr matrix [2-5]. Very small, high-pressure ($\approx 2\text{g/r}$) bubbles efficiently store helium in a way that prevents its deleterious effects with respect to void nucleation and various manifestations of helium embrittlement [2-6]. For example, both in situ He injection and dual ion irradiation studies show that, in contrast to tempered martensitic steels (TMS) with bi-modal distributions of cavities composed of small bubbles and larger growing voids, only small nm-scale bubbles are observed in NFA [2-6].

In addition to the NF, NFA contain high dislocation densities and fine grains [2,3]. It is well established that bubbles and voids in many other irradiated alloys, including TMS and austenitic stainless steels, are often associated with various microstructural features predominantly dislocations, precipitates and grain boundaries. These associations and bubble sites are critical to the consequences of helium as well. For example, larger bubbles on precipitates and grain boundaries are favored void and creep cavity nucleation sites, respectively [2,3,6]. Helium on grain boundaries also leads to severe degradation of fracture toughness [6]. However, the NF associated bubbles are more numerous and smaller in NFA. Thus characterizing such associations is critical to developing helium transport, fate and consequence models.

Dual beam (helium plus heavy) ion irradiation coupled with transmission electron microscopy (TEM) is a powerful method to study helium behavior [6]. In this study, we clarify the associations relationships that exist among various features in dual ion irradiated NFA. To the

best of our understanding, this is the first systematic and comprehensive evaluations of bubble-boundary-interface-precipitate associations in NFA.

Experimental Procedure

MA957 was irradiated by dual 6.4 MeV Fe⁺ plus 1.0 MeV He⁺ ion beams at 650°C using the DuET facility at Kyoto University in Japan, to a nominal condition of 48 dpa at 2200 appm at a depth of 600 nm. The actual dpa, He, and He/dpa vary with depth. TEM specimens were prepared by in-situ lift out in a FEI Helios-FIB; a low final low energy, 2 KV at 5.5 pA minimized the gallium ion beam damage. TEM was performed using a FEI Titan at 300 KV. Conventional TEM Fresnel contrast imaging at defocuses of ± 1.0 - $1.5 \mu\text{m}$ was used to image the helium bubbles. Bubbles image with bright contrast in the under-focus images and dark contrast for over focus. It is especially important to compare under-focus and over-focus images from the same location observing for small bubbles with $d < 2 \text{ nm}$. The NF oxide precipitates were imaged in-focus. Adobe Photoshop was used to overlap the in-focus and under-focus images to simultaneously reveal the precipitates and bubbles. Finally, high angle annular dark field (HAADF) scanning transmission electron microscopy (STEM) and energy dispersive X-ray (EDX) techniques were used to investigate the composition of the larger features with bright contrast (bubbles) in under-focus images.

Results and Discussion

The under-focused ($\approx 1500 \text{ nm}$) bright field image in Figure 1 shows the distribution of He bubbles in the irradiated region. A large angle grain boundary (LAGB) runs diagonally from the top to the right side of the image. The white features are bubbles. The bubbles located on the LAGB appear to be larger than in the matrix. However, as shown in Figure 2, further detailed investigation shows that the apparent size of boundary bubbles is misleading. Figure 2a shows that larger precipitates are also located on the LAGB. The under- and over-focus images in Figure 2b and c show that bubbles on the larger and smaller precipitates are similar, but they appear larger in the former case due to overlap locally and through the foil thickness. Further, the larger LAGB precipitates are associated with more numerous bubbles than on the smaller oxides in the matrix. Figure 2d illustrates that while bubbles are essentially always associated with the precipitates, the latter appear to be bubble free in some cases (see arrows).

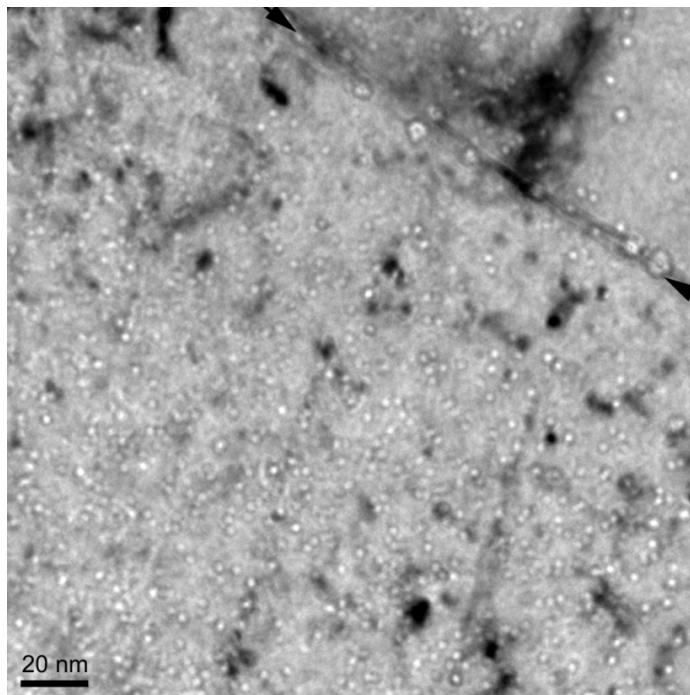


Figure 1. An under focus bright field image showing larger features with bright contrast lie along the LAGB, while the smaller features with bright contrast reside in the matrix.

Energy dispersive X-ray (EDX) spectroscopy was used to measure the composition of the larger features lying along the LAGB's in the under-focus bright field images. Figure 3 shows the EDX results. Figure 3a is an under focus bright field image of a triple junction area and Figure 3b shows the corresponding HAADF STEM image (Z-contrast image). The bright spots in the bright field images appear as dark spots in the HAADF image indicating the presence of lower-Z elements. In order to optimize the experimental condition for recording EDX signals, the HAADF image is tilted at 10° from the bright field image; therefore, the dark spots in the HAADF images may not appear at exactly at the same locations as in the bright field image. EDX on 12 large features showed that they all are enriched in Ti and Y. Examples of EDX spectra from the larger LAGB Y-Ti-O precipitates are shown in Figures 3c and d, for dark regions 10 and 11, respectively. These results are consistent with many previous observations of bubble precipitate associations at both matrix and grain boundary sites [6]. Figures 1 and 4 shows that the bubbles are distributed more unevenly on LAGB compared to those on SAGB that are again highly associated with precipitate features.

The possible enhanced association of bubbles and dislocations was also examined. Lines drawn along a random segment of dislocations were compared to parallel lines of the same length in the adjoining matrix. No significant differences in the number of bubbles along the dislocation and matrix lines were observed. In the example shown in Figure 5, there are 6 bubbles in the matrix and 5 easily visible along the dislocation.

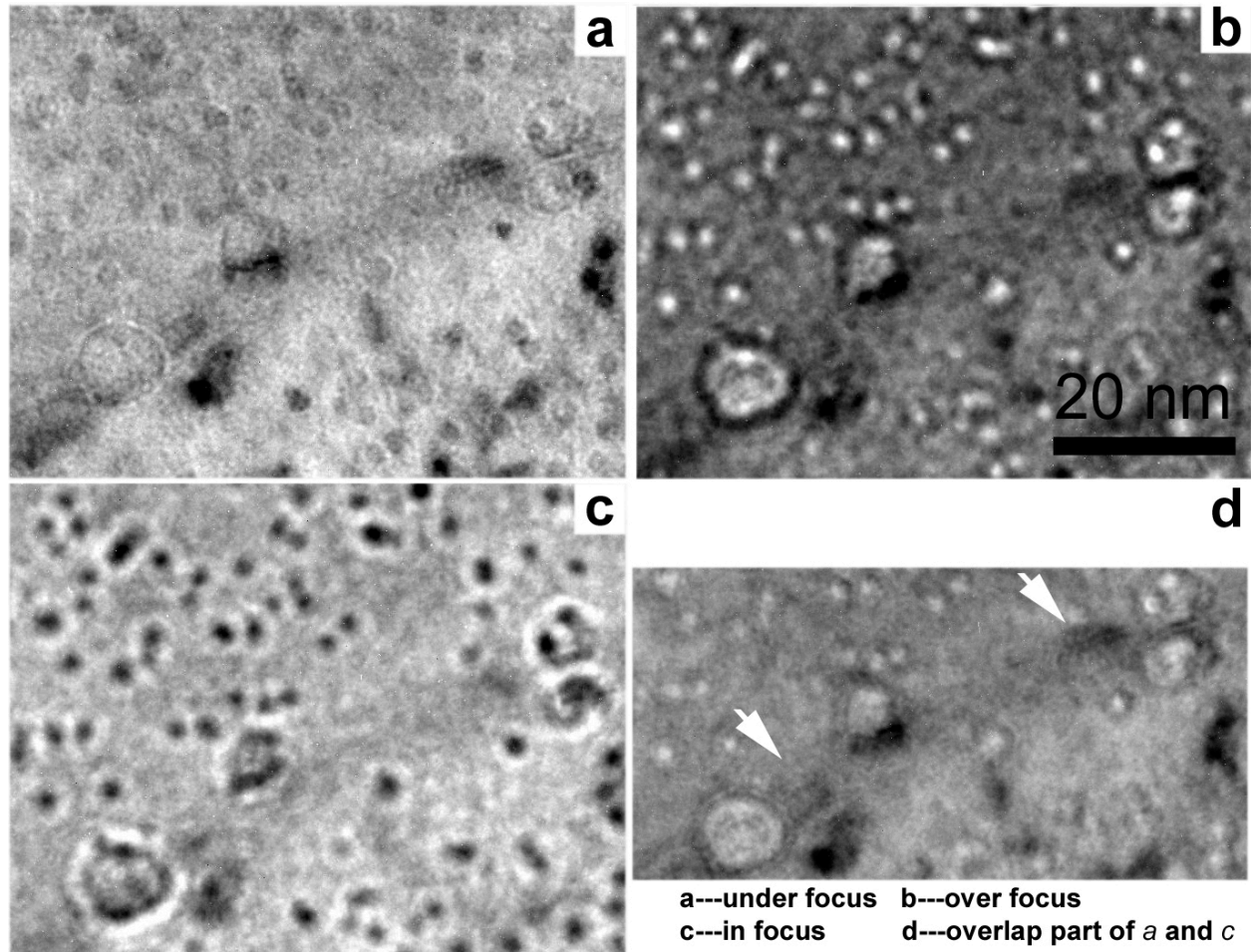


Figure 2. a) In-focus bright field image; b) under focus bright field image; c) over focus bright field image; and, d) overlapping a and b images.

A similar evaluation of precipitates-dislocation associations was also carried out. Again the matrix and dislocation precipitate populations are similar. In the example shown in Figure 6, there are 10 precipitates along the dislocation segment compared to 9 in the adjoining matrix. Thus, neither bubbles nor precipitates show a strong preference to be associated with dislocations.

Summary and Conclusions

The results of this study can be summarized as follows:

- Bubbles are always associated with oxide NF precipitates;

- Bubbles are observed on most, but not all, precipitates;

- The precipitates on LAGB are larger;

The size of the bubbles on the larger NF along LAGB is similar to those on smaller matrix features;

Matrix features typically are associated with one bubble while the larger LAGB precipitates often contain several bubbles;

SAGB are decorated with smaller NF similar to this found in the matrix; and

The NF along SAGB typically is associated with one bubble that is similar in size to those in the matrix and on LAGB.

REFERENCES

- [1] Y. Wu, E. Haney, N. Cunningham and G. R. Odette, *Acta Mater.* **60** (2012) 3456.
- [2] G. R. Odette, M. J. Alinger, and B. D. Wirth, *Annu. Rev. Mater. Res.* **38** (2008) 471.
- [3] G. R. Odette and D. T. Hoelzer, *JOM* **62** (2010) 84.
- [4] G. R. Odette, P. Miao, D. J. Edwards, T. Yamamoto, R. J. Kurtz, and H. Tanigawa, *J. Nucl. Mater.* **417** (2011) 1001.
- [5] T. Yamamoto, Y. Wu, G. R. Odette, K. Yabuuchi, S. Kondo, and A. Kimura, Fusion Reactor Materials Program. June 30, 2012, DOE/ER 0313-52 (2012) 8.
- [6] Y. Dai, G. R. Odette, and T. Yamamoto, "The Effects of helium on irradiated structural alloys," Chapter 6, in *Comprehensive Nuclear Materials*, R. Konings, T. R. Allen, R. E. Stoller, and S. Yamanaka Eds. (2012) Elsevier.

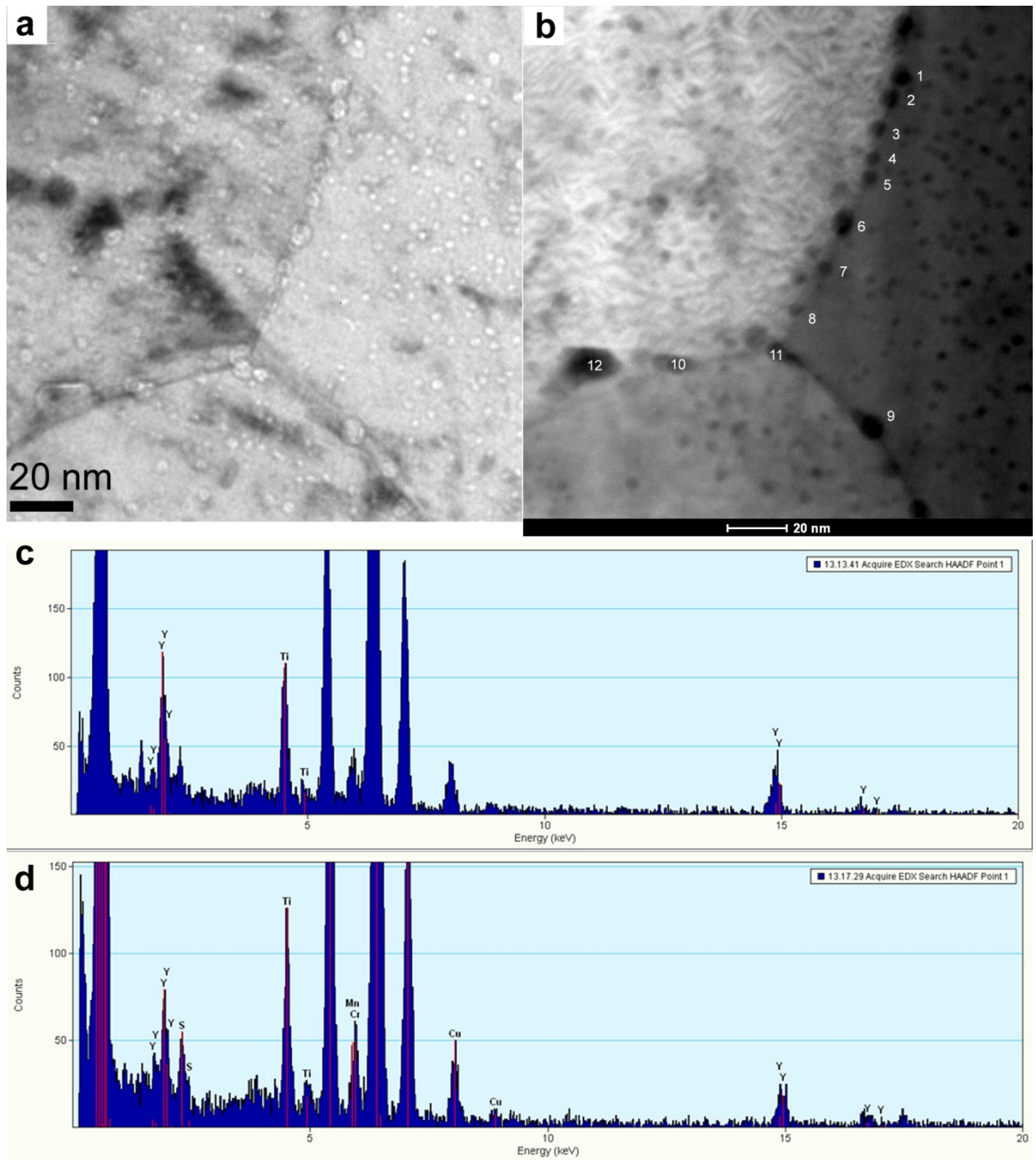


Figure 3. a) An under focus bright field image of a triple junction; b) the corresponding HAADF STEM image; c, d) EDXS spectra for features labeled 10 and 11, respectively.

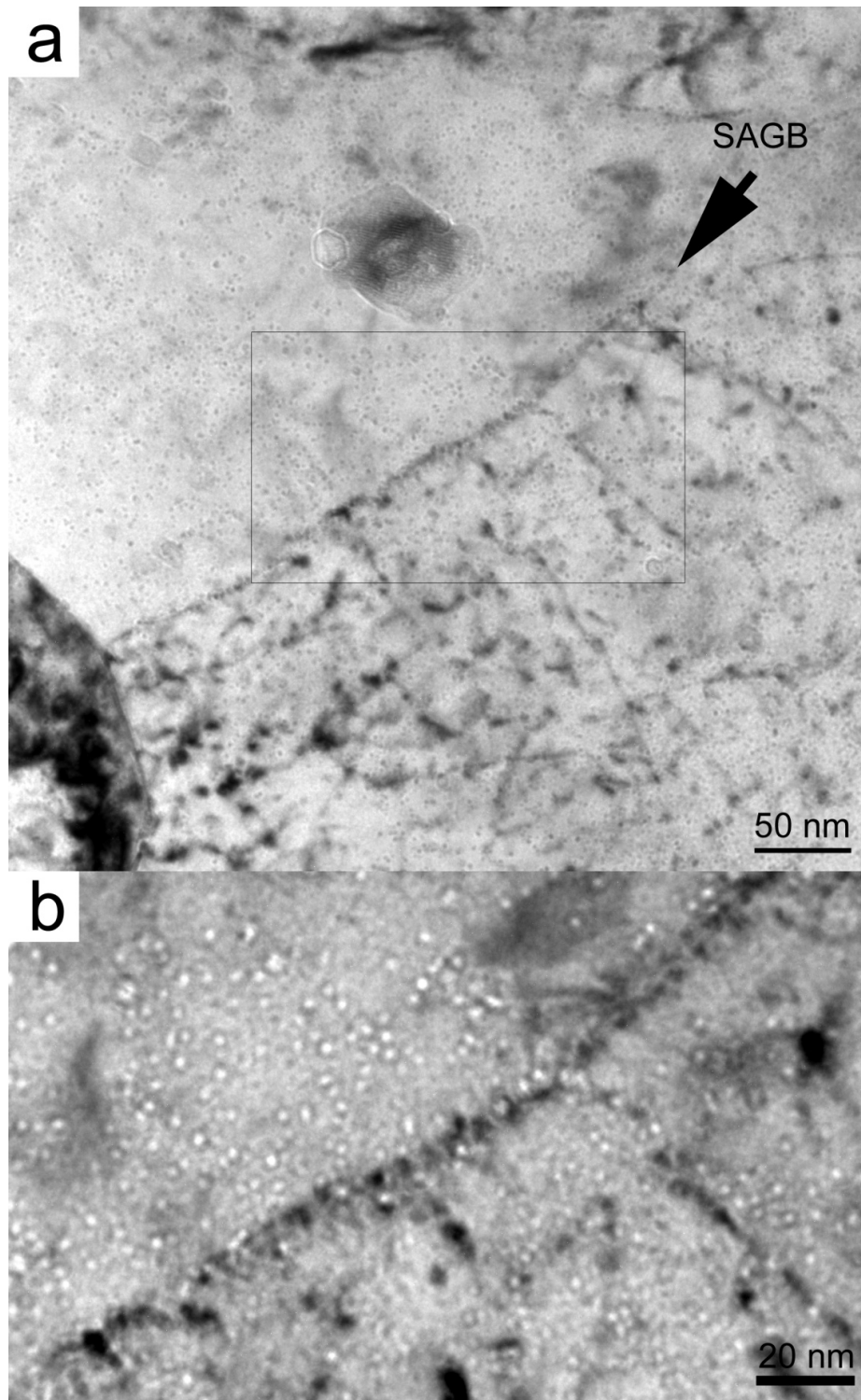


Figure 4. a) An over focus bright field image showing a SAGB, indicated by an arrow; and, b) an under focus image of the rectangular area in a.

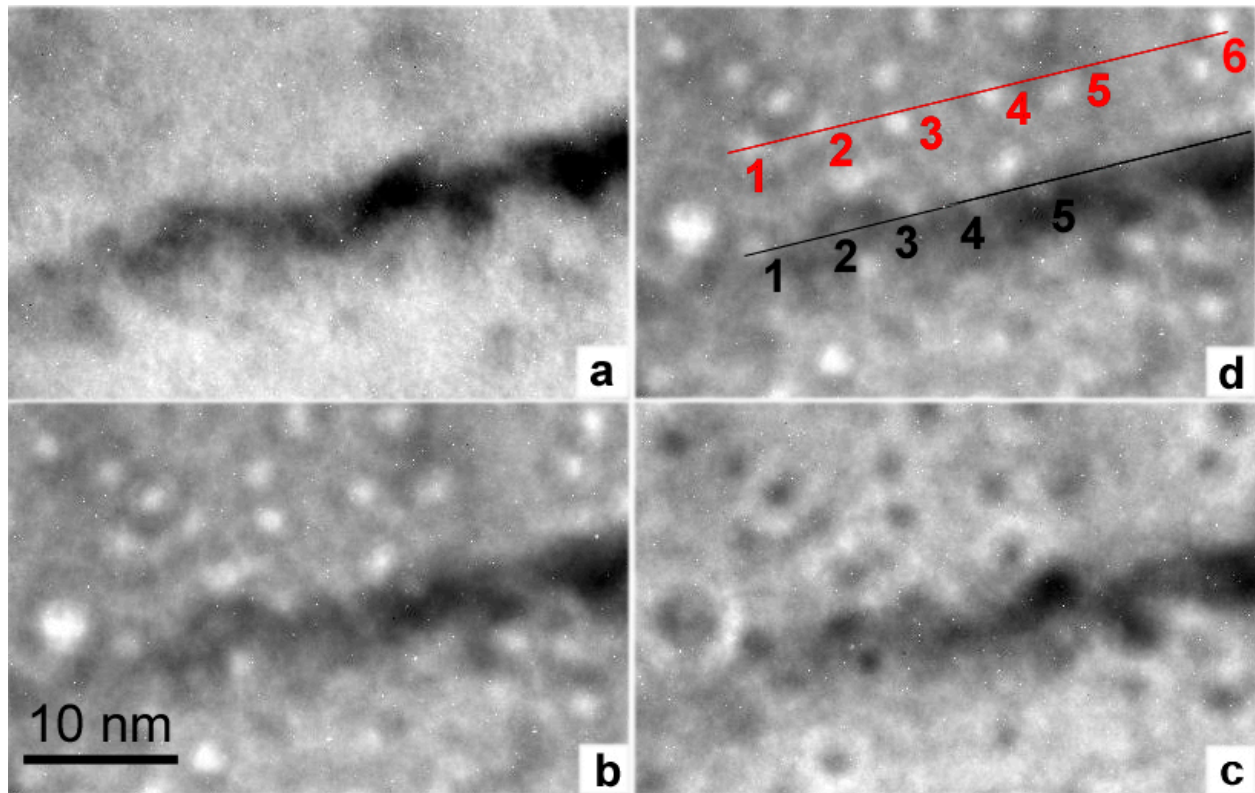


Figure 5. a) An in focus bright field image showing precipitates; b) an under focus bright field image of bubbles lying along dislocations vs. those residing in the matrix; c-d) under and over focus bright field images showing bubbles.

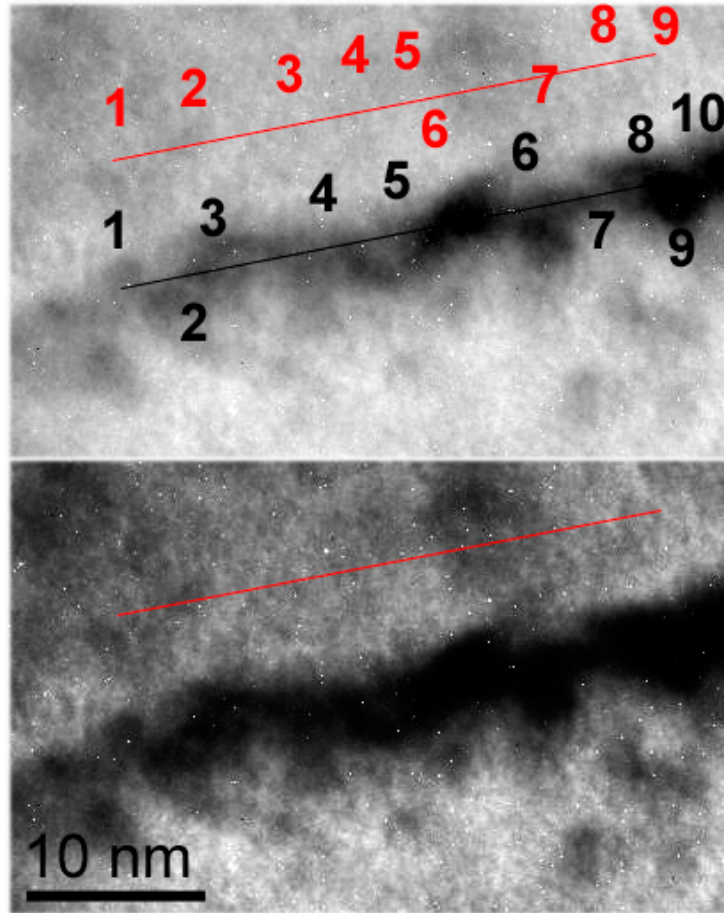


Figure 6. a-b) Bright field images showing the relationship between precipitates and dislocations where the brightness and contrast have been adjusted to be favorable for counting precipitates along the dislocation and in the matrix, respectively.

2.5 FRICTION STIR WELDING OF ODS STEELS AND ADVANCED FERRITIC STRUCTURAL STEELS — Z. Feng, Z. Yu, D. Hoelzer, M. A. Sokolov, and L. T. Tan (Oak Ridge National Laboratory)

OBJECTIVE

This project addresses the critical technology gap of joining oxide dispersion strengthened (ODS) steels, nanostructured ferritic alloys (NFAs), reduced-activation ferritic/martensitic (RAFM) steels, and dissimilar metal joining between ODS/NFAs and RAFM steels through friction stir welding technology. The research focuses on understanding the stability of the strengthening phases in the weld region, and the bonding mechanisms between dissimilar structural steels as a function of FSW process conditions.

Specific project objectives are (i) developing the process parameter space to consistently produce defect-free welds of the same and dissimilar metals, (ii) developing the knowledge base and practically applicable approaches to tailor and optimize the microstructure features in the weld to match the properties of the base metal through process innovation, and (iii) producing representative weld joints and welded components to support future testing and evaluation at high temperature and irradiation environments in collaboration with JAEA and other international collaborators.

SUMMARY

Initial friction stir trial welds were made on ODS alloy MA965, RAFM steels EUROFER97 and F82H, and between MA956 and EUROFER97 (dissimilar weld). Defect-free similar and dissimilar welds were obtained. The microstructure of the welded region was characterized using optical microscopy (OM) and small-angle neutron scattering (SANS). OM examination showed that the microstructures in the stir zone (SZ), thermo-mechanically affected zone (TMAZ) and heat affect zone (HAZ) were significantly different from these in the base metal (BM). Small angle neutron scattering measurements were performed in the base metal and welded region to characterize the changes in nano-scale oxide features. Aggregation of the fine nano-scale particles was observed in the SZ. Micro-hardness mapping on the cross section of welds clearly revealed the effects of FSW.

PROGRESS AND STATUS

Introduction

Future fusion reactors will require utilization of advanced structural materials that must safely sustain the extremely hostile environment involving intense heat fluxes, high temperatures, reactive chemicals, significant cyclic thermomechanical stresses, and intense fluxes of high-energy neutrons and electromagnetic radiation. These structural materials typically feature highly complex and unique microstructures tailored for high-performance properties.

For example, the nanostructured ferritic alloys (NFAs), an emerging class of fusion structural material, exhibit remarkable radiation damage resistance and high-temperature tensile, creep and fatigue strengths [1,2]. NFAs derive from oxide dispersion strengthened (ODS)

Steels [3-10]. The outstanding performance characteristics of NFAs are attributed to the presence of an ultrahigh density of Y-Ti-O rich nanofeatures that are produced through carefully engineered and sophisticated mechanical alloying (MA) routes. NFAs and ODS alloys must be welded for construction of fusion reactors and other large-scale industry systems. However, these high-performance steels are very difficult, if not impossible, to weld with the conventional welding processes such as arc welding, laser welding and electron beam welding. The bulk melting in these fusion-welding processes inevitably destroys the fine particle distribution by causing the particles rejected and aggregated at the solidification front in weld pool. The poor fusion weldability has been the major technical bottleneck limiting the application of the entire ODS alloy family.

Reduced-activation ferritic/martensitic (RAFM) steels are considered as the reference first-wall and blanket structural material for both ITER test blanket modules and future fusion power systems in essentially all of the worldwide fusion materials research programs [11,12]. While considered to have relatively good weldability, RAFM steels can suffer from welding induced property degradations. Softening of the heat-affected zone (HAZ) is a major factor for performance degradation [13].

The plasma chamber of a fusion reactor will comprise different subsystems and modules that utilize different materials to meet the challenging performance requirements [11]. Dissimilar material joining – joining vastly different materials such as ODS/NFAs to RAFM steels – is central to successful development of fusion power systems but it also poses an even greater technological challenge in materials joining than joining ODS alloys or RAFM steels alone.

In this project, friction stir welding (FSW) technology, a solid-state joining process, was utilized to join ODS/NFAs, RAFM steels, and, in particular, dissimilar metal joining between ODS/NFAs and RAFM. Initial trials were made to develop the process space to consistently produce defect-free welds of ODS alloy, and develop the knowledge base and practical approaches to tailor and optimize the microstructure features in different zones of the welds to match the properties of the base metal through process innovation.

Experimental Procedure

FSW trials were made on the ODS alloy MA965, RAFM steels EUROFER97 and F82H. In addition, FSW was used to join MA956 to EUROFER97 (dissimilar weld). The FSW experimental matrix and basic welding conditions are summarized in Table 1. The thickness of MA956, EUROFER97 and F82H sheets are 1mm, 25mm and 8mm, respectively. Polycrystalline boron nitride was chosen as the welding tool material, due to its excellent hardness and thermal stability.

Table 1. Parameters used for FSW trials on different advanced steels.

Case No.	Material	Rotation Speed (rpm)	Travel Rate (ipm)	Tool Tilt Angle (°)	Plunge Depth (inch)	Note
1	EUROFER97	400	2	0.5	0.22	Tool A
2	MA956 to EUROFER97	400	2	0.5	0.22	Tool A pin was worn out.
3	F82H	400	2	0.5	0.208	Tool B
4	F82H	400	2.5	0.5	0.208	Tool B shoulder fractured.

Microstructures within the stir zone (SZ), thermo-mechanically affected zone (TMAZ), and HAZ were examined under optical microscope. Hardness mapping was also performed on the cross section of the welds using LM100AT micro-hardness tester, in order to reveal the effect of FSW on the mechanical property of ODS alloys and RAFM steels. Sample surface was grinded, polished, and etched with a mixture of 30ml HCl and 10ml HNO₃ for Cases 1 and 2, and Nital for Cases 3 and 4, to study the microstructure and to exam the welding defects.

Small-angle neutron scattering (SANS) measurements were conducted at CG-2 beamline of the High Flux Isotope Reactor (HFIR) at ORNL, in order to examine the influence of FSW on the dispersion of nano-scale particles in MA956 weld (made in this reporting period), as well as 14WT and 14YWT (made previously). Two specimens with a thickness of 0.4mm and an area of 5x5mm² were sliced out from the top and middle region of stir zone (SZ), respectively, for each friction stir welds. The neutron beam wavelength was 4.72Å, and sample to detector distances were 6 and 0.3 m. Magnetic field was applied along horizontal direction to differentiate the scattering amplitudes contributed by non-magnetic oxides from these contributed by the magnetic ferrous alloy matrix.

Results

Based on the optical microstructure examination, defect-free similar and dissimilar welds were successfully made in all the four cases. The microstructures in the SZ, TMAZ, and HAZ were significantly different from these in the base metal (BM). For instance, Figure 1 illustrates the optical micrographs of the dissimilar weld between MA956 and EUROFER97 (Case 2 in Table 1). The boundary of the SZ is highlighted by the blue dotted line. It is worth noticing that on the retreating side of the friction stir weld, a significant amount of the MA956, which is on the top of the EUROFER97, is stirred down to the bottom of stir zone, and embedded inside the EUROFER97 by the downward stirring motion of the threaded tool pin. It is noted that the original grains in the base metal of MA965 were very large, over several mm in the plane of the thin sheet. As shown in Figure 1 (a), (b) and (d), a few coarsened grains with a size larger than half millimeter are generated in the lower part of heat affected zone (HAZ) of MA956 on both the advancing and retreating sides. In comparison, Figure 1 (e) indicates that on the retreating side, there are no coarsened grains in the upper HAZ of MA956. After FSW, in the SZ, the grain size of MA956 is around 10µm, as shown in Figure 2 (c). As for EUROFER97, grain coarsening is observed in the SZ, by comparing its micrograph in Figure 2 (b) to that of the EUROFER97 base material (BM) in Figure 2 (d). In the SZ of F82H welds, which is now shown here, much refined grains were observed.

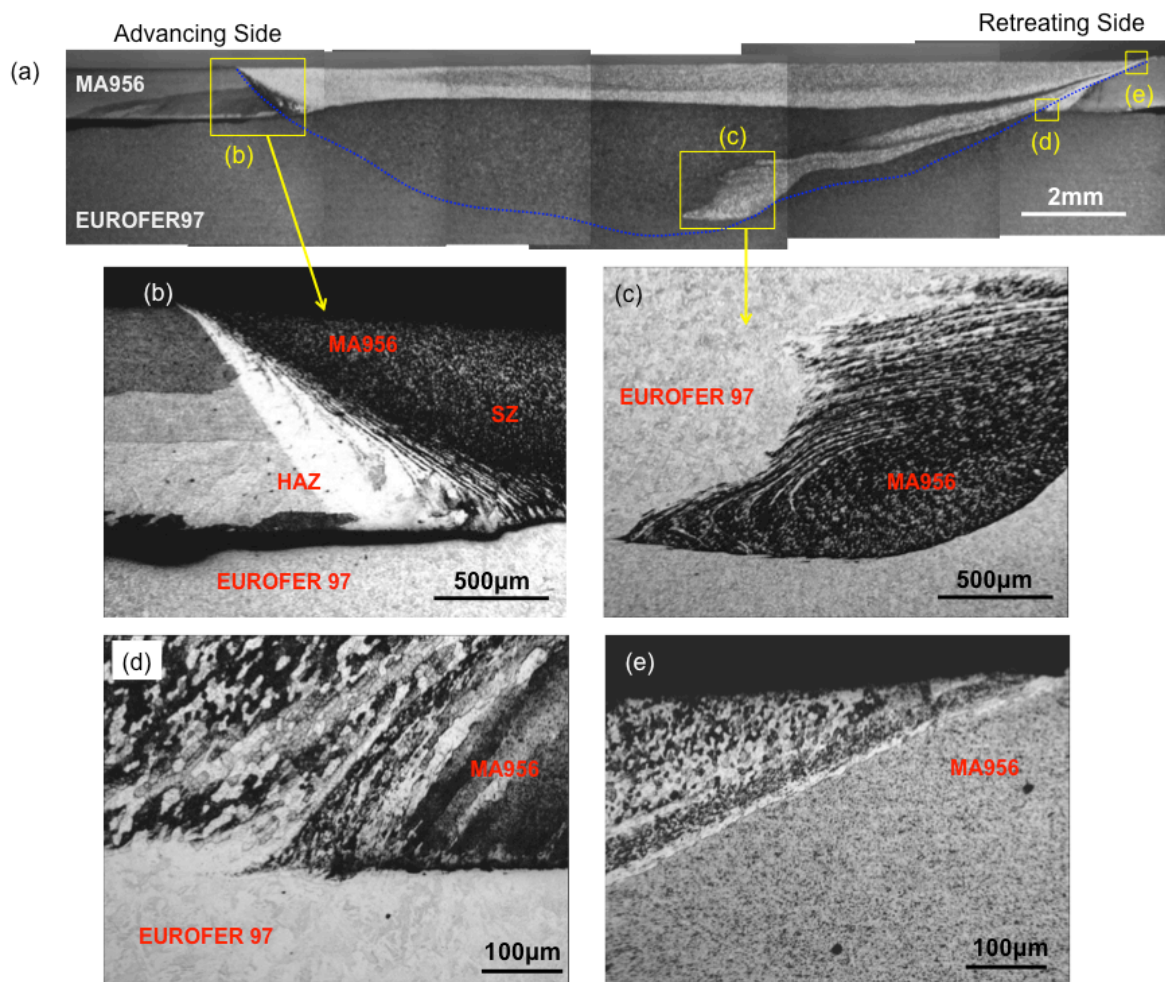


Figure 1. Optical micrographs of the dissimilar friction stir weld cross-section of MA956 to EUROFER97.

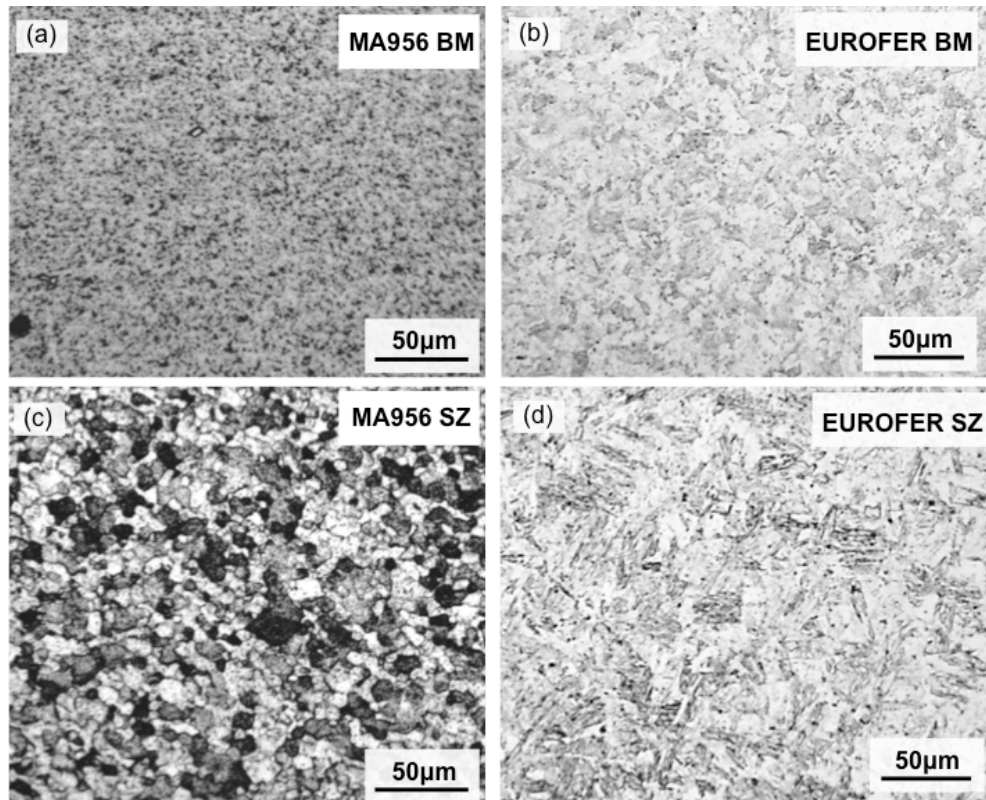


Figure 2. Optical micrographs of the base materials and stir zones of MA956 (a) and (c), and EUROFER97 (b) and (d), respectively, within the dissimilar friction stir weld of MA956 to EUROFER97.

Figures 3-6 show the micrographs of the welds cross sections of the four cases and their hardness distributions. Figure 7 summarizes the hardness profiles are plotted along the horizontal dotted lines marked in Figures 3-6 (b) within the upper part of the stir zone (SZ). Note that in Figure 7, x axis is the relative distance away from the center of SZ, as marked by the vertical dash dot lines in Figures 3-6 (b). As illustrated in Figures 3 (b), 4 (b) and 7(a), EUROFER97 base metal (BM) has an averaged hardness of ~220HV. FSW leads to a near twofold increase in the hardness within the SZ of EUROFER97. The highest hardness is observed on the retreating side of SZ. The boundary of thermo-mechanically affected zone (TMAZ) can be clearly identified in Figure 3(b), where the hardness in average is lower than that in SZ but higher than BM. A relatively large heat-affected zone (HAZ) with hardness lower than that of BM can be found outside the TMAZ, indicating softening in hardness and strength in the HAZ under the FSW conditions used in the welding trials. Figure 4(b) illustrates the hardness mapping on a dissimilar weld of MA956 and EUROFER97. MA956 BM has an averaged hardness ~268HV. After FSW, hardness of MA956, both on the top and in the middle of SZ, is decreased to as low as 190HV, as shown in Figures 4 (b) and 7 (a). Similar hardness distributions were observed within EUROFER97 welds in Cases 1 and 2. Figure 5 (b) shows that the F82H BM has an averaged hardness of ~320HV, and significant decrease in hardness was observed in HAZ. Note that for Case 4, the weld was made close to the edge of the F82H plate on the advancing side (AS). The relatively low thermal conductivity between steel and air leads to a more severe property degradation on the AS, as shown in Figure 6 (b).

By comparing Figure 6 (b) to Figure 5 (b), it can be concluded that faster travel rate, i.e., less heat input, during FSW results in higher hardness within SZ. Further characterization of the microstructure will be made to understand the hardness variation in different zones. FSW parameters will be modified to minimize the property degradation within HAZ.

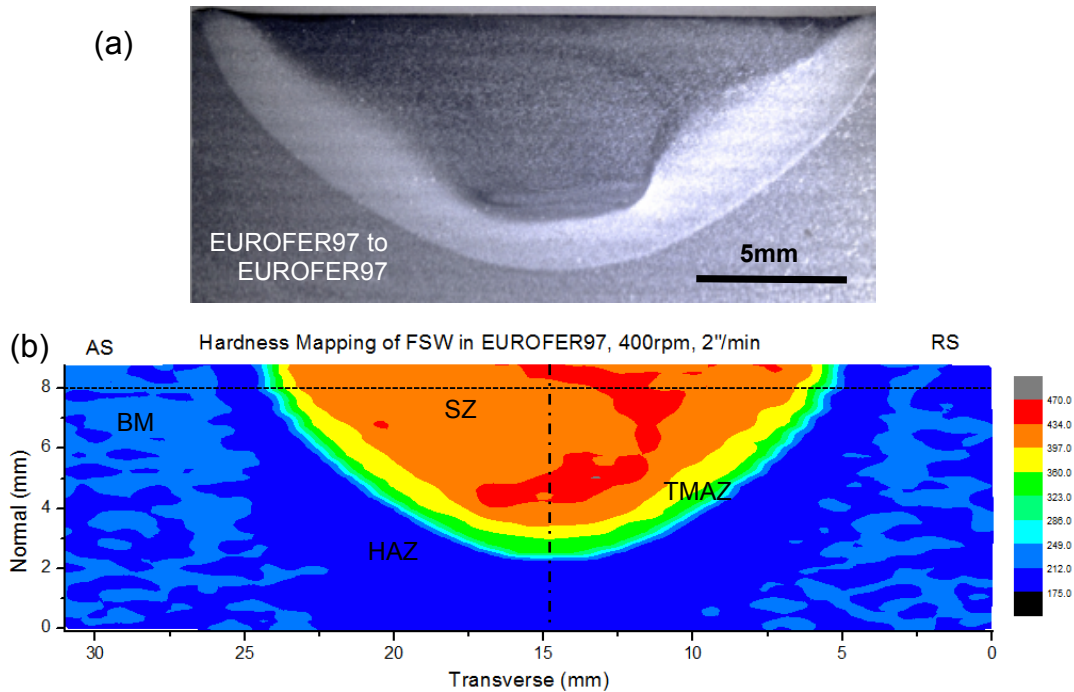


Figure 3. Friction stir welding of EUROFER97 (Case No. 1): (a) optical micrograph and (b) hardness mapping of the weld cross-section. AS and RS denote advancing and retreating sides. BM, SZ, TMAZ, HAZ represent base metal, stir zone, thermo-mechanically affected zone, and heat-affected zone.

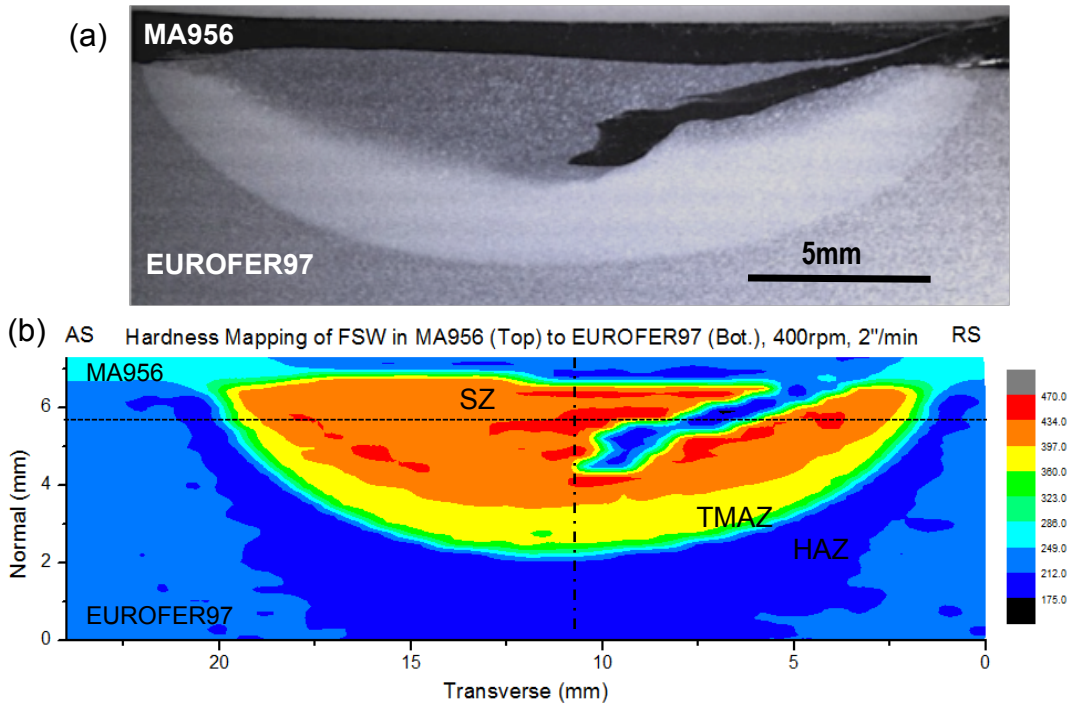


Figure 4. Friction stir welding of MA956 to EUROFER97 (Case No. 2): (a) optical micrograph and (b) hardness mapping of the weld cross-section.

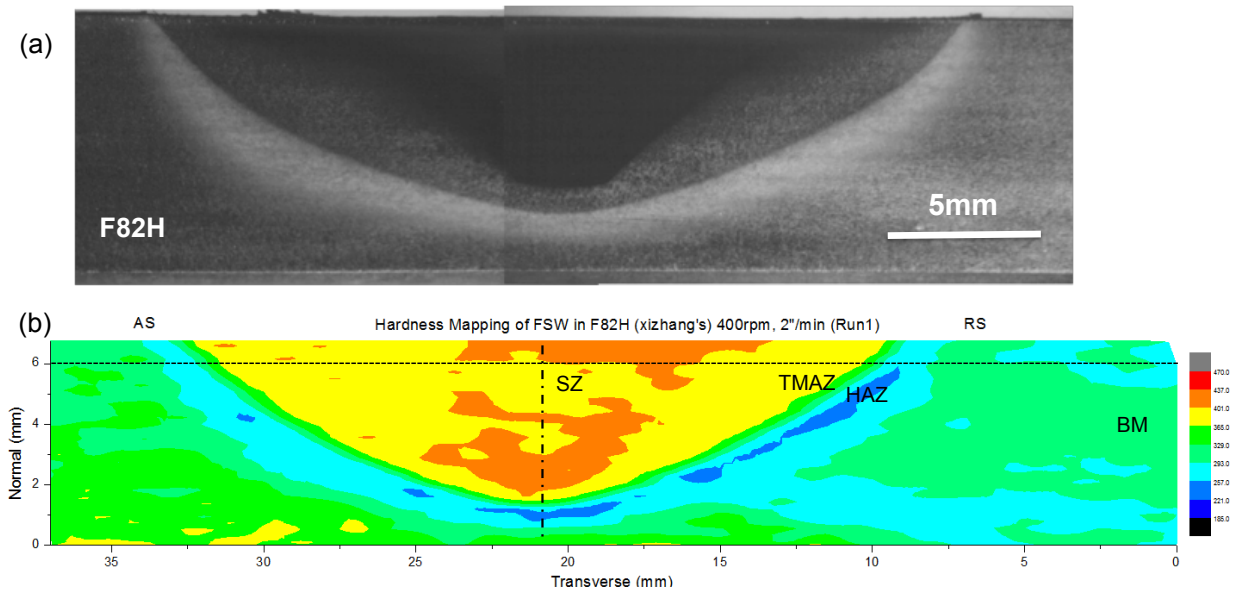


Figure 5. Friction stir welding of F82H (Case No. 3): (a) optical micrograph and (b) hardness mapping of the weld cross-section.

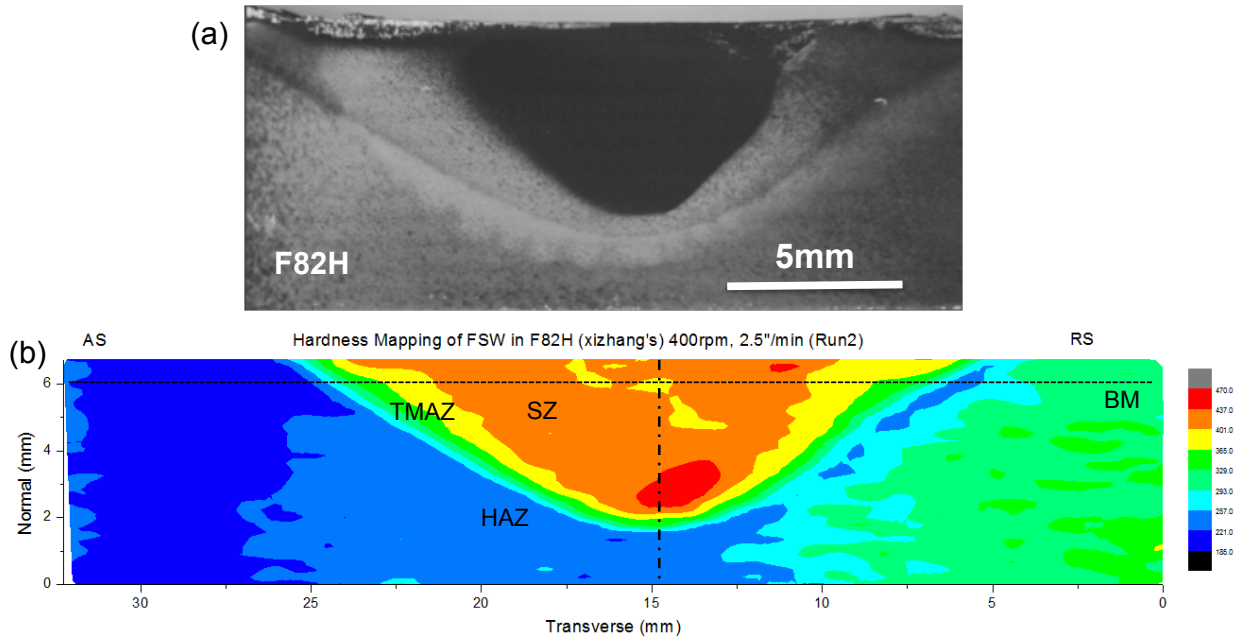


Figure 6. Friction stir welding of F82H (Case No. 4): (a) optical micrograph and (b) hardness mapping of the weld cross-section.

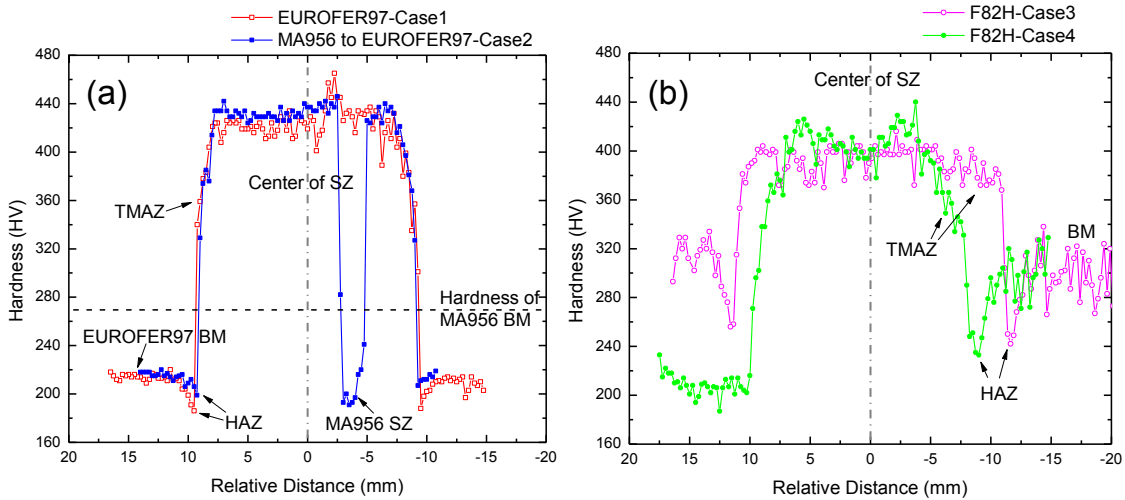


Figure 7. Hardness profile along the horizontal dotted lines marked in Figures 1-4 (b) within the upper part of SZ in the four cases.

Based on the hardness mapping result, it was observed that the selected FSW parameters led to reduction of hardness within the SZ of MA956. In order to reveal the effect of FSW on the dispersion of nano-particles, SANS measurements were performed in the BM and SZ of ODS alloys. Figure 8 (a)-(c) summarizes the obtained SANS images from the BM, top layer and 2nd layer of friction stir welds of 14WT. Data analysis is made on the SANS images, and the calculated probability of nano particles size are shown in Figure 8 (d)-(f). It indicates that in the

BM of 14WT, the nano particles are mostly about 3nm. Within the top layer of friction stir welds, the nano particles aggregate, and the mean size increases to near 5nm. In the second layer of friction stir welds, the nano particles are less influenced.

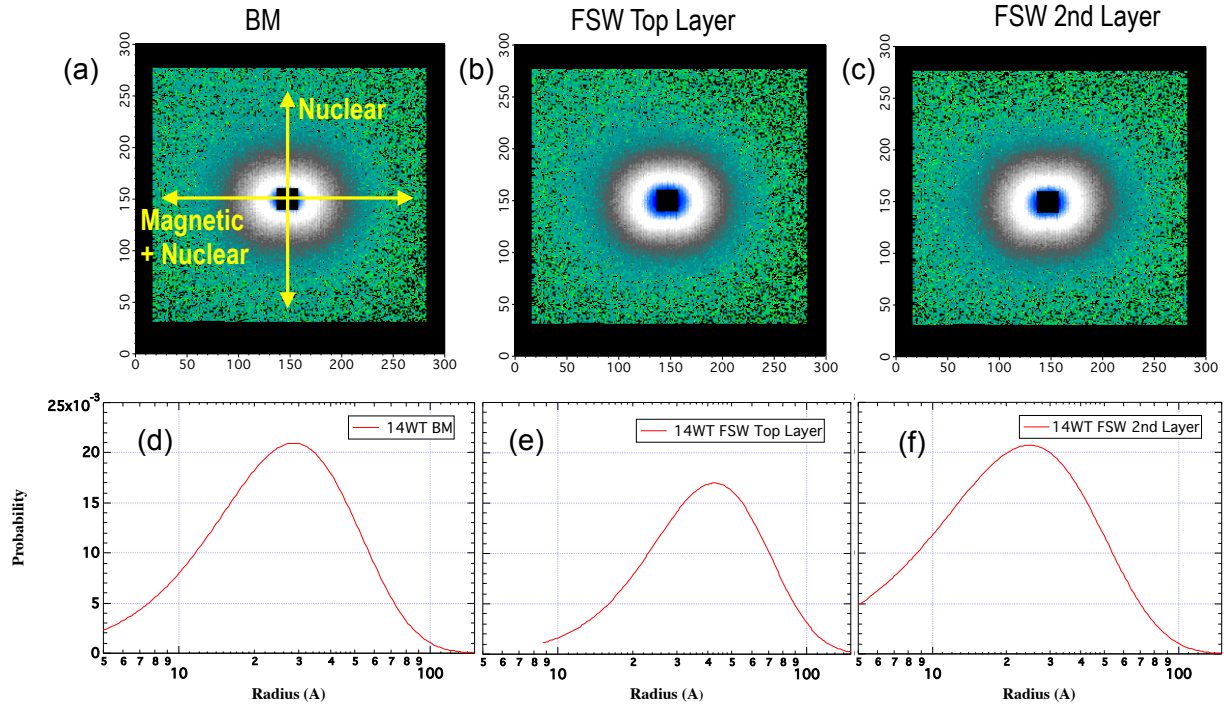


Figure 8. Small angle neutron scattering images (a)-(c) and the analyzed probability of nano particle size (d)-(f) in the BM, top layer and 2nd layer of friction stir welds in 14WT.

FUTURE WORK

Phases present in the SZ, TMAZ, HAZ and BM of EUROFER97, MA956 and F82H materials will be further analyzed through electron backscatter diffraction (EBSD) method. Also, more investigation will be made on the interface between the MA956 and EUROFER97 through scanning electron microscope (SEM) to reveal the bonding mechanisms in the dissimilar weld. Further analysis will be made in the SANS results of 14YWT and MA956 alloys.

REFERENCES

- [1] G. R. Odette, M. J. Alinger, and B. D. Wirth, "Recent Development of Irradiation-Resistant Steels," *Annu. Rev. Mater. Res.* **38**, 417-503 (2008).
- [2] G. R. Odette and D. T. Hoelzer, "Irradiation-Tolerant Nanostructured Ferritic Alloys: Transforming Helium from a Liability to an Asset," *JOM* **62** (9), 84-92 (2010).
- [3] G. A. J. Hack, "Superalloys for the 80s," *Metallurgia*. **49** (6), 256-257 (1982).
- [4] W. Sha and H. K. D. H. Bhadeshia, "Characterization of Mechanically Alloyed Oxide Dispersion-Strengthened Nickel-Base Superalloy MA760," *Metall. Mater. Trans. A* **25** (4), 705-714 (1982).

- [5] M. J. Fleetwood, "Mechanical Alloying-the Development of Strong Alloys," *Mater. Sci. Tech.* **2** (12), 1176-1182 (1986).
- [6] T. S. Chou and H. K. D. H. Bhadeshia, "Grain Control in Mechanically Alloyed Oxide Dispersion-Strengthened MA-957 Steel," *Mater. Sci. Tech.* **9** (10), 890-897 (1993).
- [7] M. T. Shaw, "Incoloy Alloy MA956 for High Temperature Industrial Applications," *Metallurgia.* **54** (11), S32-S33 (1987).
- [8] E. Grundy, C. J. Precious, and D. Finder, "Hot Forming of Mechanically Alloyed Gas Turbine Components," *Metal Powder Reports* **40** (10), 565-569 (1985).
- [9] J. J. Fischer, "Properties of Mechanical Alloyed Super-Alloy Related to Industrial Heating Uses," *Ind. Heating* **40** (12), 25-26 (1988).
- [10] R. K. Wilson and F. L. Perry, "Superior Heat Treatment Capabilities of MA Superalloys Developed by Thermo-Mechanical and Heat Treatment Processes," *Ind. Heating* **51** (5), 27-30 (1984).
- [11] R. J. Kurtz, A. Alamo, E. Lucon, Q. Huang, and S. Jitsukawa, "Recent Progress Towards Development of Reduced Activation Ferritic/Martensitic Steels for Fusion Structural Applications," *J. Nucl. Mater.* **386-388**, 411-417 (2009).
- [12] H. Serizawa, S. Nakamura, M. Tanaka, Y. Kawahito, H. Tanigawa, et al., "Effect of Mechanical Restraint on Weldability of Reduced Activation Ferritic/Martensitic Steel Thick Steels," *J. Nucl. Mater.* **417**, 55-88 (2011).
- [13] N. Inoue, T. Muroga, A. Nishimura, and O. Motojima, "Correlation Between Microstructure and Hardness of a Low Activation Ferritic Steel (JLF-1) Weld Joint," *J. Nucl. Mater.* **258-263**, 1248-1252 (1998).

3.1 SWELLING AND X-RAY PEAK BROADENING OF HIGH DOSE NEUTRON IRRADIATED SiC COMPOSITES — C. Shih, R. Meisner, Y. Katoh, and L. L. Snead (Oak Ridge National Laboratory)

OBJECTIVE

The main objective of this work is to study the effect of high dose neutron irradiation on an early generation nuclear grade SiC/SiC composite, focusing on lattice parameter changes (using XRD techniques) and macroscopic dimensional changes following neutron irradiation up to ~70 dpa.

SUMMARY

The lattice parameter changes in high dose (up to ~70 dpa) neutron irradiated nuclear grade SiC/SiC composites were studied with room temperature powder XRD and compared with macroscopic dimensional changes at nominal irradiation temperatures of 300, 500 and 800°C. The results show no lattice parameter change for all high dose neutron irradiated SiC/SiC composites while macroscopic volume swelling is observed. This observation agrees with the very limited literature data on XRD studies of high dose CVD SiC and high dose hot pressed SiC. The lattice parameter changes disagree with macroscopic dimensional changes, suggesting progressive evolution of microstructures involving transition of ultra-fine interstitial clusters into larger interstitial loops as the very high irradiation doses are achieved. However, the errors in lattice parameter measurements caused by high surface roughness of the unpolished composites remains an issue and need to be further studied.

PROGRESS AND STATUS

Introduction

Nuclear grade SiC fiber reinforced SiC matrix (SiC/SiC) composites have excellent thermal, mechanical, and chemical stability with nuclear systems [1-3]. They also showed high radiation stability and low neutron activation; render them suitable for application in fission and fusion reactors. The thermal physical and mechanical properties of SiC/SiC composites have been studied intensively. Moreover, it is generally agreed that the “prove-of-principle” phase of nuclear grade SiC/SiC composites development has been finished and the R&D on SiC/SiC composites is shifting to the more pragmatic phase [4]. However, there is a lack of experimental data on the effect of high dose (>20 dpa, displacement per atom) irradiation partly because the lack of affordable neutron sources. Since the core materials in a fusion reactor is expected to suffer radiation damage of hundreds of dpa, it is critically important to study the effect of high dose irradiation on those candidate materials.

In this report, x-ray diffraction (XRD) analysis with Bragg-Brentano geometry was used to study the phase composition and lattice parameter changes in nuclear grade SiC/SiC composites upon neutron irradiation to fluences of up to ~70 dpa at irradiation temperatures of 300, 500 and 800°C. The results are compared with the measured macroscopic length changes. Some other property changes of the same composites under the same irradiation campaign can be found if ref [1].

Experimental

The composite material studied was two-dimensional (2D) 5-harness satin-weave Hi-Nicalon™ Type-S SiC fiber reinforced chemically vapor-infiltrated SiC matrix composites (HNLS composite). The HNLS composite was fabricated by Hyper-Therm High Temperature Composites, Inc. (Huntington Beach, CA) using the isothermal chemical vapor infiltration (I-CVI) method with multilayer fiber coating of pyrocarbon (PyC) and SiC. In the multilayer PyC/SiC interphase, the first SiC layer of 100 nm thick was deposited following the deposition of a thin PyC layer of 20 nm directly onto the fiber surface. Then, three SiC/PyC bi-layers were deposited, followed by the CVI SiC matrix deposition. Transmission electron microscopy images of the non-irradiated multilayered interphase structure and the selected area diffraction patterns showing the polycrystalline beta-phase SiC as the dominant phases in all the constituents, namely the fiber, interphase, and matrices, are presented in Fig. 1 [3].

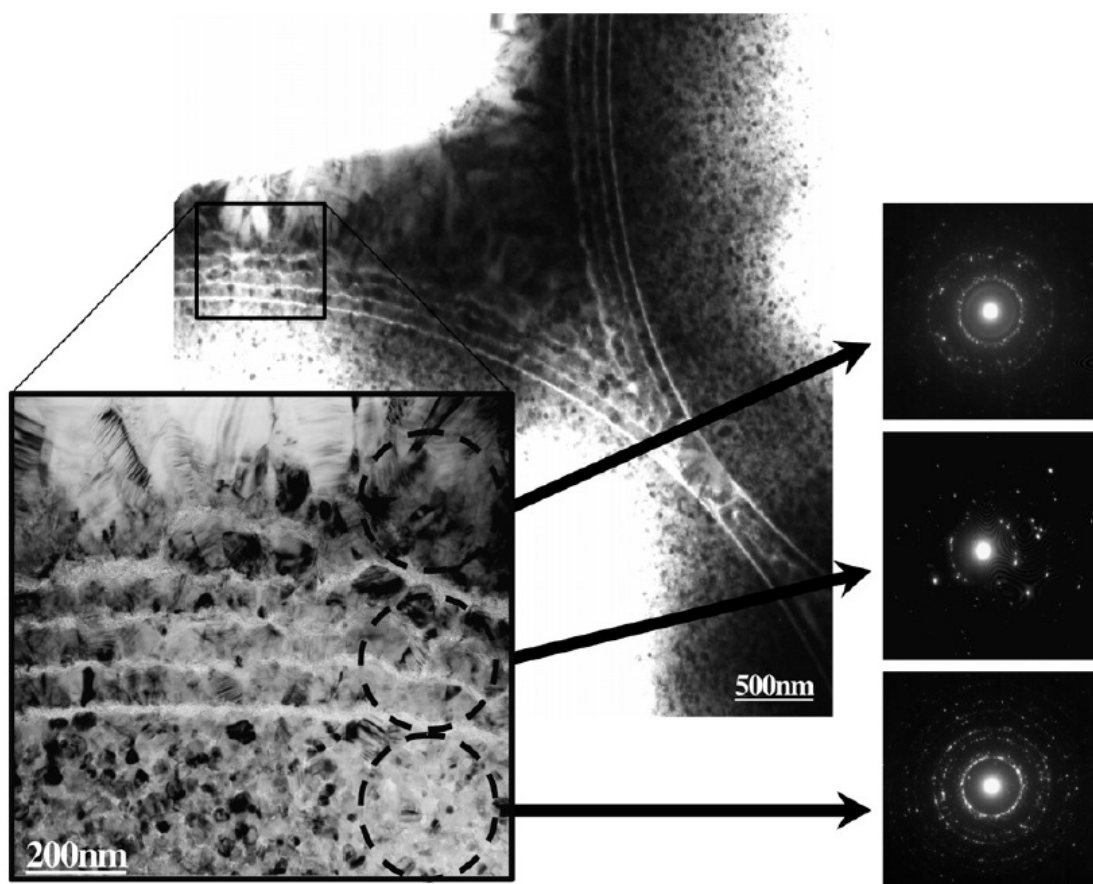


Fig. 1. TEM images of multilayer interphase of SiC/SiC composites [3].

The HNLS composites were machined into rectangular bars of various sizes and were irradiated in HFIR at ORNL using the flux trap fixed rabbit tube facility with a fast neutron flux of $\sim 1 \times 10^{19}$ n/m²/s ($E > 0.1$ MeV). Photographs of a typical rabbit capsule before assembly and the HNLS composite samples are shown in Fig. 2. The samples were irradiated to neutron fluences of ~ 28 dpa (irradiation temperature of 300°C (27.8 dpa), 500°C (28.2 dpa), and 800°C (28 dpa)), 40.7 dpa (irradiation temperature of 800 °C) and ~ 70 dpa (irradiation temperature of 300°C 71

dpa), 500°C (74 dpa), and 800°C (71 dpa)); 1 dpa equals 10^{25} n/m² (E>0.1 MeV) is assumed throughout this report. The irradiation temperature was determined by post-irradiation annealing of room temperature electrical resistivity of dedicated CVD SiC thermometry samples, which had been irradiated in contact with the rectangular HNLS composites samples [5].



Fig. 2. HFIR rabbit capsules before assembly (left: capsule housing, specimen holder, and springs are shown on top, middle, and bottom, respectively, and capsule end cap and centering thimble are shown on right) and a pair of HNLS composite samples. Length of specimens and specimen holder are about 5 mm.

Following irradiation, the dimensions of the samples were measured using a caliper to an accuracy of 10 μ m. The length change of the rectangular bars was used to calculate the macroscopic volume change of the samples, with the assumption that sample irradiation swelling is isotropic. For the lattice space change study with XRD, continuous θ - 2θ scans were performed on the Panalytical X'pert diffractometer (Westborough, MA) from nominally 5° to 110° 2θ angles in 60-minute scans using CuK α radiation ($\lambda=1.540598$ Å) and the X'Celerator detector. All scans used $\frac{1}{4}^\circ$ fixed slits and $\frac{1}{2}^\circ$ anti-scatter slit. The height of the sample was adjusted using the (111) peak of Moissanite-3C (β -SiC) with the sample placed on a zero background plate with a Kapton™ film. A search match was conducted using the “Jade” and/or “HighScore” software and the ICDD database. Power XRD was also conducted on non-irradiated HNLS composite, CVD SiC (Dow Chemical, Marlborough, MA), and bare Hi-Nicalon™ Type-S SiC fibers as reference materials. In order to accurately determine the lattice parameters, Si powder was sprinkled on top of the specimens as an internal standard for all the XRD studies except for ~70 dpa irradiated SiC/SiC composites and un-irradiated bare SiC fibers.

Results and Discussion

XRD profiles of non-irradiated samples

The XRD profiles of non-irradiated samples, including Hi-Nicalon Type S (HNLS) bare fibers, CVD SiC, and HNLS composites (with and without Si powder) are shown in Fig. 3. Only 3C-SiC (β -SiC) phase is identified in CVD SiC and HNLS bare fibers. One unique character for the profile of HNLS fibers is the obvious shoulder on the low angle side of the (111) peak near 36° 2θ angle. The XRD profiles of HNLS bare fibers appear to be indistinguishable from the work by Gosset *et al.* on the same fibers [6], validating that the XRD diffractometer worked correctly. The HNLS fiber XRD profile suggests that the fibers contain a high density of planer defects, such as stacking faults. CVD SiC showed narrower peak width, suggesting less planer defects than HNLS fiber. The HNLS composites profiles show both β (3C) and α (2H) polytypes of SiC. Since the α peaks were not observed for HNLS fibers heat treated up to 1900°C [6]. The α (2H) peaks from the HNLS composites are likely from the CVI SiC matrix.

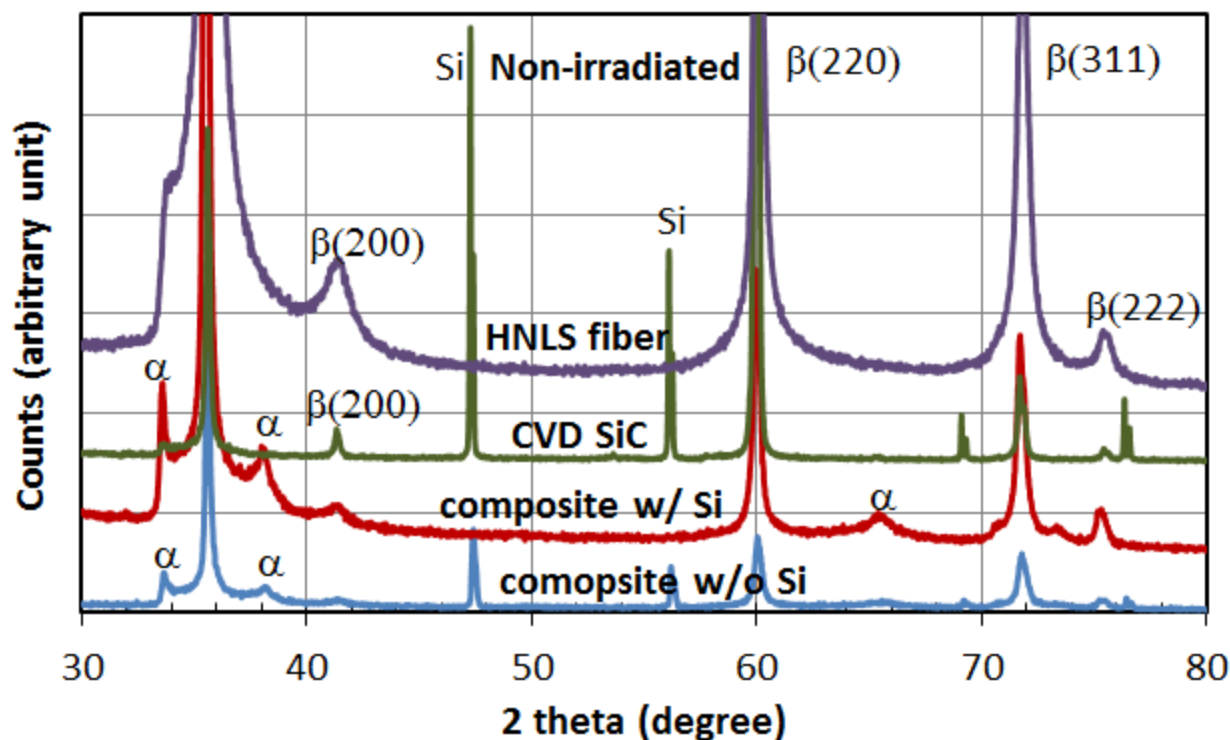


Fig. 3. XRD profiles of non-irradiated samples, including Hi-Nicalon Type S bare fiber, CVD SiC, and HNLS composites with and without Si powder.

Neutron irradiated HNLS composites

The ~28 dpa and ~70 dpa irradiated HNLS SiC/SiC composites XRD profiles are shown in Fig. 4 and Fig. 5, respectively, with un-irradiated composite profile as a reference. Because of the complex structure of the woven composites and the inherent high stacking fault density of both fiber and matrix in the composites [6,7], rigorous analysis of the XRD profiles are not feasible. XRD peaks from both 3C-SiC (β type) and 2H-SiC (α type) polymorphs are identified and are labeled in Fig. 4 and Fig. 5. The high stacking faults in the composites likely contribute to the 2H-SiC peaks. No new phases were detected by the XRD techniques following irradiation. The insert in Fig. 4 shows the details of the 35.6° peaks for ~28 dpa irradiated composites. The higher peak intensity of the 300°C irradiated composites is caused by larger sample size. It can be clearly seen from the insert that the non-irradiated composite has the smallest full peak width at half maximum (FWHM). The irradiated composites showed increased FWHM, caused likely by radiation-induced defects and associated lattice micro strains. A general observation is that peak broadening on the $\sim 35.6^\circ$ peak is larger for the lower temperature irradiated composites. This indicates that defect caused lattice strain might contribute to the observed peak broadening. However, no conclusion could be drawn from the Williamson-Hall analysis because the peak broadening is inconsistent along 2θ angles, causing very poor linearity. This behavior is likely caused by high density of certain type of defects, leading to line broaden of certain peaks [6]. A more rigorous analysis is ongoing and will be discussed in future reports.

The lattice constant (d space) of SiC, calculated with the software using Si powder as an internal standard (except ~70 dpa irradiated samples, which did not have internal standard) is presented in Table 1. The d space value for non-irradiated HNLS composites with Si powder is used as a

reference to calculate the percent lattice constant change of all the irradiated composites. The macroscopic length changes for the same samples are also presented. Some historical data of CVD SiC high dose neutron irradiation studies are included in Table 1. To the authors' best knowledge, no data are available for XRD profiles of neutron irradiated SiC/SiC composites in the open literature.

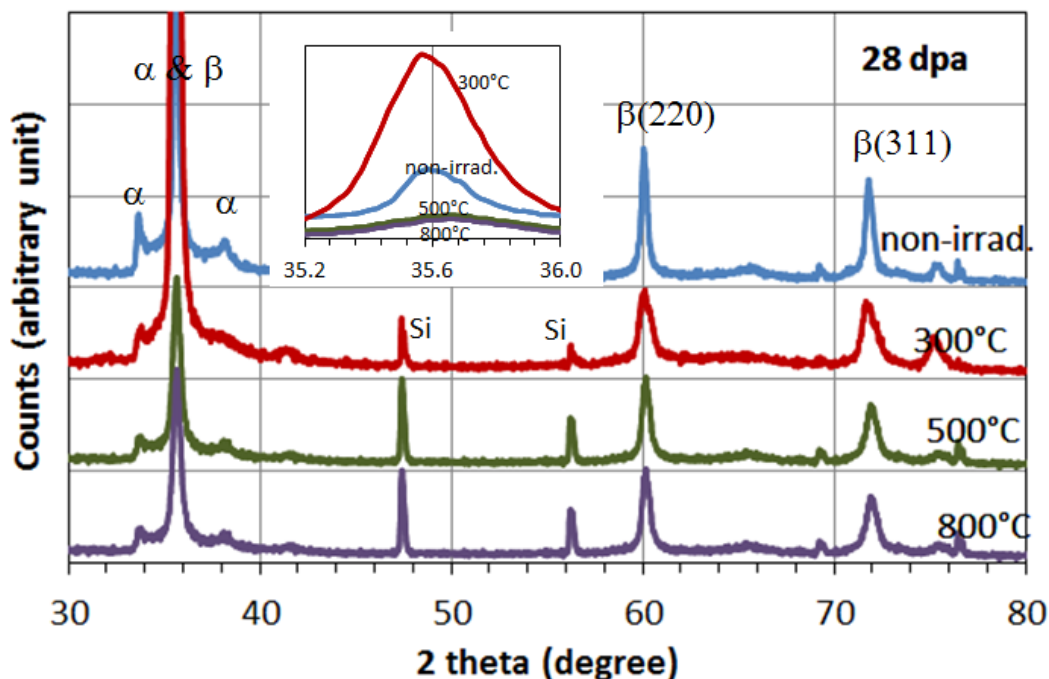


Fig. 4. XRD profiles of the ~28 dpa irradiated composites.

The results in Table 1 are graphically summarized in Fig. 6. The macroscopic length change is independent of irradiation fluence between ~28 and ~70 dpa and appears to be in a saturation regime. The magnitude of length swelling is inversely proportional to the irradiation temperature, which has been well known for CVD SiC and nuclear grade SiC/SiC composites in the point defect regime [1,3,8,9]. It is known that fairly good agreement between dimensional expansion and lattice constant expansion exists for SiC under neutron irradiation when irradiation conditions are at point defect regime (150 to 1000 °C) at intermediate neutron fluences (<5 dpa) [8,9] because very tiny interstitial clusters scattered in the matrix can account for both the XRD lattice swelling and volume swelling. However, there is a clear discrepancy between the macroscopic length change and the lattice space change of the HNLS composites in this study. This discrepancy has been previously reported in a couple of papers in the open literature that discussed about lattice space changes of high dose CVD SiC [8,10]. Considering the similar microstructure of the fiber and the matrix to that of CVD SiC, it is reasonable to believe that the same mechanism is account for the discrepancy in the high dose irradiated HNLS composites.

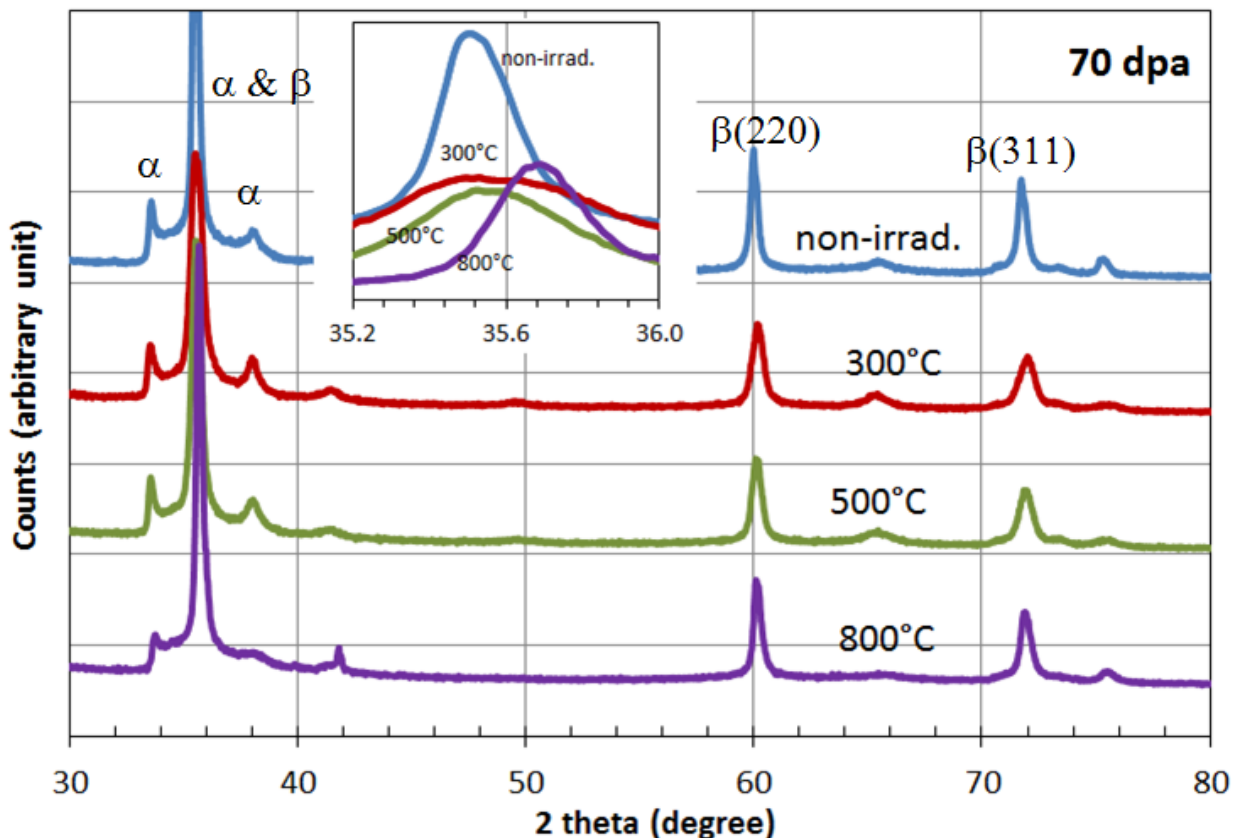


Fig. 5. XRD profiles of the ~70 dpa irradiated composites.

It should be noted that precise determination of lattice parameters requires a flat sample surface and a well-distributed internal standard (Si powder). In this study, the composite samples are not polished because of radiation contamination concerns. Moreover, the Si powder internal standard was sprinkled on top of the composites and was not well distributed. These factors all contribute to the errors associated with the lattice parameter determined by the XRD technique. It should also be noted that the two historical papers [8,10] that discussed about high dose CVD SiC are published in the 1970s. The materials in those studies, while claimed to be CVD SiC, might have more impurities than today's high purity CVD SiC or the CVI SiC matrix in the HNLS composites. Since impurities are known to affect the behavior of SiC materials under irradiation [9], readers should be skeptical about these historical results.

More recently, Yano and coworkers [11] reported lattice parameter changes and volume swelling of high dose neutron irradiated monolithic SiC. Their results showed similar trend of discrepancy between the two types of measurements. However, their material is not of high purity CVD SiC but has sintering aids, rendering direct comparison impractical.

Table 1. Summary of the d space change and the macroscopic length change following irradiation

Material	Irradiation condition		XRD		macroscopic	
	fluence (dpa)	Irrad. temp (°C)	d space (Å)	% change	% liner change from dimension	standard deviation
HNLS composite w/ Si	Non-irradiated		4.360	-	-	-
HNLS composite w/o Si	Non-irradiated		4.366	-	-	-
HNLS composite	27.8	300	4.366	0.14	0.45	0.03
HNLS composite	28.2	500	4.356	-0.09	0.48	0.09
HNLS composite	28.0	800	4.359	-0.02	0.33	0.08
HNLS composite	40.7	800	4.363	0.06	0.23	N/A
HNLS composite	71	300	4.349	-0.25	0.64	0.09
HNLS composite	74	500	4.355	-0.11	0.48	0.03
HNLS composite	71	800	4.352	-0.18	0.33	0.04
HNLS bare fiber	Non-irradiated		4.360	-	-	-
CVD SiC	Non-irradiated		4.357	-	-	-
CVD SiC, 1975[10]	50	550	4.356	-0.09	0.43	N/A
CVD SiC, 1977 [8]	12	1000	-	0.03	0.14	0.05

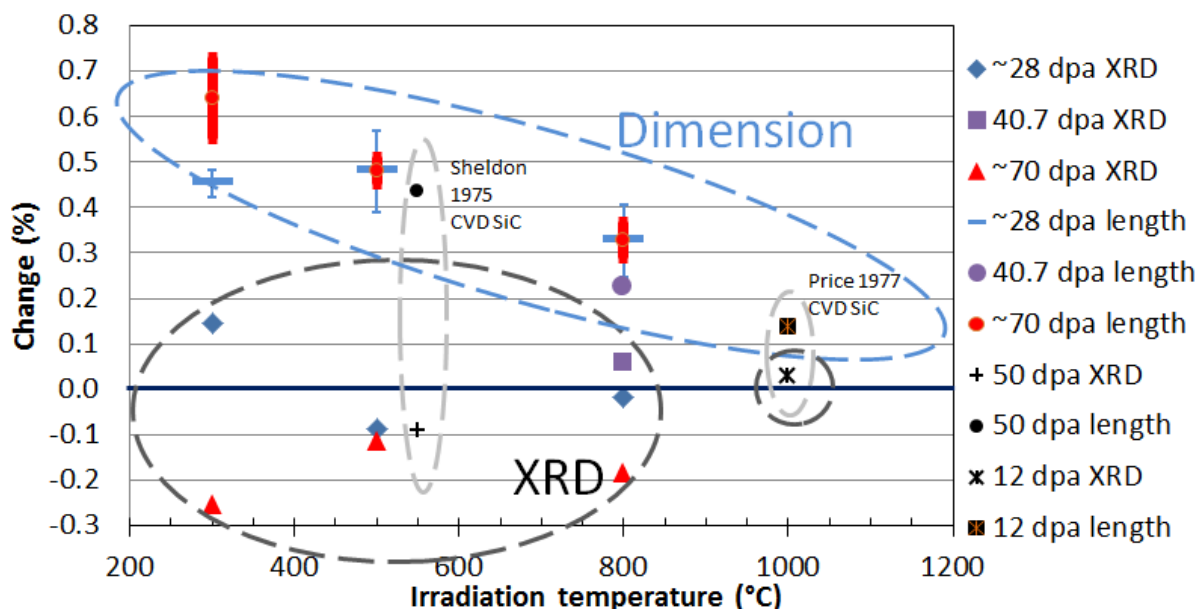


Fig. 6. Lattice parameter changes and macroscopic length changes of SiC materials at various irradiation conditions.

CONCLUSIONS

In summary, our XRD results of high dose neutron irradiated HNLS SiC/SiC composites show very little swelling or even shrinkage of lattice d space while macroscopic length swelling for the same samples is observed. Similar behaviors have been reported for high dose neutron irradiated CVD SiC [8,10] and hot pressed SiC [11]. However, the impurities of the materials used in the literature papers and the uncertainties in lattice space determined in this study, caused by the high sample surface roughness, make it difficult to draw a sound conclusion. More work is needed to verify whether the observed discrepancy is true and the cause of it.

REFERENCE

- [1] Y. Katoh, T. Nozawa, L. L. Snead, K. Ozawa and H. Tanigawa, *J. Nucl. Mater.* **417** (2011) 400-405.
- [2] Y. Katoh, K. Ozawa, T. Hinoki, Y. Choi, L. L. Snead and A. Hasegawa, *J. Nucl. Mater.* **417** (2011) 416-420.
- [3] G. Newsome, L. L. Snead, T. Hinoki, Y. Katoh and D. Peters, *J. Nucl. Mater.* **371** (2007) 76-89.
- [4] T. Nozawa, T. Hinoki, A. Hasegawa, A. Kohyama, Y. Katoh, L. L. Snead, C.H. Henager and J. B. J. Hegeman, *J. Nucl. Mater.* **386-388** (2009) 622-627.
- [5] J. E. Palentine, *J. Nucl. Mater.* **61** (1976) 243-253.
- [6] D. Gosset, C. Colin, A. Jankowiak, T. Vandenberghe and N. Lochet, *J. Am. Ceram. Soc.* **96** (2013) 1622-1628.
- [7] U. Lindefelt, H. Iwata, S. Oberg and P. R. Briddon, *Phys. Rev. B* **67** (2003).
- [8] R. J. Price, *Nucl. Technol.* **35** (1977) 320-336.

- [9] L. L. Snead, T. Nozawa, Y. Katoh, T. S. Byun, S. Kondo and D. A. Petti, *J. Nucl. Mater.* **371** (2007) 329-377.
- [10] B. E. Sheldon. 1975, U.K. Atomic Energy Research: Establishment, Harwell.
- [11] T. Yano, M. Akiyoshi, K. Ichikawa, Y. Tachi and T. Iseki, *J. Nucl. Mater.* **289** (2001) 102-109.

3.2 PROPERTIES OF DEFECTS AND IMPLANTS IN Mg⁺ IMPLANTED SILICON CARBIDE — W. Jiang, Z. Zhu, T. Varga, M. E. Bowden, S. Manandhar, T. Roosendaal, S. Y. Hu, C. H. Henager, Jr., R. J. Kurtz, (Pacific Northwest National Laboratory); and Y. Wang (Los Alamos National Laboratory)

OBJECTIVE

As a candidate material for fusion reactor designs, silicon carbide (SiC) under high-energy neutron irradiation undergoes atomic displacement damage and transmutation reactions that create magnesium as one of the major metallic products. The presence of Mg and lattice disorder in SiC is expected to affect structural stability and degrade thermo-mechanical properties that could limit SiC lifetime for service. We have initiated a combined experimental and computational study that uses Mg⁺ ion implantation and multiscale modeling to investigate the structural and chemical effects in Mg implanted SiC and explore possible property degradation mechanisms.

SUMMARY

Implantation of 3C-SiC, 6H-SiC and CVD-SiC has been performed with 200 keV Mg⁺ ions to fluences up to 3.2×10^{16} ions/cm² at 773 K. Rutherford backscattering analyses of the as-produced damage states along multiaxial channeling directions indicate that there are interstitial-type defect configurations that are well aligned with the <100> axis, such as Si-Si <100> interstitial splits. The depth profile of the as-implanted Mg exhibits a Gaussian-like distribution without evidence of considerable diffusion-driven mass transport during implantation. A post implantation thermal annealing study shows that there is a significant recovery of the structural defects with essentially immobile Mg in SiC up to 1473 K. Further annealing at higher temperatures is currently in progress with intent to recover implantation damage to the maximum extent possible while retaining Mg implants in the sample. Characterizations will follow using spectroscopy and microscopy to study microstructure and Mg behavior in SiC.

PROGRESS AND STATUS

Introduction

Due to their outstanding properties and attractive features, silicon carbide composites (SiC/SiC) have been investigated as candidates for structural materials [1] and flow channel inserts [2] in the designs of fusion power plants. The materials will be subjected to high-energy neutron irradiation in the fusion environment, resulting in elemental transmutations and atomic displacements. Recent calculations by Sawan, *et al.* [3] predict that at a fast neutron dose of ~100 dpa (displacements per atom), there will be ~0.5 at.% Mg generated in SiC among other major transmutants that include 0.15 at.% Al, 0.2 at.% Be, 0.01 at.% P, 2.2 at.% He and 0.84 at.% H through (n, α), (n,d) and (n, β γ) nuclear reactions. The effects of those impurities in SiC on structural stability and thermo-mechanical properties are currently unknown and need to be studied in order to assess property degradation that could limit the material lifetime for service. We have initiated a study that uses a combination of Mg⁺ ion-implantation and multiscale modeling to simulate and examine the structural and chemical effects. The goal is to identify and understand the Mg roles in disordered SiC structure and to assess its impact on properties. This initial experimental report summarizes the data on the defect accumulation and recovery as well as Mg behavior in implanted and annealed SiC. Further studies will address

microstructures, Mg locations, possible Mg-containing precipitates, swelling in conjunction with helium, grain boundaries, etc.

Experimental Procedure

Three polymorphs of 3C-SiC single-crystal film on Si substrate, 6H-SiC single-crystal wafer, and polycrystalline CVD-SiC bulk were implanted 7° off normal with 200 keV Mg⁺ ions to fluences up to 3.2×10¹⁶ ions/cm² at 773 K. The elevated temperature was applied to avoid full amorphization in SiC. The maximum ion fluence corresponds to a dose of ~18 dpa at the damage peak according to SRIM simulation [4], where the threshold displacement energies for C and Si in SiC are assumed to be 20 and 35 eV, respectively. The epitaxial film used in this study was determined by pole-figure measurements (data not shown) to be single-crystal 3C-SiC with (100) orientation. Exfoliation in some areas of the 3C-SiC film (~2 μm thick) occurred during ion implantation. 3C-SiC single crystal is chosen in this study because it has the same crystal structure of potentially used SiC/SiC and should allow for a detailed study of damage states and Mg locations in the crystal structure. CVD-SiC is used to study any grain-boundary effects on Mg transport. X-ray diffraction (XRD) analysis (data not shown) shows that the CVD-SiC in this study is a single phase of 3C-SiC with an average grain size of ~33 nm. The 6H-SiC single-crystal wafer obtained from Cree has high crystalline quality and serves as a 3C-SiC surrogate for studying damage accumulation and recovery as well as Mg behavior.

Multiaxial ion channeling [5] based on 2.0 MeV He⁺ Rutherford backscattering spectrometry (RBS/C) was used to analyze the lattice disorder on the Si sublattice in the Mg⁺ ion implanted 3C-SiC. Time-of-flight secondary ion mass spectrometry (ToF-SIMS) was applied to profile Mg implants in both 6H-SiC and CVD-SiC. Isochronal (2 hours) annealing at temperatures up to 1473 K in an Ar environment was conducted and the same characterization methods were employed to study damage recovery and thermal behavior of Mg in the SiC samples. Further annealing at higher temperatures is currently in progress. These step-by-step procedures are needed to recover implantation-induced defects to the maximum extent possible while retaining a majority of Mg in SiC. The annealed samples will be characterized using a variety of methods, including PIXE (Particle-Induced X-ray Emission) or PIGE (Particle-Induced γ-ray Emission) under multiaxial channeling conditions, TEM (transmission electron microscopy) and APT (atom probe tomography) to identify Mg locations in the crystal structure, microstructural features, defect configurations, minor phases, precipitates, interfaces, etc.

Results and Discussion

RBS/C spectra along the <100>, <110> and <111> axes in 3C-SiC irradiated to 3.2×10¹⁶ Mg⁺/cm² at 773 K are shown in Figure 1. Also included are random and channeling spectra from an unirradiated area, which respectively define the upper and lower levels of the backscattering yields from the completely amorphized SiC material and essentially defect-free SiC crystal. According to Figure 1, the minimum yields for the Si sublattice in the unirradiated 3C-SiC are 2.8%, 3.6%, and 4.2%, as observed along the <110>, <100>, and <111> axes, respectively. The results indicate that the unirradiated 3C-SiC in the near-surface region of interest has high crystalline quality, as previously reported [6]. The depth scale for Si, shown on the top axis of Figure 1, is converted based on the SRIM-2003 database [4] of random stopping powers for both incoming and outgoing paths. The conversion also adopted a surface energy approximation [7]. The broad damage peak for the same damage states in the irradiated sample is apparent from observation along each axis. Because the RBS method used in this study does not resolve Mg and Si, the damage peak also includes Mg contributions. However, this contribution is negligibly small as compared to the percentage of Si displacements, about

2% vs. 50% or more (see Figure 2). The irradiated SiC is not fully amorphized because the sample temperature during irradiation was above the critical temperature for amorphization. At the elevated temperature (773 K), the interaction of point defects not only leads to simultaneous recovery to avoid full amorphization, but also formation of extended defects. The residual damage state in the as-implanted SiC is expected to contain a high concentration of defect clusters.

The relative disorder on the Si sublattice is obtained from the RBS/C spectra in Figure 1 using an iterative procedure [8,9] that is based on dechanneling from the actual disorder present. This procedure extracts the probability of close encounters between the energetic particles and the displaced atoms, which is directly proportional to the disorder concentration. The depth profiles of the relative disorder on the Si sublattice in the irradiated 3C-SiC observed along the $\langle 100 \rangle$, $\langle 110 \rangle$, and $\langle 111 \rangle$ axes are shown in Figure 2. The peak-fitted curves in the figure are to aid the eye. In the near-surface region, lattice disorder cannot be determined due to the influence of the surface peak from the surface-atom scattering. From Figure 2, the disorder levels on the Si sublattice observed along $\langle 110 \rangle$ and $\langle 111 \rangle$ are comparable in the depth region, but they are noticeably higher than along $\langle 100 \rangle$. The data suggest that in addition to randomly distributed Si atoms around the damage peak, there are interstitial defect configurations that are well aligned with the $\langle 100 \rangle$ axis, such as Si-Si $\langle 100 \rangle$ interstitial splits. Those aligned Si atoms are effectively shielded by the $\langle 100 \rangle$ atomic rows, leading to a reduction in the dechanneling yield. Orientation dependence of Si disorder in 3C-SiC [6] and 6H-SiC [5] irradiated at low and room temperatures was also previously observed. Our recent *ab initio* calculation [10] on Mg-incorporated 3C-SiC reveals that although Si-Mg $\langle 100 \rangle$ and C-Mg $\langle 100 \rangle$ configurations are unstable, the energetically favored interstitial site of Mg is at the tetrahedral center of C. The Mg and Si interstitials align with the $\langle 100 \rangle$ axis. In addition, Si-Si $\langle 100 \rangle$ interstitial splits or dumbbells are stable with a relatively high defect formation energy (9.48 eV).

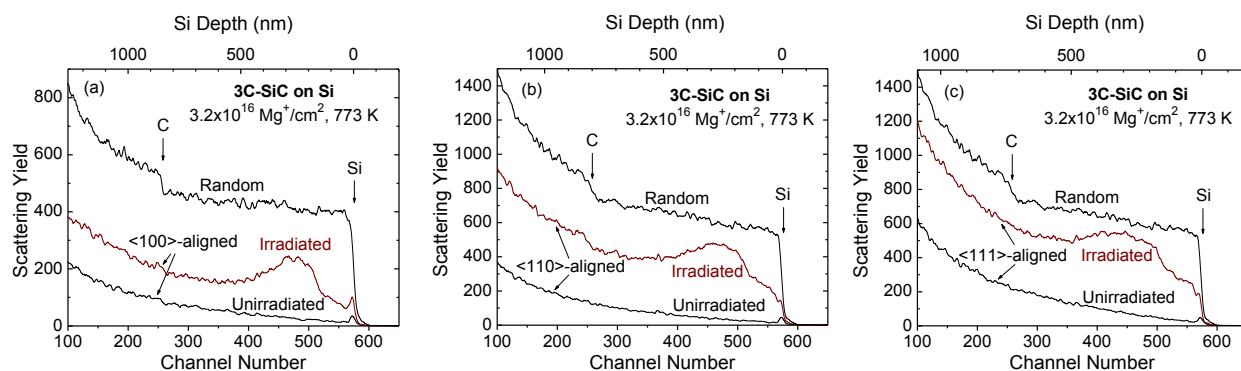


Figure 1. 2.0 MeV He⁺ RBS/C spectra along (a) $\langle 100 \rangle$, (b) $\langle 110 \rangle$ and (c) $\langle 111 \rangle$ axes for 3C-SiC irradiated with 200 keV Mg⁺ to 3.2×10^{16} ions/cm² at 773 K. Also included are random and channeling spectra from an unirradiated area.

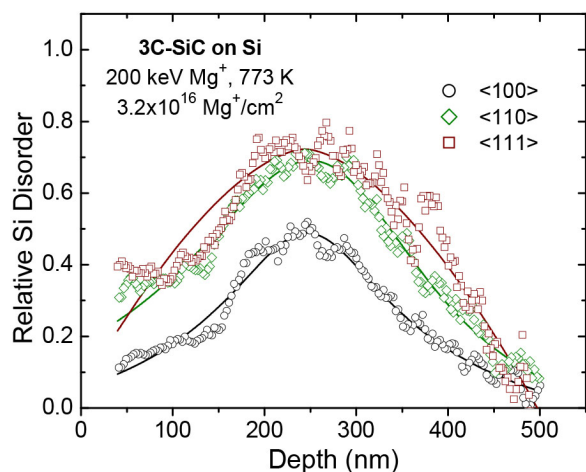


Figure 2. Depth profiles of disorder on the Si sublattice in 3C-SiC irradiated with 200 keV Mg^+ to 3.2×10^{16} ions/cm² at 773 K, as observed along the $\langle 100 \rangle$, $\langle 110 \rangle$ and $\langle 111 \rangle$ axes. Symbols are experimental data derived from Figure 1 and lines are drawn to aid the eye.

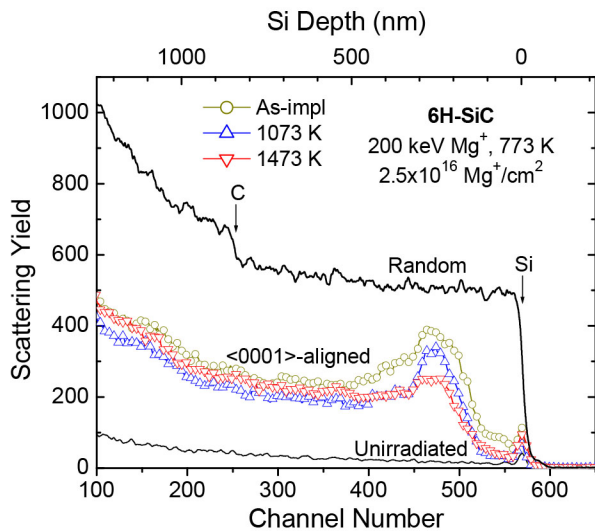


Figure 3. Isochronal (2 hours in Ar) annealing at 1073 and 1473 K for 6H-SiC irradiated with 200 keV Mg^+ to 2.5×10^{16} ions/cm² at 773 K.

to 1473 K does not lead to a significant change in the peak shape and position, as shown in Figure 4(a). The peak width is also identical within the experimental error (Table 1). The data suggest that the implanted Mg in 6H-SiC structure is essentially immobile up to the high temperature (1473 K). This behavior is similar to Ag in crystalline and amorphized SiC at

Figure 3 shows representative RBS/C spectra for 6H-SiC implanted to 2.5×10^{16} Mg^+ /cm² at 773 K and 2-hour isochronally annealed at 1073 and 1473 K. Channeling and random spectra from an unirradiated area are also included in the figure. It is apparent that as temperature increases, the intensity of the damage peak decreases, indicating that defect recovery occurs in the thermal annealing process. In general, the recovery behavior of 6H-SiC is similar to that of 3C-SiC [6] as the local tetrahedral structure in all SiC polymorphs is identical. Further annealing at higher temperatures, which is being conducted, may lead to more recovery of defects in the sample. It should be noted that at larger depths (>500 nm), the RBS/C spectrum for 1473 K is slightly higher than for 1073 K, primarily due to the additional damage produced by the 2.0 MeV He^+ ion beam that was used to refine the channeling direction and take the spectrum data in the same area.

The implanted Mg in 6H-SiC and CVD-SiC following implantation at 773 K and thermal annealing up to 1473 K was analyzed using TOF-SIMS. The peak-height normalized profiles of the implanted Mg are shown in Figure 4 as a function of depth with ~ 1.6 at.% and ~ 2.0 at.% Mg at the peak maxima in 6H-SiC and CVD-SiC, respectively. The corresponding peak positions and widths are given in Table 1. The depth calibration for 6H-SiC was performed by measuring the depth of the sputtered craters. The accuracy for the depth measurement is within a few percent. Since the surface of the CVD-SiC sample is not very smooth microscopically, its depth scale is determined based on the sputtering rate in units of nm/(nA-sec) for 6H-SiC under the same sputtering conditions (2 keV O^+). The Mg profile in the as-implanted 6H-SiC in Figure 4(a) is located at 250 nm with FWHM = 103 nm. Annealing at higher temperatures up

elevated temperatures [11]. A similar conclusion for Mg in CVD-SiC can be drawn, which indicates that the grain boundaries in the polycrystalline CVD-SiC do not provide a faster diffusion path for Mg to migrate at temperatures up to 1473 K. It is noticed that the Mg peak position in CVD-SiC [Figure 4(b)] is comparable to that in 6H-SiC [Figure 4(a)], but its peak width is systematically larger by 20-30%, which could be attributed to the surface roughness. Further investigations are needed to determine how the implanted Mg is structurally and chemically incorporated in SiC and whether any Mg-containing precipitates are formed.

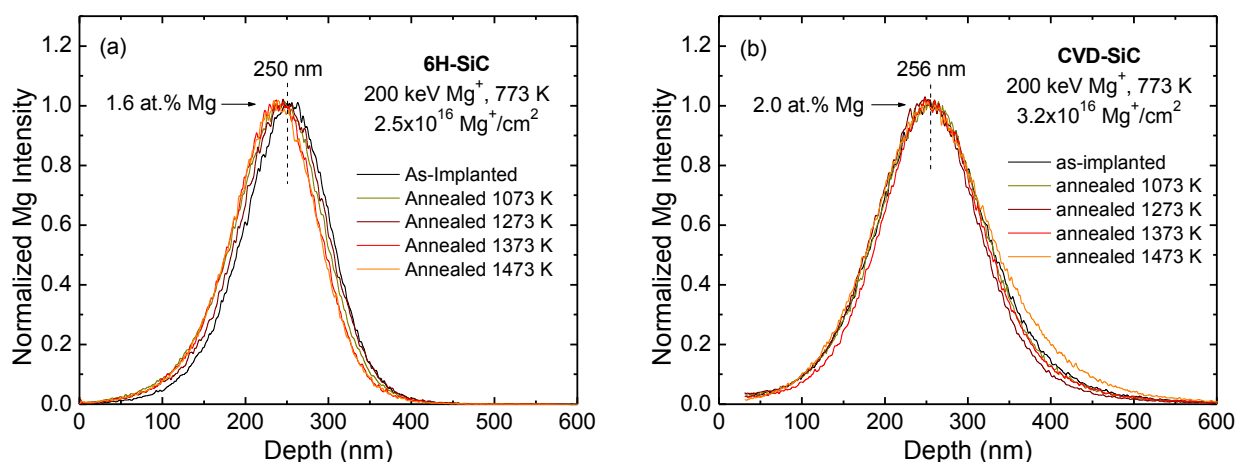


Figure 4. SIMS depth profiles of Mg in (a) 6H-SiC and (b) CVD-SiC implanted at 773 K and annealed at temperatures from 1073 to 1473 K for 2 hours at each temperature in an Ar environment.

Table 1. Peak position and width of implanted Mg in 6H-SiC and CVD-SiC.

Implantation/Annealing Temperature (K)	Peak Position (nm)		Peak FWHM (nm)	
	6H-SiC	CVD-SiC	6H-SiC	CVD-SiC
773	250	256	103	135
1073	240	256	108	131
1273	245	250	106	127
1373	236	257	104	126
1473	235	258	104	147

Note: 1 Implantation was performed using 200 keV Mg⁺ ions at 773 K. 2. Thermal annealing was conducted for 2 hours at each temperature in an Ar environment.

ACKNOWLEDGEMENTS

This research was supported by Office of Fusion Energy Sciences, U.S. Department of Energy (DOE) under Contract DE-AC05-76RL01830. A portion of the research was performed using EMSL, a national scientific user facility sponsored by the DOE's Office of Biological and Environmental Research and located at PNNL. Ion implantation was conducted at Ion Beam

Materials Laboratory through a partial support from Center for Integrated Nanotechnologies in Los Alamos National Laboratory.

REFERENCES

- [1] A. R. Raffray, R. Jones, G Aiello, M. Billone, L. Giancarli, H. Golfier, A. Hasegawa, Y. Katoh, A. Kohyama, S. Nishio, B. Riccardi, and M. S. Tillack, *Fusion Eng. Des.* **55** (2001) 55.
- [2] C. P. C. Wong, M. Abdou, M. Dagher, Y. Katoh, R. J. Kurtz, S. Malang, E. P. Marriott, B. J. Merrill, K. Messadek, N. B. Morley, M. E. Sawan, S. Sharafat, S. Smolentsev, D. K. Sze, S. Willms, A. Ying, and M. Z. Youssef, *Fusion Eng. Des.* **85** (2010) 1129.
- [3] M. E. Sawan, Y. Katoh, and L. L. Snead, *J. Nucl. Mater.*, in press (2013).
- [4] J. F. Ziegler, J. P. Biarsack, and U. Littmark, "The stopping and Range of Ions in Solids," (Pergamon Press, New York, 1985); available from: <http://www.SRIM.org/>.
- [5] W. Jiang and W. J. Weber, *Phys. Rev B* **64** (2001) 125206.
- [6] W. Jiang, W. J. Weber, J. Lian, and N. M. Kalkhoran, *J. Appl. Phys.* **105** (2009) 013529.
- [7] W. K. Chu, J. W. Mayer, and M. A. Nicolet, "Backscattering Spectrometry," (Academic Press, San Diego, CA, 1978) 63.
- [8] J. R. Tesmer and M. Nastasi, "Handbook of Modern Ion Beam Materials Analysis," (Materials Research Society, Pittsburgh, 1995) 267.
- [9] J. R. Bird and J. S. Williams, "Ion Beams for Materials Analysis," (Academic Press, San Diego, 1989) 286.
- [10] S. Y. Hu, W. Setyawan, R. van Ginhoven, W. Jiang, C. H. Henager, Jr. and R. J. Kurtz, *J. Nucl. Mater.*, submitted (2013).
- [11] W. Jiang, W. J. Weber, V. Shutthanandan, L. Li, and S. Thevuthasan, *Nucl. Instr. Math. Phys. Res. B* **219-220** (2004) 642.

3.3 EMTA THERMAL CONDUCTIVITY PREDICTIONS FOR UNIRRADIATED AND IRRADIATED SiC/SiC COMPOSITES — B. N. Nguyen, C. H. Henager, Jr., and R. J. Kurtz (Pacific Northwest National Laboratory¹)

OBJECTIVE

The objective of this work is to achieve a predictive engineering tool to assess and tailor the thermophysical properties of unirradiated and irradiated SiC/SiC composites. Towards this objective, first, PNNL's EMTA (Eshelby-Mori-Tanaka Approach) software was successfully applied to predict the thermal conductivity of unirradiated 2D SiC/SiC composites [1]. Next, we have extended the EMTA model reported in [1] to predict the thermal conductivity of these composites subjected to neutron irradiation at elevated temperatures and irradiation doses leading to defect saturation [2]. As EMTA thermal conductivity predictions compared well with the experimental results [1-2], in the future, a unified EMTA for SiC/SiC composites will be developed that addresses both thermal and mechanical properties.

SUMMARY

This study first applied an Eshelby-Mori-Tanaka approach implemented in PNNL's EMTA software to predict thermal conductivities of unirradiated 2D SiC/SiC composites. The EMTA homogenization method is structured in three steps to capture the effects of the constituent materials including the pyrolytic carbon (PyC) fiber coating on the thermal conductivities of as-formed composites [1]. EMTA also applies an iterative reverse engineering procedure to identify an unknown constituent material thermal conductivity. EMTA reverse engineering was shown to be efficient and accurate to compute the thermal conductivities of the SiC matrix and of the fiber coating as functions of temperature, and consequently, to achieve better agreement between the predicted and experimental thermal conductivities for the composites. Next, a new method that builds on EMTA to estimate the thermal conductivity of SiC/SiC composites subjected to neutron irradiation at elevated temperature up to a dose of 10 dpa was developed [2]. This method considers the irradiation-induced conductivity degradation behavior of chemical vapor deposited (CVD) SiC and defines an equivalent CVD-SiC material with an equivalent pore content to estimate the thermal conductivity of a SiC/isothermal-chemical-vapor-infiltration (ICVI)-SiC composite. It was shown that the proposed method effectively mimics the irradiation effect that induces the reduction of composite thermal conductivity [2].

PROGRESS AND STATUS

Introduction

Due to their excellent high-temperature fracture, creep, corrosion, and thermal shock resistance in addition to their high thermo-chemical stability, low-induced radioactivity, and low-radiation-induced afterheat, SiC/SiC composites are being developed as structural materials for first wall and breeder blanket applications in advanced fusion power plants. In such applications these materials will be subjected to a high heat flux that imposes extremely stringent requirements on the minimum thermal conductivity needed. Recently, an EMTA method [1, 3-6] was applied to compute the thermal conductivity of unirradiated SiC/SiC composites with excellent results. EMTA has been shown to provide accurate predictions of thermal conductivity for typical SiC/SiC systems based on knowledge of the constituent thermal conductivities and the

¹ PNNL is operated for the U.S. Department of Energy by Battelle Memorial Institute under Contract DE-AC06-76RLO 1830.

composite microstructural features (i.e., fiber coating, fiber volume fraction, fiber orientation, etc.). Although the transverse thermal conductivities of unirradiated SiC/SiC are in an acceptable range ($\sim 20 - 30$ W/m K), the corresponding values of irradiated SiC/SiC for a large irradiation temperature range may be too low and thus present an important issue for the use of SiC/SiC for fusion power reactors since it appears that much higher thermal conductivity values are required [7]. The following step of our work was therefore to develop a computational model to predict and tailor the thermal conductivities of SiC/SiC composites subjected to neutron irradiation. To this end, we extended the previous EMTA model reported in [1] to predict the thermal conductivity of these composites subjected to neutron irradiation at elevated temperatures and irradiation doses leading to defect saturation. The extended approach makes use of a reasonable surrogate material by replacing irradiated SiC with an equivalent porous SiC that exhibits the same thermal conductivity decrement as does the irradiated SiC using experimental data. Given that a complete microstructural evolution description of radiation damage in SiC is lacking, the approach taken here was a reasonable first step in creating a more comprehensive and fundamental thermal conductivity model for SiC.

Computational Procedure

The EMTA computational procedure to predict the thermal conductivity of unirradiated SiC/SiC composites was described in [1] and summarized in our previous report [8]. This section gives a summary of the extended EMTA method to estimate the thermal conductivity for irradiated SiC/SiC composites [2].

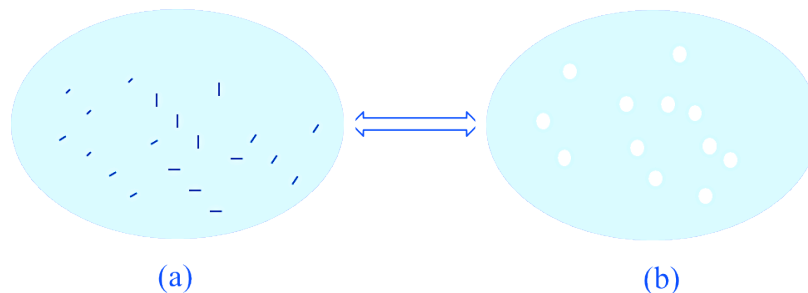


Figure 1. The equivalence between the CVD-SiC with a concentration of irradiation-induced defects (a) and the CVD-SiC containing a pore volume fraction (b) producing the same overall thermal conductivity.

Figure 1 schematically illustrates the equivalence between the irradiated CVD-SiC with a concentration of saturated irradiation-induced defects (Figure 1(a)) and the unirradiated CVD-SiC containing a fictitious spherical pore volume fraction (Figure 1(b)) that leads to the same thermal conductivity as the irradiated CVD-SiC material. The problem consists of determining the equivalent pore volume fraction for the irradiated equivalent material. To this end, the measured thermal conductivity data as a function of temperature and irradiation temperature for the unirradiated and irradiated CVD-SiC materials, respectively, are used in the EMTA reverse engineering to solve for this parameter. Next, the computation continues by assigning the same pore volume fraction representing the radiation damage to the ICVI-SiC matrix of an ICVI SiC/SiC composite subject to the same irradiation conditions as the CVD-SiC reference material. Such an assignment explicitly assumes that subject to the same irradiation conditions,

the CVD-SiC and ICVI SiC/SiC composite would contain the same concentration of defects at saturation; and that the defects that concentrate in the ICVI-SiC matrix and at the fiber/matrix interface are captured by the equivalent pore volume fraction affecting the thermal conductivity of the ICVI-SiC matrix. It also assumes that the fibers are unaffected by neutron irradiation, and this is a reasonable assumption for an irradiation dose up to about 10 dpa [9].

RESULTS

The first typical EMTA application examines the 2D SiC/SiC composite studied in [7]. DuPont processed this material from plain weave Hi-Nicalon fabric using an ICVI processed matrix. Two versions of this composite were examined in [7] including one with a 0.11-micron-thick and one with a 1.044-micron-thick PyC fiber coating layer, termed *thin* and *thick*, respectively. Constituent data for EMTA were taken in [7], however, the thermal conductivity of the PyC coating $k_c(T)$ as a function of temperature is not known, and therefore must be determined numerically by EMTA reverse engineering using measured conductivity data for the thick coating composite version. The as-identified $k_c(T)$ was then used by EMTA to refine the prediction of thermal conductivity for the thin fiber-coating version, and the transverse thermal conductivity results predicted for both thin and thick versions are presented in Figure 2 [1]. Accounting for the temperature-dependent $k_c(T)$ gives very good agreement between the predicted transverse thermal conductivity and experimental results for the whole temperature range studied, and for both versions of the DuPont composite.

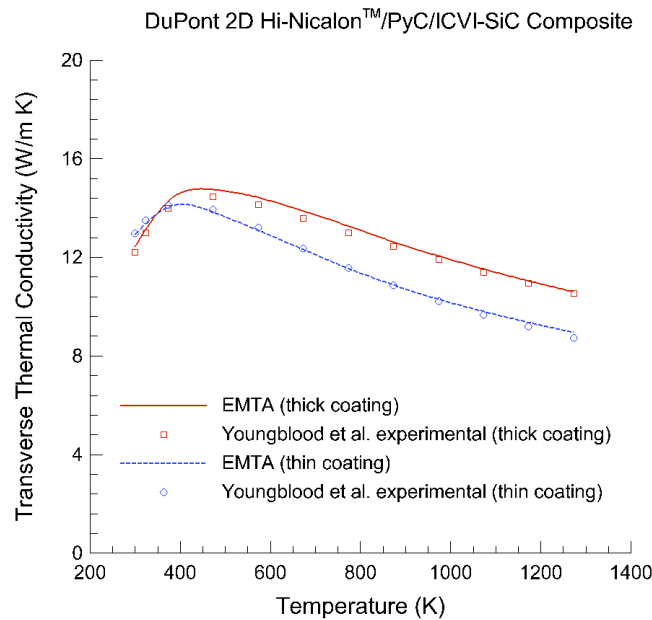


Figure 2. Transverse thermal conductivities predicted by EMTA for the DuPont 2D SiC/SiC composite with the thin and thick fiber coating layers accounting for the temperature-dependent fiber coating thermal conductivity, $k_c(T)$. The symbols denote Youngblood et al.'s experimental results from [7].

The second application illustrates the extended EMTA method to compute the thermal conductivity for the 2D Tyranno™-SA3/ICVI-SiC composite studied by Katoh et al. [10]. This composite was irradiated according to the following temperature/irradiation dose conditions: 713 K/0.8 dpa, 723 K/2 dpa, 773 K/3 dpa, 1123 K/3.5 dpa, and 1133 K/5.3 dpa [10]. These conditions are assumed to have led to saturation of irradiation-induced defects in the composite. Using the equivalent pore volume fraction calculated from the data determined for CVD-SiC at room temperature [10] and at each irradiation temperature [11], the ambient thermal conductivity of the ICVI-SiC matrix as a function of the irradiation temperature was computed by EMTA and reported in (Figure 3(a)), which shows the effect of irradiation-induced defects at the irradiation temperatures on the ambient thermal conductivity of the ICVI-SiC matrix. Finally, the thermal conductivity values predicted for the ICVI-SiC matrix were used by EMTA to calculate the ambient thermal conductivity of the irradiated Tyranno™-SA3 composite as a function of the irradiation temperature Figure 3(b).

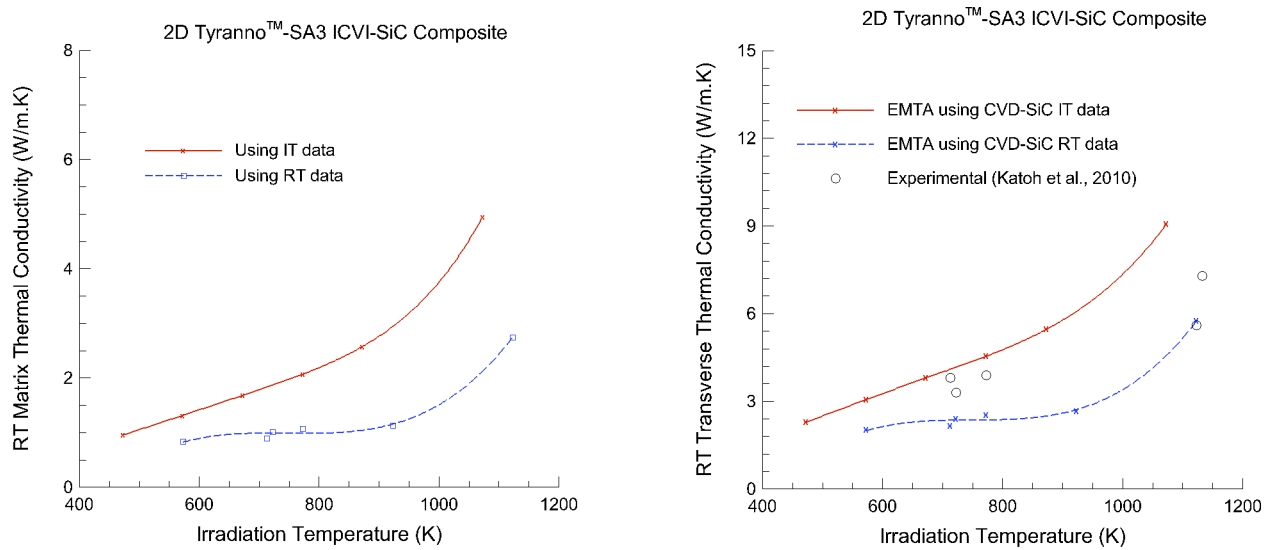


Figure 3. Ambient thermal conductivity vs. irradiation temperature predicted for the ICVI matrix (a) and 2D Tyranno™-SA3/ICVI-SiC composite (b) using the irradiation temperature (IT) and room temperature (RT) data for the CVD-SiC based on [10-11].

The prediction reported in Figure 3(b) globally agrees in trend and values with the measured data by Katoh et al., [10] presented on the same figure. The extended EMTA method appears to fairly estimate the thermal conductivity of irradiated SiC/SiC for a wide range of irradiation temperatures. As this method depends on the data taken from an irradiated CVD-SiC, its prediction also depends on data variance. The equivalent pore volume fraction approach can be completed by a more fundamental approach using appropriate defect densities and phonon scattering models. The difficulty here is that currently there is no detailed radiation damage evolution model for CVD-SiC that can be used to make these predictions [12]. The power of the EMTA approach, on the other hand, lies in the coupling of the matrix thermal conductivity analysis with the composite architecture and interfacial analysis appropriate to SiC/SiC composites.

Current and Future Work

As the transverse thermal conductivity of 2D woven SiC/SiC composites subjected to neutron irradiation is reduced to small values (several W/m K) although high thermal conductivity fibers (i.e., Tyranno™ SA or Hi-Nicalon™ Type-S fibers) are used, there have been interests in 3D SiC/SiC composites that were processed from 3D preforms directly woven with these fibers and an ICVI-SiC matrix. Currently, we are using EMTA to predict the thermal conductivity of unirradiated 3D woven SiC/SiC composites with different 3D fiber architectures characterized by the relative fiber content in the thickness direction. EMTA's predictions will be compared with experimental data found in literature to validate EMTA for 3D SiC/SiC composites. Next, our extended EMTA method to irradiated composites [2] will be used in a sensitivity analysis to determine the neutron irradiation effect on the thermal conductivity of various 3D woven SiC/SiC composites subjected to the same irradiation conditions leading to defect saturation. The 3D fiber configurations for these composites are varied by varying the relative fiber content in the thickness direction. Such an analysis will show the benefit of through-thickness reinforcement to improve the transverse thermal conductivity of SiC/SiC composites.

Toward achieving a predictive engineering tool to assess and tailor the thermophysical properties of SiC/SiC composites for fusion reactor applications, a unified EMTA for these composites will be developed that addresses both thermal and mechanical properties.

REFERENCES

- [1] B. N. Nguyen and C. H. Henager, Jr., *J. Nucl. Mater.* **440** (2013) 11.
- [2] B. N. Nguyen, C. H. Henager, Jr., and R. J. Kurtz, *J. Nucl. Mater.* (2013), *submitted*.
- [3] J. D. Eshelby, *Proc. Roy. Soc. London A* **241** (1957) 376.
- [4] T. Mori and K. Tanaka, *Acta Metall.* **21** (1973) 571.
- [5] Y. Benveniste, *Mech. Mater.* **6** (1987) 147.
- [6] H. Hatta and M. Taya, *Int. J. Eng. Sci.* **24** (1986) 1159.
- [7] G. E. Youngblood, D. J. Senior, R. H. Jones, and W. Kowbel, *J. Nucl. Mater.* **307-311(Pt. B)** (2002) 1120.
- [8] C. H. Henager Jr., B. N. Nguyen, and R. J. Kurtz, Fusion Materials Semiannual Progress Report for Period Ending December 31, 2012, DOE/ER-0313/53, U. S. Department of Energy, 118.
- [9] G. E. Youngblood, D. J. Senior, and R. H. Jones, *J. Nucl. Mater.* **329-333** (2004) 507.
- [10] Y. Katoh, L. L. Snead, T. Nozawa, S. Kondo, and J. Busby, *J. Nucl. Mater.* **403** (2010) 48.
- [11] Y. Katoh, T. Nozawa, L. L. Snead, T. Hinoki, and A. Kohyama, *Fusion Eng. Design* **81** (2006) 937.
- [12] J.-P. Crocombette and L. Proville, *Appl. Phys. Lett.* **98** (2011) 191905.

3.4 PROCESS DEVELOPMENT AND OPTIMIZATION FOR SILICON CARBIDE JOINING AND IRRADIATION STUDIES-II — Takaaki Koyanagi, Jim O. Kiggans, Ting Cheng, Yutai Katoh (Oak Ridge National Laboratory)

OBJECTIVE

The objective of this task is to develop and optimize joining processes for silicon carbide (SiC) ceramics and composites for fusion energy applications.

SUMMARY

The candidate joining methods for SiC ceramics and composites in the ongoing work to develop and optimize performance in neutron irradiation environments include chemically vapor-deposited (CVD) SiC bonded by the NITE (nano-infiltration and transient eutectic-phase) – like processes, diffusion bonding utilizing active titanium or molybdenum inserts, and transient eutectic-phase-assisted bonding with yttria-alumina-garnet (YAG) solder. In previous work the optimal processing conditions for Ti foil joining have been established. During the present reporting period, joint specimens with high shear strength were successfully produced through the active Mo metal insert methods, and then evaluated for as-fabricated properties.

PROGRESS AND STATUS

Development of Joining Process

In the preparation of joining specimens, flat plates of chemical vapor deposition (CVD) SiC (“CVD SILICON CARBIDE,” Dow Chemical, Marlborough, MA) were joined by hot pressing with inserts of molybdenum (Mo) foil (0.025 mm thick, 99.95%, 150 × 150 mm, Alfa Aesar), YAG slurry (35.1wt% Y₂O₃-64.9wt% Al₂O₃-7.5wt% SiO₂) or nano-infiltrated transient eutectic-phase (NITE) SiC slurry (6wt% Y₂O₃-Al₂O₃-SiO₂ sintering additives) [2, 3]. The CVD SiC samples were ultrasonically cleaned in acetone, and then dried in an oven. Mo diffusion bonding was carried out under a vacuum of 10⁻⁵ torr or Ar atmosphere with a uniaxial pressure of ~20 MPa for temperature verify from 1300 to 1700°C. Ti powder or 5%H₂ gas were used during hot pressing in order to remove gas impurities in vacuum and Ar atmosphere, respectively. For the specimens joined by NITE and YAG, a thin layer of NITE and YAG slurry was ultrasonic-sprayed through a Sonaer Sonozap (120 KHz) ultrasonic nozzle on the face of two SiC specimens, which were then placed face to face to form a sandwich. Joining was performed in a hot-press at 1875°C in a flowing Ar atmosphere with a uniaxial pressure of 20 MPa. The holding time and the uniaxial pressure applied on the samples were 1 h and 20 MPa in all the fabrication conditions in this work. The processing conditions and the results of the testing are summarized in Table 1.

Table 1. Processing conditions, nominal shear strength, joint microstructures, and fracture behavior of CVD-SiC joined by different filler materials

Insert materials	Specimen ID	Processing Conditions				Joint Strength		As-Joined Microstructure	Failure Location upon Shear Test
		Atmosphere	Temperature (°C)	Pressure (MPa)	Time (h)	Mean Shear Strength (MPa)	Standard Deviation (MPa)		
Mo foil	Mof-1300-1-Ti	Ti powder, Vacuum	1300	20	1	46.4	30.6	Porous at joint interface	Joint/base interface
Mo foil	Mof-1500-1	Vacuum	1500	20	1	55.2 [1]	15.4	No debonding [1]	Through the joint [1]
Mo foil	Mof-1500-1-Ti	Ti powder, Vacuum	1500	20	1	83.1	41.7	No debonding	Primarily at base
Mo foil	Mof-1500-1-H ₂	5%H ₂ /Ar	1500	20	1	105.5	4.6	No debonding	Base
Mo foil	Mof-1700-1	Vacuum	1700	20	1	68.2	18.7	No debonding	Primarily at base
Mo foil	Mof-1700-1-H ₂	5%H ₂ /Ar	1700	20	1	94	20.6	No debonding	Primarily at base
NITE slurry	NITEs-1860-1	Ar	1860	20	1	43.9 [1]	38.8	Fair/porous joint; debonding at porous joint [1]	Porous/base interface [1]
NITE coating	NITEc-1875-1	Ar	1875	20	1	67.3	33.2	Porous joint; No debonding	Joint/base interface
YAG coating	YAGc-1875-1	Ar	1875	20	1	60.3	41.6	Dense Al ₂ O ₃ and YAG joint	Interface 75 % Base 25 %

Note: Four replicates were used in tests in order to achieve statistical accuracy.

Mechanical testing and characterization

As mentioned in the earlier report [1], the joint strength was estimated by loading a double-notched test specimen of uniform width in compression, which is the standard test method ASTM C1292 for inter-laminar shear strength of continuous fiber-reinforced advanced ceramics at ambient temperatures. This test method, often referred to as double-notch shear (DNS) test, is in principle a variation of the offset single lap shear test as defined in ASTM D905 with an improved alignment capability due to the presence of the extended end sections. The bonded plates were machined into DNS specimens according to the dimension scheme shown in Fig. 1. The actual dimensions adopted were $L = 20.0$ mm, $W = 6.0$ mm, $t = 7.6$ mm, $h = 1.3$ mm, and $d = 3.0$ mm. Figures 2 (a) and (b) show a schematic and a photograph of the test setup and a specimen. Failure of the test specimen occurs by shear between two centrally located notches machined halfway through the thickness and spaced a fixed distance apart on opposing faces (ASTM C1292). The test fixture has been slightly modified, shown in Fig. 2, based on the initial one used previously [1].

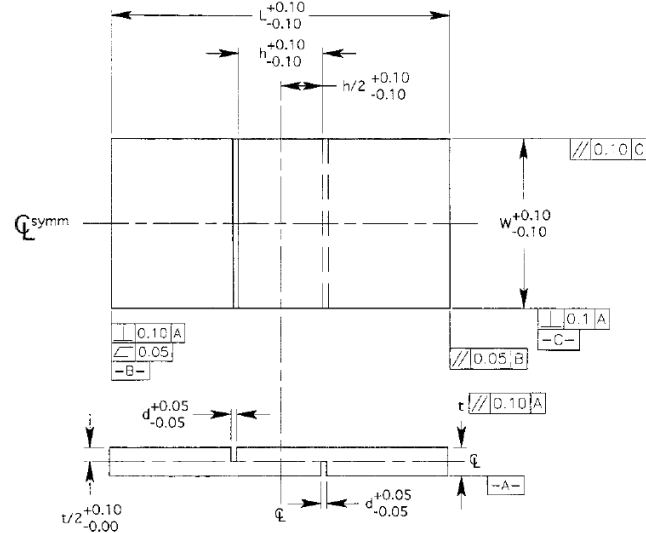


Fig. 1. Schematic of the double-notched compression test specimen.
 Note: All dimensions are in millimeters [1].

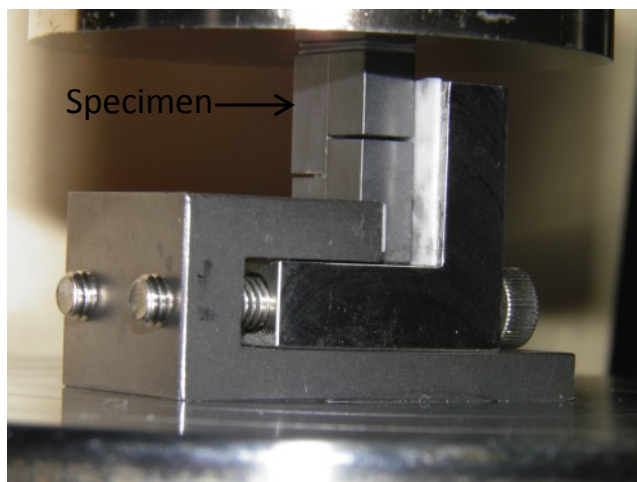


Fig. 2. An image of test fixture for the double-notched compression test specimen.

Polished cross-sections of the tested specimens were characterized using field-emission-gun scanning electron microscopy (FEG-SEM) in a Hitachi Model S4800, equipped with energy dispersive spectroscopy (EDS). The surface phases formed and their relative amounts were determined by X-ray diffraction (XRD) analysis (Model Scinatag Pad V, Thermo ARL). (NOTE: all SEM images shown below were taken on specimens after shear testing.)

Results of As-fabricated Characterization

Multiple joining conditions were attempted for each joining material in order to determine their optimal processing conditions, which will be used for fabricating the joint specimens for irradiation behavior study. Table 1 lists processing conditions, nominal shear strengths, joint microstructures, and fracture behaviors of CVD-SiC joined by Mo foil, NITE slurry, and YAG slurry.

Mo foil joints

Previously reported results indicated: (1) short-time (1 h) hot pressing is sufficient to obtain good quality joints; (2) Mo foil is favored over Mo powder slurry as the insert material because it experiences much less volume shrinkage during hot pressing; and (3) oxygen is suspected to have caused the low strength observed in certain joining condition because a detectable amount of oxygen was observed in the EDS spectrum of the joint [1]. Therefore, an oxygen getter (e.g. Ti) or a hydrogen gas flow were used in the present Mo foil joining processes, performed at temperatures of 1300, 1500, and 1700°C and pressures of 20 MPa for 1 h (Table 1). The nominal shear strength of joints produced under the above conditions was plotted in Fig. 3. Compared with other Mo joints, the one formed at 1500°C for 1 h in 5% H_2 /Ar gas exhibits the maximum strength of 106 MPa and minimum data deviation of 4.6 MPa. In contrast, the Mo joint formed in vacuum shows a significantly lower strength of 55 MPa. Using Ti powder to absorb O_2 also improves the Mo joint strength to a moderate extent. However, Ti powder tends to aggregate due to sintering at high temperatures, gradually losing its reactivity during hot pressing, which is also the reason of using H_2 instead of Ti at 1700°C. As expected, applying H_2 gas increases strength of the Mo joint formed at 1700 °C from 68 to 94 MPa on average, as shown in Table 1 and Fig. 3.

The low strength of the Mo joint produced at 1300°C for 1 h is likely caused by the large number of pores formed along the joint interface (Fig. 4 (a)), because the fracture location was mainly at joint/base interface as shown in Fig.4 (b). The Mo₅Si₃ phase was formed adjacent to the bond layer /SiC interface. While some Si was detected in the middle of the joint due to atom diffusion, extensive amount of Mo foil still remains intact in this joining condition.

The Mo joints formed at 1500 and 1700 °C with and without oxygen eliminator show similar microstructure to each other as shown in Fig 5 and 6. These joint layers mainly consisted of Mo₂C at the center of the joint layer and Mo₅Si₃ sandwiched by Mo₂C and SiC, based on XRD and SEM-EDS analysis. Note that vertical cracks to the joint interface were observed in all the specimens. A phase containing Mo and Si is lying between CVD SiC and Mo₅Si₃ (arrowed in Fig. 6), the thickness of which is similar among those joints. This thin layer was also observed and identified as Mo₅Si₃C by Martinelli using XRD and EDS [4]. A few μm pores located at the joint interface formed at 1500 °C using H₂, despite its highest nominal shear strength. This result indicates that this kind of small pore was not critical flaw for the Mo joint in this work. The similar microstructure with the different strength may be caused by the difference of the quality of the joint layer. The impurities oxygen is one of the causes affecting that. Differential amount and distribution of carbon and/or Mo₅Si₃C phase formed in Mo₅Si₃ phase [4] also potentially affect the mechanical properties of the Mo₅Si₃ phase.

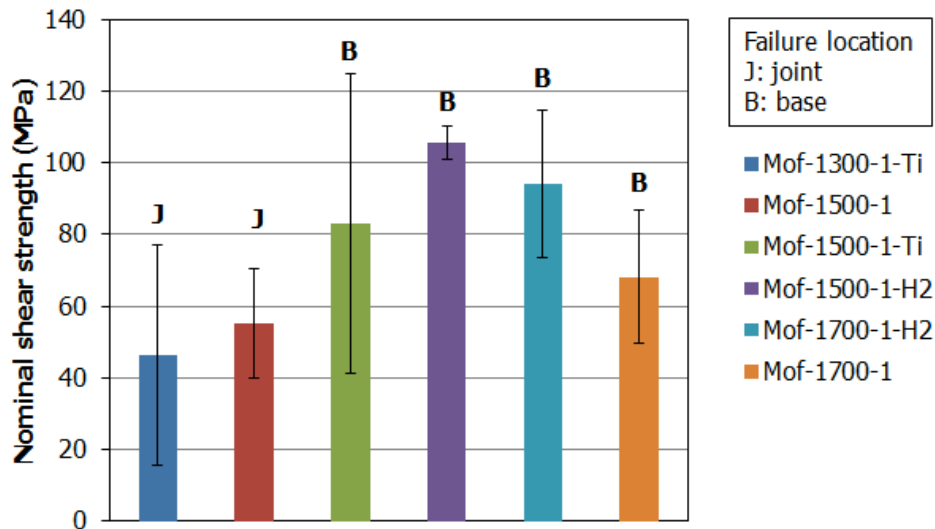


Fig. 3. Shear strength of joint formed between SiC plate and Mo foil filler hot pressed at various conditions.

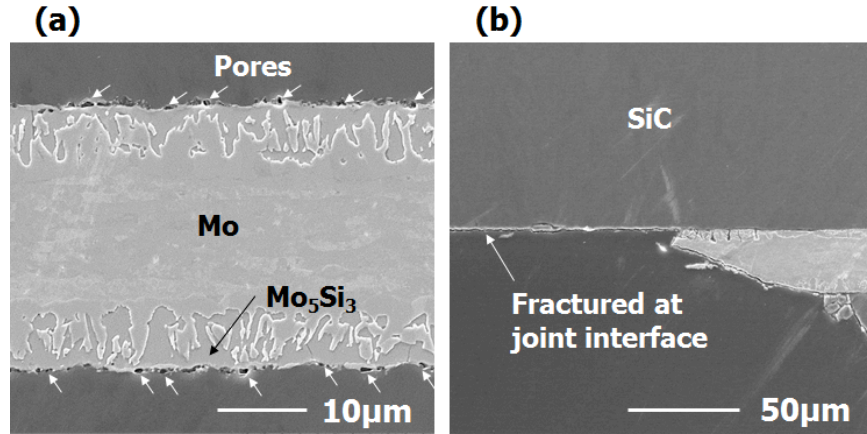


Fig. 4. Secondary electron images of Mo foil joint hot pressed at 1300°C for 1 h: (a) Joint interface before DNS test, (b) Joint interface after DNS test.

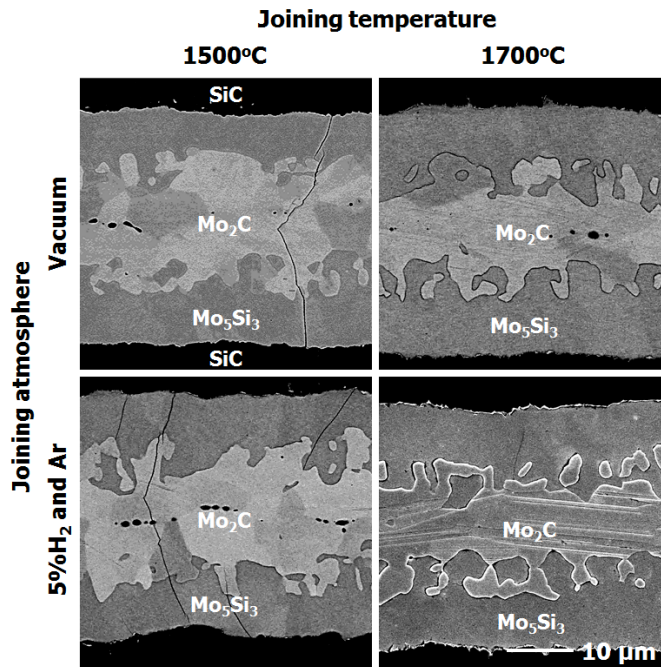


Fig. 5. Back scattering electron images of the Mo joints formed at 1500 and 1700 °C with and without oxygen eliminator.

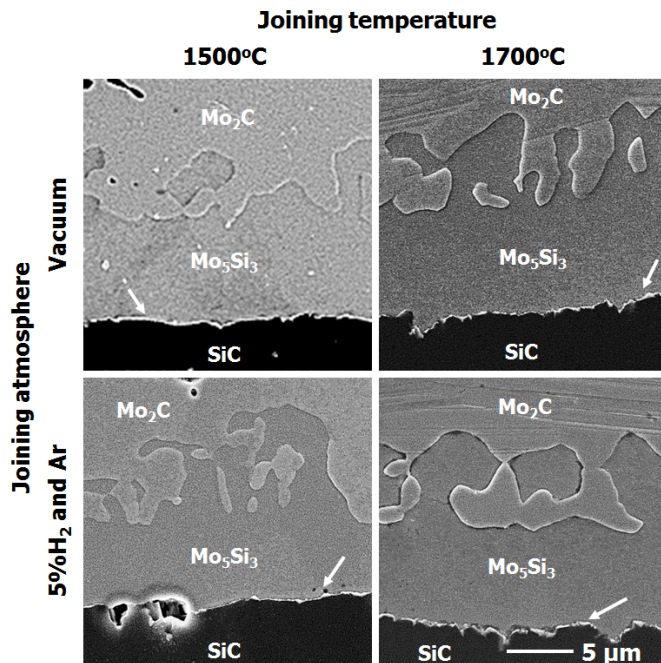


Fig. 6. Secondary electron images of the Mo joints formed at 1500 and 1700 °C with and without oxygen eliminator. The thin layers between SiC and Mo₅Si₃ are indicated by arrows.

Ultrasonically spray-coated (USC) NITE slurry joint

In an earlier effort, the NITE joints fabricated through a hand painting of the precursor slurry appeared to involve inhomogeneous microstructure with relatively dense regions and relatively porous regions spatially separated. While a good physical contact between the bonding layer and the SiC base was achieved at the dense regions, the porous joint apparently resulted in insufficient bonding. In order to achieve a uniform and dense NITE joint with good contact with the SiC base, multiple approaches have been implemented, including increasing viscosity of the NITE slurry or the sintering aids concentration, improving the uniformity of the NITE slurry layer by ultrasonic spray coating (USC), screen printing, or grinding CVD SiC to minimize bonding interface unevenness, etc. Figure 7 shows an example of microstructure of the USC NITE slurry joint hot pressed at 1875°C for 1 h at 20 MPa (slight temperature difference from the earlier work shall not lead to significant joint quality evolution). Unlike the NITE joint applied by manually painting onto the CVD SiC [1], the USC NITE joint appears to be much denser, whereas significant big pores observed within the joint (Fig. 7 (a) and (b)). However, fairly porous locations were also found, shown in Fig. 7 (c) and (d), implying limited sintering at some localized regions. The fracture occurred at the joint/base interface due to less base contact at the fairly porous joint. The average shear strength of the USC NITE joint, shown in Table 1, increased to 67.3 MPa from 43.9 MPa for the manual painted slurry joints. However, strength of the USC NITE joint is still significantly lower than those reported previously. The large standard deviation of 33.2 MPa indicates that a significant improvement in the spatially uniformity for this joint is achievable.

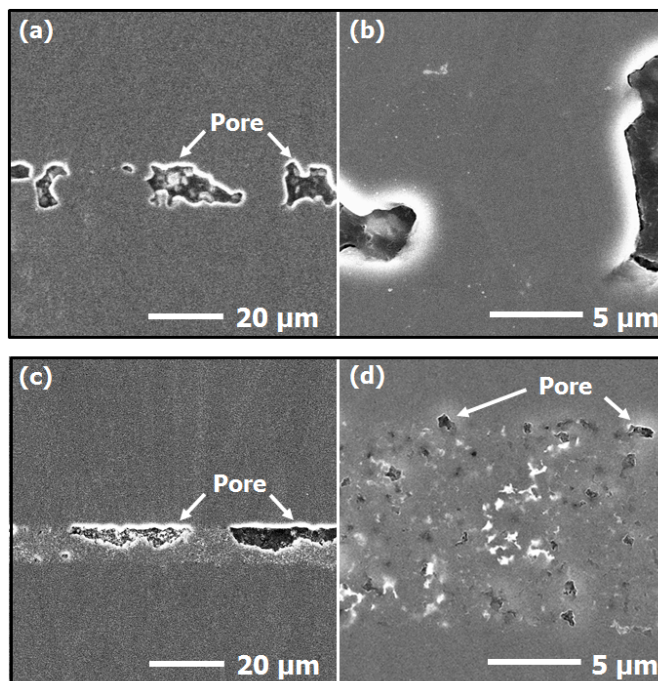


Fig. 7. SE images of ultrasonic-spray coated NITE slurry joint hot pressed at 1875°C for 1 h. (a), (b): well-sintered region with large pores. (c), (d): fairly porous region.

Ultrasonic-spray coated (USC) YAG slurry joint

The same USC technique was used to apply the YAG slurry onto the CVD SiC substrates. The four replicates exhibited considerable variance in shear strength: 32, 48, 39 and 122 MPa. A representative cross sectional image for the first three specimens of low strength was shown in Fig. 9 (a) and (b). While the joint appears to be dense without debonding from the SiC base, it is primarily composed of Al_2O_3 in lieu of the YAG phase, resulting to the unacceptably low strength. These specimens fractured at the Al_2O_3 joint/SiC base interface, summarized in Table 1, possibly due to few micron pores at the joint interface and/or weak bonding between SiC and Al_2O_3 , and/or the effect of the secondary phases along the joint interface as shown in Fig. 9 (b). In contrast, microstructure of the YAG joint with much higher strength (122 MPa) is also shown in Fig. 9 (c). While Al_2O_3 joint was still observed in this specimen, two pieces of CVD SiC substrates are joined together by Y-Al oxides in some region. This specimen, which fractured at the SiC base, shows the adequate strength, despite the non-uniform microstructure. This result shows that the YAG joining process has high potential for achieving robust SiC joint. Further improvement of this technique will focus on achieving homogeneously mixing the yttria, alumina and silica powder to obtain uniform microstructure.

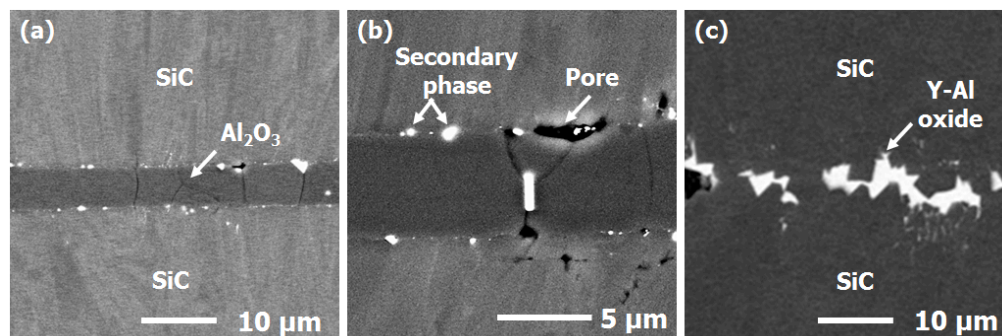


Fig. 8. Backscattered electron images of ultrasonic-spray coated YAG slurry joints hot pressed at 1875°C for 1 h. (a), (b) Specimen showing low strength (32 MPa), (c) Specimen showing high strength (122 MPa).

CONCLUSIONS

The candidate joint materials for the ongoing work to evaluate the neutron irradiation effects on CVD SiC includes bonds produced by diffusion bonding utilizing active titanium or molybdenum inserts, the NITE – like transient eutectic phase processes, YAG solder, and Ti-Si-C MAX phase through displacement reaction. In a previous report, the optimal processing conditions for Ti foil joining have been established. During the present reporting period, joint specimens with high shear strength were successfully produced through the active Mo metal insert methods, and then evaluated for as-fabricated properties.

A high level summary of the status of joining development at Oak Ridge National Laboratory is provided in Table 2. The Mo foil insert joint of CVD SiC hot pressed at 1500°C for 1 h in 5% H₂/Ar exhibited adequate strength.

Table 2. Status summary of SiC joint processing at ORNL

Method	Insert Material	Status
Metallic diffusion bonding	Ti foil	Optimum joining condition established
	Mo foil	Optimum joining condition established
Transient eutectic-phase joining	NITE* slurry	Optimum joining condition being studied
	YAG solder	Optimum joining condition being studied

*NITE: Nano-Infiltration and Transient Eutectic-phase process for sintering SiC

REFERENCES

- [1] T. Cheng, J. O. Kiggans, Y. K. Jr., L. L. Snead, "Process development and optimization for silicon carbide joining and irradiation studies-I," in: Fusion Materials Semiannual Report, Oak Ridge National Laboratory, 2012.
- [2] Y. Katoh, S. M. Dong, A. Kohyama, "Thermo-mechanical properties carbide composites fabricated and microstructure of silicon by nano-infiltrated transient eutectoid process," *Fusion Eng. Design*, **61-2** (2002) 723-731.
- [3] T. Hinoki, N. Eiza, S. Son, K. Shimoda, J. Lee, A. Kohyama, "Development of joining and coating technique for SiC and SiC/SiC Composites Utilizing NITE processing," *Ceram. Eng. Sci. Pro.* **26**(2) (2005) 399-405.

- [4] A. E. Martinelli and R. A. L. Drew, "Microstructural development during diffusion bonding of α -silicon carbide to molybdenum," *Mater. Sci. Eng.* **A191** (1995) 239-247.

3.5 LOW ACTIVATION JOINING OF SiC/SiC COMPOSITES FOR FUSION APPLICATIONS: TAPE CASTING TiC+Si POWDERS — C. H. Henager, Jr., R. J. Kurtz, N. L. Canfield, Y. Shin, W. G. Luscher, J. T. Mansurov, T. J. Roosendaal, and B. A. Borlaug (Pacific Northwest National Laboratory¹)

OBJECTIVE

This work discusses the latest developments in TiC + Si displacement reaction joining at PNNL based on new work to produce tape cast powders for improved SiC-joints.

SUMMARY

The use of SiC composites in fusion environments likely requires joining of plates using reactive joining or brazing. One promising reactive joining method uses solid-state displacement reactions between Si and TiC to produce $Ti_3SiC_2 + SiC$. We continue to explore the processing envelope for this joint for the TITAN collaboration in order to produce optimal joints to undergo irradiation studies in HFIR. One noted feature of the joints produced using tape-calendared powders of TiC+Si has been the large void regions that have been apparently unavoidable. Although the produced joints are very strong, these voids are undesirable. In addition, the tapes that were made for this joining was produced about 20 years ago and was aging. Therefore, we embarked on an effort to produce some new tape cast powders of TiC and Si that could replace our aging tape calendared materials.

PROGRESS AND STATUS

Introduction

SiC is an excellent material for fusion reactor environments, including first wall plasma facing and breeder materials. SiC is low-activation, temperature-resistant, and radiation damage tolerant compared to most materials. In the form of woven or braided composites with high-strength SiC fibers it has the requisite mechanical, thermal, and electrical properties to be a useful and versatile material system for fusion applications, especially since microstructural tailoring during processing allows control over the physical properties of interest [1-6]. However, it is difficult to mechanically join large sections of such materials using conventional fasteners so the analog of welding is being pursued for these ceramic materials [2, 4-15]. This paper reports on the current status of producing tape cast powders that can be used for strong SiC-joining materials while reducing the large voids observed from previous joints made with tape calendared powders.

Experimental Procedures

Tapes are cast using a prepared powder, binder, solvent, and plasticizer mixture that consists of a slurry preparation and tape casting operation using blended TiC+Si powders (all high purity and $d < 10 \mu m$), ethanol and methyl ethyl ketone (MEK) as solvents, polyvinyl butyral resin (PVB) as binder, n-butyl benzyl phthalate (BBP) as a plasticizer, and EMPHOS PS-21A organophosphate ester as a dispersant. The powder loading was optimized at about 55% by volume for the dry tape after casting and drying. The initial TiC+Si powders were blended in a 3:2 molar ratio. The final tape thickness was varied and joints were made from tapes that were

¹ Battelle Memorial Institute under Contract DE-AC06-76RLO 1830 operates PNNL for the U.S. Department of Energy.

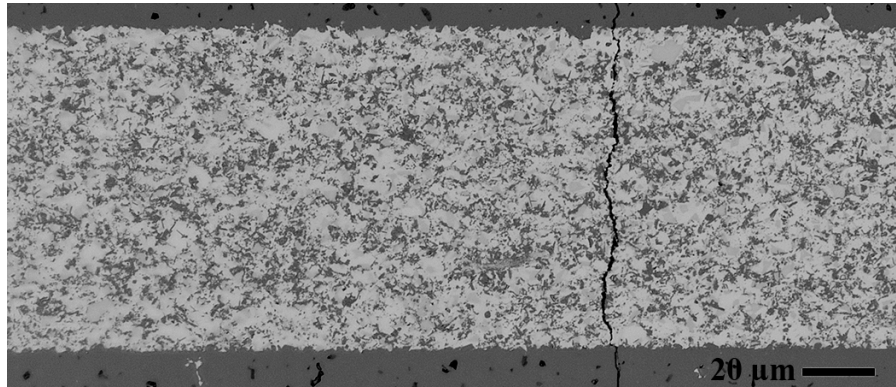
43 μm , 90 μm , and 195- μm thick as starting green tape thicknesses. The tapes were smooth and easy to handle. Small Hexoloy SiC bars were joined at 1698 K using 30 MPa of pressure for 2 h during joint formation. The joined bars were then sectioned for optical microscopy and quantitative metallographic analysis of SiC-phase content in the joint.

RESULTS

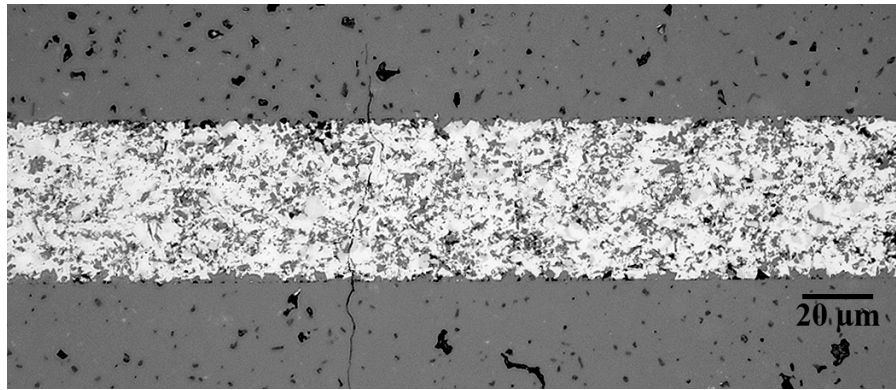
Figure 1 shows optical micrographs of the joints made from tapes with three starting tape thicknesses of 43, 90, and 195- μm . After processing, the joints have average thicknesses of 22, 47, and 92- μm , respectively. Table 1 shows the data for the three tapes with thickness and SiC-phase content for each tape. Characteristically, SiC preferentially nucleates at the Hexoloy/joint interface and complicates the quantitative metallography since the joint SiC-phase is attached to the Hexoloy SiC-phase and it is difficult to determine the actual interface location.

The optical images and quantitative data match quite well with the images and data from the previous joints made with the older tape calendared materials. In fact, these joints appear to be superior in that the large void regions in the older joints are not observed in the new tape cast joints. This may be due to trapped air in the older tape calendared joining materials since mass loss data from the new tapes matched the data from the older tapes but the new tapes are much thinner. Even though the tapes are thinner, though, the new joints are not thinner indicating that we reduced the total amount of binder and plasticizer (and perhaps trapped air) but did not reduce the total amount of powders per unit area in the new tapes.

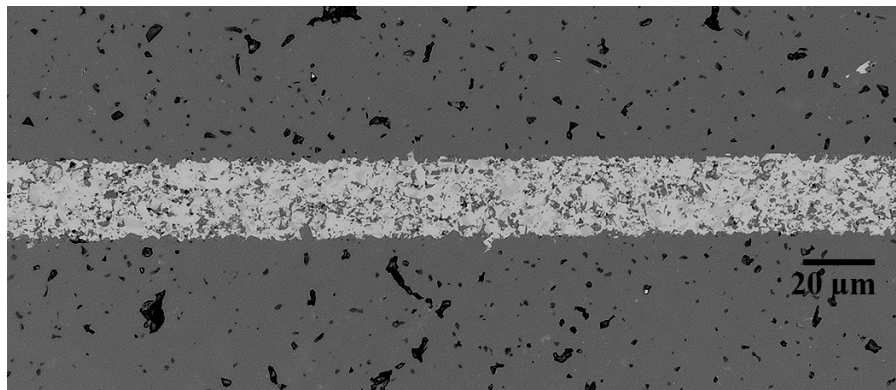
Future work will have to be performed to further characterize the tapes using SEM and TEM, while new CVD SiC miniature torsion joints will also be fabricated to start unirradiated strength testing and preparing for HFIR irradiation testing later.



(a)



(b)



(c)

Figure 1. Optical micrographs with 20- μm dimension markers for the three thicknesses of new tape cast joints described above. Shown in (a) is the 190- μm thick tape joint, (b) is the 90- μm thick tape joint, and in (c) is the 43- μm thick tape joint. Thinner joints are preferred and the joint from the 43- μm thick tape compares favorably with thin joints from the tape calendared materials used for all the PNNL joints previously.

Table 1: New Tape Cast Joint Dimensions and SiC-phase Content

Tape Designation	Tape Thickness (μm)	Joint Thickness (μm)	SiC-phase Area Fraction (%)
3TiC+2Si-5 (43)	43	22	31
3TiC+2Si-5 (90)	90	47	32
3TiC+2Si-5 (195)	195	92	33

ACKNOWLEDGEMENTS

This research was supported by Office of Fusion Energy Sciences, U.S. Department of Energy (DOE) under Contract DE-AC05-76RL01830.

REFERENCES

- [1] Y. Katoh, L. L. Snead, C. H. Henager Jr, A. Hasegawa, A. Kohyama, B. Riccardi, and H. Hegeman, *J. Nucl. Mater.* **367-370** (2007) 659.
- [2] C. H. J. Henager, Y. Shin, Y. Blum, L. A. Giannuzzi, B. W. Kempshall, and S. M. Schwarz, *J. Nucl. Mater.* **367-370** (2007) 1139.
- [3] P. Yvon and F. Carre, *J. Nucl. Mater.* **385** (2009) 217.
- [4] T. Nozawa, T. Hinoki, A. Hasegawa, A. Kohyama, Y. Katoh, L. L. Snead, C. H. Henager Jr, and J. B. J. Hegeman, *J. Nucl. Mater.* **386-388** (2009).
- [5] H.-C. Jung, Y.-H. Park, J.-S. Park, T. Hinoki, and A. Kohyama, *J. Nucl. Mater.* **386-388** (2009) 847.
- [6] S. Nogami, A. Hasegawa, L. L. Snead, R. H. Jones, and K. Abe. "Effect of He pre-implantation and neutron irradiation on mechanical properties of SiC/SiC composite," in *Proceedings of the 11th Conference on Fusion Research, December 7, 2003 - December 12, 2003*. 2004. Kyoto, Japan: Elsevier.
- [7] M. Ferraris, P. Appendino, V. Casalegno, F. Smeacetto, and M. Salvo, *Adv. Sci. Tech.* **33** (2003) 141.
- [8] B. Riccardi, C. A. Nannetti, T. Petrisor, and M. Sacchetti, *J. Nucl. Mater.* **307-311** (2002) 1237.
- [9] R. H. Jones, L. Giancarli, A. Hasegawa, Y. Katoh, A. Kohyama, B. Riccardi, L. L. Snead, and W. J. Weber, *J. Nucl. Mater.* **307-311** (2002) 1057.
- [10] R. L. Bruce, S. K. Guharay, F. Mako, W. Sherwood, and E. Lara-Curzio, IEEE/NPSS Symposium on Fusion Engineering (2002) 1078.
- [11] M. Zucchetti, M. Ferraris, and M. Salvo, *Fusion Eng. Des.* **58-59** (2001) 939.
- [12] A. R. Raffray, R. Jones, G. Aiello, M. Billone, L. Giancarli, H. Golfier, A. Hasegawa, Y. Katoh, A. Kohyama, S. Nishio, B. Riccardi, and M. S. Tillack, *Fusion Eng. Des.* **55** (2001) 55.
- [13] C. A. Lewinsohn, R. H. Jones, T. Nozawa, M. Kotani, Y. Katoh, A. Kohyama, and M. Singh, *Ceram. Eng. Sci. Proc.* **22** (2001) 621.
- [14] C. A. Lewinsohn, M. Singh, T. Shibayama, T. Hinoki, M. Ando, Y. Katoh, and A. Kohyama, "Joining of silicon carbide composites for fusion energy applications." 2000. Colorado Springs, CO, USA: Elsevier.
- [15] P. Colombo, B. Riccardi, A. Donato, and G. Scarinci, *J. Nucl. Mater.* **278** (2000) 127.

4.1 RECENT PROGRESS IN THE DEVELOPMENT OF DUCTILE-PHASE TOUGHENED TUNGSTEN FOR PLASMA-FACING MATERIALS — K. H. Cunningham, K. Fields, D. Gragg, F. W. Zok, (University of California, Santa Barbara); C. Henager, R. Kurtz, and T. Roosendaal (Pacific Northwest National Laboratory)

OBJECTIVE

The objective of this study is to develop the materials science of fiber-reinforced tungsten composites as candidates for plasma-facing components in future fusion reactors [1].

SUMMARY

Fracture testing was performed on notched and pre-cracked specimens of a W - 28w% Cu plate at room temperature and at 679K, as a follow-up to previous work. An order-of-magnitude toughness increase from that of monolithic tungsten was observed as a result of ductile Cu bridging. Pure W samples were consolidated from elemental powder using spark plasma sintering, achieving a maximum of 95.2% of the theoretical density. Commercially available tungsten wire was tested in tension, showing significant ductility and strength. The tungsten wire was plated with copper using electrodeposition, and continuing research will investigate methods of incorporating the Cu-coated W wire into a consolidated W matrix using spark plasma sintering. We expect the addition of ductile W wire to provide significant toughening compared to monolithic W, with the Cu coating preventing the wire from strongly bonding to the matrix.

PROGRESS AND STATUS

Background

Tungsten and W-alloys are the leading candidates for the plasma facing components because of their high melting point, strength at high temperatures, and low sputtering yield. However, W exhibits low fracture toughness and poor ductility. The ductile-brittle transition temperature (DBTT) typically ranges from several hundred up to $\approx 1000^{\circ}\text{C}$; and radiation hardening further elevates the DBTT [2-9]. Metallurgical approaches to toughen W-alloys, including Re alloying and severe plastic deformation (SPD), result in modest DBTT decreases [10-11]. However, they would be difficult or impossible to implement, due to high costs and implications to irradiation hardening (Re) or extremely complex processing demands (SPD) [12-14]. In contrast, W-composites toughened by a wide range of engineered reinforcement architectures are much more promising, especially those based on ductile phase toughening (DPT). There are many choices for ductile phases. Indeed, heavy metal commercial alloys, W-Cu-Ni-X, are composites. Copper is immiscible with W, does not form brittle intermetallic phases, and has low solubility in other elements like Fe. Thus copper coatings may be useful [17]. Limited studies of using fine-grained W-wire have had some success, and will be further studied. W-sheet or foils could also provide toughening given that a proper debonding behavior is established, perhaps by exploiting brittle intermetallic interface phases. Particle-toughened composites will also be considered. W-composite processing primarily will be by powder metallurgy that may involve use of commercial vendors, as well as coupon-size composite fabrication at UCSB using spark plasma sintering and at PNNL using hot- and cold-isostatic pressing and sintering. Powder processing will facilitate the exploration of a variety of ductile phases and more advanced approaches like functional grading.

Fracture Testing W-Cu Model System

Room Temperature Tests and Pre-Cracking (UCSB)

This research was conducted as part of this program and followed-up previous work prior to the proposal award. Specimens were prepared from a W-28 wt.% Cu plate obtained from Goodfellow. The nominal volume fraction of Cu particles is 50%. Initial fracture testing of the tungsten-copper composite began with manufacture of single edge-notched bend (SEB) specimens. The specimen geometry was 3.3 mm x 1.6 mm x 16 mm with the notch depth being 0.6 mm. The primary goal initially was to establish a method to produce pre-cracked fracture specimens for testing to measure ambient temperature fracture toughness, after which high-temperature testing could be conducted.

The first concept was to load the specimen monotonically in three-point flexure to introduce a sharp crack of known length. Since the crack growth in this material is bridged, the load-line deflection bears a complicated and *a priori* unknown relation to crack length, rendering conventional compliance correlation methods inadequate. Optical methods were used to measure and monitor crack growth during testing to establish not only final crack length, but also to plot the resistance curve behavior of the material. A number of optical systems were attempted, with the problem of specimen surface finish being a recurring issue. Conventional polishing techniques yielded a surface unsuitable for crack length measurements due to the preferential erosion of the copper, leaving raised “islands” of tungsten. Good results were obtained using 1500 grit sandpaper, which yields a uniformly flat surface, allowing good resolution of the crack formation and growth. In the end, an instrumented, long-distance microscope with oblique lighting and a digital camera provided good in situ imaging. It was found that monotonic loading of the SEB specimens did indeed produce stable crack growth, however, the level of plastic deformation and hinging of the specimen made this an unsuitable pre-cracking technique. However, the information obtained in these experiments yielded fracture data and proved the concept that the composite material exhibited rising R-curve behavior due to extensive crack bridging as illustrated in Figure 2.

Using the fracture data from the initial monotonic tests, a fatigue pre-cracking regimen was established to produce the desired fracture specimens. Successful pre-cracking was accomplished by high-frequency (80 Hz) fatigue in a displacement-controlled mode. Displacement-controlled fatigue was essential, since as the crack advanced, the load must decrease with the compliance, hence providing a stable, controlled crack growth mechanism. The crack length was monitored microscopically throughout pre-cracking. An example micrograph is shown in Figure 1.

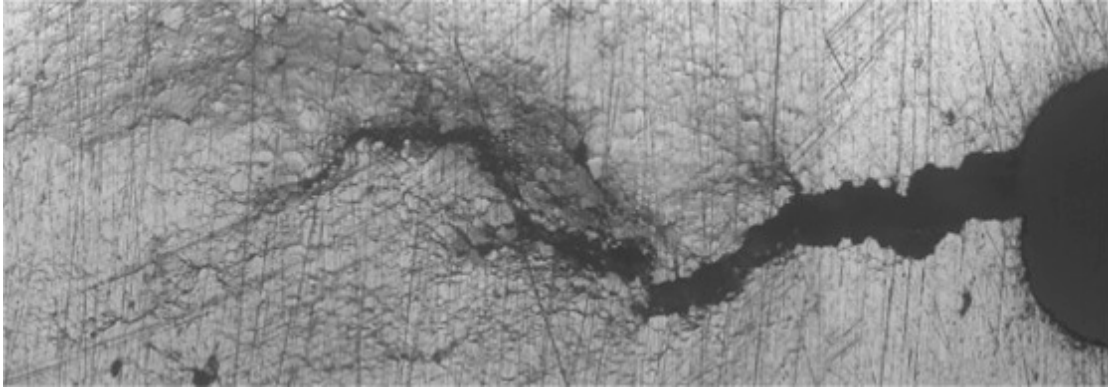


Figure 1. Stable crack growth from initially fatigued pre-crack.

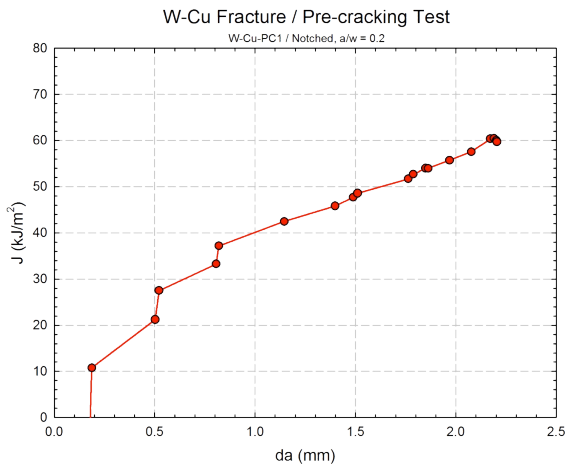


Figure 2. A representative example of R-curve behavior.

Once the ability to produce accurate, consistent fracture specimens was established, ambient temperature fracture tests were performed. There was some concern about a potentially large difference between surface crack length and through-thickness crack length. This led to extensive investigation into crack detection and monitoring techniques, including heat-tinting and use of dye penetrants. Heat-tinting proved of questionable use, since only the copper oxidized and changed color, leaving the apparent crack front essentially unchanged. However, this technique shows promise in revealing the individual tungsten zones to allow for microhardness testing of the tungsten itself. Dye penetrant proved a very useful method in understanding the formation and propagation of the crack front. By utilizing different colors at various stages of crack growth it is possible to visualize the length and shape of the crack, but also the level of bridging, since the copper ligaments are not marked while they are intact. A representative area of the fracture surface from specimen #7 is shown in the scanning electron microscope (SEM) image in Figure 3.

Table 1. Room temperature fracture data for notch and pre-cracked specimens.

Spec. #	a/w	K (MPa-√m)
1	0.20	$K_{el-pl} = 96$
2	0.20	$K_{max} = 24$
3	0.20	$K_{max} = 22$
4	0.20	$K_{max} = 24$
5	0.20	$K_{init} = 14$
6	0.32	$K_{el-pl} = 82$
7	0.49	$K_{el-pl} = 79$

Fracture testing of the pre-cracked SEB specimens at room temperature, along with the extensive microscopy, provided fracture toughness values (See Table 1), resistance curves (See Fig. 2 for example), and a wealth of understanding regarding the crack formation, propagation and bridging behavior in the tungsten-copper composite.

Elevated Temperature Tests (PNNL)

Preliminary experiments were performed to determine the effects of test temperature and displacement rate on ductile phase toughening of W-Cu composites. Single-edge notched bend (SENB) bars with nominal dimensions 3.38 mm width, 1.60 mm thickness, and 13.0 mm span were tested in three-point bending at room temperature (RT) and 679 K, which represent 21.6% and 50% of the homologous temperature for Cu, respectively. Based on an Ashby deformation mechanism map for pure Cu the higher test temperature places Cu in the power-law creep regime. Specimens were tested in both notched and fatigue pre-cracked conditions. Pre-cracking was performed at RT in displacement control at 80 Hz. Table 2 gives the measured dimensions, notch or crack depth, test temperature and displacement rate for each specimen.

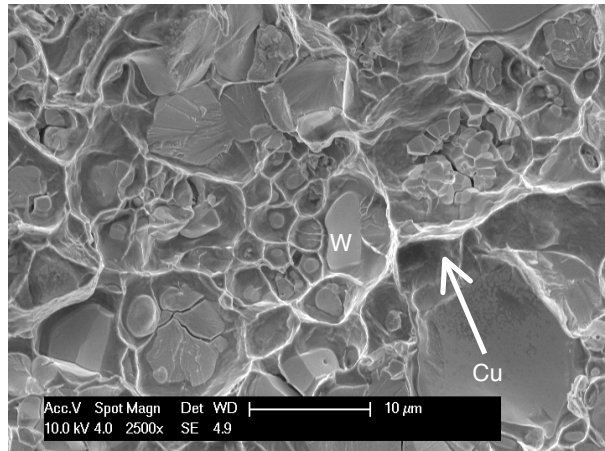


Figure 3. SEM image of fracture surface from SENB specimen #7. W grains show cleavage fracture and Cu shows failure by ductile bridging.

Table 2. Measured dimensions, notch or crack depth, test temperature, and displacement rate for room temperature (~293 K) and 679 K tests.

ID	Type*	Thick (mm)	W (mm)	S (mm)	a (mm)	T (°K)	Rate (mm/min)
11	N	1.610	3.345	13.335	0.643	293	0.2
12	N	1.595	3.317	13.335	0.671	293	0.02
13	N	1.593	3.325	13.335	0.648	293	0.002
14	N	1.604	3.299	13.335	0.597	679	0.2
15	N	1.585	3.329	13.335	0.632	679	0.02
16	N	1.597	3.182	13.335	0.52	679	0.002
8	PC	1.603	3.289	13.335	1.023	293	0.2
9	PC	1.595	3.317	13.335	1.219	293	0.02
10	PC	1.590	3.312	13.335	1.092	293	0.002
17	PC	1.617	3.318	13.335	1.296	679	0.2
18	PC	1.584	3.319	13.335	1.383	679	0.02
19	PC	1.584	3.269	13.335	1.309	679	0.002

*N = Notched, PC = pre-cracked

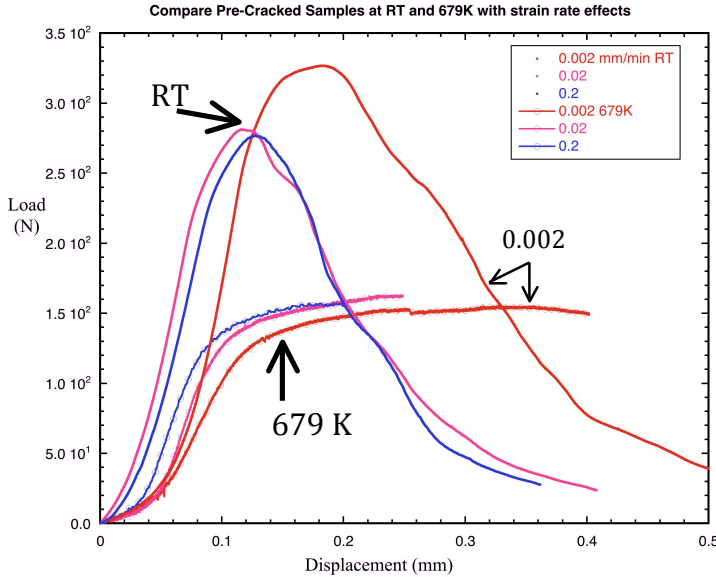


Figure 5. Displacement rate dependence of the load-displacement curves for pre-cracked tungsten-28 wt.% copper SENB specimens tested at RT and 679 K.

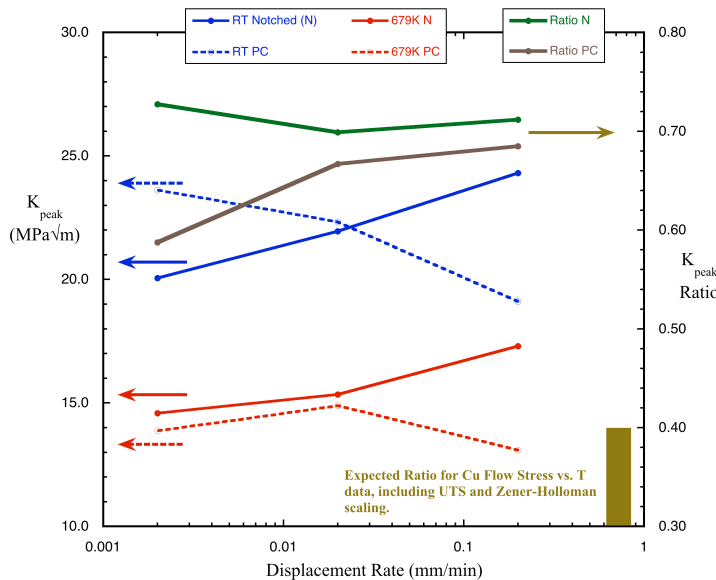


Figure 6. Peak load linear elastic stress intensity factor (left ordinate) versus displacement rate for notched (N) and pre-cracked (PC) W-28 wt.% Cu SENB specimens tested at RT and 679 K. The right ordinate plots the ratio K_{RT}/K_{679} at peak load.

increases markedly with decreasing displacement rate.

A working hypothesis for this composite material is that the fracture properties are determined by the ductile-phase mechanical properties, which in this case is the Cu phase. Since the Cu is in power-law creep at 679 K, it is not expected that the temperature dependence of the flow stress (yield or ultimate tensile strength) of Cu will be fully appropriate for scaling these results. Differences in specimen geometry, and notch or crack depths are accounted for, in an

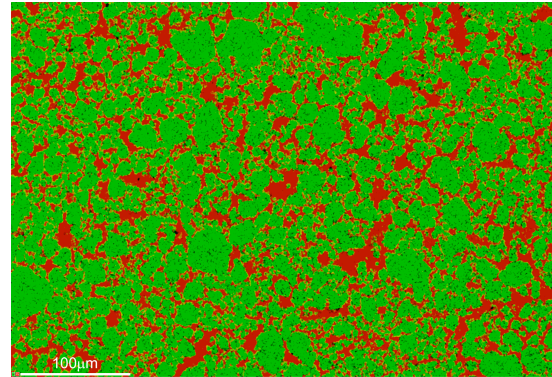


Figure 4. Elemental map of Goodfellow W-28 wt.% Cu plate showing W grains (green) surrounded by a network of Cu particles (red). The Cu particle areal fraction is between 31 and 38%.

The area fraction of Cu particles was determined from SEM image analysis indicating a range between 31 and 38% on the fracture surface. Figure 4 shows an elemental map derived from SEM energy dispersive X-ray spectroscopy. Tungsten is colored green and copper is red. The powder-processed material is best characterized as W grains surrounded by a Cu network.

Elevated temperature testing was performed in a tube furnace with a thermocouple directly contacting the specimen to control temperature to within ± 3 K. Displacement rates of 0.002, 0.02 and 0.2 mm/min were employed. Purified Ar gas flowed through the tube furnace to prevent specimen oxidation.

Load-displacement curves are plotted in Figure 5 for RT and 679 K tests as a function of displacement rate for the pre-cracked specimens. Note the results show a large effect from temperature, but a smaller effect from displacement rate. The total SENB specimen displacement

approximate manner, by computing the peak-load linear elastic stress intensity factor, K_{peak} , for each specimen. These results are shown in Figure 6 as a function of displacement rate for each case, notched (N) and pre-cracked (PC) and RT and 679 K. The right hand axis in Figure 6 shows the K_{peak} ratio of the RT and 679 K values, which is a parameter that should reflect the temperature dependence of the Cu. Note the similarity in K-values for the N and PC cases.

It is evident that the measured K-ratio of about 0.7 is significantly higher than the ratio of Cu flow stress, which is indicated by the shaded box and ranges from 0.4 to 0.3. Therefore, not surprisingly, additional factors affect this K-ratio. One factor that needs to be included in a more rigorous analysis of these data is creep of Cu bridges restraining crack growth in W. The optical and SEM images shown in Figures 7 and 8 illustrate another factor, namely the width of the process or deformed and cracked zone ahead of the crack tip observed at 679 K. The process zone, a diffuse microcracked region, is more than twice as large at 679 K compared to RT. This will offset the expected K-ratio decrement due to decreasing Cu ultimate tensile strength. Creep of Cu bridges allows the Cu to absorb additional strain and the process zone growth distributes the stress and deformation over a larger volume. Both elevated temperature mechanisms act to offset the K-ratio decrement due to the higher test temperature.

Figure 7. Optical micrographs of tested RT (left image) and 679 K (right image) SENB bars showing an increase in the crack process zone (severely microcracked region) that develops during slow displacement rate testing.

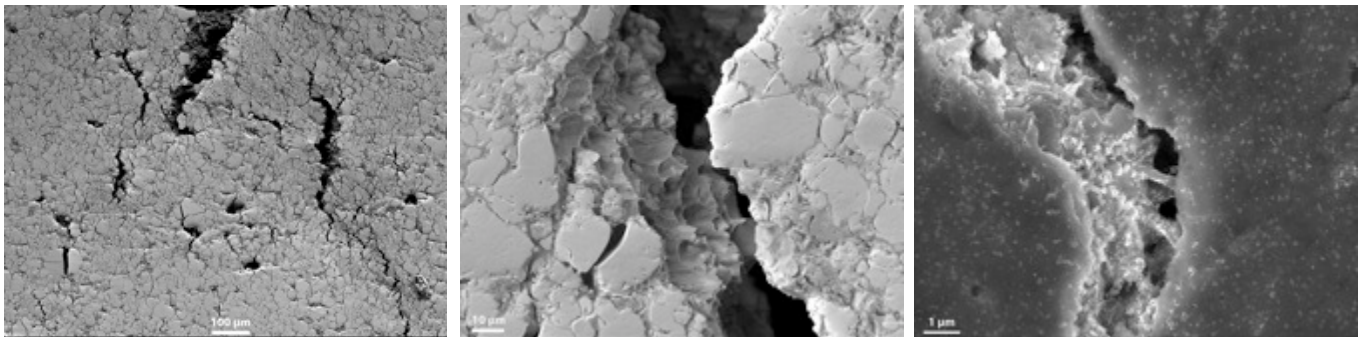
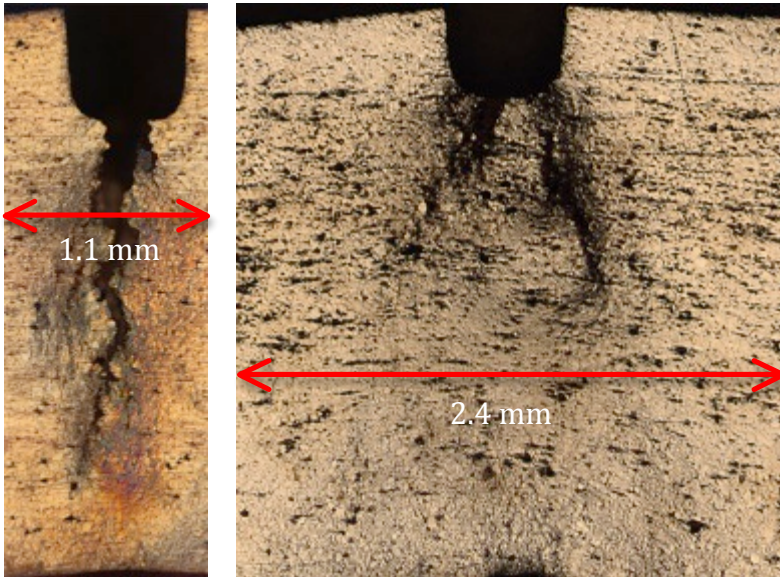


Figure 8. SEM image (left) of the crack process zone at 679 K. Cu bridges spanning the crack opening at RT (center) and 679 K (right). Plasticity in the Cu bridges is evident.

Processing W and W-Composites

Sintering of Pure Tungsten Disks

Two elemental tungsten powders, one of 4-6 μ m particle size and 99.95% purity (Stanford Materials Corp.) and the other of unknown particle size and purity (Aegis Tech.; assumed <4 μ m after cryogenic milling from 4-6 μ m powder) were used separately for this study. The powder was loaded under an argon environment into a 20mm inner-diameter graphite die with a layer of graphite foil between the powder and die (0.15" foil around circumference; 0.3" foil on faces). Two samples were prepared using 0.005-in. niobium foil, to reduce formation of tungsten carbide and potentially simplify processing [15]. For the Nb foil disks, one layer of foil was used for each face of the disk, and two layers were used around the circumference of the die. The powder was then consolidated by spark plasma sintering (Systeme GmbH, FCT Group) at various processing conditions summarized in Table 3.

After sintering, the tungsten disks were polished to remove any residual graphite. For the disks sintered at higher temperatures and longer dwell times, this exposed a cracked tungsten carbide outer layer. The disks were sectioned using a low-speed diamond saw (Buehler). One section per disk, cut along a chord of the circular face roughly 3mm from the edge, was mounted in thermosetting plastic. The visible cross-section of the disk was polished down to 0.5 μ m. An additional section no more than 5x5mm on the face was cut from the center of each disk to be used for density measurements.

The hardness of the consolidated tungsten was measured using a Leco M-400A microhardness tester. A series of 8-10 indents was made along the cross-section of each disk with a load of 500g. The density of each disk was measured using a helium pycnometer (MicroMeritics AccuPyc 1330) for the small center-cut sections. The grain size was roughly determined optically after etching in a 30% hydrogen peroxide solution for 10 minutes in an agitated bath [16].

On the disk sintered from the Aegis cryomilled powder, a second phase was visible in the tungsten matrix under optical microscopy. A section of the disk was cut and mounted in conductive thermosetting plastic for energy-dispersive x-ray spectroscopy (EDXS) analysis (FEI Sirion XL40 / Oxford Inca). The as-received Aegis powder was also mounted and analyzed with EDXS.

Table 3. Summary of SPS processing conditions and tungsten disk properties. Percent theoretical density (%TD) references 19.3g/cm³ for pure single-crystal tungsten. All heating rates are 100°C/min approaching the maximum temperature. The relative density of the Aegis disk is not listed because of the presence of a second phase. (Nb) refers to the substitution of niobium foil as opposed to the standard graphite foil.

Powder	T(°C)	Dwell / cool t (minutes)	Density (g/cm ³)	% TD	Vickers hardness (dph)	Grain d (µm)
Stanford	1700	1/3	15.42	79.8	165.1 (6.1)*	6.09 (1.52)*
Stanford	1700	60/3	17.78	92.0	332.4 (9.6)	8.63 (3.02)
Stanford	1900	21/3	17.64	91.3	322.0 (9.2)	9.03 (2.78)
Stanford	1900	60/3	17.79	92.1	338.6 (7.3)	12.57 (5.80)
Aegis	1900	60/3	15.95	NA	495.8 (30.5)	29.78 (9.29)
Stanford (Nb)	1900	60/3	18.14	93.9	343.6 (6.8)	28.57 (6.48)
Stanford (Nb)	1900	5/3	18.39	95.2	224.6 (3.3)	

*(Standard deviation)

The disk consolidated at 1700°C was relatively soft, which prompted extending the sintering time, after which the disks attained a higher density and hardness. The third disk was planned for a 60-minute dwell time, but the sintering machine’s alarms were set off because the maximum piston travel setting was not high enough. The Aegis powder disk contained a tantalum oxide phase, as shown in Figure 9.

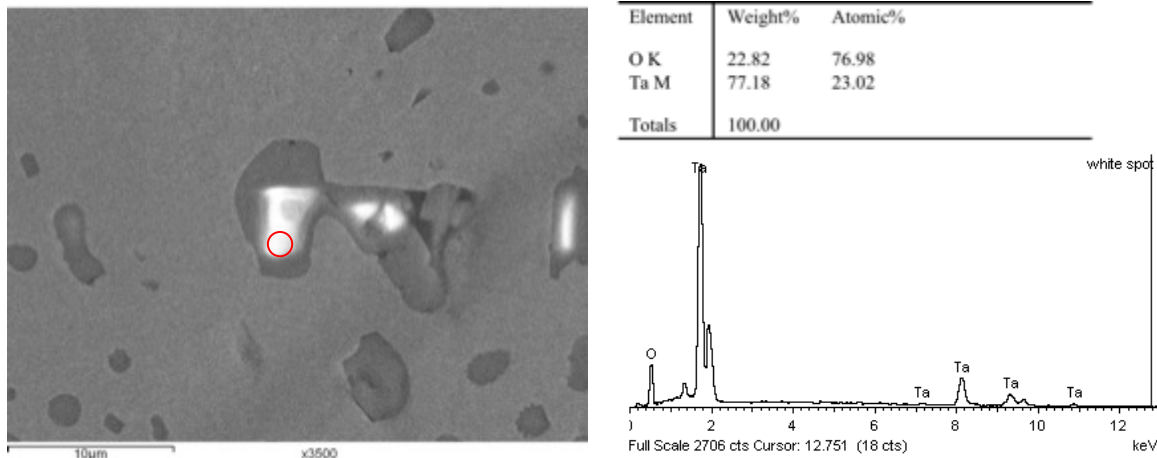


Figure 9. Oxidized tantalum phase in cross-section of consolidated Aegis powder disk. Data collected with Oxford Inca EDXS system. The elemental composition and spectrum shown for the spot highlighted in red on the SEM image. The scale bar is 10µm.

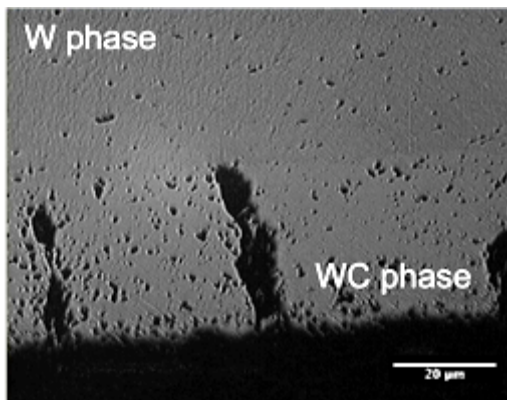


Figure 10. Optical micrograph of W-WC interface from disk 4 (Stanford, 1900°C, 60 min). Crack does not penetrate W matrix. Scale bar: 20μm.

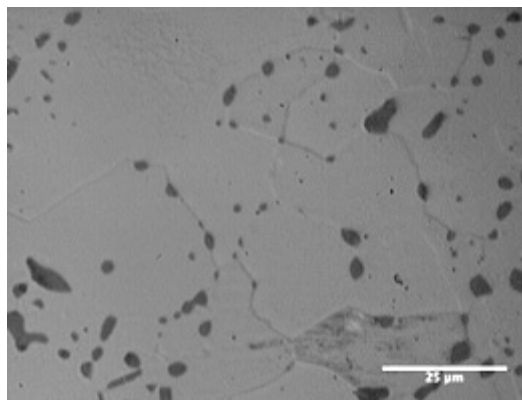


Figure 11. Optical micrograph of Aegis disk W matrix (lighter) with Ta second phase (darker) showing grain structure after 2.5-hr vibratory polish. Scale bar: 25μm.

All disks sintered with graphite foil except the first showed some amount of tungsten carbide on the outer surface. For the second disk (1700°C, 60 min), the WC was only present on a small area of the face of the disk; for the remaining three (1900°C), the entire disk was encased with a cracked WC layer. Figure 10 shows an optical micrograph with an example of cracks occurring only in WC.

After a 2.5-hour vibratory polish of the Ta-contaminated disk, an apparent grain structure was visible under optical microscopy as shown in Figure 11. None of the other disks showed a visible grain structure after such a polish. The disks consolidated using Nb foil appeared under optical microscopy not to contain any WC. This will be confirmed using EDXS. An example cross-section of one disk at the face edge is shown in Figure 12.

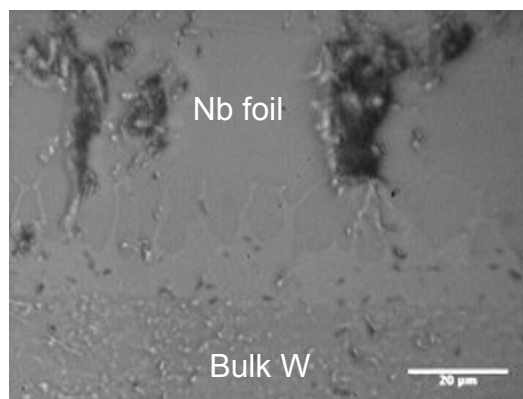


Figure 12. Optical micrograph of Nb foil at face of W disk showing diffusion of W into Nb. Scale bar: 20μm.

Tungsten Wire Characterization

The concept of manufacturing a composite using copper-coated tungsten wire required the tensile testing of several candidate wires to quantify yield and ultimate tensile strength values to use in modeling. Tensile testing of 250- and 500-micron tungsten wire was performed using techniques and equipment developed for ceramic fiber testing. Several tests of each size wire were conducted to establish statistically valid results for tensile yield and ultimate tensile strength. Figure 13 shows typical engineering tensile stress-displacement curves for each of the three wire diameters, and Table 4 summarizes the wire tensile properties. If necessary, laser extensometry could be utilized to measure Young's modulus. The 15-micron diameter wire taxed the capabilities of the test equipment. However, preparing the test specimens by mounting them in rigid holders and then severing the holders once installed in the tensile machine proved successful with a 50% attrition rate. The tested specimens were examined microscopically to

verify cup-and-cone fracture to confirm uniform stress distribution in the wire (See Fig. 13). Unfortunately, measuring strain directly on the 15 μm wire is extremely problematic, therefore, modulus measurements are not planned.

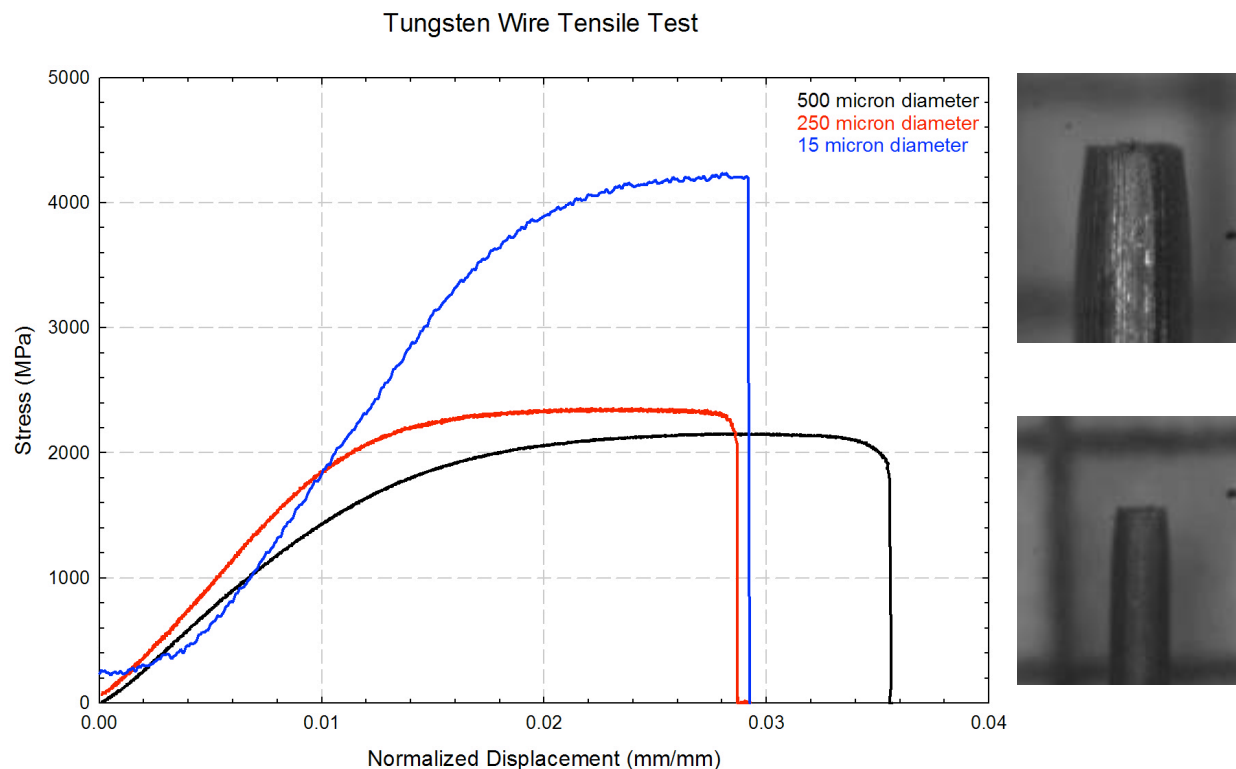


Figure 13. Typical test curves from three sizes of tungsten wire and optical micrographs of W wires after tensile test, showing necking before failure. Upper right: 500 μm wire. Lower right: 250 μm wire.

Plating Tungsten Wire with Copper

The initial process used to plate copper onto the tungsten wire is as follows: rinse and wipe wire with mineral oil to remove large particles; soak in ultrasonic bath in alkaline solution at 50°C for 15 minutes (solution: 0.1g sodium carbonate, 0.3g sodium borate in 19.6g water); plate in ultrasonic bath at 50°C under direct current, 162 A per m² of immersed wire (aqueous solution of 0.625M sulfuric acid, 0.4M copper sulfate, and 2 g/L urea) [17-19]. Plating for 1 minute did not result in full coverage of the wire with copper, as shown in Figure 14. Plating for 5 minutes resulted in a coating of maximum thickness 25µm, shown in Figure 15. Additional measurements are needed to quantify the variation in coating thickness, but the required thickness for achieving an appropriate interface once consolidated into a tungsten matrix is not known, but will be determined.

Table 4. Yield and ultimate tensile strengths of three sizes of tungsten wire.

Wire diameter (µm)	Avg. Yield Stress (GPa)	Average Ultimate Tensile Strength (GPa)
15	3.58	4.24
250	1.78	2.30
500	1.34	2.16

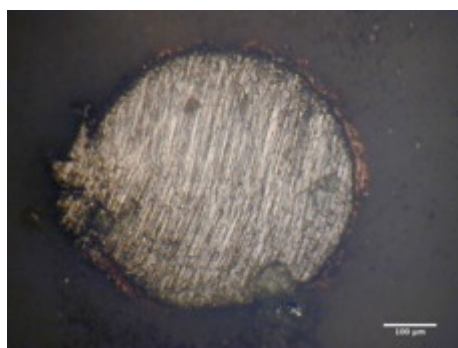
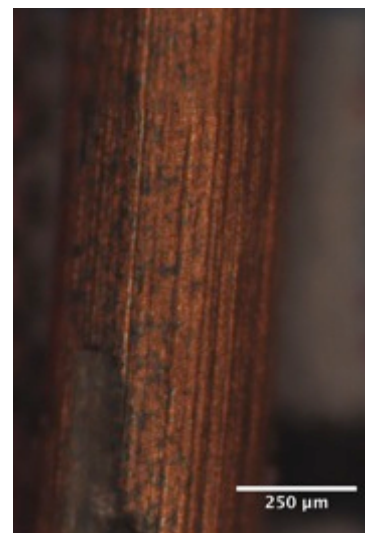


Figure 14. (Right) Optical micrograph of Cu-coated W wire after 1 minute of plating, showing gaps in coverage. Scale bar: 250µm.

Figure 15. (Left) Optical micrograph of cross-section of Cu-coated W wire after 5 minutes of plating, with a maximum coating thickness of 25µm. Scale bar: 100µm.



In an effort to increase the output of plated wire, a small-scale plating apparatus was constructed using a rectangular bath (w=3, l=5, h=10cm) with three bus wires running above the plating solution. Two of the bus wires were connected and run along the sides of the bath. Lengths of copper wire were hung from these buses to form the cathode. Tungsten wire was hung from the center bus to form the anode (See Fig. 16 for diagram). Eight lengths of tungsten wire were wiped with mineral oil and then hung from the anode bus so that approximately 8cm of each length was immersed in the plating solution. After plating at room temperature without agitation for 35 minutes, micrometer measurements indicated an average coating thickness of 30µm. Additional trials are required to establish a relationship between the wire preparation, plating process, and coating character.

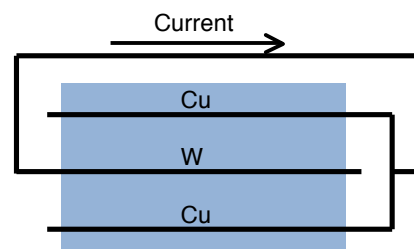


Figure 16. Top-down schematic of plating apparatus. The bare wire above the plating bath allows multiple lengths of current-carrying wire to be suspended within the bath. The W and Cu labels indicate the wire that hangs from each bus.

FUTURE RESEARCH

The next step in development of ductile-phase toughened tungsten composites is to combine the copper-coated wire study with the sintering study, and create composite materials to characterize. The largest challenge for this study is working with copper in the liquid phase, as the effective sintering temperatures for tungsten are well above copper's melting point. In order to create a composite, the copper must form a barrier between the tungsten wire and the tungsten matrix.

A poster on this research was presented in May 2013 at the 14th International Conference on Plasma-Facing Materials and Components for Fusion Applications, Forschungszentrum Juelich, Germany, in the poster "Ductile Phase Toughening in Tungsten-Copper Alloys at Elevated Temperatures."

REFERENCES

- [1] C. H. Henager, et al., "Ductile-phase toughened and fiber-reinforced tungsten for plasma facing materials," Proposal to the U.S. Department of Energy Office of Science, Fusion Energy Sciences. *Materials Solicitation with Focus on Structural Materials, Blanket First Walls, and Divertor Plasma Facing Components*, 2011.
- [2] M. Rieth, et al., "Review on the EFDA programme on tungsten materials technology and science," *J. Nucl. Mater.* **417**, 463-467, 2011.
- [3] R. A. Pitts, et al., "Status and physics basis of the ITER divertor," *Phys. Scr. Vol. T*, 014001, 2009.
- [4] P. Mertens, et al., "A bulk tungsten divertor row for the outer strike point in JET," *Fusion Eng. Des.* **84** (7-11), 1289-93, 2009.
- [5] A. Gervash, et al., "Fabrication of a He-cooled divertor module for DEMO reactor," *J. Nucl. Mater.* **367-370 B** (SPEC. ISS.), 1472-1475, 2007.
- [6] M. Merola, et al., "EU RD on divertor components," *Fusion Eng. Des.* **75-79** (Suppl.), 325-331, 2005.
- [7] P. Mertens, et al., "Clamping of solid tungsten components for the bulk W divertor row in JET- precautionary design for a brittle material," *Phys. Scr. Vol. T* **2009** (T138), 014032, 2009.
- [8] A. Moslang, et al., "Towards reduced activation structural materials data for fusion DEMO reactors," *Nucl. Fusion* **45** (7), 649-655, 2005.
- [9] M. A. Abdou, et al., "On the exploration of innovative concepts for fusion chamber technology," *Fusion Eng. Des.* **54** (2), 181-247, 2005.
- [10] B. Gludovatz, S. Wurster, A. Hoffmann, and R. Pippan, "Fracture toughness of polycrystalline tungsten alloys," *Int. J. Refract. Met. Hard Mater.* **28** (6), 674-8, 2010.
- [11] M. Faleschini, H. Kreuzer, D. Kiener, and R. Pippan, "Fracture toughness investigations of tungsten alloys and SPD tungsten alloys," *J. Nucl. Mater.* **367-370 A** (SPEC. ISS.), 800-805, 2007.
- [12] T. Tanno, A. Hasegawa, J. C. He, M. Fujiwara, M. Satou, S. Nogami, K. Abe, and T. Shishido, "Effects of transmutation elements on the microstructural evolution and electrical resistivity of neutron-irradiated tungsten," *J. Nucl. Mater.* **386-388 C**, 218-221, 2009.
- [13] T. Tanno, A. Hasegawa, M. Fujiwara, H. Jian-Chao, S. Nogami, M. Satou, T. Shishido, and K. Abe, "Precipitation of solid transmutation elements in irradiated tungsten alloys," *Mater. Trans.* **49** (10), 2259-64, 2008.

- [14] T. Tanno, A. Hasegawa, H. Jian-Chao, M. Fujiwara, S. Nogami, M. Satou, T. Shishido, and K. Abe, "Effects of transmutation elements on neutron irradiation hardening of tungsten," *Mater. Trans.* **48** (9), 2399-402, 2007.
- [15] I. Charit, et al., "Fabrication of tungsten-rhenium cladding materials via spark plasma sintering for ultra high temperature reactor applications," U.S. Department of Energy (FY2009 NE-UP Program), 10/1/2009 to 9/30/2012.
- [16] K. Williams, et al., "Etch rates for micromachining processing," *J. Microelectromech. Syst.* **5** (4), 256-269, 1996.
- [17] ASTM Standard B322, 1999 (2009), "Guide for Cleaning Metals Prior to Electroplating," ASTM International, West Conshohocken, PA, 2006, DOI: DOI: 10.1520/B0322-99R09, www.astm.org.
- [18] ASTM Standard B482, 1985 (2008), "Practice for Preparation of Tungsten and Tungsten Alloys for Electroplating," ASTM International, West Conshohocken, PA, 2006, 10.1520/B0482-85R08, www.astm.org.
- [19] I. S. Mahmoud, "Copper plating bath and process for difficult to plate metals." Patent 4,990,224. 5 February 1991.

4.2 EFFECT OF GREEN DENSITY AND FAST SINTERING ON GRAIN GROWTH OF NANO W — X. Wang and Z. Z. Fang (University of Utah)

OBJECTIVE

The objective of this research is to evaluate the effect of green density and fast sintering (rapid heating and high pressure) on the grain growth of nano W and W-TiC powders produced by a high energy planetary ball milling process.

SUMMARY

Two novel processing techniques were developed for inhibiting the grain growth of W during sintering of nano W and W alloy powders; one of which is a hot-pressing green compaction technique for increasing the relative density of green compacts of the nano powders. The second is a fast sintering technique for applying a combination of rapid heating and high pressure during sintering. Nano W and W-TiC powders were used to investigate the effect of green density and fast sintering on grain growth. The following preliminary results were obtained:

- (1) The maximum obtainable green density of cold-pressed samples was 38% of the theoretical full density at 800 MPa, while the hot-pressed sample exhibited an 18% increase in green density (56% TD).
- (2) Higher green density enabled the samples to be fully sintered at lower temperature.
- (3) Near fully dense bodies with a grain size smaller than 300 nm were obtained via fast sintering.

PROGRESS AND STATUS

Introduction

From a structural viewpoint, the major concerns in the development of W alloys for future fusion reactors are their high ductile-to-brittle transition temperature (DBTT) and low fracture toughness. Nanostructuring of tungsten and tungsten alloys could provide a solution to address those concerns [1-4]. In the past, severe plastic deformation processes, such as high-pressure torsion (HPT) have been investigated to obtain nanoscale grain structure. These processes, however, are not suitable for producing industrial-scale finished products. Therefore in this work, we developed new strategies following powder metallurgy routes.

Our previous work [8] has shown that a high energy milled nano tungsten powder can be sintered to 99% relative density at 1100°C under hydrogen, but the final grain size after sintering is larger than 2 micrometers, far beyond the nanoscale. The initial grain growth takes place rapidly when the relative density of the material is very low at low temperatures. Increasing green density and/or lowering sintering temperature will effectively minimize this part of the grain growth. However, the milled nanosized tungsten powders are difficult to press into green compact with only 35-40% relative density using conventional approaches, which makes the material prone to rapid grain growth before densification.

For controlling grain growth of nano W, a novel method to compact nano W powders has been recently developed. The compaction is being done at a moderate temperature that is above its DBTT, but below temperatures that would cause rapid grain growth. This process is expected to yield green compacts with high relative densities, which would significantly improve the chance of obtaining full densification with minimum grain growth during subsequent sintering.

Additionally, a modified rapid omni-directional compaction (m-ROC) process has been investigated for sintering the nano W powders. The ROC process is known to be very effective for consolidating metal or ceramic powders to full density [9]. The m-ROC, which combines rapid, heating ($>200^{\circ}\text{C}/\text{min}$) with a high pressure (up to 1.0 GPa), offers one of the most promising approaches for limiting grain growth while achieving full densification [10]. Rapid heating minimizes sample exposure in the temperature range for rapid coarsening of grains, which results from grain/particle coalescence and is controlled by surface diffusion [11]. The use of high pressure aids the densification process at relatively low temperature.

W-TiC nano powder was processed together with the nano W powder to study the effect of green density and fast sintering on grain growth. This preliminary investigation effectively demonstrated that the W grains grew slowly under higher relative green density and faster sintering.

Experimental Procedure

Improving green density

Nano W and W-1TiC powders were prepared by using a unique high-energy planetary ball milling (HEPM) process. The powders were milled for 6 hours in heptane. The particle size of most of the particles was in the range of 10–55nm. The average W crystallite size was determined to be 12 nm by using X-ray diffraction (XRD) and the Stokes and Wilson formula for grain size determination from peak broadening. Milled nano tungsten powders were compacted using a uniaxial press with heaters shown schematically in the Fig. 1. This hot-pressing system includes a die assembly, a heating device, and a gas control system. The die components can operate at temperatures, up to $\sim 700^{\circ}\text{C}$. During compaction, the die assembly is heated under a cover gas of flowing argon. When the temperature reaches a point above the DBTT, high pressures are applied. Sintering experiments to validate this method were carried out at 1100°C for 1 h in a hydrogen atmosphere using a tube furnace. Our previous results have shown that the HEPM process significantly enhances the sinterability of the nanosized tungsten powders, achieving near-full density at 1100°C but with final grain size larger than $2\ \mu\text{m}$.

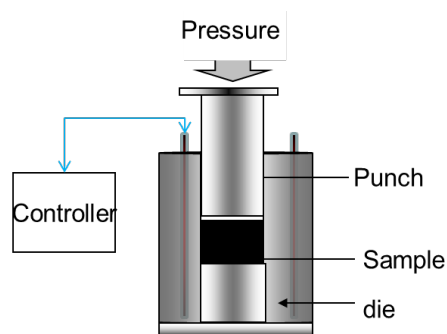


Figure 1. Schematic for the novel green compaction technique with temperatures up to 700°C .

Fast sintering

Figure 2 shows the schematic diagram of the modified rapid omni-directional compaction (m-ROC) process. The milled powder was first compacted at 250 MPa into cylindrical samples. The samples were introduced into a graphite cell of the m-ROC system. The processing was carried out at 1100°C with ultrahigh isostatic pressure of 800 MPa. During the m-ROC processing, the samples were heated in situ using resistance heating. In m-ROC processing, the pressure medium conveys the isostatic pressure.

Characterization

After sintering, the densities of the samples were measured by using Archimedes method. The microstructural changes of the fractured surface of the sintered samples were observed using Scanning Electron Microscopy (SEM). Tungsten grain sizes were determined from the SEM micrographs by using the linear intercept method.

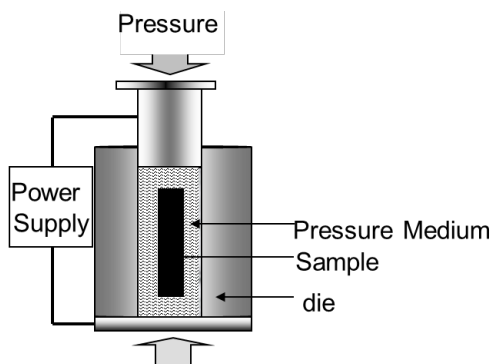


Figure 2. Schematic diagram of apparatus for modified rapid omni-directional compaction (m-ROC) process

RESULTS

Effect of green density

Figure 3 shows the relative green density of hot pressed samples as a function of temperature at 800 MPa. As shown, a continuous increase in green density was observed above 250°C. Below 250°C, the relative density varies slightly. A significant increase of 18% in density was achieved at 450°C. These results indicated that the DBTT for the milled nano W powder is between 200-300°C.

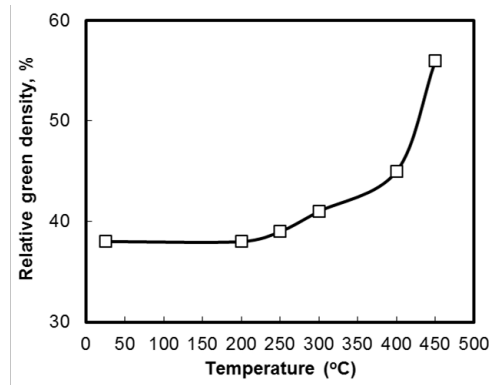


Figure 3. The effect of pressing temperature on the relative green density of nano W powder

The effect of green density on the W grain growth and densification is shown in Fig. 4. It can be seen that at the same sintering temperature, the higher the relative green density, the smaller the grain size and the higher the sintered density are. As the densification rate is enhanced by higher density in the green compacts, sintering temperature, as well as sintering time, can be reduced more and grain growth further suppressed. Incrementally increasing the green density of W-TiC alloys indicates promise for obtaining W grain sizes < 100 nm.

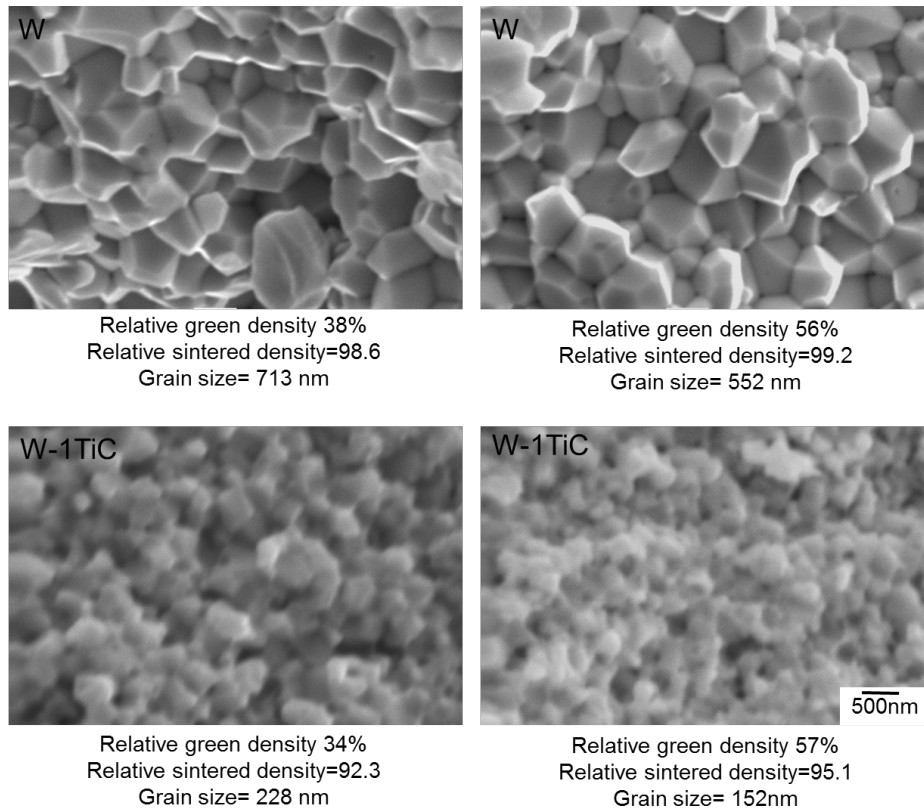
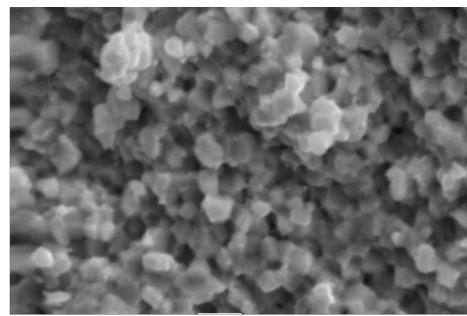


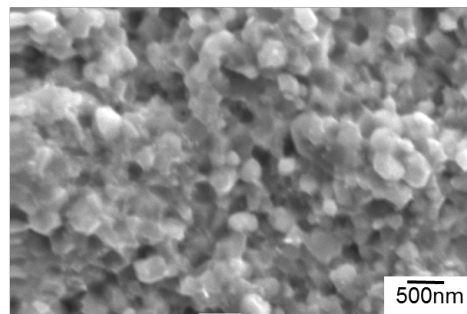
Figure 4. SEM images of fracture surface of sintered nano W and W-1TiC 1100 °C for 1h.

Effect of fast sintering

Preliminary Investigations on the consolidation of nano W alloy powders by the m-ROC have shown that the rapid heating ($>200^{\circ}\text{C}/\text{min}$) and high pressure are beneficial to achieving small grain size. Figure 5 shows two micrographs from a W sample and a W-1TiC after pressing in the m-ROC with a heating rate of $\sim 300^{\circ}\text{C}/\text{min}$ and a maximum temperature of about 1200°C for 2 min. Compared to the W grain size measured from a sample sintered at 1200°C for 5 min in a tube furnace (not shown, but measured at $1\ \mu\text{m}$), the W grain size by m-ROC is much smaller, Fig. 5.



W



W-1TiC

Figure 5. SEM images of fracture surface of sintered nano W- and W-1TiC by M-ROC.

FUTURE WORK

The processes discussed will be further optimized to achieve high density and minimized grain size after sintering of the nano W and W alloy powders. Additionally, mechanical properties of sintered samples will be evaluated.

REFERENCES

- [1] M. Rieth, et al., *J. Nucl. Mater.* **432** (2011) 482-500.
- [2] M. Jain, et al., *Int. J. Powder Metall.* **42** (2006) 53.
- [3] Q. Wei, K. T. Ramesh, E. Ma, et al., *Acta Mater.* **54** (2006) 54.
- [4] L. J. Kecskes, K. C. Cho, R. J. Dowding, et al., *Mater. Sci. Eng.* **467** (2007) 33.
- [5] O. El-Atwani, D. V. Quach, M. Efe, et al., *Mater. Sci. Eng. A* **528** (2011) 5670.
- [6] K. C. Cho, *Mater. Manuf. Process.* **19** (4) (2004) 619.
- [7] A. Mondal, A. Upadhyaya, and D. Agrawal, *Int. J. Refract. Met. Hard Mater.* **28** (2010) 597.
- [8] H. Wang and Z. Z. Fang, *Int. J. Refract. Met. Hard Mater.* **28** (2010) 312.
- [9] C. A. Kelto and E. E. Timm, *Ann. Rev. Mater. Sc.* **19** (1989;) 527X.
- [10] X. Wang, Z. Z. Fang, and H. Y. Sohn, Proceedings of the 2007 International Conference On Powder Metallurgy & Particulate Materials, May 13–16, Denver, Colorado, 2007, page 08-1.
- [11] X. Wang, Z. Z. Fang, and H. Y. Sohn, *Int. J. Refract. Met. Hard Mater.* **26** (2008) 232.

4.3 ELECTRON-BEAM ADDITIVE MANUFACTURING OF TUNGSTEN MATERIALS FOR FUSION — E. K. Ohriner, R. Dehoff, and L. L. Snead (Oak Ridge National Laboratory)

OBJECTIVE

The objective of this work is to produce graded tungsten-iron layers on a steel substrate using the ARCAM electron beam melting (EB) additive manufacturing system now under development at ORNL.

SUMMARY

Initial experiments were performed with the ARCAM A2 electron beam additive manufacturing unit using standard beam deflection conditions. Local regions were observed with the desired microstructure of a solid tungsten surface layer and a liquid phase sintered boundary layer of tungsten particles in a steel matrix. A new ARCAM unit is currently being installed for use in future experiments.

PROGRESS AND STATUS

Single layers of tungsten powder of from 0.8 and 1.6 mm thick have been deposited on steel and EB melted. A steel coupon with melted tungsten powder is shown in Fig. 1. Tungsten powder bed depths of about 1 mm result substantial melting of the steel substrate. A powder bed depth of 1.6 mm resulted in melting of the top surface of the tungsten powder bed, no melting of the steel substrate, and little adherence of the melted tungsten layer to the steel. A powder bed depth of 1.4 resulted in a nearly continuous fully melted tungsten powder with a porous subsurface region of liquid phase sintered tungsten particles in a steel matrix. A powder bed depth of 1.2 mm produced in some local areas with the desired microstructure of a surface layer of essentially pure tungsten bonded to the steel substrate by a subsurface layer of steel infiltrated tungsten particles (Fig 2.)

Since the melting is accomplished by deflection of the electron beam across the surface of the powder bed in an arbitrary and non-optimal pattern, the melting of the surface is not uniform. An example of this can be seen in Fig. 3 on the surface of a melted tungsten powder layer of 1.4 mm thickness. It is increasingly apparent that a much more sophisticated beam deflection pattern that accounts for thermal cycles, with localized in-process changes in thermal conductivity, is needed to obtain consistent uniform surface layers with the desired structure such as in Figure 2.

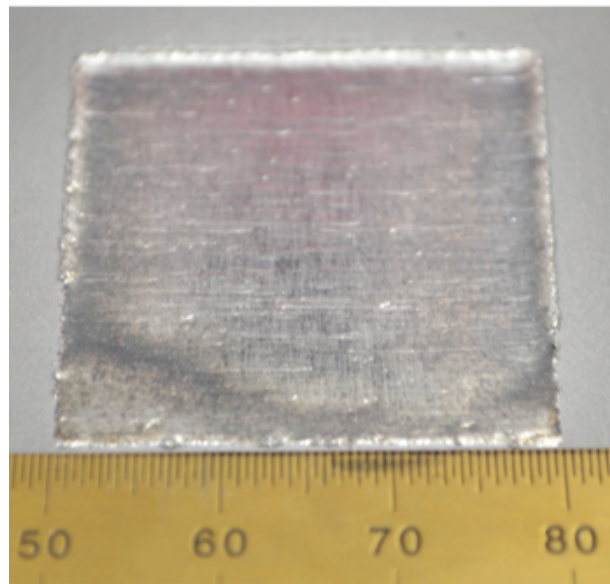


Fig. 1. Melted tungsten powder incorporated into H-13 steel coupon.

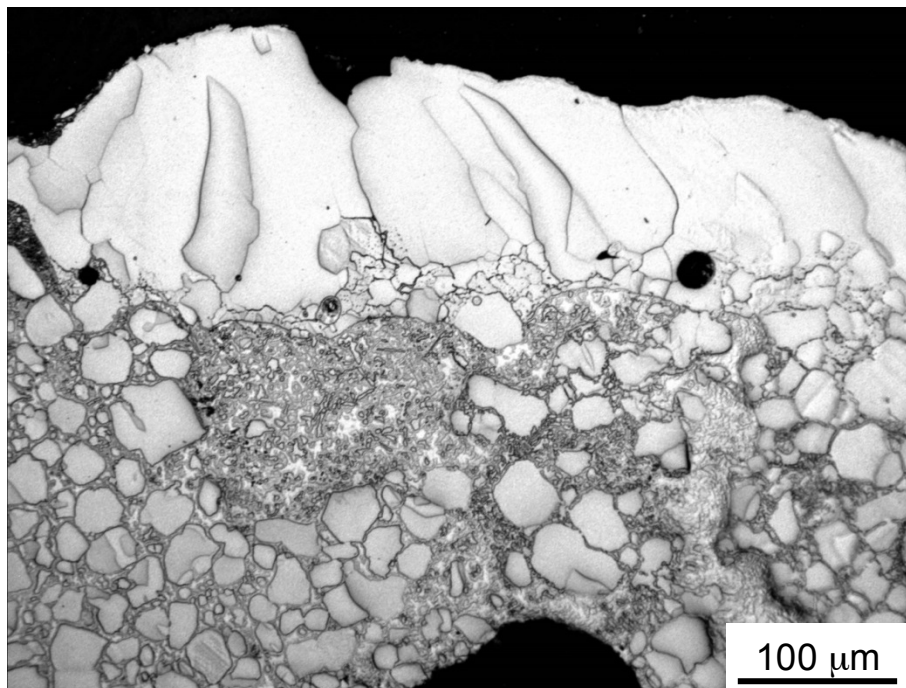


Fig. 2. Cross-sectional view of melting with powder bed depth of 1.2 mm shows a local area of continuous fully melted layer of tungsten powder, at top, bonded to the steel substrate by an intermediate layer of tungsten particles (light contrast) infiltrated by steel (dark contrast).

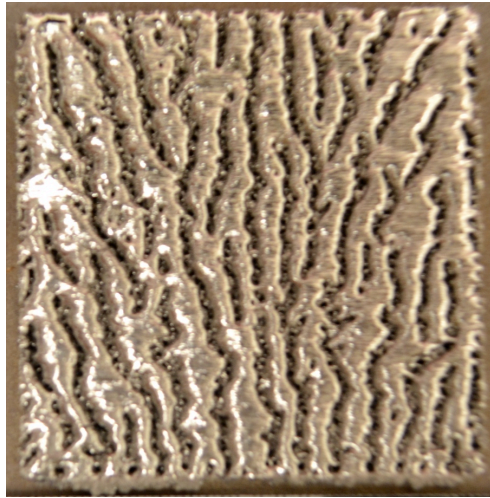


Fig. 3. Surface view of melting with powder bed depth of 1.4 mm shows pattern of fully and partially melted areas associated with the pattern of beam deflection across the sample surface.

4.4 HIGH-HEAT FLUX TESTING OF LOW-LEVEL IRRADIATED MATERIALS USING PLASMA ARC LAMPS — A. S. Sabau, E. K. Ohriner, Y. Katoh, and L. L. Snead (Oak Ridge National Laboratory)

OBJECTIVE

The objective of this work is to test irradiated materials that are candidate divertor component materials and mock-up divertor components under high-heat flux conditions using Plasma Arc Lamps (PAL).

SUMMARY

The Research Safety Summary (RSS) was approved for high-heat flux testing of irradiated specimens. The radiation safety during high-heat flux testing was enhanced by the installation of a digital flow meter on the outlet part of the rod cooling circuit in order to monitor the flow rate during high-heat flux testing. One of the most difficult tasks is the measurement of sample temperature. The best data on sample temperature was obtained using a thermocouple welded to the sample during the high-heat flux testing. A pyrometer was used to measure the surface temperatures on either the specimen holder or the specimen. It was found that at high IR energies the pyrometer data is affected by the infrared energy from the PAL. Thus calibration runs are needed in order to enhance the accuracy of the pyrometer data.

PROGRESS AND STATUS

Effort was conducted on two main areas: (a) enhancing the radiation safety during testing of irradiated specimens and (b) enhancing the measurement accuracy of the sample temperature.

Results for enhancing the radiation safety during high-heat flux testing of irradiated specimens

The current efforts for enhancing the radiation safety during testing of irradiated specimens included:

- Installation of a water flow meter (0.2-2 gpm) to monitor the variation of coolant flow rate into the cooling rod.
- Installation of an automatic pressure controller – for Ar inlet and outflow - to regulate the vacuum pressure to approximately 4 psi in the test section during HHF testing to prevent the liftoff of main quartz window and escape of radioactive gases.
- Installation of a vacuum pressure transducer to monitor the vacuum pressure in the test section during testing and identify accidental vacuum leaks during HHF testing.
- A vacuum leak was repaired.
- In-situ data will be acquired for all experiments on coolant flow rate and vacuum pressure in the test section.

The coolant flow rate can now be measured in-situ for all experiments. As an example, the coolant flow rate was measured during high-heat flux testing consistent of five pulses. The flow rate monitoring will be used to assess the possibility identifying incipient boiling of the water that would lead to an overheating of the hottest section in the cooling rod. The PAL current for the 5 consecutive pulses was 700, 650, 625, 600, 600 A for 15 s, with a dwell time of 2 min between

pulses. The results show that the coolant flow rate drops by less than 2% during high heat flux testing (Figure 1), ensuring that the coolant does not exceed the critical heat flux.

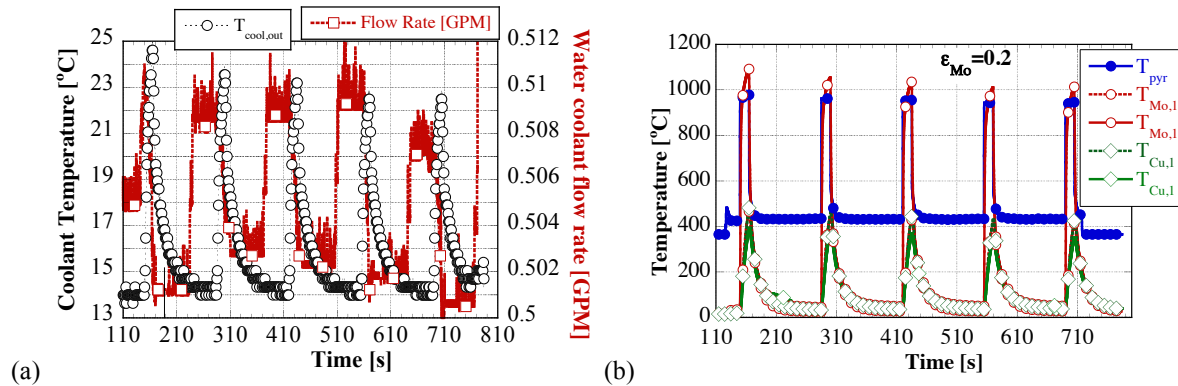


Figure 1. The variation of coolant temperature and coolant flow rate into the cooling rod was measured. (b) The variation of temperatures in the Mo holder during the five pulses.

Vacuum pressure was measured during HHF testing to insure that appropriate vacuum conditions are maintained. The results shown in Figure 2 show that appropriate vacuum pressure is maintained during typical HHF testing. The standard deviation of the pressure variation was found to be 0.09 psi during several pulses (while the mean vacuum pressure was 3.9818 psi).

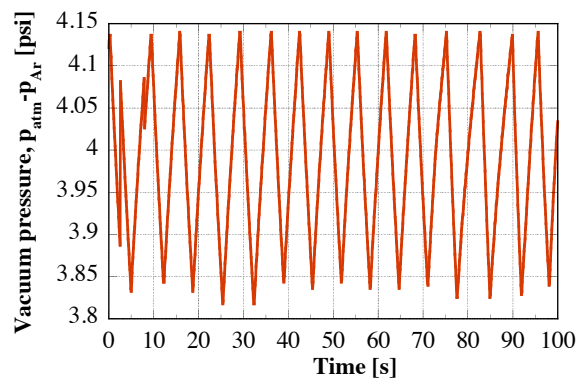


Figure 2. Vacuum pressure during 100 s of a typical test run.

Results for enhancing the temperature measurement

The current efforts for enhancing the temperature measurement during testing of irradiated specimens included:

- Assessment of pyrometer applicability in the actual PAL conditions.

- Use of a second generation of molybdenum specimen holder, for which the thermocouples could be installed closer to the backside surface of the specimen.
- Machining of 2G v2 Mo specimen holders with four thermocouples.
- Conduct calibration experiments in which the pyrometer was used to measure directly the temperature the W specimen surface while a thermocouple was welded on the backside of the W specimen.

The temperature variation during one pulse at 700A (roughly 70% power), for the thermocouples and pyrometer, are shown in Figure 3. The placement of thermocouple tips within the first generation of molybdenum specimen holder, 1G Mo, is shown for the sake of completion to aid in data interpretation (Figure 4a). The pyrometer aims at the sample holder side (Figure 4b) at an angle of 34° with the respect to the normal direction to the sample holder surface. The data shown in Figure 3 indicate the following:

- 1) The pyrometer data is affected by the infrared energy from the PAL during high-energy pulses. The proof of artifact is the sharp raise and drop in pyrometer temperatures right at the onset and end of pulses. The fact that the temperature varies during the high energy indicates that the reflections from the PAL into the pyrometer, which creates the artifact at high-energies, is not dominant and thus it can be corrected.
- 2) The pyrometer data is not affected by the infrared energy during the idle period, after the end of high-energy pulses. The pyrometer temperature at idle has the similar temperature ranges as those measured by thermocouples inserted in the 1G Mo holder.

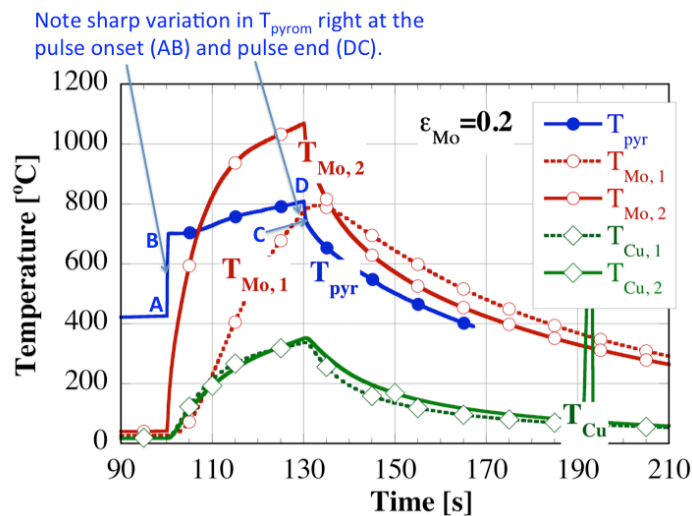


Figure 3. The temperature measured by the pyrometer on the side of Mo holder exhibits sharp variations right the onset and end of the energy pulse of PAL (one pulse of 30 s at 700 A).

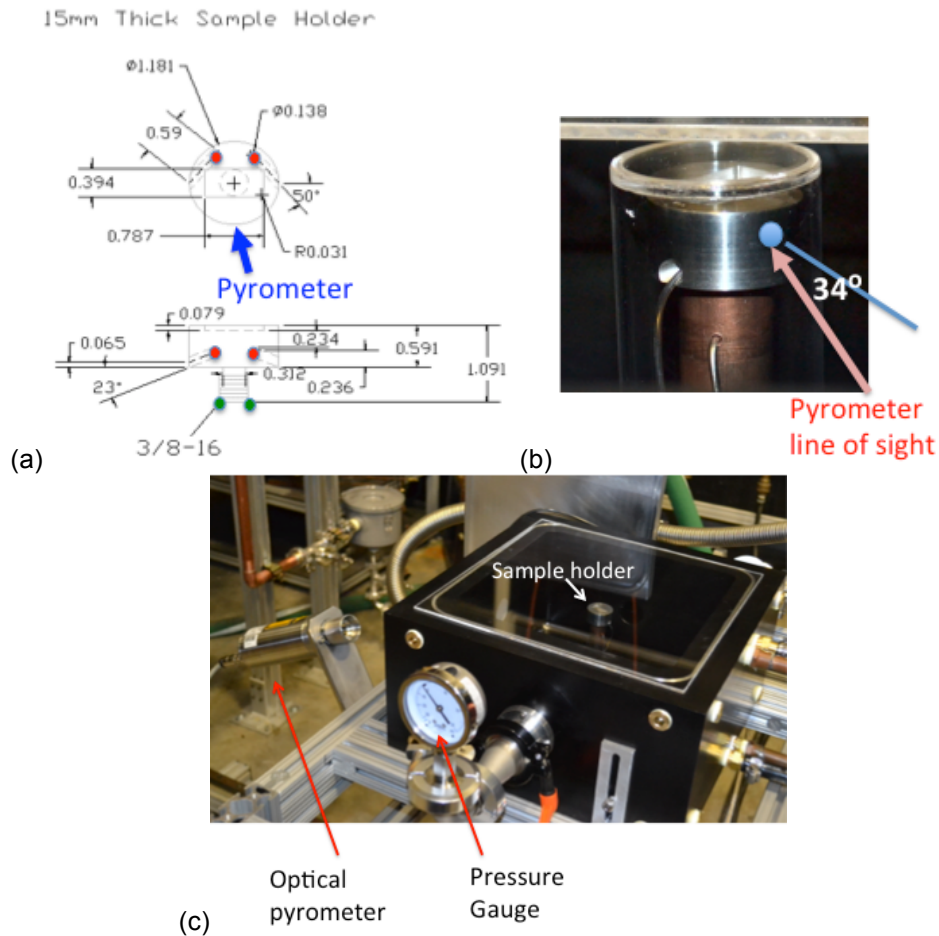


Figure 4. (a) The placement of the thermocouple tips, (b) pyrometer spot on the 1G Mo holder showing pyrometer spot size and direction with respect to the normal to the surface, and (c) pyrometer placement for the measurement of the Mo holder surface temperature.

Temperature data was obtained when the W specimen was placed in the second prototype of molybdenum specimen holder, or 2G Mo (Figure 5). Two holes were drilled in the 2G Mo holder contains for inserting thermocouples close to the back surface of the specimen. The 2G Mo holders have a conical surface and a cutout in order to reduce the heat flux absorbed in the testing fixture (Figure 6). During the HHFT, one thermocouple that was in contact with the W on its back side was bonded to the W specimen, providing one the best set of data for specimen temperature (showed in Figure 5 with open circle symbols). This data shows an actual increase from room temperature to 1,000s in the first 2 s. The sample-reflector distance was 2 cm, the incident heat flux was about 3.2 MW/m^2 , while the absorbed heat flux was into the specimen was approximately 1.6 W/m^2 (50% of the incident heat flux).

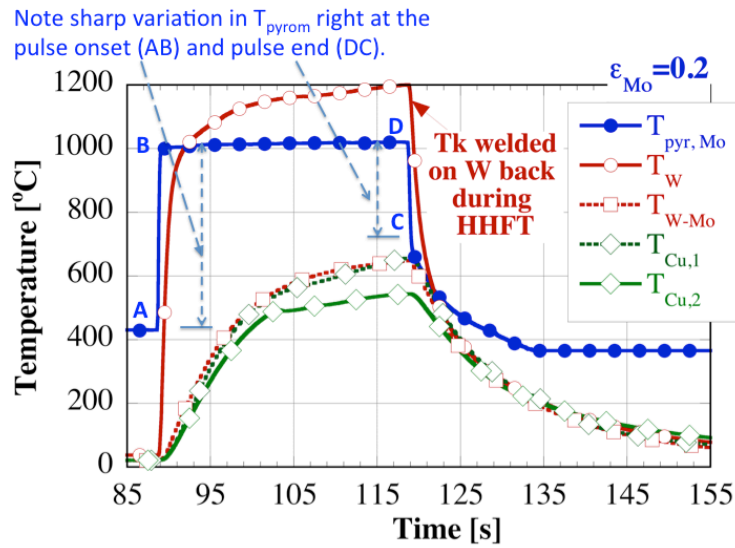


Figure 5. Temperature measured by the pyrometer on the side surface of 2G Mo holder ($T_{pyr,Mo}$) thermocouple welded on W specimen back surface during HHFT (T_W), thermocouple between W specimen and Mo holder (T_{W-Mo}), and thermocouples in the cooling rod at the ends of Mo holder thread (Figure 6). The sample was exposed to one pulse of 30 s at 800 A and the sample-reflector distance was 2 cm.

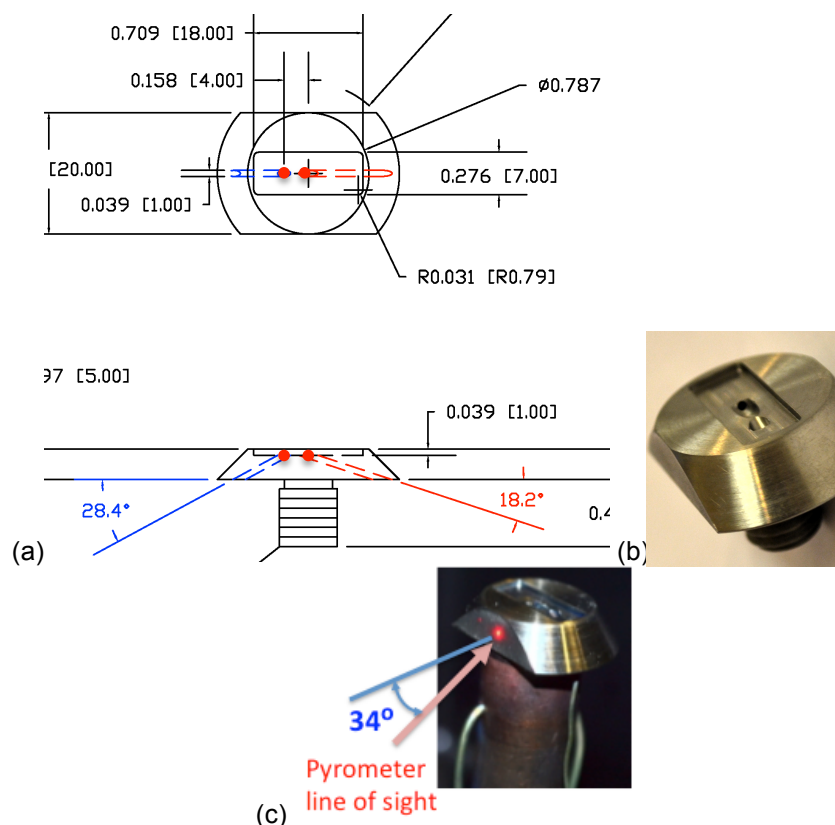


Figure 6. 2-nd generation of Mo specimen holder (a) dimensions; thermocouple tips are shown with red dots, (b) picture, and (c) pyrometer spot size and direction with respect to the normal to the surface.

Calibration experiments for the pyrometer temperature

Calibration experiments, in which the pyrometer was used to measure directly the temperature the W specimen surface, while a thermocouple was welded on the backside of the W specimen, were conducted. The pyrometer was mounted on a tripod and raised above the top level of the test section in order to allow direct line of sight to the sample. The pyrometer was inclined at 58° with respect to the vertical direction (Figure 7a). There were significant difficulties associated with welding the thermocouple tip to the W specimen, which is 0.5 mm thick. Other difficulties were due to the sample support, as it could not be laid down in the Mo sample holder. The sample was placed on a quartz plate, above a steel block, such that the distance between the reflector and sample surface was approximately 9 cm. The sample was not actively cooled as it laid on a quartz plate at an angle of 30° with respect to the quartz plate, making contact with the quartz plate on one edge (Figure 7b and 7c). In this arrangement the specimen was cooled mainly by thermal radiation to the ambient and by thermal conductance through the edge contact with the quartz plate. One minor disadvantage of this placement was the variation of the heat flux on the specimen surface due to its inclination from the horizontal. The laser spot that indicates the pyrometer measurement spot is also shown in Figures 7b and 7c with a red dot. In Figure 7, the temperature results from an experiment are shown. The incident heat flux

was about 0.46 MW/m^2 while the absorbed heat flux was into the specimen was approximately 0.23 W/m^2 . After the experiments were conducted, it was observed that the specimen oxidized, a likely cause being the placement of the woven ceramic inside the test section to shield thermocouples from direct IR heating.

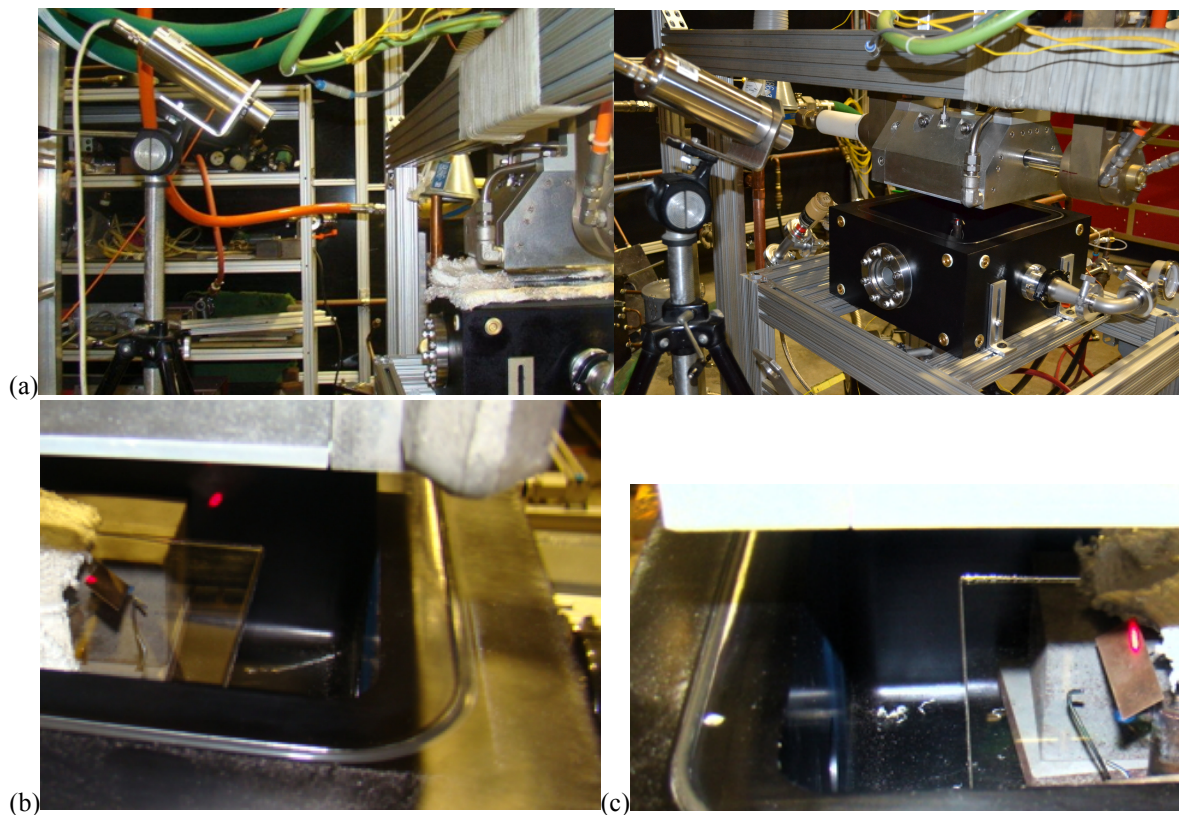


Figure 7. (a) Side view of the pyrometer mount in a raised position to enable direct line of sight to the specimen top surface. Laser spot marked with red color points to the pyrometer measurement spot: (b) side view and (c) front view – opposite side from pyrometer.

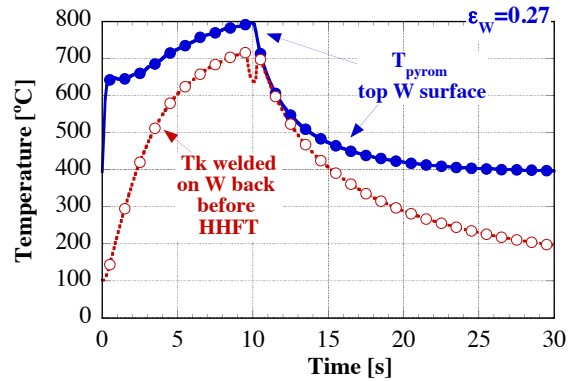


Figure 8. Temperature measured by the pyrometer on the top surface of an uncooled W specimen (solid circle symbols) and thermocouple welded on W specimen back surface before HHFT (empty circle symbols). The sample was exposed to one pulse of 30 s at 200 A.

ACKNOWLEDGMENTS

The authors would like to thank Charles Ross (Chuck) Schaich for assisting with CAD design, fabrication specifications, and assembly; Jim Kiggans for design and fabrication of the Al enclosure, Alta Marie Williams for radiation safety considerations, and David Harper for operating the PAL.

5.1 IRRADIATION RESPONSE OF NEXT GENERATION HIGH TEMPERATURE SUPERCONDUCTING RARE-EARTH AND NANOPARTICLE-DOPED $\text{YBa}_2\text{Cu}_3\text{O}_{7-x}$ COATED CONDUCTORS FOR FUSION ENERGY APPLICATIONS — K. J. Leonard, T. Aytug, F. A. List, III, (Oak Ridge National Laboratory); A. Perez-Bergquist, W. J. Weber, (University of Tennessee); and A. Gapud (University of South Alabama)

OBJECTIVE

The goal of this work is to evaluate the irradiation response of the newest generation of coated conductors based on rare earth and nanoparticle doping of the $\text{YBa}_2\text{Cu}_3\text{O}_{7-x}$ (YBCO) high temperature superconductor. The materials under investigation represent different methods for enhanced flux pinning for improved performance under externally applied magnetic fields. Ion beam irradiation will be used to simulate neutron damage cascades in the materials to examine the effect that radiation damage has on the different pre-existing defect structures used for flux pinning and to evaluate the superconductors capability for use in fusion reactor systems.

SUMMARY

The irradiated superconducting properties of Zr-doped (Y,Gd) $\text{Ba}_2\text{Cu}_3\text{O}_{7-x}$, (Dy,Y) $\text{Ba}_2\text{Cu}_3\text{O}_{7-x}$ and $\text{Gd}_2\text{Ba}_2\text{Cu}_3\text{O}_{7-x}$ are being evaluated for 5 MeV Ni, and 25 MeV Au irradiations to fluences between 10^{11} and 10^{12} ions/cm². For low fluence irradiations, small decreases were observed in the critical current for a-b pinning in both the $\text{GdBa}_2\text{Cu}_3\text{O}_{7-x}$ and (Dy,Y) $\text{Ba}_2\text{Cu}_3\text{O}_{7-x}$ conductors, but increased pinning at other angular orientations, decreasing angular field isotropy. The 10^{12} cm⁻² 25 MeV Au irradiated (Dy,Y) $\text{Ba}_2\text{Cu}_3\text{O}_{7-x}$ did show a reduction in critical current, J_c , for externally applied magnetic fields of less than 7 Tesla for tests conducted at 77 K. However, at higher field strengths the irradiated J_c values exceed that of the unirradiated material. Properties of the Zr-doped (Y,Gd) $\text{Ba}_2\text{Cu}_3\text{O}_{7-x}$ conductor also show positive results following low fluence 5 MeV Ni and 25 MeV Au irradiation, where increases in a-b pinning are observed over the control samples.

PROGRESS AND STATUS

Introduction

During the first half of the year, work has been performed in examining the ion irradiation response of the three advanced high temperature-superconducting (HTS) tapes. The HTS materials under examination include Zr-doped (Y,Gd) $\text{Ba}_2\text{Cu}_3\text{O}_{7-x}$, (Dy,Y) $\text{Ba}_2\text{Cu}_3\text{O}_{7-x}$ and $\text{Gd}_2\text{Ba}_2\text{Cu}_3\text{O}_{7-x}$. The supplied Zr-doped (Y,Gd) $\text{Ba}_2\text{Cu}_3\text{O}_{7-x}$ and (Dy,Y) $\text{Ba}_2\text{Cu}_3\text{O}_{7-x}$ conductors had critical current, I_c , values in self-field of approximately 239 A/cm-width and 525 A/cm-width over 1 meter length of tape, respectively. These tapes have been cut down into smaller test samples. The purchased $\text{Gd}_2\text{Ba}_2\text{Cu}_3\text{O}_{7-x}$ tape was already pre-cut into ~ 1 inch test samples. Patterned current bridges were laser scribed into the HTS test samples for electrical characterization in order to accommodate the high current samples on the available measurement equipment. Silver was deposited at specific sites for the pad positions of the four-probe voltage and current contacts. Following this, the samples were given a thermal anneal in oxygen at 500°C for 1 hour. Ion irradiations at the University of Tennessee Ion Beam Materials Laboratory were performed on the samples at and around the electrical bridge location where the Ag contact is not present. Beam penetration through the Ag contact is not considered due to the >2mm thickness of the Ag layer.

Irradiations to date include 25 MeV Au to fluences of $1 \times 10^{11} \text{ cm}^{-2}$ and $1 \times 10^{12} \text{ cm}^{-2}$, and 5 MeV Ni to $5.5 \times 10^{11} \text{ cm}^{-2}$. The low ion energies were selected to produce defect cascades similar to that observed in neutron irradiations rather than ion track formation, while being energetic enough to produce implantation only in the Ni-base substrates. The fluence of the 5 MeV Ni was selected to match damage levels of the lower fluence 25 MeV Au irradiations in the material as estimated through TRIM calculations. The high fluence of the 25 MeV Au irradiation was estimated to be near the peak damage level of the films prior to degraded properties, based on ion irradiation studies of $\text{YBa}_2\text{Cu}_3\text{O}_{7-x}$ films using different ion and energy ranges by Hensel and coworkers [0]. Pre and post-irradiation electrical characterization was performed at both ORNL and University of South Alabama (USA). The work performed at ORNL consisted of angular field dependency of critical current (I_c vs. ϕ) for applied fields up to 1.5 Tesla at 77 K. Measurement of critical temperature, T_c , resistivity versus temperature and critical current, J_c , as a function of magnetic field were done at USA. Microstructural characterization was performed at ORNL by transmission electron microscopy (TEM) through focus ion beam processing of TEM specimens.

Less than 1 K change in the T_c of the superconducting samples was measured for the 10^{11} cm^{-2} 25 MeV Au irradiated samples as compared to that of the unirradiated control. Values of T_c were reduced between 4 and 6 K from the unirradiated values (92.4 to 93.4 K) following irradiation to the higher fluences ($1 \times 10^{12} \text{ cm}^{-2}$, 25 MeV Au). The reduction in T_c is similar to the effects of oxygen deficiency within the conductor [0].

The current progress of work is outlined in

Table 1 for the three HTS sample types. The 25 MeV Au irradiated samples have completed or are nearing completion of their electrical characterization, but the more recent 5 MeV Ni irradiated specimens are beginning testing at the time of writing this report. Furthermore, some specific retesting of samples is being performed to confirm data (marked as R in the table), or to replace a sample that had shown a large defect in the film layer (marked as S in the table). While microstructural characterization of the 25 MeV Au samples has been completed, characterization of the 5 MeV Ni samples is pending on results of electrical characterization.

The $\text{GdBa}_2\text{Cu}_3\text{O}_{7-x}$ conductor

The pre-irradiated microstructure (see winter 2012 Fusion semi-annual report for details of microstructures of all unirradiated HTS materials) of the $\text{GdBa}_2\text{Cu}_3\text{O}_{7-x}$ (GdBCO) conductor contained a significant amount of anti-phase domain boundaries as well as $\text{Gd}_2\text{BaCuO}_4$, or Y211 type intergrowths in the film structure. The amount of intergrowths appeared to be significantly greater than that observed in the other HTS types examined in this work. Furthermore, the GdBCO film contained small (3.8 nm average size) particles of Gd_2O_3 distributed evenly, but with some ordering along the a-b directions in the film.

A comparison of the microstructures developed on irradiation is shown in Figure 1. Irradiation of the GdBCO film by 25 MeV Au resulted in the observed reduction in length of the anti-phase domain boundaries extending up from the buffer layer interface. While this may suggest some healing of the structure, it can reduce effective pinning centers as well as sources for intergrowths, which can improve electrical properties (flux pinning) under external magnetic fields. Radiation induced defects visibly appear in the microstructure by $1 \times 10^{12} \text{ cm}^{-2}$. These defects were on the order of only a couple nanometers in size and consisted of localized lattice disorder. However, the strain within the GdBCO lattice from these defects produce lobe-type diffraction contrast through the interaction with the beam electrons of the microscope that makes these defects easily visible at lower magnifications. The irradiated samples also showed an even mixture of Y211 and $\text{GdBa}_2\text{Cu}_4\text{O}_8$ (Y124) type intergrowths, while only Y211 were

identified in the unirradiated control. It is not clear at this time how this may influence the electrical properties of the film, but suggests some chemical ordering in the matrix resulting in increased Ba-Cu in the intergrowths. Another observed change in the irradiated microstructure is the disappearance of the Gd₂O₃ particles within the film following 25 MeV Au fluences above 1x10¹¹ cm⁻².

Table 1. Summary of ion irradiation work to date on the HTS conductors, with electrical work performed at ORNL and University of South Alabama (USA).

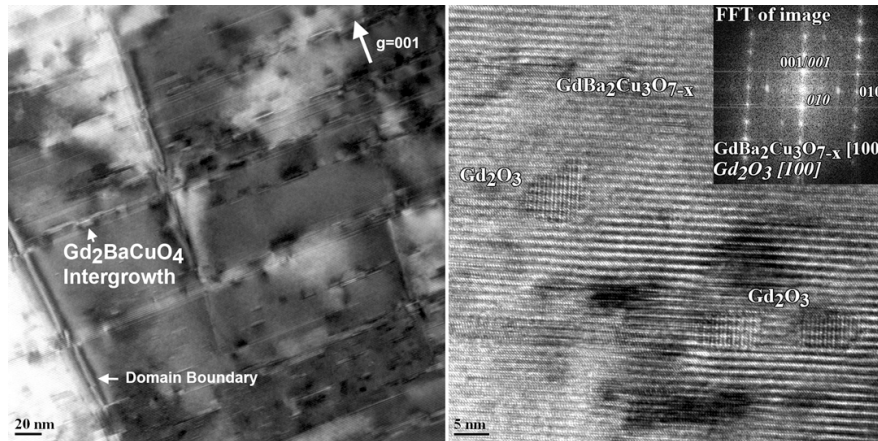
HTS type	Ion Irradiation Conditions	Electrical		Microstructural
		ORNL	USA	
GdBa ₂ Cu ₃ O _{7-x}	25 MeV Au, 1x10 ¹¹ cm ⁻²	C	M	C
	25 MeV Au, 1x10 ¹² cm ⁻²	C	C	C
	5 MeV Ni, 1x10 ¹¹ cm ⁻²	C	M	P
(Dy,Y)Ba ₂ Cu ₃ O _{7-x}	25 MeV Au, 1x10 ¹¹ cm ⁻²	R	C	C
	25 MeV Au, 1x10 ¹² cm ⁻²	S	C	C
	5 MeV Ni, 1x10 ¹¹ cm ⁻²	C	M	P
Zr-YBa ₂ Cu ₃ O _{7-x}	25 MeV Au, 1x10 ¹¹ cm ⁻²	C	C	C
	25 MeV Au, 1x10 ¹² cm ⁻²	M	M	M
	5 MeV Ni, 1x10 ¹¹ cm ⁻²	C	M	P

C = completed, M = currently being measured/examined, P = pending, S = second sample being tested, R = sample being remeasured to confirm properties.

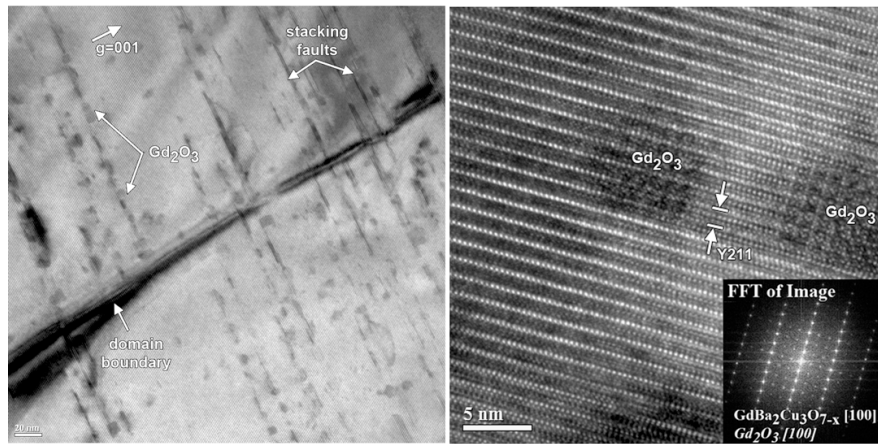
Similar responses in electrical transport properties were observed for the 5 MeV and low dose 25 MeV Au irradiations (Figure 2a), which were irradiated to equivalent damage levels. For the 1 T applied magnetic field in the H//ab direction (f=0°), a slight reduction in the I_c is observed. However, increased critical currents through enhanced pinning are observed throughout the other angles. Irradiation to higher doses, 25 MeV Au at 1x10¹² cm⁻², results in the suppression of a-b axis pinning with little damage to the superconductor as noted by the equivalent response at higher applied angles to that of the unirradiated control. This effect is seen in plotting of I_c versus applied magnetic field (Figure 2b), where the sample currents of the lower fluence irradiations increase over the unirradiated values at fields of 0.3 T and higher. The loss in pinning associated with the high fluence 25 MeV Au irradiation is evident in both the diminished H//ab peak suggesting a significant effect that the changing structure of the intergrowths and loss of Gd₂O₃ particles have on the overall property of the films.

Reduced values of J_c are measured for higher magnetic fields (Figure 2c), which suggest limited effects of the radiation-induced defects on pinning properties. While the loss in J_c can be associated with consolidation of cascade damage resulting in regions of amorphous material that begin to interlink [0,0], the microstructure of the irradiated film did not show this. Furthermore, no decrease in I_c was observed in the high fluence irradiations for the H//c condition. Therefore, the loss in J_c of the high dose 25 MeV Au irradiations is due to the loss of pinning rather than accumulated damage in the superconductor. The J_c vs applied field data for the low fluence irradiations remains to be tested, but should show greater currents than the unirradiated control at high fields. While J_c values at high H fields are low, this can be increased through reductions in measurement temperatures.

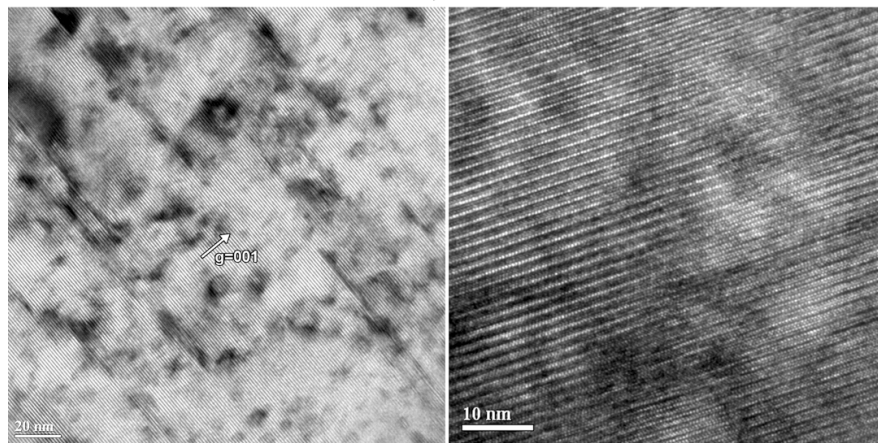
Critical temperature, T_c, of the 1x10¹¹ cm⁻² 25 MeV Au irradiated GdBCO films showed a small decrease with respect to the unirradiated control (93.4 versus 93.2 K) and is within the error of the measurement. However, the 1x10¹² cm⁻² 25 MeV Au irradiated showed a decrease in T_c to 87.3 K.



Control



25 MeV Au, $1 \times 10^{11} \text{ cm}^{-2}$



25 MeV Au, $1 \times 10^{12} \text{ cm}^{-2}$

Figure 1. Comparison of the changes in the microstructure of the $\text{GdBa}_2\text{Cu}_3\text{O}_{7-x}$ conductor with 25 MeV Au irradiation. Micrographs taken from low and higher magnifications to illustrate the development of visible radiation induced defects and the disappearance of Gd_2O_3 particles by $1 \times 10^{12} \text{ cm}^{-2}$.

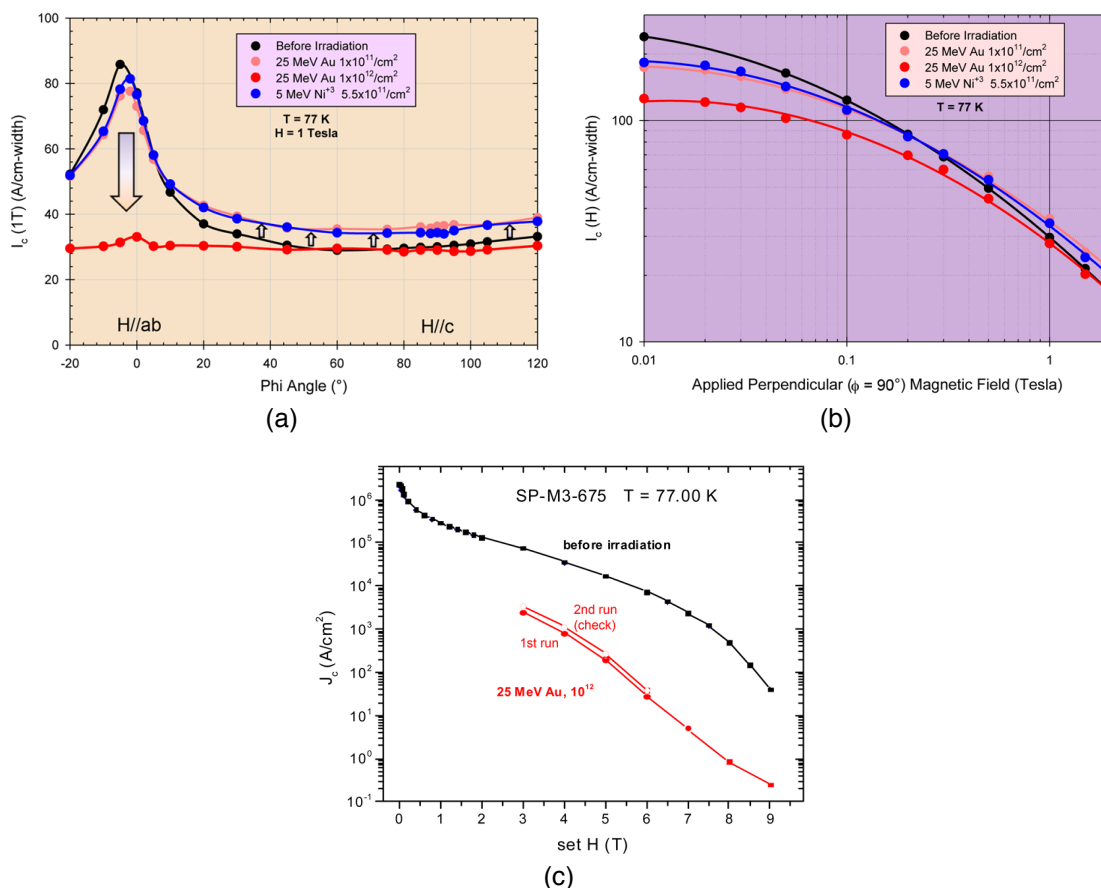


Figure 2. Changes in electrical property of $\text{GdBa}_2\text{Cu}_3\text{O}_{7-x}$ conductor following irradiation by 5 MeV Ni and 25 MeV Au ions. (a) Angular dependence of critical current showing substantial decrease in a-b pinning in the high fluence irradiations, but improvements overall pinning at lower fluences. (b) Critical current as a function of magnetic field to 1.5 T for the H//c condition of the data shown in (a), and (c) the critical current density as a function of applied field to 9 T for the high fluence 25 MeV Au irradiation compared to the control. The J_c vs field data for the lower dose samples remain to be tested.

The $(\text{Dy}, \text{Y})\text{Ba}_2\text{Cu}_3\text{O}_{7-x}$ conductor

Very little difference was observed between the pre-irradiated and post irradiated microstructures of the $(\text{Dy}, \text{Y})\text{Ba}_2\text{Cu}_3\text{O}_{7-x}$ conductor (DyBCO). Examples of the microstructures are shown in Figure 3. The microstructure of the $1 \times 10^{11}\text{ cm}^{-2}$ 25 MeV Au irradiated material was found to be indistinguishable with the unirradiated control and is not shown in the figure. Average $(\text{Dy}, \text{Y})_2\text{O}_3$ particles size and density measured in the irradiated and unirradiated samples were found to be statistically unchanged with values around 26 nm and $4.7 \times 10^{21}\text{ m}^{-3}$, respectively. Intergrowths in the control and irradiated samples were typically found to be Y124 type, assuming that Dy is also substituting for Y in these layers as well. Similar to the previously discussed GdBCO, visible radiation-induced defects in the DyBCO sample do not begin to appear in the TEM samples until a dose of $1 \times 10^{12}\text{ cm}^{-2}$ 25 MeV Au. However, in

addition to the small (~ 2 nm) defects that appear as localized disorder in the stacking sequence of the conductor in the high dose sample, there are also larger (~ 5 nm) defects that are amorphous in structure. The amorphous defects are very few in number (too few to obtain statistics), and do not show the strain contrast surrounding them as the smaller defects show. The 1×10^{12} cm $^{-2}$ 25 MeV Au irradiated DyBCO sample was the only sample to show the amorphous defect features.

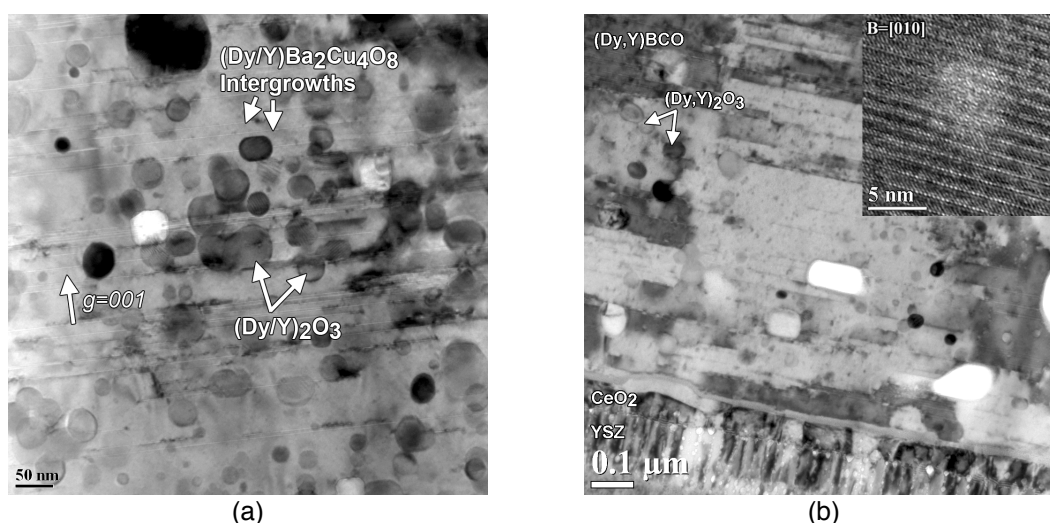


Figure 3. Micrographs of $(\text{Dy,Y})\text{Ba}_2\text{Cu}_3\text{O}_{7-x}$ (a) control and (b) 1×10^{12} cm $^{-2}$ 25 MeV Au irradiated samples. The speckling appearing in the irradiated sample are radiation-induced defects. The insert of (b) shows a larger radiation-induced defect in the conductor consisting of an amorphous sphere.

Irradiation to 5.5×10^{11} cm $^{-2}$ 5 MeV Ni was found to decrease the H//ab pinning in the conductor, but generally increases pinning over other angular field directions (Figure 4). Therefore, reducing the anisotropy of the sample, which in itself can be a positive effect in terms design flexibility for these conductors in applications. For H//c conditions, the 5 MeV Ni irradiated films show higher I_c values with increasing magnetic field starting at 0.5 T. The sample irradiated to 1×10^{12} cm $^{-2}$ by 25 MeV Au showed a significant loss in the I_c over all angular field measurements for the 1 T condition. A retesting of this sample will be performed to verify this. Comparatively, a second sample tested at USA for field dependence of J_c (Figure 4c) did not show as significant of a loss as the sample that ORNL retained for angular dependence tests. For the field dependence study, the high dose 25 MeV irradiated sample shows a cross-over point with the unirradiated condition, in which higher J_c values are found in the irradiated material above 7 T for the samples tested at 77 K. The lower dose, 1×10^{11} cm $^{-2}$, Au irradiated sample showed consistently higher J_c values over that of the unirradiated values (of which are from the same sample in the pre-irradiated condition).

While defects are not visible in the lower dose irradiation, which may consist of lattice site disorder in the conductor, they do contribute to improved properties of the conductor with irradiation. For the DyBCO sample, the high dose irradiated material does show some loss in conduction under low applied fields, but demonstrates improved high field pinning from the defects generated. The 5 MeV Ni irradiated samples are currently undergoing field

dependence, irreversibility and T_c testing at USA. Furthermore, the lower dose 25 MeV Au irradiated sample retained by ORNL for testing requires a second sample to be tested as the first sample showed a visible crack at the bridge location of the sample.

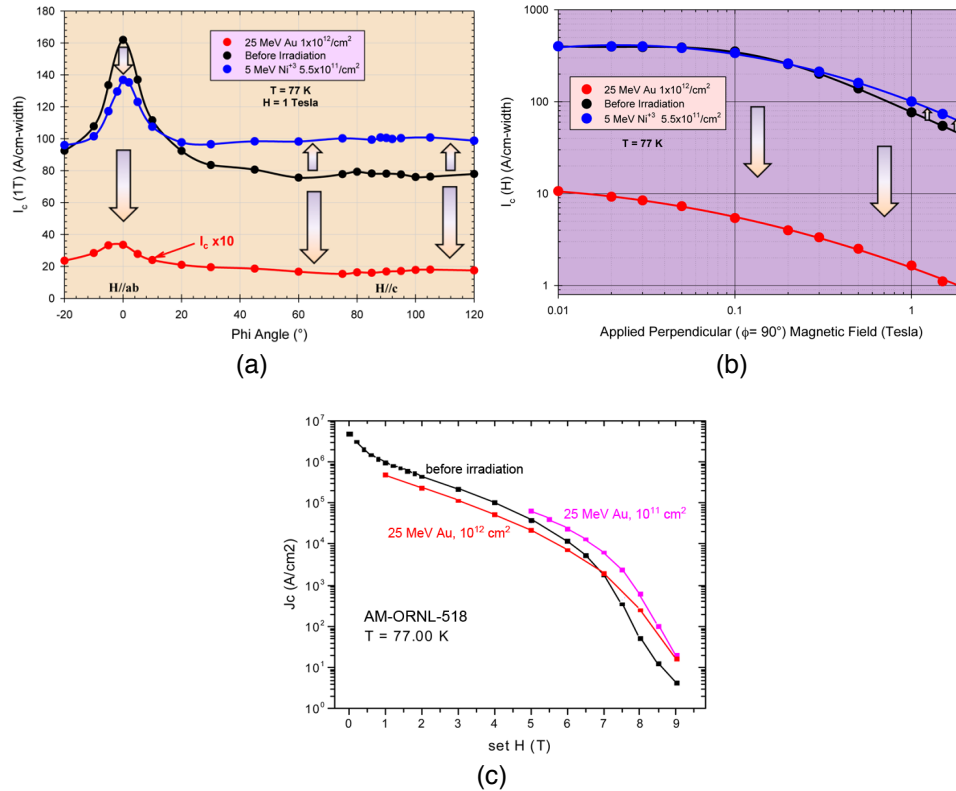


Figure 4. Changes in electrical property of (Dy,Y)Ba₂Cu₃O_{7-x} conductor following irradiation by 5 MeV Ni and 25 MeV Au ions. (a) Angular dependence of critical current showing dramatic loss in sample irradiated to 1×10^{12} cm⁻² 25 MeV Au, while increased pinning observed in the 5 MeV Ni irradiated material. (b) Critical current as a function of magnetic field to 1.5 T for the H//c condition of the data shown in (a), and (c) the critical current density as a function of applied field to 9 T for the 25 MeV Au irradiations compared to the control. A retesting of the angular field dependence of the 25 MeV Au sample, shown in (a), is planned to confirm the result.

The change in T_c with irradiation for the low fluence 25 MeV Au irradiated sample was within a degree of the unirradiated control (92.4 K). The higher fluence 25 MeV Au irradiation resulted in a reduction of T_c to 87.9 K. This was less of a change as compared to the high fluence 25 MeV irradiated GdBCO sample.

The Zr-doped YBa₂Cu₃O_{7-x} conductor

At this time the microstructure of only the control and the 1×10^{11} cm⁻² 25 MeV Au irradiated Zr-doped (Y,Gd)Ba₂Cu₃O_{7-x} (Zr-YBCO) sample has been examined. The irradiated material shows a substantial difference in comparison to the microstructure of the unirradiated control (Figure 5). A significant change in the size and distribution of the BaZrO₃ (BZO) particles is observed following irradiation, in which the

length of the c-axis oriented chains of BZO particles is dramatically reduced by as much as 25% in the c-axis direction. While the width of the BZO particles is relatively unchanged and averages 8 nm. Furthermore, the aligned BZO particle chains show a distinctive and orderly spacing in the irradiated material as compared to a more random distribution in the control. However, the thickness of the irradiated TEM specimen was a little thinner than that of the control, and may account for some of the spatial differences observed between the irradiated and control specimens.

Another difference observed between the control and irradiated Zr-YBCO microstructure is that the conductor immediately around the BZO particles is more faulted in the irradiated material. However the extension of the faults, or intergrowths, into the matrix does not frequently occur. In fact the length of the intergrowths in the control appears longer than those in the irradiated material, but further statistical analysis is required. The irradiated microstructure show Y124 type intergrowths exclusively, compared to a mixture of Y211 and Y124 observed in the control material.

Electrical characterization testing at ORNL has been completed on the $1 \times 10^{11} \text{ cm}^{-2}$ 25 MeV Au and $5.5 \times 10^{11} \text{ cm}^{-2}$ 5 MeV Ni irradiations; the higher fluence 25 MeV Au irradiations still remain to be completed. Shown in Figure 6, an increase in a-b pinning is observed following irradiation with no decrease in I_c for the H//c condition. While the length of the BZO particles in the c-axis direction is reduced, this was not significant enough to create any reduction in the effectiveness of pinning in the H//c condition. The increased H//ab pinning may be related to either the increased point defects in the conductor or the increased faults present at the BZO particle interfaces. As the Zr-YBCO sample is the only conductor in this study to show a rise in the H//ab pinning with irradiation, the faults at the BZO samples are more likely to be the contributor.

The T_c value of the $1 \times 10^{11} \text{ cm}^{-2}$ 25 MeV Au irradiated Zr-YBCO sample only decreased by 0.6 K over that of the unirradiated control.

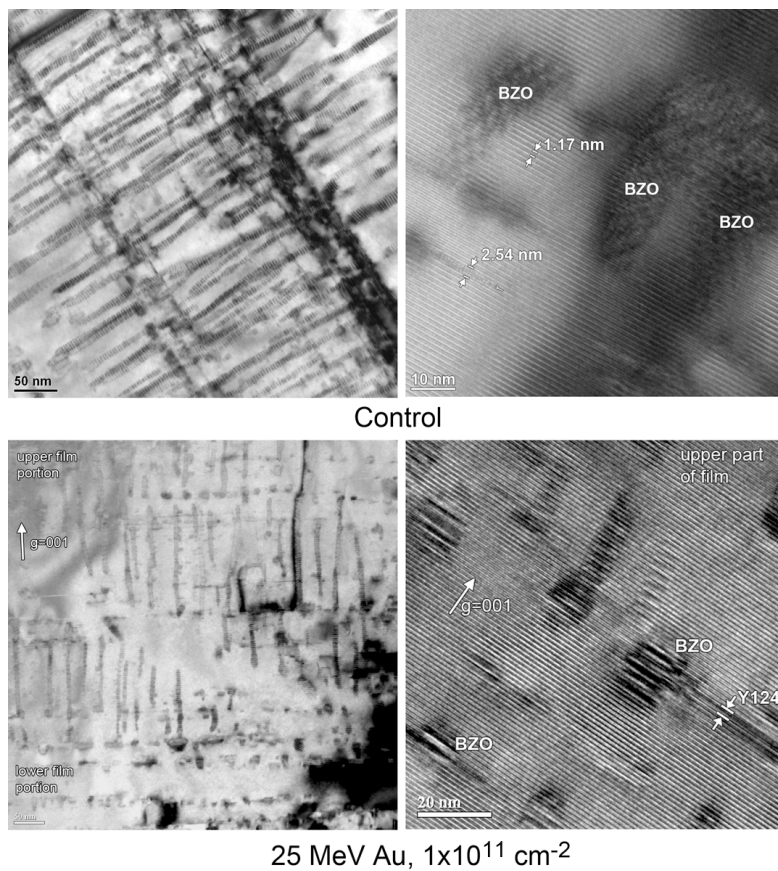


Figure 5. Comparison micrographs of Zr-doped $(\text{Y,Gd})\text{Ba}_2\text{Cu}_3\text{O}_{7-x}$ in the unirradiated and 25 MeV Au irradiated conditions, showing the decrease in BaZrO_3 particle chain lengths in the c-axis direction of the conductor and in the increased localized faulting around the particles in the irradiated material.

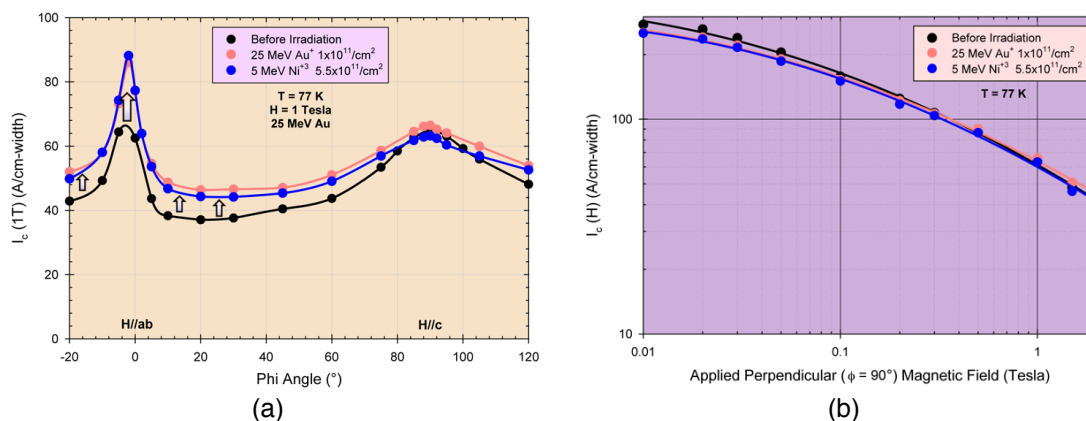


Figure 6. Comparison of 5 MeV Ni and 25 MeV Au irradiation to similar damage levels in Zr-doped $(Y,Gd)Ba_2Cu_3O_{7-x}$ to that of the control sample. (a) Angular dependence of I_c in a 1 T field at 77 K, and (b) a replot of I_c versus field for the H//c condition comparing the samples.

CURRENT AND FUTURE WORK

Continued testing of ion irradiated samples both at ORNL and USA will progress, based on the needed information to complete the gaps shown in Table 1. This will include the full electrical characterization of the irradiated HTS conductors. Some follow up microscopy may be performed to verify or address uncertainties based on analysis of electrical characterization. Additional structural characterization may be performed on the irradiated conductors that could include energy electron loss spectroscopy using the TEM, or Raman spectroscopy in evaluating the local bonding and changes within the conductors resulting from radiation induced damage. Further evaluation of possible in situ testing of the HTS materials under ion irradiation will also begin to be considered.

REFERENCES

- [1] R. Feenstra, D. K. Christen, J. D. Budai, S. J. Pennycook, D. P. Norton, D. H. Lowndes, C.E. Klabunde and M. D. Galloway, "Properties of Low Temperature, Low Oxygen Pressure Post-annealed $YBa_2Cu_3O_{7-x}$ Thin Films, in High T_c Superconductor Thin Films," L. Corraera ed., Elsevier Science Publishers (1992) 331.
- [2] B. Hensel, B. Roas, S. Henke, R. Hopfengartner, M. Lippert, J. P. Stobel, M. Vildic and G. Saemann-Ishenko, *Phys. Rev B* **42** 7, (1990) 4135.
- [3] M. A. Kirk and Y. Yan, *Micron* **30** (1999) 507-526.
- [4] J. R. Liu, J. Kulik, Y. J. Zhao and W. K. Chu, *Nucl. Instrum. Methods Phys. Res. B* **80/81** (1993) 1255.

5.2 HIGH NEUTRON DOSE IRRADIATION OF DIELECTRIC MIRRORS — K. J. Leonard, G. E. Jellison Jr., N. A. P. Kiran Kumar, and L. L. Snead (Oak Ridge National Laboratory)

OBJECTIVE

The goal of this work is to evaluate the upper neutron irradiation dose and thermal limits of two promising dielectric mirror types, through an investigation of the radiation and thermally induced microstructural and optical property changes. While specifically of interest for use in laser control of inertial confinement fusion systems, the examination of the radiation induced structural changes in the films will be beneficial for the development of other thin-film based electronic components and sensors used in nuclear applications.

SUMMARY

HfO₂/SiO₂ and Al₂O₃/SiO₂ dielectric mirrors show impressive resistance to neutron irradiation to 0.1 dpa. However, for the HfO₂/SiO₂ mirror the neutron dose causes crystallinity changes in the film layers of the mirrors and substrate resulting in decreases in reflectivity of the HfO₂/SiO₂ mirror following post irradiation annealing. Cooling following annealing resulted in delamination. Al₂O₃/SiO₂ mirrors appear to have added stability with little microstructural and optical property changes in samples irradiated up to 0.1 dpa and annealed to 673 K. However significant Si and Al interdiffusion cause compositional variation that will eventually result in the formation of aluminum-silicate structures on the layer interface, disrupting the optical properties.

Optical tests of samples irradiated to 1 and 4 dpa during the first half of 2013 confirmed that both the HfO₂/SiO₂ and Al₂O₃/SiO₂ do not survive exposure to 4 dpa, resulting in film delamination. Microstructural evaluations of the 4 dpa samples are now being performed to verify and build upon the low dose results.

PROGRESS AND STATUS

Introduction

The changes in the microstructure of film layers and their effect on optical properties of Al₂O₃/SiO₂ and HfO₂/SiO₂ mirrors will be presented at the 17th International Radiation Effects in Insulators (REI-17) conference held June 30 through July 5, in Helsinki, Finland. A journal paper is currently undergoing ORNL peer review prior to external submission to the Journal of Nuclear Materials. The following is a condensed description of that work.

Irradiation to 0.1 dpa

Dielectric mirrors of HfO₂/SiO₂ and Al₂O₃/SiO₂ designed for optimum reflectivity at 248 nm with 11 and 30 bi-layer coatings, respectively, survived irradiation to 0.1 dpa at 448 K without film cracking or delamination from their sapphire substrates. Subsequent post-irradiation annealing of only the 0.1 dpa samples resulted in a loss of reflectivity in the HfO₂/SiO₂ mirror, while the Al₂O₃/SiO₂ type remained unaffected. Microstructural changes that correlate to optical property changes of the mirror were investigated.

In the case of the Al₂O₃/SiO₂ mirror, no significant changes were measured in the optical properties under the varying exposure conditions, with only a few nanometer shifts to shorter

wavelengths of the mirror peak reflectivity. The film layers of the $\text{Al}_2\text{O}_3/\text{SiO}_2$ mirror remained amorphous over all exposure conditions tested. While fused silica bars also tested with the mirrors underwent up to ~2.25% densification [1], no changes could be measured in the SiO_2 layers of the $\text{Al}_2\text{O}_3/\text{SiO}_2$ mirror. Increasing irradiation dose and thermal annealing temperature (in either the unirradiated control or post-irradiated condition), the amount of interdiffusion between the Al_2O_3 and SiO_2 layers was measurably increased. Despite the composition changes observed across the film layers no secondary phases appear at the film interfaces.

The stability of the $\text{Al}_2\text{O}_3/\text{SiO}_2$ mirror to irradiation arises from the amorphous structure of the constituent layers that are more accepting of damage. Though point defect formation can still occur in the amorphous structures, the retained damage in the amorphous structure is much less than that of crystalline structures [2]. The amorphous structure of the films may be more accommodating to the Si/Al interdiffusion, providing with it an added level of stability to the mirror. The flexibility and variation in the Si-O-Si bond with little energy differences makes this material very stable against thermal degradation and crystallization.

The 0.1 dpa irradiated $\text{HfO}_2/\text{SiO}_2$ mirror showed the largest shift in the peak reflectivity range toward shorter wavelengths, the result of a substantial decrease in SiO_2 layer thickness. This was also the case for the 673 K annealed control where a reduction in the SiO_2 layer was measured. As no significant interdiffusion of Hf and Si were detected between the constituent layers in the examined mirrors, irradiation densification of SiO_2 is suspected along with the removal film layer defects and irregularities related to the fabrication of the mirrors.

Changes in the crystalline structure of the HfO_2 layer in the $\text{HfO}_2/\text{SiO}_2$ mirrors was observed through electron and X-ray diffraction following irradiation and subsequent annealing treatments. The as-deposited mirrors displayed polycrystalline monoclinic structured grains with some retained amorphous regions between crystallites. The intensity of the diffracting grains of the as-deposited films is much less than that recorded in the annealed or irradiated diffraction patterns (Figure 1) in both X-ray and electron diffraction patterns. The amorphous regions disappeared on irradiation to 0.1 dpa or with thermal aging of the unirradiated control material. With irradiation, additional reflections from the HfO_2 film appear in the XRD spectrum. However, these reflected peaks are too few to positively distinguish between the tetragonal and cubic structures due to the dominance of the monoclinic reflections in the pattern. The appearance of non-monoclinic structured grains in irradiated HfO_2 films have been observed in ion-irradiated films in both the electronic as well as nuclear stopping dominating conditions [3,4]. The amount appearing in the 0.1 dpa mirrors is relatively little, approximately 8% from XRD intensity calculations based on the technique of Benyagoub [5] for similar transformations in ZrO_2 , and could not easily be positively identified through TEM. Based on ion irradiation studies in ZrO_2 [6], the structural transformation from the monoclinic phase in the low energy ion nuclear stopping dominated regime is the result of the imposing strain field associated with the oxygen deficiencies from irradiation. While experimental characterization of the transformation in ZrO_2 conclusively identified the transformed phase as tetragonal, clear confirmation in our work could not be made. The cubic/tetragonal intensities in the electron and X-ray diffraction patterns fade with subsequent annealing of the 0.1 dpa irradiated mirrors, presumably due to recovery of some of the irradiation-induced defects. In the irradiated and/or annealed conditions, an increase in the 100 reflections of the monoclinic HfO_2 grains is observed in the suggesting an increase in twinning in the HfO_2 possibly as the result of increased grain growth.

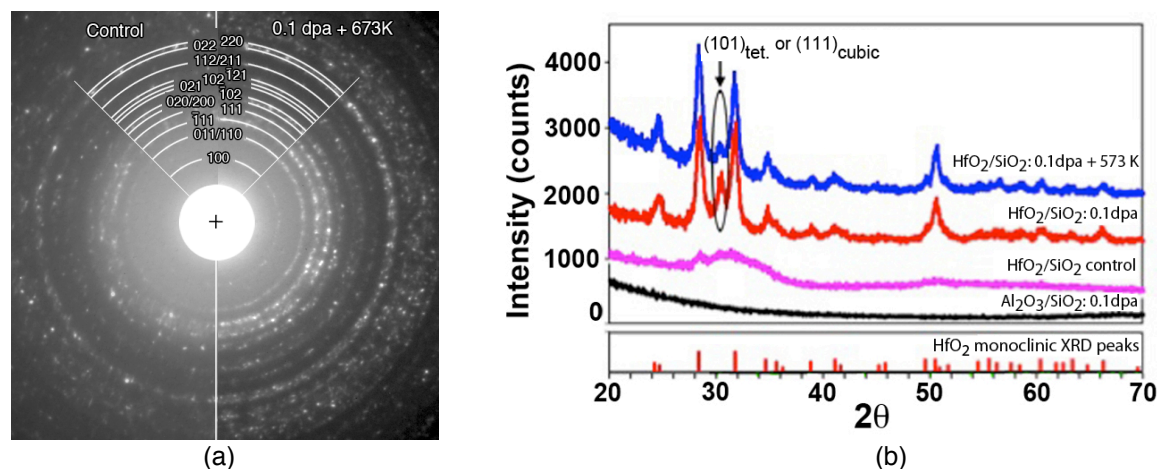


Figure 1. Electron (a) and (b) X-ray diffraction (XRD) patterns of the $\text{HfO}_2/\text{SiO}_2$ mirrors following different exposure conditions. Both patterns show an increase in the crystallinity of the mirror following irradiation and annealing. The amorphous XRD spectra of the $\text{Al}_2\text{O}_3/\text{SiO}_2$ mirror following irradiation to 0.1 dpa is also shown for comparison.

Loss in reflectivity with annealing was only observed in post-irradiate annealing of the 0.1 dpa $\text{HfO}_2/\text{SiO}_2$ mirrors and not observed at lower doses or in the unirradiated plus annealed material. Irradiation to 0.1 dpa resulted in the formation of a semi-amorphous layer within the sapphire at the interface with the first deposited HfO_2 layer (Figure 2a). This observation is similar to that reported by Usov *et al* [7] in HfO_2/MgO multi-layer films on sapphire irradiated by 10 MeV Au ions between 90 and 800 K. In which irradiation temperatures <300 K promoted amorphization of the HfO_2 film layer in contact with the substrate, while higher irradiation temperatures favored amorphization in the sapphire. In our work, neutron irradiation at 448 K produced an amorphous boundary within the sapphire layer for the 0.1 dpa mirrors. In the 0.1 dpa $\text{HfO}_2/\text{SiO}_2$ mirror the amorphization of the sapphire in the near surface region may have been aided by the state of stress at the interface as well as the transfer of oxygen to the HfO_2 layer due to losses in the film layer.

Microstructural examination of the 0.1 dpa $\text{HfO}_2/\text{SiO}_2$ mirror annealed at 673 K revealed buckling of the first HfO_2 layer adjacent to the sapphire (Figure 2b,c). Under the detached regions an amorphous interlayer was present. This amorphous layer was identified as containing Al and O based on EDS examination. No Hf was detected in either the amorphous region or within the near surface layer of the substrate. In the locations where detachment of the HfO_2 layer has not occurred, strain in the sapphire is observed through the distortions in the lattice images and could be seen extending to 1.5 nm from surface.

The compressive stress associated with the HfO_2 films likely has increased with irradiation or thermal exposure as indicated by the development of non-monoclinic HfO_2 polymorphs as well as the development of the larger columnar grain structures and the removal of the amorphous component of the as-deposited films. The annealing of the 0.1 dpa-irradiated materials appears to have facilitated the reduction of the stresses in the films through buckling and coalescence of the amorphous phase under the detached layers.

The detachments observed in the HfO₂ film layer at the substrate create little disruption in the subsequent film layers. The perturbations observed in the TEM sample alone would not be responsible for the substantial drop in reflectivity of the mirrors. Therefore, what is observed at the substrate in the TEM of the 0.1 dpa annealed material can be viewed as starting points for the cause of delamination. As the fractured film layers were no longer in-place on the mirrors, the samples extracted for TEM examination were taken from regions where film layers are still attached and had not progressed to the extremes of delamination. The HfO₂ film at the interface shows a buckle-type delamination mode of failure. While there are many locations along the substrate interface that show these buckles, with spacing between peaks in the bent locations averaged near 350 nm, the high stiffness of the substrate eliminates the possibility of other delamination modes such as wrinkling [8-10]. However, some measure of compliance may be afforded by the substrate through the amorphous Al-O that fills under the deviations in the film layer.

Following on work by Nowacki [11], Reichling *et al.* [12] showed that the stress produced by thermal changes imposed on a surface defect between the substrate and film can be calculated by equation 1. Damage through delamination of the mirror layers can be initiated when this stress needed to overcome film adhesion exceeds a critical value based on the size of the flaw with radius *b*, as described in terms of equation 2.

$$\sigma = \frac{(1-\nu)E}{(1-2\nu)(1-\nu)} \alpha T \quad (\text{Eq. 1})$$

$$\sigma_c = \left[\frac{\pi E \gamma_s}{2(1-\nu^2)b} \right]^{1/2} \quad (\text{Eq. 2})$$

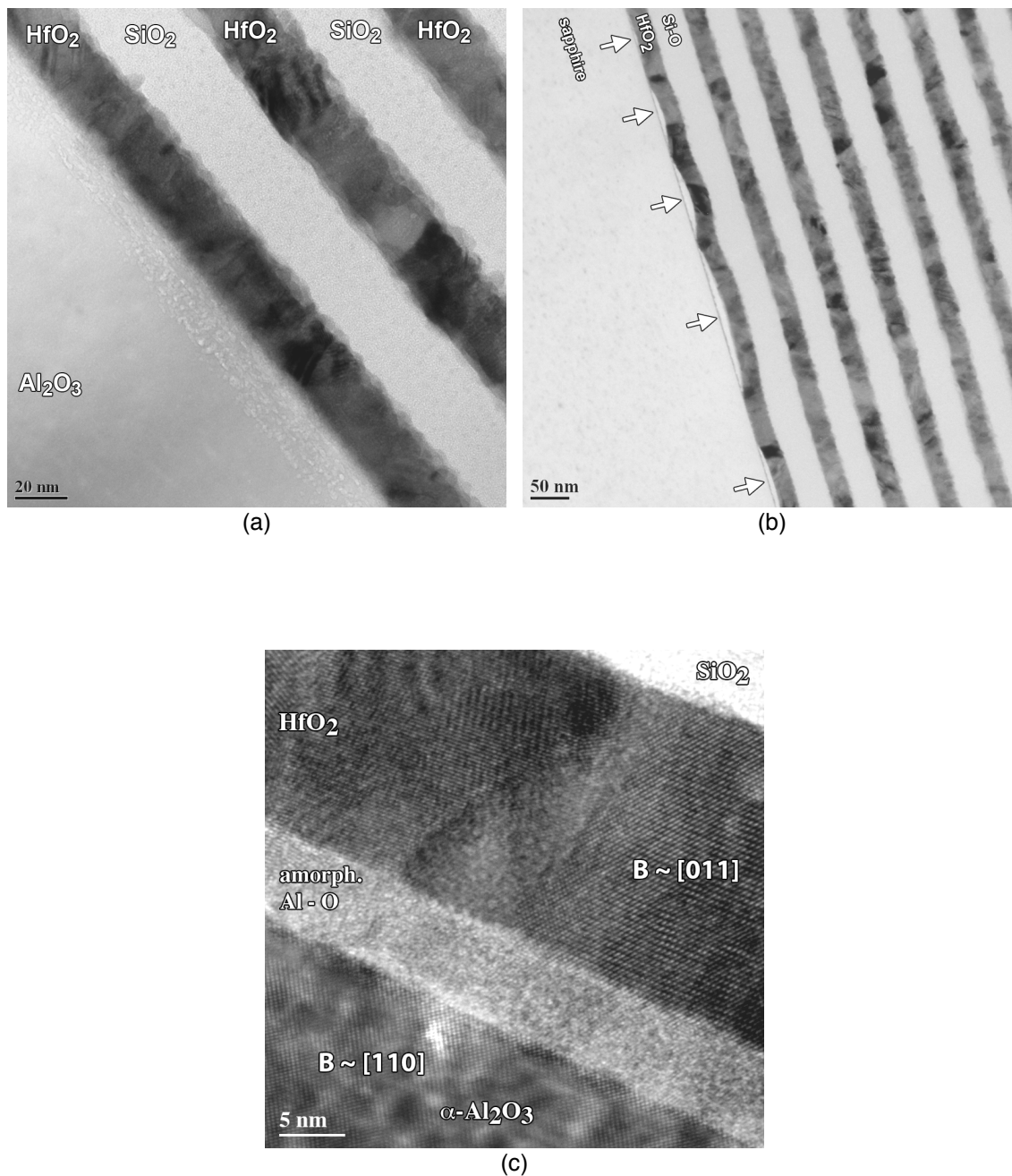


Figure 2. TEM micrographs of the 0.1 dpa irradiated $\text{HfO}_2/\text{SiO}_2$ (a) at the interface of the sapphire substrate showing a semi-amorphous boundary formed within the substrate. Post-irradiation annealed 1 hour at 673K showing (b) delamination of the HfO_2 layer at the interface of the sapphire substrate (indicated by arrows). Higher magnification image (d) at the interface showing a section of the buckled HfO_2 first layer with an amorphous aluminum oxide interlayer between it and the substrate.

Assuming the stress initiates through the thermal changes during annealing and is equal to that of the critical delamination stress, the critical flaw size can be solved for. This assumes that much of the damage is driven by the HfO₂/substrate interface, with a disc-shaped flaw. Taking available data for monoclinic HfO₂ of $E = 220 \text{ GPa}$ [13], $n = 0.25$ [0], $\alpha = 9 \times 10^{-6} \text{ }^\circ\text{C}^{-1}$, and that for the surface energy of HfO₂ (110) $\gamma_s = 2.2 \text{ J/m}^2$ [15], the critical flaw radius size is calculated at 370 nm. As expected, this is larger than the smaller surface deviations observed in the TEM from which the non-fractured portions of the film were examined.

The increase in reflectivity loss with annealing temperatures supports the premise that the thermal induced stresses associated with fracture are at play. Additionally, since only the 0.1 dpa irradiated HfO₂/SiO₂ mirror showed delamination failures following annealing, it is assumed that the amount of strain and amorphous volume formed within the substrate is less for the 0.001 and 0.01 dpa-irradiated samples.

CONCLUSIONS

Our experimental work to date on HfO₂/SiO₂ and Al₂O₃/SiO₂ dielectric mirrors indicate an impressive irradiation resistance relative to the previous studies and the expected exposure conditions expected for application in inertial confinement fusion devices. However, for the case of the HfO₂/SiO₂ mirror, increased neutron dose causes crystallinity changes in the film layers of the mirrors and substrate resulting in decreases in reflectivity of the HfO₂/SiO₂ mirror following post irradiation annealing. During annealing, stress relaxation created buckling in the first HfO₂ layer, which creates defects at the substrate/film interface. On thermal cooling from annealing these defects were sources of increased film stress resulting in delamination initiated from defects that have reached a critical size.

The amorphous layers of the Al₂O₃/SiO₂ mirrors appear to afford added stability under irradiation, where little microstructural and optical property changes occur in samples irradiated up to 0.1 dpa and in post-irradiated annealing to 673 K. However, significant Si and Al interdiffusion was measured across the interface of the constituent layers. This compositional variation will eventually reach a level in which the amorphous structure can no longer accommodate and will result in the possible formation of aluminum-silicate structure on the layer interface disrupting the optical properties.

CURRENT AND FUTURE WORK

Work has continued on the optical testing of the high neutron dose samples irradiated to 1 and 4 dpa during the first half of 2013. In brief, optical tests have confirmed that both the HfO₂/SiO₂ and Al₂O₃/SiO₂ do not survive exposure to 4 dpa, resulting in film delamination. The detailed microstructural examination performed in the low dose work as outlined in this semiannual has firmly established an understanding of the root causes of failure. Microstructural evaluations of the 4 dpa samples are now being performed to verify and build upon the low dose results.

Current work also includes the testing of absolute reflectivity of the mirror samples through the newly installed and tested NeCu deep UV laser system. Measurement of absolute reflectivity of the mirrors will complete the optical testing work.

Additional optical testing through ellipsometry of single layer SiO₂, Al₂O₃ and HfO₂ films on sapphire has also been performed for the 0.001, 0.01, 0.1, 1 and 4 dpa conditions. The results are now being analyzed.

Future work will include microstructural evaluation of the 1 dpa mirrors. The $\text{Al}_2\text{O}_3/\text{SiO}_2$ mirror shows differences compared to the lower dose samples in the photospectrometry data collected. In that the peak reflectivity range is contracted and shifted to longer wavelengths in the 1 dpa mirror, opposite of that observed at lower doses. It is suspected that interfacial compounds may be forming between the film layers. While the 1 dpa $\text{HfO}_2/\text{SiO}_2$ mirror has showed no change in its photospectrometry spectrum compared to the 0.1 dpa exposures, microstructural analysis will confirm the radiation-induced changes that led to failure at 4 dpa.

REFERENCES

- [1] L. L. Snead, K. J. Leonard, G. E. Jellison Jr., M. Sawan and T. Lehecka, *Fusion Sci. Technol.* **56** 2, 1069 (2009).
- [2] W. J. Weber, et al., *J. Mater. Res.* **12**, 1946 (1997).
- [3] I. O. Usov, J. A. Valdez, J. Won, M. Hawley, D. J. Devlin, R. M. Dickerson, B. P. Uberuaga, Y. Q. Wang, C. J. Olson, G. D. Jarvinen, and K. E. Sickafus, *Nucl. Instr. Methods Phys. Res. B* **267**, 1918 (2009).
- [4] A. Benyagoub, *Nucl. Instr. Meth. B* **218**, 451 (2004).
- [5] A. Behyagoub, *Phys. Rev. B* **72**, 094114 (2005).
- [6] G. Baldinozzi, D. Simeone, D. Gosset, I. Monnet, S. LeCaër and L. Mazerolles, *Phys. Rev. B* **74**, 132107 (2006).
- [7] I. O. Usov, J. A. Valdez, J. Won and D. J. Devlin, *J. Nucl. Mater.* **420**, 262 (2012).
- [8] H. Mei, R. Huang, J-Y Chung, C. M. Stafford and J-H Yu, *Appl. Phys. Lett.* **90**, 151902 (2007).
- [9] H. Mei, C. M. Landis and R. Huang, *Mech. of Mater.* **43**, 627 (2011).
- [10] E. A. Jagla, *Phys. Rev. B* **75** 8, 85405 (2007).
- [11] W. Nowacki, *Thermoelasticity*, 2nd edition, Pergamon Press, Oxford (1986).
- [12] M. Reichling, A. Bodemann and N. Kaiser, *Thin Solid Films* **320**, 264 (1998).
- [13] K. Tapily, J. E. Jakes, D. S. Stone, P. Shrestha, D. Gu, H. Baumgart and A. A. Elmustafa, *J. Electrochem. Soc.* **155** 7, H545 (2008).
- [14] S. L. Dole, O. Hunter, Jr. and C. J. Wooge, *J. Amer. Ceram. Soc.* **60** 11, 488 (1977).
- [15] G. H. Chen, Z. F. Hou and X. G. Gong, *Comp. Mat. Sci.* **44**, 46 (2008).

6.1 LIQUID METAL COMPATIBILITY – A THERMAL CONVECTION LOOP FOR Pb-Li COMPATIBILITY TESTING — S. J. Pawel, A. W. Willoughby, M. S. Stephens, Z. M. Burns, B. A. Pint, and J. D. McNabb (Oak Ridge National Laboratory, USA)

OBJECTIVE

The objective of this task is to develop structural materials having sufficient compatibility with flowing Pb-Li eutectic that the maximum metal temperature for operation can be increased. This will improve overall system efficiency of fusion reactor power conversion systems.

SUMMARY

Fabrication of the first Pb-Li thermal convection loop has been completed. The loop was fabricated using dispersion strengthened FeCrAl (Kanthal APMT) tubing. This alloy is known for high strength and creep resistance at elevated temperature, and based on capsule testing, it is also anticipated to have excellent resistance to Pb-Li.

PROGRESS AND STATUS

Introduction

Currently, the maximum allowable wall temperature for the dual coolant lead-lithium (DCLL) blanket concept is set at 475°C based primarily on corrosion limitations of the structural containment materials. To increase overall system efficiency, potential structural materials are being sought with a combination of high strength and creep resistance with simultaneous resistance to dissolution in eutectic Pb-Li at temperatures > 500°C. Preliminary research using static capsule exposures has indicated that dispersion strengthened FeCrAl (Kanthal APMT) may be resistant to dissolution in eutectic Pb-Li at temperatures in the range of 600-800°C, at least in part due to the stability of an Al-rich oxide film. However, corrosion data in a flowing system must be generated to analyze the potential for issues associated with thermal gradient mass transfer – relatively high dissolution in hotter portions of the flow system with concomitant deposition in the colder portions – which has been known to disrupt heat transfer and even plug flow paths completely in some temperature gradient – material combinations.

Thus, thermal convection flow loops (TCLs) are being incorporated as the follow-on step to capsule testing for evaluation of liquid metal compatibility. The initial laboratory testing associated with this effort will utilize a mono-metallic TCL fabricated of Kanthal APMT with APMT specimens for post-exposure evaluation in each of the hot leg and cold leg of the TCL. Fabrication of the first such TCL utilizing APMT tubing (26.7 mm OD, 3.1 mm wall), which evaluated welding and heat treatment procedures to be used in subsequent TCL construction with this alloy, was successfully completed at the end of the reporting period. Corrosion testing is expected to begin early in FY14.

Results

Figures 1-3 depict key aspects of the fabrication process. The loop was fabricated in two major steps – completion of all saddle welds to join tubing sections, and then completion of all welds to insert the thermowells – with each step followed by post weld heat treatment (PWHT) of the entire loop within a large box furnace at 850°C (1 h in air, slow cool). Heat tapes were used to maintain pre-heat temperatures (250°C) at all weld locations prior to PWHT. After each PWHT

event, welds were inspected with a combination of visual examination (borescope for loop internals), radiography, and dye-penetrant. A helium leak check of the final assembly revealed one small pinhole in the weld of a thermowell insert, which was repaired and followed by PWHT. Subsequently, the entire loop was subjected to pre-oxidation treatment (1050°C in air, 8 h, slow cool) to prepare it for service in Pb-Li. The completed loop passed the final inspection and leak check.

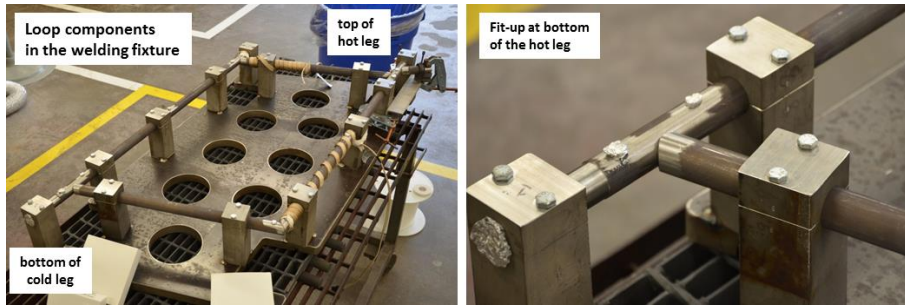


Figure 1. Initial loop fabrication. At left, the sections of loop tubing are shown positioned within the support fixture, with the first of several heat tapes already in place (for maintenance of pre-heat requirements). At right, detail of a saddle weld fit-up prior to welding.



Figure 2. Welding and heat treatment. At left, completion of a saddle weld at the bottom of the loop. At right, the loop is shown within the box furnace for post-weld heat treatment (PWHT).

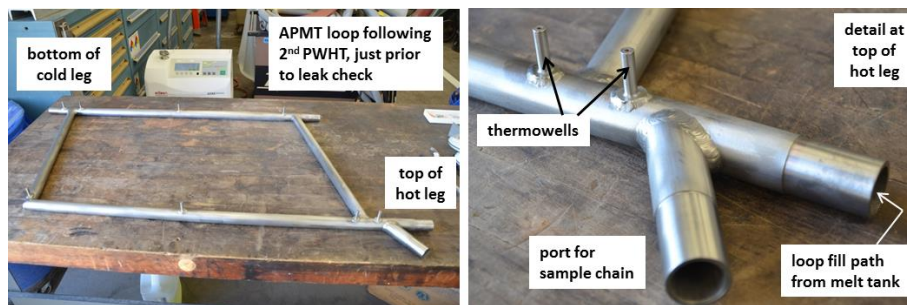


Figure 3. Completed thermal convection loop. At left, the loop is shown with all saddle welds and thermowell inserts in place after completion of PWHT (approximate dimensions are 120 cm tall and 60 cm wide). At right, detail at the top of the hot leg is shown. After final pre-oxidation heat treatment (not shown here), the loop developed a uniform dull straw-brown discoloration.

7.1 ION IRRADIATION EFFECTS ON HIGH ENTROPY ALLOY — N. A. P. Kiran Kumar^{1,2*}, K. J. Leonard¹, H. Bei¹, T. S. Byun¹, Y. Zhang^{1,2}, and S. J. Zinkle¹ (Oak Ridge National Laboratory¹, University of Tennessee²)

OBJECTIVE

The goal of this study is to investigate the basic radiation behavior of structurally unique High Entropy Alloy (HEA).

SUMMARY

Preliminary microstructural and nanoindentation examinations have been performed on Fe-28%Ni-27%Mn-18%Cr high entropy alloy specimens irradiated with 3 MeV Ni ions at room temperature to 0.1 and 1 dpa and at 500°C to 1 and 10 dpa. The hardness in the ion irradiated region of the crystalline face centered cubic HEA samples increased rapidly with increasing dose at room temperature, from ~40% higher than the unirradiated value at 0.1 dpa to approximately double the unirradiated hardness at 1 dpa. The increase in the irradiated hardness was less pronounced for irradiations at 500°C, with values of 15-20% increase at 1 dpa and ~20% increase at 10 dpa. Microstructural characterization of the irradiated HEA specimens found small defect clusters after room temperature irradiation and larger defect clusters after 500°C irradiation; voids were not observed at any irradiation condition in the preliminary examination. After irradiation at 500°C, evidence of significant solute segregation was observed at grain boundaries and discrete precipitates were observed; precipitation was not observed in the room temperature irradiated samples. The grain boundary precipitates were highly enriched in Cr and Mn. Overall, the behavior of the high entropy alloy following irradiation at 500°C appears to be significantly different from the behavior observed in irradiated Fe-Cr-Ni austenitic alloys.

PROGRESS

Introduction

High entropy alloys introduced by Yeh *et al.* in 1995 [1-4] have changed the conventional alloy design in which only one or two principle elements decides the material primary properties. High entropy alloys (HEAs) are composed of four or more metallic elements mixed in an equimolar or near equimolar ratio. HEAs are specifically designed to form ductile solid-solution structures like face centered cubic (FCC) or body centered cubic (BCC) or mixtures of the two, instead of brittle intermetallic compounds. In recent years, HEAs have attracted significant attention due to their high strength, ductility, wear resistance, high temperature softening resistance and corrosion resistance, making them potential candidates for high temperature fusion structural applications. However, there is practically nothing known about their neutron radiation resistance. It is hypothesized that the high configurational entropy might promote enhanced point defect recombination in irradiated materials; the key objective of the present study is to examine the extent of microstructural and mechanical property changes produced by irradiation, compared to standard Fe-Cr-Ni FCC alloys.

Experimental

A high entropy alloy of composition 27%Fe-27%Mn-28%Ni-18%Cr, manufactured at ORNL, has been chosen for the present study. The material was prepared by arc melting by mixing

constituent metals of high purity. In general, the high entropy alloy should consist of approximately equimolar compositions in order to maximize configurational entropy. However, exploratory studies determined that the Fe-25%Mn-25%Ni-25%Cr alloy was not a single phase. Reducing the Cr composition resulted in a single FCC phase for an alloy composition of 27%Fe-27%Mn-28%Ni-18%Cr high entropy alloy.

The cast bar was homogenized at 1200 °C for 48 h, cold rolled and recrystallized at 900°C for 4hr in a vacuum furnace to obtain fully recrystallized microstructure with grain size of ~35µm. The neutron and ion irradiation experiments have been divided into two phases (Table 1). The first phase work covers the low temperature irradiation regime. The ion irradiations with 3 MeV Ni ions to fluences of 4.2×10^{13} , 4.2×10^{14} and 4.2×10^{15} ions/cm² (0.1, 1.0 and 10 dpa at a depth of 1.07 mm) were performed at room temperature and high temperature in the newly commissioned ORNL/University of Tennessee ion beam laboratory. The damage and implanted profile generated using SRIM [5] for 3 MeV Ni ions is shown in Fig-1. The Phase-I neutron irradiations to 0.1 and 1 dpa utilized perforated rabbit capsules in direct contact with the HFIR coolant water and were completed during the May fuel cycle. Rabbit capsule design work has been initiated for the Phase II (high temperature, 500°C) HFIR neutron irradiations, and the irradiations are expected to begin in late fall, 2013.

Table 1. Summary of completed (phase I) and planned/ in progress (phase II) neutron and ion irradiation conditions for the high entropy alloy.

Material		Ion irradiation (mid-range dose, ~3 MeV Ni ions)	HFIR neutron irradiation
HEA (Fe-28%Ni-27%Mn-18%Cr)	Phase I	0.1 dpa, room temp.	0.1 dpa, 70°C (perf. rabbit)
		1 dpa, room temp.	1 dpa, 70°C (perf. rabbit)
	Phase II	1 dpa, 500°C	1 dpa 500 °C
		10 dpa, 500°C	

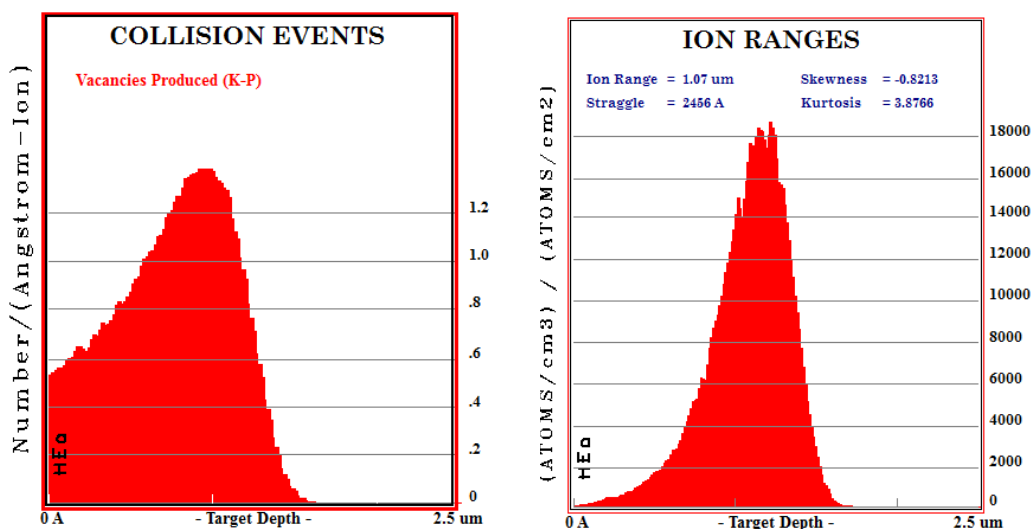


Fig 1. SRIM plots comparing the damage profile with the implanted Ni-atom profile.

Hardness measurements were performed at room temperature using a MTS XP nanoindenter. A Berkovich diamond indenter (3-sided pyramidal tip) was used for the tests. All the tests were performed in continuous stiffness measurement mode with a constant loading rate $\dot{P}/P = 0.05\text{s}^{-1}$ and the maximum load applied is 150 mN [6]. For good statistical analysis, each sample was indented with at least 16 to 25 indents and the average of the results was used in the analysis. PANalytical Xpert diffractometer with $\text{MoK}\alpha$ ($\lambda = 0.709319 \text{ \AA}$) target was used to perform grazing incidence X-ray measurements (incidence beam fixed at 2°) on the ion-irradiated samples. All scans used 2mm adjustable slits and 2° anti-scatter slit so that the same portion of the sample was always in the X-ray beam throughout the scan. The detectable phase limit of the diffractometer is $\approx 3 \text{ wt.}\%$, which means, any phase with less than 3 wt.% cannot be detected using this method.

Analysis of grain boundary composition of irradiated samples was performed using a scanning transmission microscope with energy diffraction spectrometry (STEM/EDS). STEM/EDS measurements was performed in a Philips CM200/FEG STEM which produces a probe of 1.4 nm at 200 KV operating voltage.

Preliminary Results and Discussion

Fig 2 shows the optical microstructure of the control sample after final heat treatment. The control HEA sample is etched with H_2O_2 : HCl : H_2O (vol.% of 1:1:6) to obtain a better contrast of grain boundary. A single-phase polycrystalline structure was observed without any second phase. In addition, the ion-irradiated samples were investigated for potential phase and structural changes using XRD measurements. Interestingly, no detectable phase ($> 3\text{wt}\%$) was observed as a function of irradiation temperature and dose rate (see Fig 3). Even at higher dose rates and temperatures, the HEAs are stable without forming any detectable second phase.

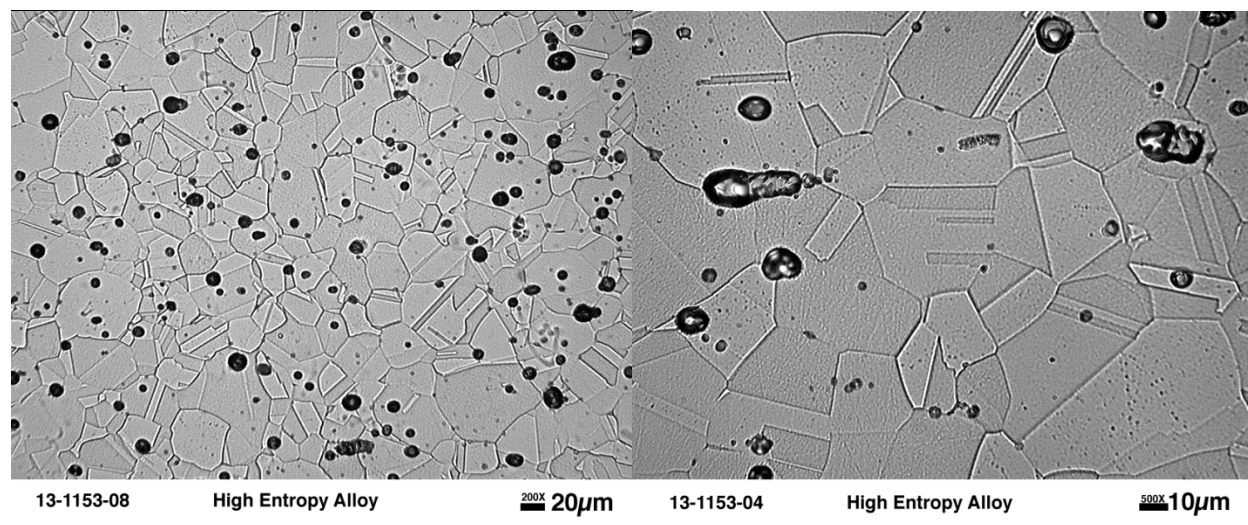


Fig 2. Optical micrographs of HEA control sample (Note: the black spots in the images are etch pits).

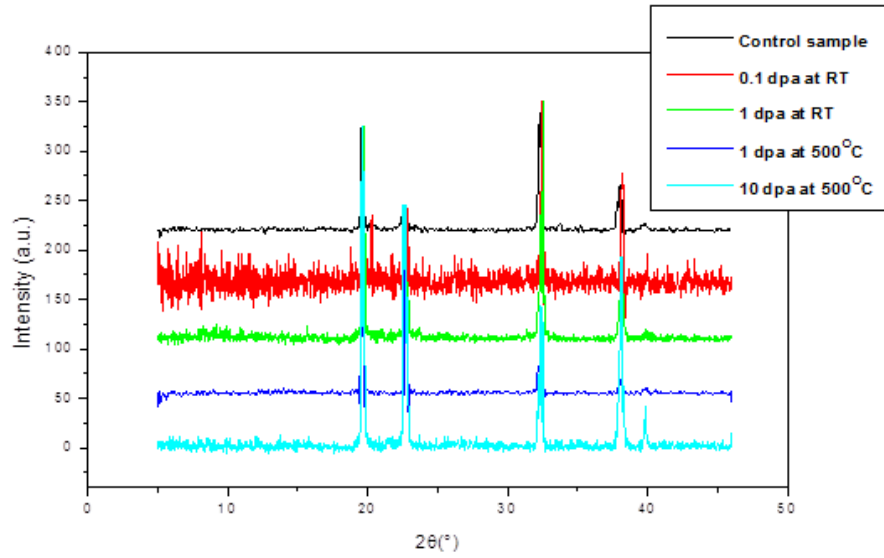


Fig 3. XRD patterns of the HEAs under different conditions.

Microstructure and Radiation Induced Segregation (RIS)

Void swelling in Fe-Ni-Cr alloys has a significant impact on its performance in the reactor [7-13]. Earlier studies have concluded that overall swelling of these alloys can be varied by varying Ni and Cr concentration [8,13]. In addition, ferritic steels showed more resistance to void swelling than austenitic steels [10]. In contrast to conventional Fe-Ni-Cr alloys, present HEA showed no pronounced void swelling for any irradiation conditions. Initial microstructural characterization focused on solute segregation and precipitation. Radiation induced segregation is a phenomenon in which the local alloy composition is altered by spatial redistribution of alloying element at the point defect sinks. This leads to enrichment or depletion of solute elements in defect sinks such as grain boundaries, phase boundaries, dislocations and voids.

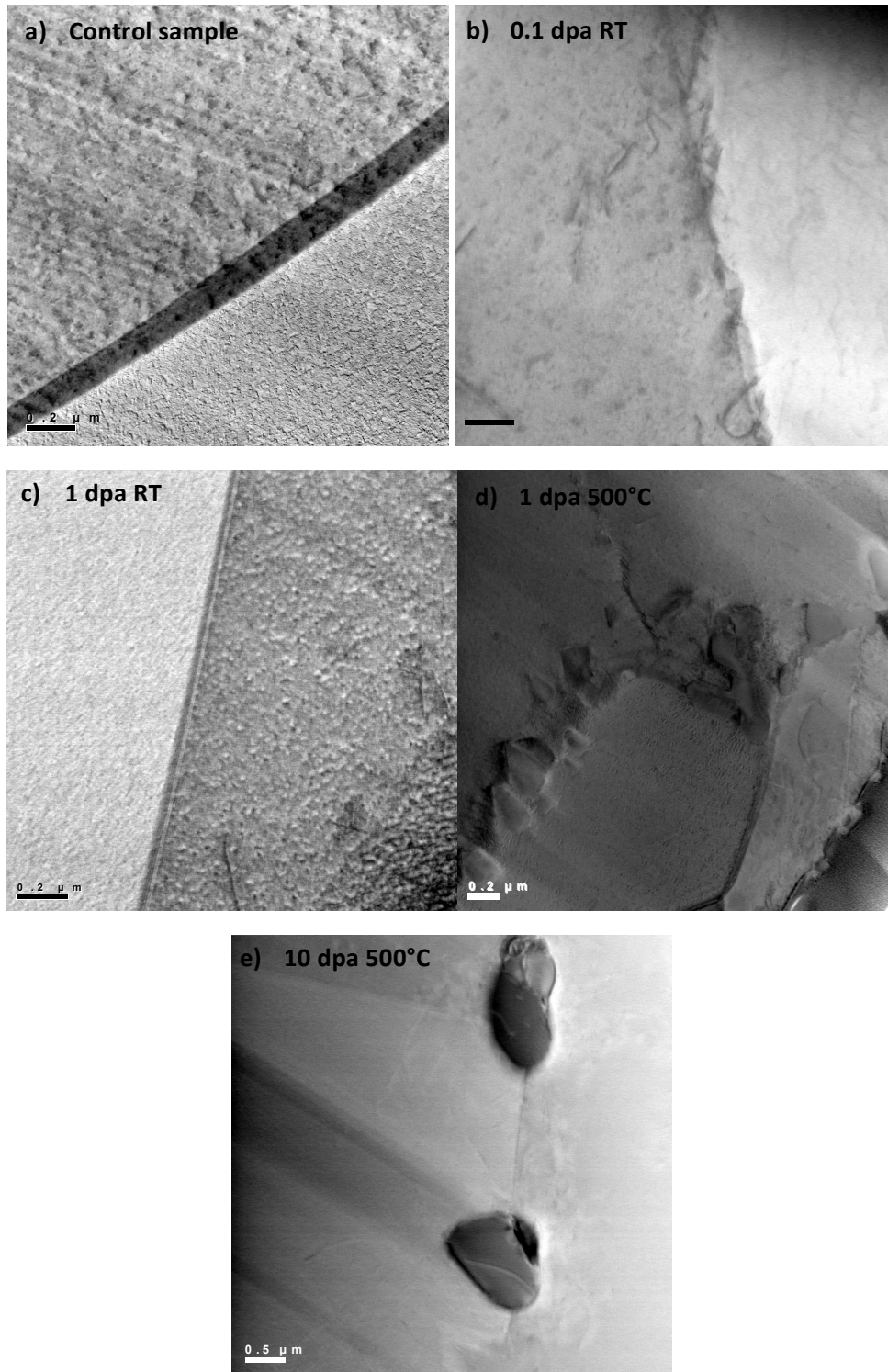


Fig 4. STEM micrographs of a) Control sample b) 0.1 dpa RT c) 1dpa RT d) 1 dpa 500°C sample d) 10 dpa 500°C (Note: detectable segregation at the grain boundary can be seen in 1 and 10 dpa, 500°C samples).

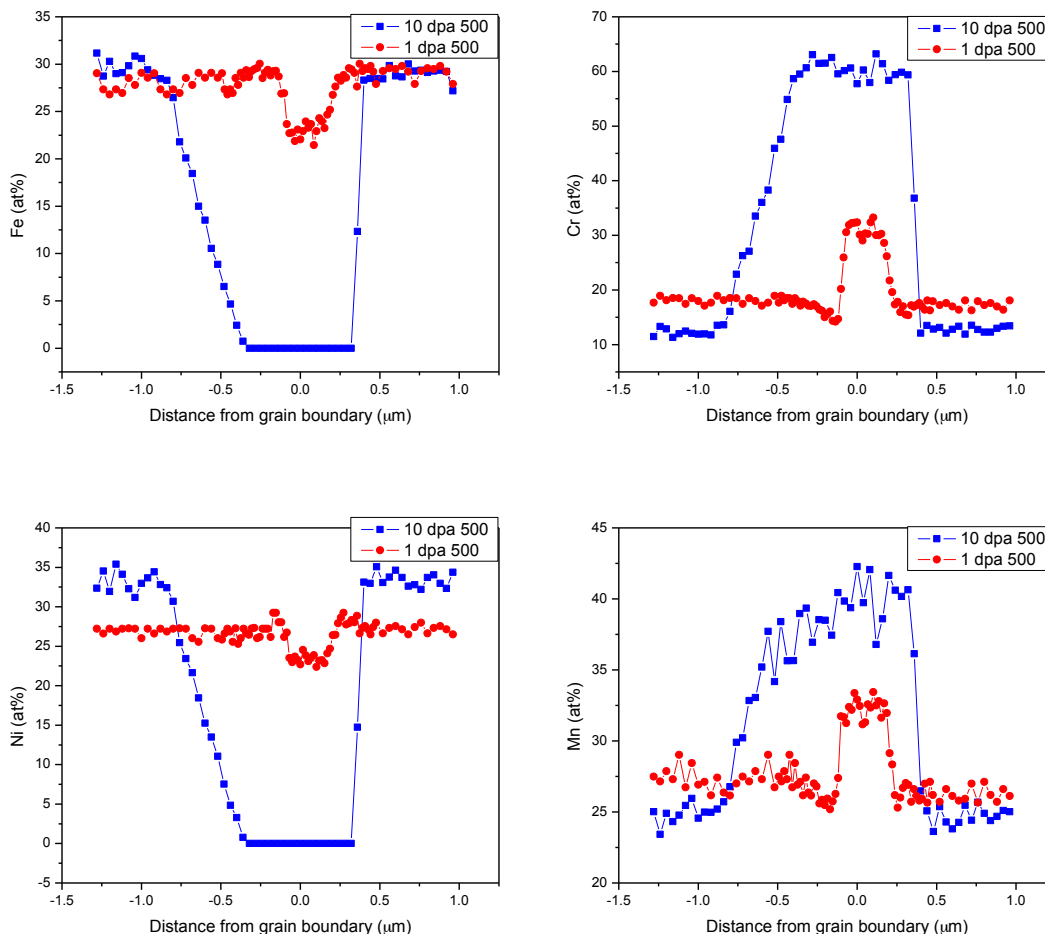


Fig-5. STEM/EDS grain boundary composition profiles of 1 dpa and 10 dpa samples irradiated at 500°C.

Fig 4 shows the STEM micrographs of the samples exposed to different irradiation conditions. As it can be seen in the micrographs, pronounced segregation (resulting in precipitation) was observed at the grain boundaries of the samples irradiated to 1 and 10 dpa at 500°C. Samples irradiated to 0.1 and 1 dpa at the room temperature showed no measurable segregation detectable by STEM/EDS. The same technique was performed across the grain boundary precipitates of the 1 and 10 dpa 500°C samples, to identify and quantify the compositions of those precipitates. Fig 5 shows the experimentally observed radiation induced segregation (RIS) of the samples that were ion irradiated to a dose of 1 and 10 dpa at 500°C. The segregation profile observed for Fe-Ni-Mn-Cr HEA (see Fig 5) is not a typical trend expected in Fe or Ni based or Fe-Ni-Cr alloys [14-16]. However, the complete understanding of RIS behavior of these alloys is still lacking. RIS typically causes depletion of fast diffusing elements like Cr. In contrast, enrichment of Cr at the grain boundaries is also reported in the literature for some ferritic alloys [17-21]. Recent studies have concluded that factors like alloying composition and temperature may determine the enrichment or depletion of an element [17]. In

the present HEA samples, Cr and Mn enrichment and Fe and Ni depletion was observed during ion irradiation at 500°C. In addition, as the radiation dose increases, the chromium and manganese becomes more enriched and the iron and nickel become progressively more depleted along the grain boundary. In general, it was shown in previous irradiation studies on conventional austenitic alloys that relatively slow diffusing Ni and Fe segregate to the defect sinks, while faster diffusing Cr and Mn atoms diffuse away from the defect sinks. The completely opposite behavior in the present FCC high entropy alloy compared to conventional Fe-Cr-Ni or Fe-Cr-Mn austenitic alloys could be due to some change in diffusion kinetics in HEAs or some other physical phenomenon. Unlike conventional alloys, in HEAs there is no solvent element that dominates the composition of the solid solution. In any case, the significant difference in radiation response for the HEA vs. conventional Fe-Cr-Ni-Mn alloys at 500°C is remarkable.

Hardness

Nanohardness is a key performance index for ion-irradiated samples. The normalized hardness values of irradiated samples are shown in Fig 6. The sample irradiated to 1 dpa at room temperature showed high hardness when compared with other irradiated samples. The increase in hardness with the increase in irradiation dose at room temperature can be due to the presence of strained regions formed by dislocation loops. In addition, it is more interesting to see that the hardness of samples irradiated to 1 and 10 dpa at 500°C is low and also very close to the hardness of control sample. Many hypothetical assumptions can be made from the present hardness results. However, one can get a clear understanding of the plot only after analyzing the irradiation defects using TEM, which will be performed in the next reporting period.

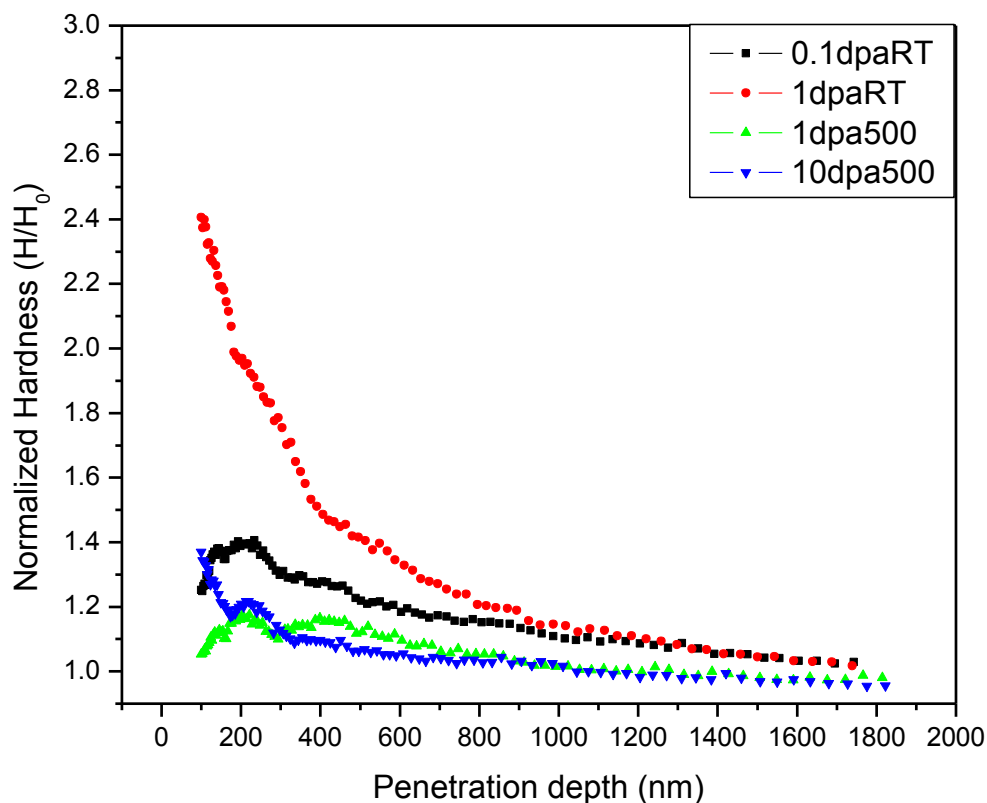


Fig 6. Nanoindentation normalized hardness plots.

FUTURE WORK

Quantitative TEM examination of ion-irradiated HEAs is ongoing. The comparison of radiation defects in irradiated samples with unirradiated control sample will be used to elucidate the self-healing through point defect recombination in HEAs. Phase-I neutron irradiation work on HEAs is complete and will undergo capsule disassembly in next few weeks. A variety of post-irradiation tests including TEM examination will be performed on the neutron irradiated samples. The capsule design for Phase II (500°C) neutron irradiations is in progress.

REFERENCES

- [1] J. W. Yeh, S. K. Chen, S. Lin, J. Y. Gan, T. S. Chin, T. Shunt, C. H. Tsau, and S. Y. Chang, *Adv. Eng. Mater.* **6** (2004) 299.
- [2] K. H. Huang and J. W. Yeh, Master's Thesis, National Tsing Hua University, (1996).
- [3] C. Y. Hsu, J. W. Yeh, S. K. Chen, and T. T. Shun, *Metall. Mater. Trans. A* **35** (2004) 1465.
- [4] J. W. Yeh, *Ann. Chim. Sci. Mater.* **3** (2006) 633.
- [5] J. F. Ziegler, SRIM Software, Retrieved 1 July 2013, from <http://www.srim.org/>.
- [6] W. C. Oliver and G. M. Pharr, *J. Mater. Res.* **7** (1992) 1564.

- [7] S. J. Zinkle and G. S. Was, *Act. Mater.* **61** (2013) 735.
- [8] F. S. James, *J. Nucl. Mater.* **141** (1986) 748.
- [9] L. Marlies and M. Lorenzo, *Acta. Mater.* **59** (2011) 6547.
- [10] H. K. D. H. Bhadeshia, *Mater. Sci. Eng. A* (1997) 64.
- [11] F. A. Garner, M. B. Toloczko, and B. H. Sencer, *J. Nucl. Mater.* **276** (2000) 123.
- [12] E. A. Little, D. A. Stow, *J. Nucl. Mater.* **87** (1979) 25.
- [13] S. Ohnuki, F. A. Garner, and H. Takahashi, *Mater. Trans JIM* **34** (1993), 1031.
- [14] G. S. Was, J. P. Wharry, B. Frisbie, B. D. Wirth, D. Morgan, J. D. Tucker, T. R. Allen, *J. Nucl. Mater.* **411** (2011) 41.
- [15] T. R. Allen, J. T. Busby, J. Gan, E. A. Kenik, and G. S. Was, *ASTM STP* **1366** (2000) 739.
- [16] S. J. Zinkle, P. J. Maziasz, and R. E. Stoller, *J. Nucl. Mater.* **206** (1993) 266.
- [17] G. Gupta, Z. Jiao, A. N. Ham, J. T. Busby, and G. S. Was, *J. Nucl. Mater.* **351** (2006) 162.
- [18] R. E. Clausing, L. Heatherly, R. G. Faulkner, A. F. Rowcliffe, and K. Farrell, *J. Nucl. Mater.* **141** (1986) 978.
- [19] Z. Lu, R. G. Faulkner, N. Sakaguchi, H. Kinoshita, H. Takahashi, and P. E. J. Flewitt, *J. Nucl. Mater.* **351** (2006) 155.
- [20] S. Ohnuki, H. Takahashi, and T. Takeyama, *J. Nucl. Mater.* **103** (1982) 1121.
- [21] H. Takahashi, S. Ohnuki, T. Takeyama, and H. Kayano, *J. Nucl. Mater.* **96** (1981) 233.

7.2 EFFECTS OF ION IRRADIATION ON BAM-11 BULK METALLIC GLASS — A. G. Perez-Bergquist^{1,2}, H. Bei¹, Y. Zhang^{1,2}, and S. J. Zinkle¹ (¹Oak Ridge National Laboratory, ²University of Tennessee)

OBJECTIVE

The goal of this study is to investigate the radiation behavior of the bulk metallic glass BAM-11 and to determine if it is a viable candidate for high-radiation structural applications in fusion applications.

SUMMARY

Preliminary microstructural and nanoindentation examinations have been performed on BAM-11 (Zr-17.9%Cu-14.6%Ni-10%Al-5%Ti) bulk metallic glass (BMG) irradiated with 3 MeV Ni⁺ ions to 0.1 and 1 dpa at room temperature and 200°C. Transmission electron microscopy (TEM) examination indicated the unirradiated and irradiated BMG samples were all fully amorphous with no evidence of nanoscale crystals. The hardness in the ion irradiated region of the BMG samples decreased by nearly 20% after irradiation at room temperature to 0.1 and 1 dpa, and decreased by ~25% and ~10%, respectively after irradiation at 200°C to 0.1 and 1 dpa. The elastic modulus of the irradiated samples decreased by ~10% after irradiation at room temperature to 0.1 and 1 dpa, and increased by ~10% and ~5%, respectively after irradiation at 200°C to 0.1 and 1 dpa. These results suggest that the BAM-11 bulk metallic glass may not have high intrinsic resistance to radiation-induced atomic rearrangements, i.e., the glass may not be in an optimized short-range order configuration for radiation damage stability.

INTRODUCTION

Metallic glasses are of potential interest for structural applications in fusion energy due to their good thermal conductivity, high strength, good ductility, good corrosion resistance, and the potential to be cast into near net shape geometries [1-3]. In addition, metallic glasses may provide unique advantages in terms of radiation resistance due to their lack of crystalline structure. Although particle irradiation can produce point defects and macroscopic changes in amorphous materials in a manner somewhat analogous to what happens in crystalline materials, there is some evidence that the amount of retained displacement damage can be significantly less in amorphous materials [4]. In addition, bulk metallic glasses may possess high helium permeability due to a larger free atomic volume and lack of grain boundaries that can act as helium traps; this would improve resistance to cavity swelling and tritium retention compared to crystalline materials [4]. A key question is whether radiation-induced defects might serve as deep traps for helium in metallic glasses.

Over the past few decades, pronounced advances have been made in metallic glass fabrication that now allows for the creation of high-performance structural glasses in bulk form, thus vastly increasing their usefulness for structural applications [5,6]. However, there is practically no information available on the effects of displacement irradiation on these new metallic glasses (simple glasses such as SiO₂ have historically exhibited poor dimensional stability following exposure to irradiation, with accompanying reductions in strength) [7,8]. In this study, we report the results of an investigation of the effects of ion irradiation on the Zr-based metallic glass BAM-11 (Composition: 52.5%Zr-17.9%Cu-14.6%Ni-10%Al-5%Ti, T_g~390°C) [9].

Preliminary

Preliminary microstructural examination of unirradiated BAM-11 bulk metallic glass was performed on a twin jet-polished BAM-11 specimen. TEM showed a feature-free sample that was revealed by diffraction to be fully amorphous (Figure 1). A baseline electron energy loss spectroscopy (EELS) scan performed via TEM gave a composition of Zr-7Al-3.8Ti-6.9Cu-15Ni with oxygen the only major impurity. This matches fairly well with the expected composition of the BAM-11 alloy [9].

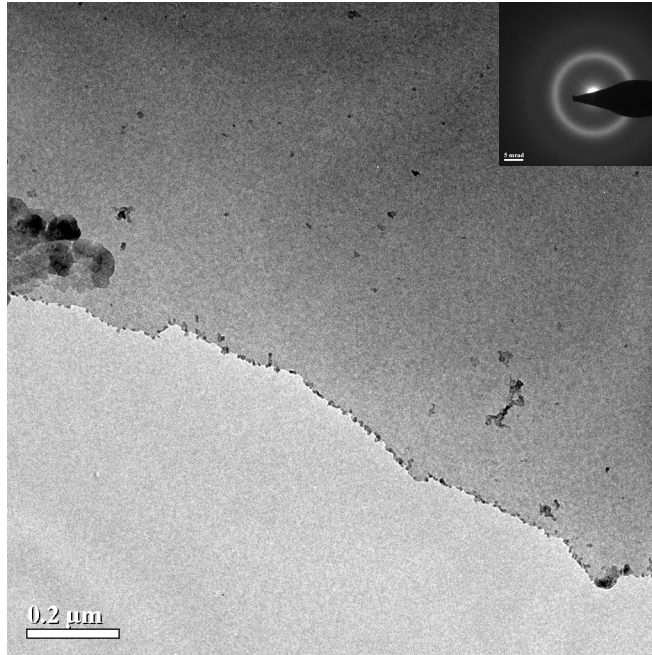


Fig. 1. TEM micrograph of the unirradiated BAM-11 alloy with DP inserted.

Irradiation

Ion irradiation experiments were performed at room temperature on BAM-11 specimens using 3 MeV Ni⁺ ions. Samples were implanted to fluences of 4.2×10^{13} and 4.2×10^{14} ions/cm², or 0.1 and 1.0 dpa, respectively, at both room temperature and elevated temperature (200°C) at the University of Tennessee. Ion range and damage event profiles generated by the SRIM software are shown in Figure 2, using average displacement energy of 40 eV [10]. Additional samples are undergoing neutron irradiation in HFIR to doses of 0.1 dpa at temperatures of 70 and 200°C. Irradiation of the 70°C samples has been completed and post-irradiation examination will be performed in a few months.

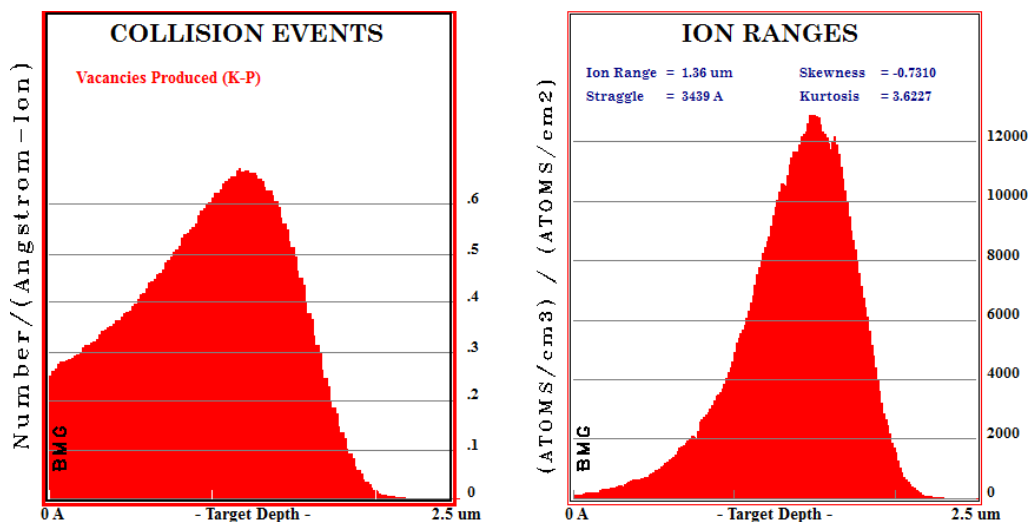


Fig. 2. SRIM plots of the vacancy production and ion range of 3 MeV Ni⁺ ions in BAM-11.

Mechanical Properties

Mechanical properties were examined via microindentation using an MTS XP nanoindenter, with the indentations performed normal to the mechanically polished control and irradiated surfaces. All tests were performed in continuous stiffness measurement mode with a maximum load applied of 150 mN [11]. For statistical purposes, each sample was indented between 18 to 25 times and the average of the results is reported here. Hardness and elastic modulus were measured as a function of depth from the point of contact of the nanoindenter with the surface to a depth of about 1200 nm. Data generated within the first ~100 nm of the surface is unreliable and was thus discarded. The remaining data is shown as a function of indenter depth in Figures 3 and 4.

Considering the ~1 micrometer depth of the implanted ions and damage peaks and the fact that indentation properties are sensitive to substrate regions that are up to ten times the indenter depth [11], the behavior of the samples in the near-surface region is of the greatest interest. Average data is presented for an indenter depth of 200 nm in Table 1, which represents a compromise in depth to minimize surface effects while also minimizing contributions to the data from unirradiated regions.

Hardness and elastic modulus both dropped from the unirradiated condition for the room temperature irradiated conditions. Hardness decreased from about 8.0 GPa to about 6.5 GPa, and modulus decreased from about 111 GPa to about 101 GPa. Hardness and elastic modulus were comparable for both the 0.1 and 1.0 dpa conditions at RT, and collected data sets were very uniform.

In the samples irradiated at 200°C, somewhat dissimilar results were obtained. Both samples at 0.1 and 1.0 dpa showed reduced hardness. The 0.1 dpa sample displayed hardness of about 5.9 GPa while the 1.0 dpa sample showed hardness of about 7.1 GPa. Young's modulus, however, increased in both samples, to 123 GPa and 117 GPa in the 0.1 and 1.0 dpa samples, respectively. It should be noted that the standard deviations of the hardness and Young's

modulus data sets increased sharply for the sample irradiated to 0.1 dpa at 200°C. This particular sample will, after cleaning, be retested due to concerns during testing of the sample's surface cleanliness.

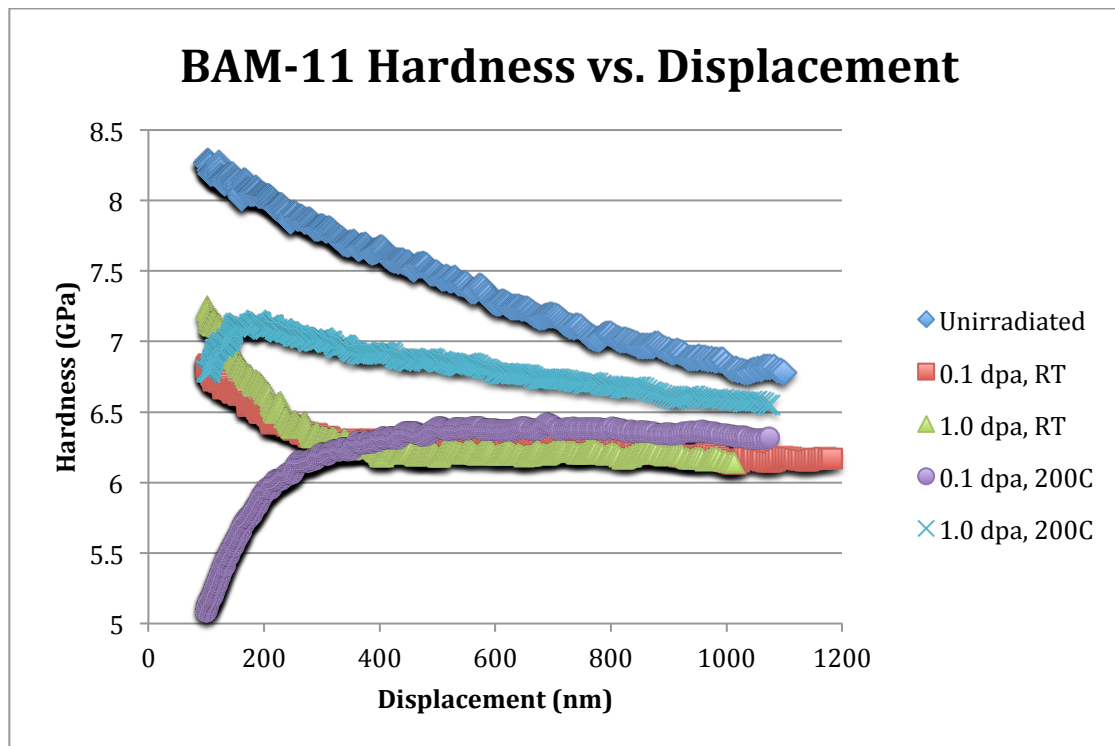


Fig. 3. Hardness as a function of indenter depth in the unirradiated and irradiated BMG specimens.

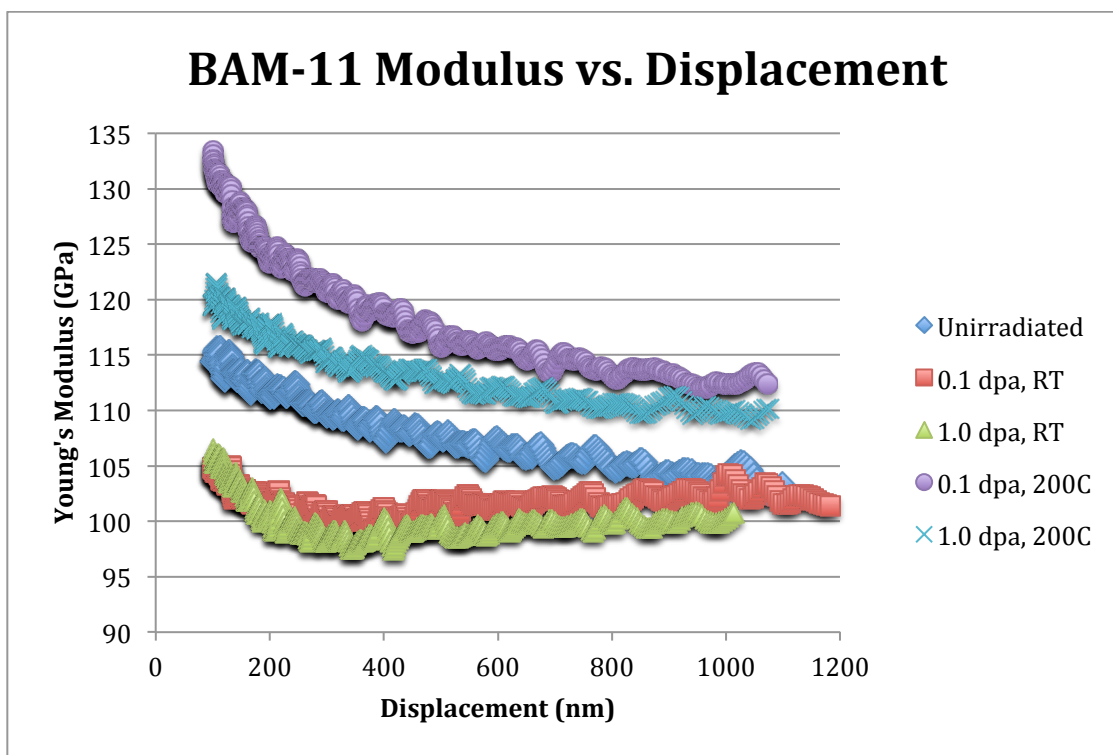


Fig. 4. Elastic modulus as a function of indenter depth in the unirradiated and irradiated BMG specimens.

Overall, however, the reduced hardness and young’s modulus results suggest that the BAM-11 bulk metallic glass may not have high intrinsic resistance to radiation-induced atomic rearrangements, i.e., the glass may not be in an optimized short range order configuration for radiation damage stability.

Table 1. Summary of nanoindentation results on the BAM-11 specimens.

	Un-irradiated	0.1 dpa, RT	1.0 dpa, RT	0.1 dpa, 200°C	1.0 dpa, 200°C
Average Hardness* (GPa)	8.0	6.5	6.6	5.9	7.1
Std. Dev. Of Hardness	0.5	0.4	0.4	0.8	0.4
Average Young's Modulus* (GPa)	111.3	101.1	100.9	123.4	117.8
Std. Dev. Of Young's Modulus	4.1	4.1	4.4	7.3	4.1

* At depth of 200 nm

Microstructure

The BAM-11 samples irradiated at RT to 0.1 and 1.0 dpa did not show any real differences from the unirradiated condition. TEM revealed the samples to be feature-free and diffraction showed the samples to be amorphous. HRTEM confirmed that no crystallites were present in the sample. Additionally, no dislocations were visible upon tilting on two different axes in the TEM.

Similarly, samples irradiated to 0.1 and 1.0 dpa at 200°C also did not show noticeable differences from the unirradiated conditions. Samples were feature-free at differing tilt conditions, revealed amorphous diffraction patterns, and showed no evidence of crystallites in HRTEM mode. Figure 5 shows low-magnification, bright field images of each sample, as well as diffraction patterns and high-resolution phase contrast images of the BMG at each irradiation condition.

Analysis of the fast Fourier transform taken at a magnification of 135,000 times is underway, but should give some insight into the atomic spacing between atoms in the material. Electron energy loss spectroscopy (EELS) is planned to be performed in the TEM and should be able to give additional insight into changes in bonding conditions between the irradiated and unirradiated samples.

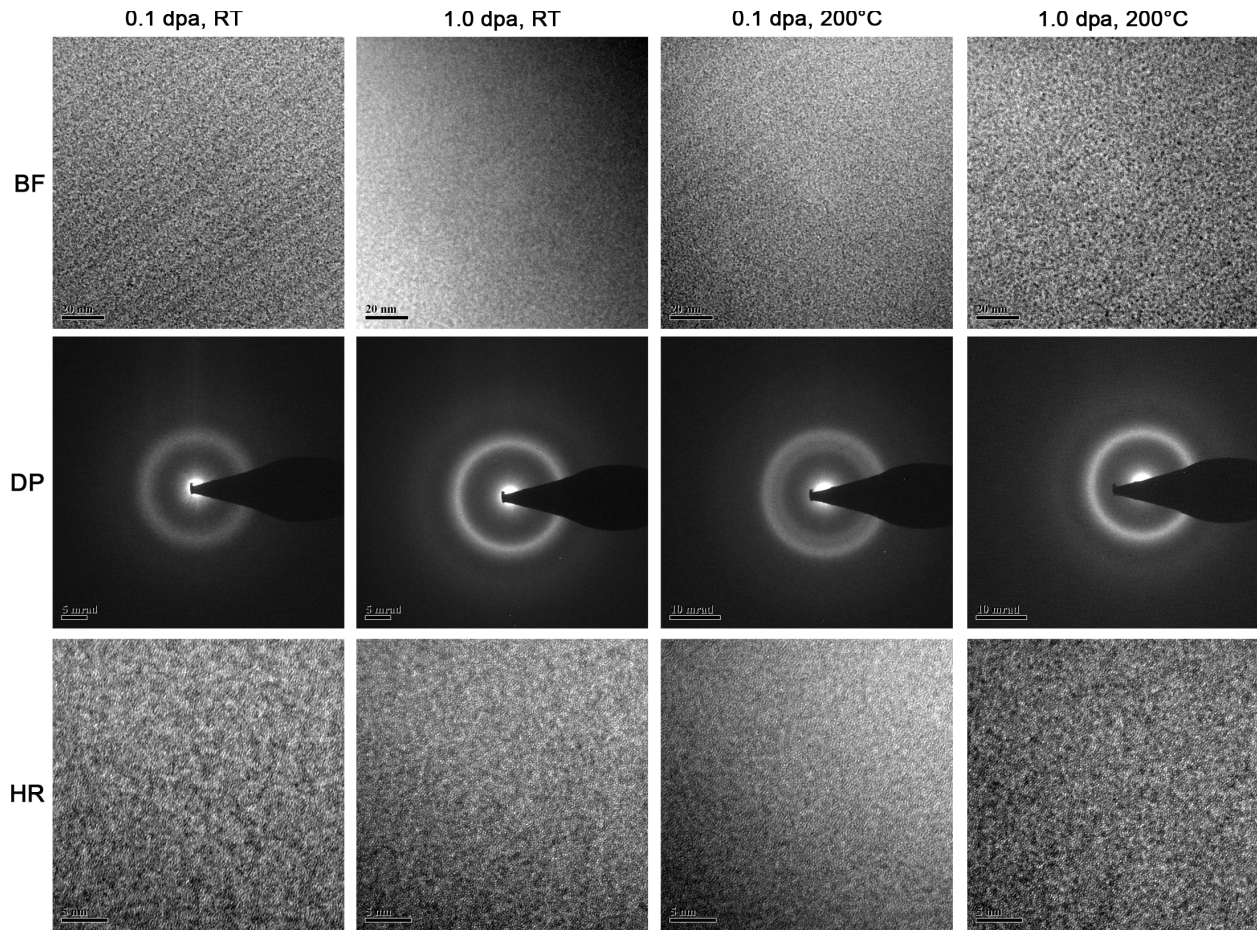


Fig. 5. TEM image showing bright field images at 135kx, diffraction patterns, and high resolution images at 580kx of ion-irradiated BAM-11 irradiated to 0.1 and 1.0 dpa at room temperature and 200°C.

Future Work

Some TEM experimentation and analysis is ongoing (EELS spectroscopy, FFT analysis). Additional mechanical testing and microstructural evaluation will need to be performed on the neutron-irradiated materials once the irradiations are complete and the samples are cool enough to handle. Further discussions will center on the viability of BAM-11 as a radiation-resistant bulk metallic glass based on the current results.

REFERENCES

- [1] R. W. Cahn, *Nature (London)* **341**, 183 (1989).
- [2] P. Chaudhari and D. Turnbull, *Science* **19**, 11 (1978).
- [3] A. L. Greer, *Science* **267**, 1947 (1995).
- [4] W. J. Weber, R. C. Ewing, C. A. Angell, G. W. Arnold, A. N. Cormack, J. M. Delaye, D. L. Griscom, L. W. Hobbs, A. Navrotsky, D. L. Price, A. M. Stoneham, and M. C. Weinberg, *J. Mater. Res.* **12**, 1946 (1997).

- [5] A. Inoue, *Acta Mater.* **48**, 279 (2000).
- [6] W. L. Johnson, *MRS Bulletin* **24**, 42 (1999).
- [7] L. F. Curtiss, *Nature (London)* **120**, 406 (1927).
- [8] E. P. EerNisse, *J. Appl. Phys.* **45**, 167 (1974).
- [9] C. T. Liu, L. Heatherly, D. S. Easton, C. A. Carmichael, J. H. Schneibel, C. H. Chen, J. L. Wright, M. H. Yoo, J. A. Horton, and A. Inoue, *Metall. Mater. Trans. A* **29A**, 1811 (1998).
- [10] James F. Ziegler, SRIM Software, retrieved 1 July 2013, from <http://www.srim.org/>.
- [11] W. C. Oliver and G. M. Pharr, *J. Mater. Res* **7**, 1564 (1992).

7.3 THE EFFECT OF DEPOSITION RATE, MISCUT ANGLE AND ORIENTATION ON Fe-Y₂Ti₂O₇ INTERFACES: IMPLICATIONS TO THE DEVELOPMENT AND OPTIMIZATION OF NANOSTRUCTURED FERRITIC ALLOYS — T. Stan, Y. Wu, and G. R. Odette (University of California, Santa Barbara)

OBJECTIVE

The objective of this work is to better understand and characterize the interfaces between Y-Ti-O nano-features (NF) and the bcc Fe-Cr ferrite matrix in nanostructured ferritic alloys (NFA).

SUMMARY

The smallest 2-3 nm features in nanostructured ferritic alloys (NFA) are Y₂Ti₂O₇ complex oxide cubic pyrochlore phase. The interface between the bcc Fe-Cr ferrite matrix and the fcc Y₂Ti₂O₇ plays a critical role in the stability, strength and damage tolerance of NFA. To complement other characterization studies of the actual nano-features, mesoscopic interfaces were created by electron beam deposition of a thin Fe layer onto {111} and {100} Y₂Ti₂O₇ bulk single crystal surfaces. Cross-section high resolution TEM was used to characterize details of the interfaces, which ranged from being atomically sharp to more diffuse interface zones that, in some cases, included a thin metallic oxide MO_x layer. The fast deposited polycrystalline Fe layer on the 5 degree miscut {111} Y₂Ti₂O₇ sample has the Nishiyama-Wasserman orientation relationship: {110}_{Fe}||{111}_{Y₂Ti₂O₇} and <001>_{Fe}||<110>_{Y₂Ti₂O₇}. Fe grains on the well-oriented {111} Y₂Ti₂O₇ sample have nano-grains at the interface. The grains on the {100} Y₂Ti₂O₇ sample were {110} textured but had no in-plane orientation relationship with the sample. We recognize that the mesoscopic interfaces may differ from those of the embedded NF, but the former will facilitate characterization and investigations of the functionality of controlled interfaces, such as interactions with point defects and helium.

BACKGROUND

Materials in fission and fusion reactor environments are subject to high temperatures, large time-varying stress, chemically reactive environments, and intense radiation fields [1]. Helium that is produced by transmutation reactions interacts with displacement damage to drive complex microstructural evolutions. Most notably, helium is insoluble in steels and precipitates as gas bubbles that act as formation sites for both growing voids and creep cavities, while also embrittling grain boundaries over a wide range of temperatures. NFA have been found to be radiation tolerant since they contain an ultrahigh density of Y-Ti-O nanofeatures (NF) that trap He in harmless [2], fine-scale bubbles, suppressing void swelling and embrittlement. NF also provides high stable sink densities for defect annihilation and high creep strength due to dislocation pinning [2].

Most previous TEM studies have indicated that the NF is complex oxides, primarily fcc cubic pyrochlore Y₂Ti₂O₇. For example, scanning transmission electron microscopy (STEM) energy dispersive X-ray (EDX) measurements on NF extracted from NFA MA957, reported by Sakasegawa et al., indicate that they are non-stoichiometric Y₂Ti₂O₇, with Y/Ti < 1.0 for precipitates in the larger size range from up to 15 nm and Y/Ti ≈ 0.5 for the smallest pyrochlore features [3]. At largest sizes, from ≈ 15 to 35 nm, the oxides are closer to stoichiometric, with

Y/Ti \approx 1.0. Yamashita et al. also found non-stoichiometric $Y_2Ti_2O_7$, but generally with a range of Y/Ti slightly greater than 1 [4,5]. Klimiankou et al. found near stoichiometric $Y_2Ti_2O_7$ in a 9Cr NFA using electron energy loss spectroscopy, HRTEM-fast Fourier transform (FFT) power spectra indexing and energy filtered TEM (EFTEM) methods [6,7]. Early x-ray diffraction (XRD) studies by Okuda and Fujiwara also indicated the presence of $Y_2Ti_2O_7$ in a 14Cr model NFA [8]. This observation has been confirmed by Sasasegawa et al., based on XRD measurements of nanopore filtered oxides extracted from a 9 Cr martensitic alloy [8]. Recently, Yu et al. reported a comprehensive TEM characterization study of NFA MA957 in different conditions, using various techniques [9]. This work clearly showed that extracted NF are structurally consistent with $Y_2Ti_2O_7$ and generally are near stoichiometric with Y/Ti ratios from 0.5 to 1. The dominant in-foil interface was found to be parallel to the {100} planes in Fe, although the oxide themselves could not be indexed. Note this paper also discusses some other recent work in the literature that did not find the pyrochlore $Y_2Ti_2O_7$. Finally, a recent high resolution TEM (HRTEM) study by Cisten et al confirmed that the in-foil NF in the same friction stirred weld variant of MA957 are $Y_2Ti_2O_7$ [10]. The study on the TEAM 0.5 showed that the dominant NF in-foil interface OR is $(100)_{\text{Matrix}}|| (100)_{Y_2Ti_2O_7}$ and $[001]_{\text{matrix}}|| [1-10]_{Y_2Ti_2O_7}$.

The high density of NF traps He in fine bubbles [11] and pin dislocations. The NF is also remarkably thermally stable [12,13]. However, the details of important processes (mechanisms and energies), such as helium trapping, are not well understood. Thus, while they may differ from those for embedded NF, creating a variety of mesoscopic surrogates, with self-selected sets of ORs with bcc Fe, will facilitate developing a general understanding of these metal-oxide interfaces in NFA, especially with respect to their structures and functional properties.

PROGRESS AND STATUS

Experimental Methods

A pure single crystal of $Y_2Ti_2O_7$ was acquired from McMaster University. The crystal was grown using a two-mirror NEC floating zone image furnace. The starting materials for the polycrystalline rods were 99.999% pure Y_2O_3 and 99.995% pure TiO_2 , both from Alfa Aesar. The feed rods were created in the same fashion as Gardner [14]. The final single crystal was grown using the floating zone technique at a speed 5 mm/hr in air [15].

A 1.8 mm thick $Y_2Ti_2O_7$ single crystal wafer was cut to have a {111} oriented surface. A wire saw was used to cut a 2 mm thick {100} oriented $Y_2Ti_2O_7$ wafer. An Allied Multiprep system was used to polish the wafers using a sequence of 15 (for flattening), 9, 6, 3, and 1 μm papers for 10 minutes each at 75 rpm. The final 15 minute polishing step used a 0.02 μm non-crystallizing silica suspension. An electron beam system was used to deposit Fe on the $Y_2Ti_2O_7$ crystals at 7×10^{-6} torr and 800°C. The deposition rate was 2 nm/s for 250 s, producing Fe layer thicknesses of \approx 500 nm. The samples were then slowly cooled to room temperature at a rate of \approx 0.16°C/s.

An XPERT MPD Thin Film Texture XRD was used to obtain gonio scans and pole figures (PFs). A MFP-3D AFM was used to measure the topology of surfaces. A FEI Quanta 400F field-emission environmental scanning electron microscope (SEM) with an electron backscatter diffraction (EBSD) detector was used to obtain the inverse and Euler PFs and maps. A FEI HELIOS Focused Ion Beam (FIB) tool was used to micromachine <30-nm-thick electron transparent lift-outs of the interface Fe- $Y_2Ti_2O_7$ interfaces. Platinum was deposited over the Fe

for protection, and a low energy gallium beam with 2 keV 5.5 pÅ was used as a final sample-cleaning step.

Results and Discussion

Initial Study

Results from Fe depositions onto pyrex glass and onto an $Y_2Ti_2O_7$ single crystal wafer, which was 5 degrees miscut from the $\{111\}$ surface, were previously reported. For these samples, the Fe was deposited at 0.3 nm/sec. Deposits of Fe on a pyrex glass substrate were used to provide a naturally selected Fe grain OR for an amorphous control surface. AFM measurements showed the deposit is characterized by many Fe polycrystals with average grain size of 1 μm and a surface roughness of about 40 nm. XRD scans showed that the grains have a $\{110\}$ out of plane texturing with no in-plane OR.

Figure 1 has been reproduced from Reference [17]. Figure 1(a) shows the EBSD inverse pole figures (PFs) from the miscut $Y_2Ti_2O_7$ substrate. The two PFs in Figure 1(a) show spots that were expected from a good quality single crystal with a $\{111\}$ orientation. Figure 1(b) shows a SEM image of Fe grown on the miscut $\{111\}$ $Y_2Ti_2O_7$ single crystal substrate. The topography of the Fe film is similar to that of the Fe found on the control sample. Some grains coalesced and formed larger islands, while others remained as isolated grains.

The EBSD inverse pole map in Figure 1(c) shows the out-of-plane crystallographic orientation of the Fe grains in Figure 1(b). Each of the Fe crystallographic surface orientations is assigned an individual color, which is shown in the octant at the top right of Figure 1(c). Most Fe grains are either $\{110\}$ oriented (green) or $\{100\}$ oriented (red). A few grains (yellow) have an orientation between $\{100\}$ and $\{110\}$, and a few grains (light blue/purple) have an orientation between $\{110\}$ and $\{111\}$. Overlaying Figures 2(b) and (c) shows that some $\{110\}$ Fe grains and some $\{100\}$ Fe grains remained as isolated islands, while both like and unlike grains frequently coalesced. Figure 1(d) shows the same crystallographic information about the Fe grains as Figure 1(c), but represented as PFs.

The in-plane Fe- $Y_2Ti_2O_7$ ORs are obtained by comparing the spots from each Fe PF in Figure 1(d) to each $Y_2Ti_2O_7$ PF in Figure 1(a). The following Fe to $Y_2Ti_2O_7$ crystallographic ORs are observed:

$$\text{OR1: } \{110\}_{\text{Fe}} \parallel \{111\}_{Y_2Ti_2O_7} \text{ and } \langle 100 \rangle_{\text{Fe}} \parallel \langle 110 \rangle_{Y_2Ti_2O_7}$$

$$\text{OR2: } \{100\}_{\text{Fe}} \parallel \{111\}_{Y_2Ti_2O_7} \text{ and } \langle 100 \rangle_{\text{Fe}} \parallel \langle 110 \rangle_{Y_2Ti_2O_7}$$

Notably, OR1 is the Nishiyama Wasserman (NW) orientation relationship. Figure 1(e) derives from the same EBSD scan as Figures 2(c) and (d), but shows the orientations of the Fe grains represented as an Euler map. The full crystallographic orientation of each grain is assigned a color that is associated with a series of three rotations around three Euler axes. The crystallographic information from the Euler map is also represented in the Euler PFs in Figure 1(f). The colors in the Euler PFs match the grain colors in the Euler map. Figure 1(g) shows that the three in-plane orientations of the $\{110\}$ and $\{100\}$ Fe grains match the threefold symmetry of the $\{111\}$ $Y_2Ti_2O_7$ substrate planes. Sketches of the substrate orientation and of the grain orientations are shown in Figure 1(g). The colors of the grains in Figure 1(g) match

the colors of the grains in the Euler map and in the Euler PFs. In conclusion, most Fe grains were epitaxially grown on the $Y_2Ti_2O_7$ substrate with two ORs.

Effect of Deposition Rate

The effect of Fe deposition rate was studied by first removing the Fe grains from the 5 degree miscut $\{111\}$ $Y_2Ti_2O_7$ sample. This was done by polishing away the grains in the same fashion as described previously. Fe was then deposited at a rate of 2 nm/s, nearly seven times faster than in the initial study. Figure 2(a) shows the EBSD inverse pole figure map from the initial study. Figure 2(b) shows the out of plane orientation of the faster deposited Fe film. The faster deposition clearly shows grains with a dominant $\{110\}$ texturing. The PFs in Figure 2(c) are from the initial study while the PFs in Figure 2(d) are from the faster deposition. Figure 2(d) confirms that there is strong $\{110\}_{Fe}$ texturing. The PFs do not have the red spots as seen in Figure 2(c), thus the $\{100\}$ Fe grains were not present. The $\{110\}$ Fe grains still matched the underlying substrate three-fold symmetry. In conclusion, the faster deposition rate prevented grains with OR2.

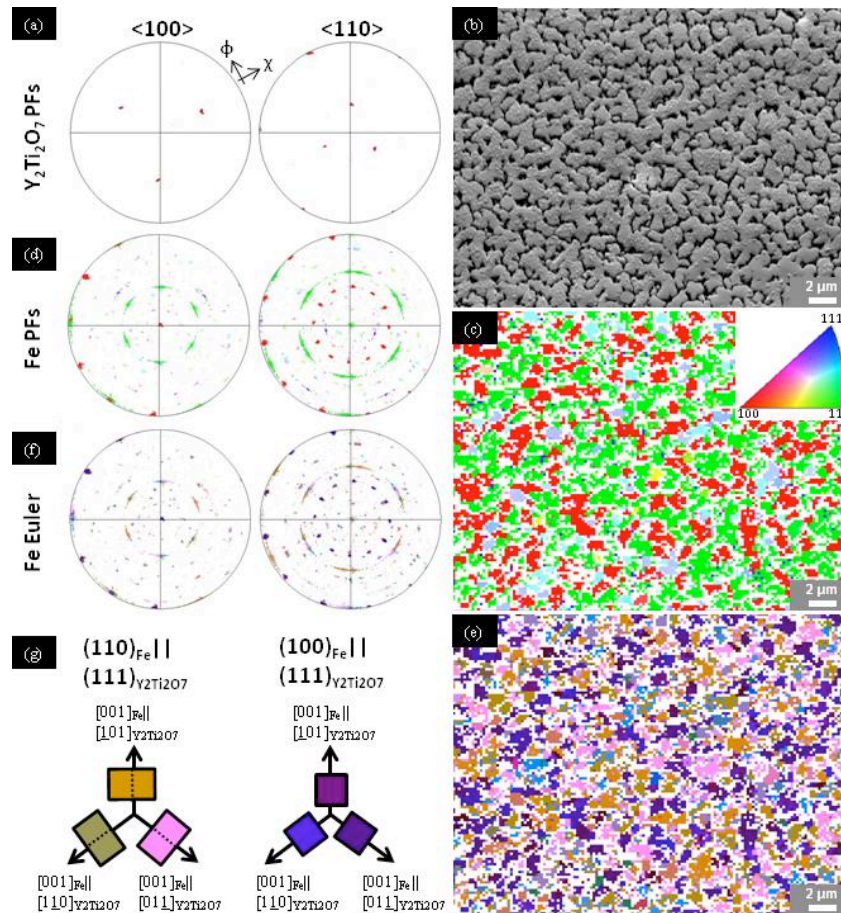


Figure 1. This figure has been reproduced from reference [17]. (a) EBSD PFs of the $Y_2Ti_2O_7$ substrate showing a good quality $\{111\}$ -oriented single crystal. (b) SEM of Fe grains on the $Y_2Ti_2O_7$ single crystal substrate. Some Fe grains coalesced, while some Fe grains remained as single islands. (c) EBSD inverse pole map of the Fe grains on the $Y_2Ti_2O_7$ substrate. The octant in the top right indicates the surface orientations of the Fe grains. (d) PFs of the grains showing reflections from $\{110\}_{Fe}$ in green and $\{100\}_{Fe}$ in red. (e) Euler map showing the full crystallographic orientation of the grains. (f) Euler PFs showing the crystallographic orientation of each grain. (g) Schematic showing how the $\langle 100 \rangle_{Fe}$ directions match the three $\langle 110 \rangle$ directions of the $\{111\}$ substrate. The colors in the schematic match the colors in (f) and (g).

Effect of Miscut Angle

The previous two depositions were done on an $Y_2Ti_2O_7$ wafer, which was 5 degrees miscut from the $\{111\}$ plane. The effect of miscut angle was studied by creating a new $Y_2Ti_2O_7$ substrate with an orientation less than 1 degree off from the $\{111\}$. This was done by using x-ray diffraction to determine the $\{111\}$ planes, cutting a wafer using a diamond wire saw, and polishing the wafer using the same procedure described previously. Fe was deposited using the fast deposition rate of 2 nm/sec. EBSD scans are seen in Figure 3(a) and show that the grains were larger than in the previous studies. The blue, purple, and red areas in Figure 3(a) show tall, pillar-like, grains that have a random OR with the substrate. The PFs in Figure 3(b) show that the grains are $\{110\}_{Fe}$ textured with OR1. The miscut angle did not affect the OR of most of the grains, but did affect the size.

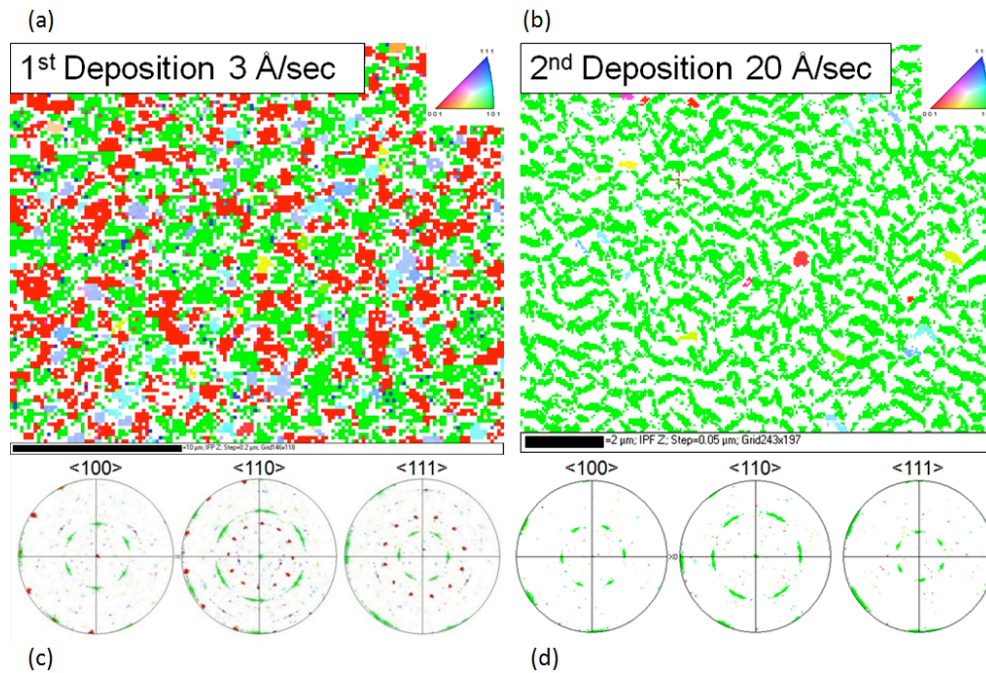


Figure 2. EBSD inverse pole figure maps from the slow deposition (a) and from the fast deposition (b) show that there are more $\{110\}_{\text{Fe}}$ grains in the fast deposition. PFs from the slow deposition (c) and from the fast deposition (d) show that the $\{110\}_{\text{Fe}}$ grains match the underlying three-fold symmetry of the substrate.

Effect of Orientation

A $\{100\}$ $\text{Y}_2\text{Ti}_2\text{O}_7$ single crystal wafer was used to investigate the effect of substrate orientation. Fe was deposited using the fast deposition rate of 2 nm/sec. Figure 4(a) shows the out of plane orientation of the Fe grains. The grains are similar in size as the previous depositions, and are strongly $\{110\}$ textured. The dark rings in the PFs in Figure 4(b) show that the Fe grains do not have an out of plane OR with the substrate. This is identical to the depositions on amorphous pyrex. The $\{100\}$ oriented $\text{Y}_2\text{Ti}_2\text{O}_7$ substrate did not affect the growth of the Fe grains.

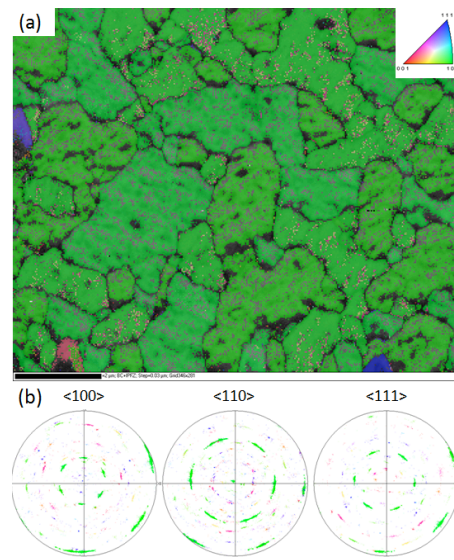


Figure 3. EBSD out of plane orientations of Fe grains are shown in (a). Pole figures in (b) show that the Fe grains are of the OR1 type.

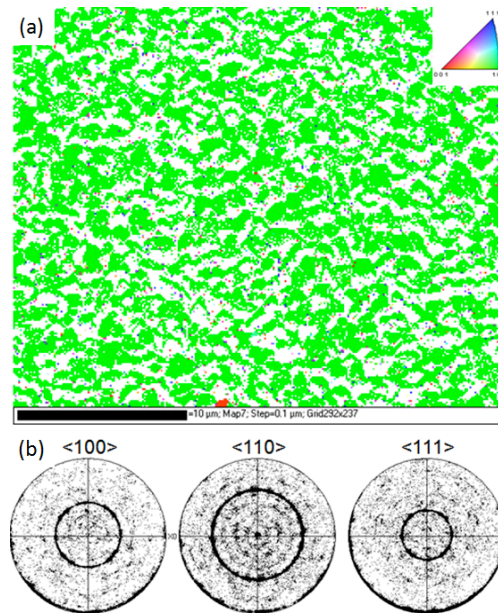


Figure 4. EBSD out of plane orientations of Fe grains are shown in (a). Pole figures show that the Fe grains do not have an out of plane orientation relationship with the {100} $Y_2Ti_2O_7$ substrate.

TEM Characterization of Initial Study

A detailed cross-sectional TEM and HRTEM study was conducted to explore the structure of the Fe- $Y_2Ti_2O_7$ interfaces. Figure 5 has been reproduced from reference [17]. The cross-sectional TEM micrographs in Figures 5(a) and (b) show the island type growth of the Fe on the 5 degree

miscut $Y_2Ti_2O_7$ substrate. Figure 3(c) illustrates the crystallographic orientations of the grains and substrate. There does not seem to be a correlation between a grain's shape and its crystallographic orientation.

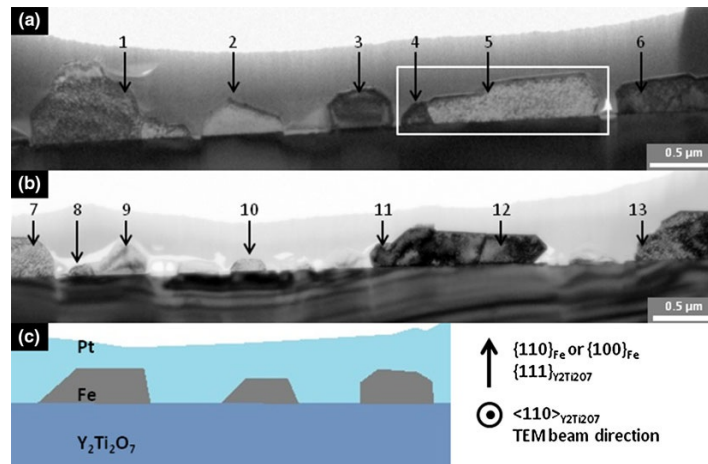


Figure 5. This figure was reproduced from reference [17]. (a), (b) Cross-sectional TEM images of Fe grains on the $\{111\} Y_2Ti_2O_7$ substrate. (c) Sketch of (a) and (b) showing the crystallographic orientation of the grains and substrate.

HRTEM was used to closely examine the interfaces between grains and the substrate. Figure 6 has been reproduced from reference [17]. Figure 6(a) shows the interface structure that is typical of NW OR1 grains. This interface is sharp and flat at the near-atomic scale. The substrate $\{111\} Y_2Ti_2O_7$ planes are visible and marked by red lines in Figure 6(a). The termination of red lines at ledges accommodates the 5 deg surface miscut from $\{111\} Y_2Ti_2O_7$. The light and dark regions about 8 nm apart coincide with the ledges and indicate that there is stress at the interface.

Figure 6(b) shows a HRTEM image of the interface between the substrate and a grain with OR2. There is a 2 to 3-nm-thick transition layer at the interface. The STEM/EDX spectrum in Figure 6(c) shows that the transition layer is rich in Ti, O, and Fe and is consistent with a MO_x metallic oxide. However, the exact composition of the transition layer has not been measured. Figure 7 shows the interface of a Fe grain with no clear OR with the $Y_2Ti_2O_7$ substrate. The interface is atomically rough and incoherent. The 5 nm thick uneven dark areas at the interface is probably also a MO_x transition layer. Grains with no OR generally have thicker MO_x transition layers than grains with OR2.

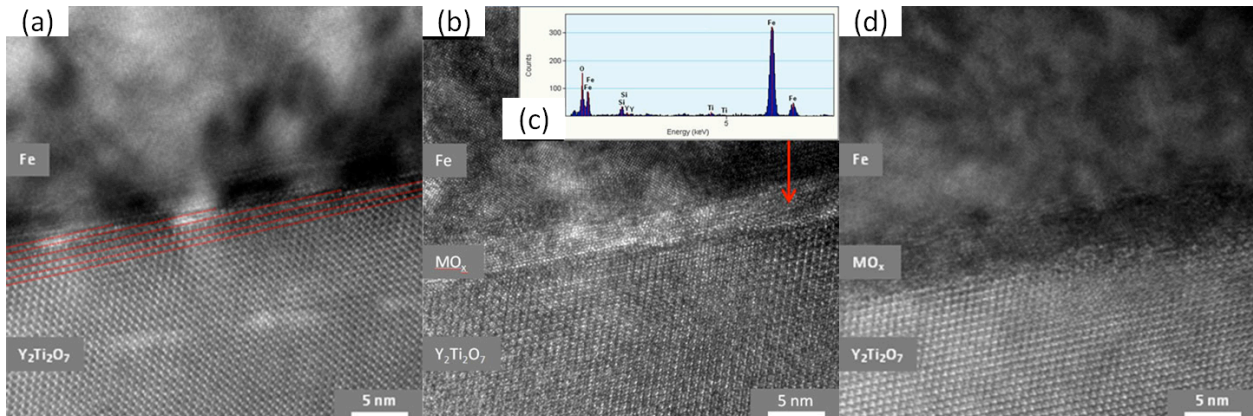


Figure 6. HRTEM image from a grain with the NW OR1. The red lines show $\{111\}$ $Y_2Ti_2O_7$ planes. Dark and light strained areas are seen at substrate ledges. (b) HRTEM image showing the MO_x interfacial transition layer found between a Fe grain and the $Y_2Ti_2O_7$ substrate with the OR2. (c) An EDX spectrum taken from the transition layer in (b). (d) The interface of Fe grains with no OR to the substrate. A thick MO_x transition layer is seen at the Fe- $Y_2Ti_2O_7$ interface.

Effect of Deposition Rate

A TEM scan of the fast deposition on the miscut $\{111\}$ $Y_2Ti_2O_7$ is shown in Figure 7(a). The grains coalesced and did not remain as isolated islands as seen in the slow deposition. Figure 7(b) is an HRTEM scan the Fe- $Y_2Ti_2O_7$ interface for a grain with NW OR1. The red lines show the $\{111\}$ $Y_2Ti_2O_7$ planes and their termination at the interface. Similar to the slow deposition, this interface is characterized by light and dark strained regions, which coincide with the $\{111\}$ plane terminations. A MO_x transition layer is not seen at the interface.

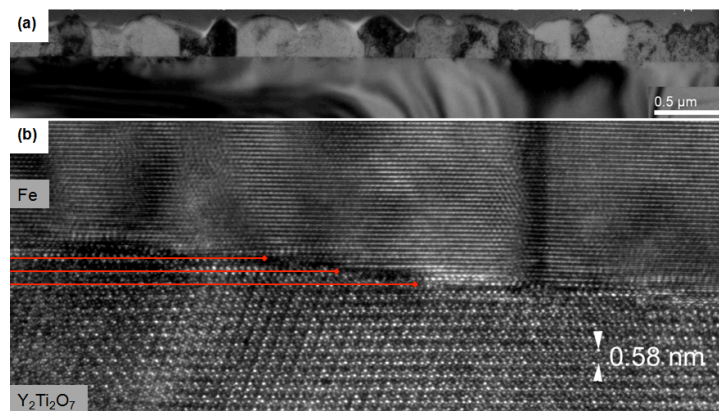


Figure 7. TEM image of Fe grains from the fast deposition rate are shown in (a). HRTEM image of the Fe- $Y_2Ti_2O_7$ interface with OR1 is shown in (b).

Effect of Miscut Angle

Figure 8(a) shows the Fe grains grown on the well oriented $\{111\}$ $Y_2Ti_2O_7$ substrate. The grains coalesced together into one thin film. There are also white pillar-like grains that are taller than the rest of the film. Diffraction patterns from these grains (not shown) indicate that the grains

have no OR with the substrate. Figure 8(b) shows an HRTEM image of the Fe- $Y_2Ti_2O_7$ interface with NW OR1. The interface is clean and sharp, without the alternating dark and light regions seen in the miscut samples. Some grains show a nano Fe grain (up to 6 nm tall and 10 nm wide) that nucleated at the interface, but did not grow. The nano grains have the same NW OR1 as the surrounding larger grain, but are generally slightly rotated in plane (by 1 degree).

Continuing and Future Research

This work is continuing and will be extended to other oxide surface orientations and different deposition conditions will also be explored. TEM was not done on the depositions on $\{100\}$ $Y_2Ti_2O_7$ since the Fe grains had no in-plane OR with the substrate. However, we are trying to obtain the $\{100\}_{Y_2Ti_2O_7} \parallel \{100\}_{Fe}$ and $\langle 110 \rangle_{Y_2Ti_2O_7} \parallel \langle 100 \rangle_{Fe}$ interface by diffusion bonding single crystals of Fe and $Y_2Ti_2O_7$. The $\{100\}$ Fe and $\{100\}$ $Y_2Ti_2O_7$ crystals were cut, polished, and matched together to have the desired OR. Attempts to diffusion bond the crystals at a temperature of 700 degrees C for 10 hours and 10 MPa have so far been unsuccessful. We are still exploring different diffusion bond parameters and conditions. There will also be studies of the interface interactions with irradiation induced defects and helium.

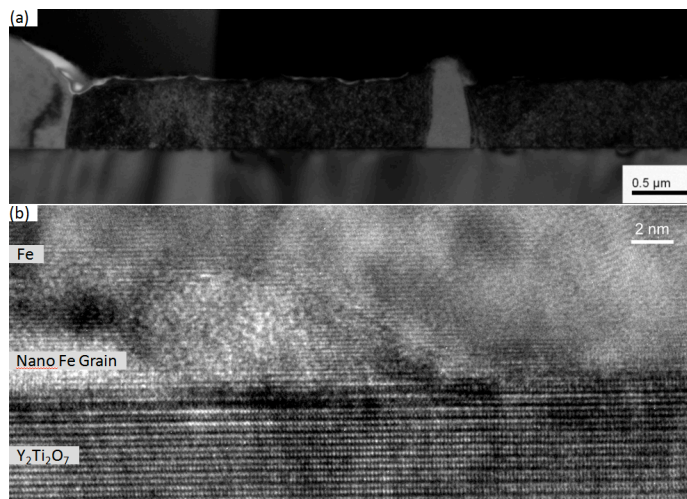


Figure 8. The TEM cross-section image from the Fe- $\{111\}_{Y_2Ti_2O_7}$ interface is seen in (a). The HRTEM image in (b) shows a nano grain, which was sometimes found at the interface.

ACKNOWLEDGEMENTS

The authors thank Erin Haney, Gareth Seward, Mark Cornish, Deryck Stave, Youli Li, and Doug Klingensmith for help with various parts of the research. The work performed at UCSB was supported by the U. S. Department of Energy, Office of Fusion Energy Sciences, under grant DE-FG03-94ER54275.

REFERENCES

- [1] G. R. Odette, M. J. Alinger, and B. D. Wirth, *Annu. Rev. Mater. Res.* **38** (2008) 471.
- [2] Y. Dai, G. R. Odette, and T. Yamamoto, *Comp. Nucl. Mater.* **1** Chap. 6 (2012) 141.
- [3] H. Sakasegawa, L. Chaffron, F. Legendre, et al., *J. Nucl. Mater.* (2009) 384.
- [4] S. Yamashita, S. Ohtsuka, N. Akasaka, et al., *Phil. Mag. Lett.* (2004) 84.
- [5] S. Yamashita, N. Akasaka, and S. Ohnuki, *J. Nucl. Mater.* (2004) 329.
- [6] M. Klimiankou, R. Lindau, and A. Möslang, *J. Nucl. Mater.* (2004) 329.
- [7] M. Klimiankou, R. Lindau, and A. Möslang, *Micron* (2005) 36.
- [8] T. Okuda and M. Fujiwara, *J. Mater. Sci. Lett.* (1995) 14.
- [9] Y. Wu, E. M. Haney, N. J. Cunningham, et al., *Acta Mater.* **60** (2012) 3456.
- [10] J. Ciston, Y. Wu, G. R. Odette, et al., *Fus. Mat. Semiann. Prog. Rep.* (2012) DOE-ER-0313/51.
- [11] G. R. Odette, et al., *J. Nucl. Mat.* (2011).
- [12] S. Y. Zhong, J. Ribis, V. Klosek, et al., *J. Nucl. Mater.* **12** (2012).
- [13] M. J. Alinger, G. R. Odette, and D. T. Hoelzer, *J. Nucl. Mater.* (2004) 382.
- [14] J. S. Gardner, B. D. Gaulin, and D. M. Paul, *J. Cryst. Grow.* **191** (1998) 740.
- [15] M. B. Johnson, H. A. Dabkowska, B. D. Gaulin, et al., *J. Solid State Chem.* **182** (2009) 725.
- [16] A. Hashibon, A. Y. Lozovoi, and P. Gumbsch, *Phys. Rev. B* **77** (2008) 094131.
- [17] T. Stan, Y. Wu, G. R. Odette, et al., *Metal. Mater. Trans. A*, Currently Online Only (2013).

7.4 AN ELECTRON ENERGY LOSS SPECTROSCOPY STUDY OF HELIUM BUBBLES IN NANOSTRUCTURED FERRITIC ALLOYS — Y. Wu, R. G. Odette, T. Yamamoto, (University of California, Santa Barbara); J. Ciston, (Lawrence Berkeley National Laboratory); and P. Hosemann (University of California, Berkeley)

OBJECTIVE

Understanding and predicting the fate of helium that is generated in large quantities within fusion irradiation environments requires experiments and modeling methods to understand the partitioning between various bubble sites.

SUMMARY

Here we compare a measurement of the helium content in bubbles with a model based on the capillary approximation and a high-pressure equation of state. Electron Energy-Loss Spectroscopy (EELS) measurements on bubbles were carried out using the TEAM 0.5 microscope at the National Center for Electron Microscopy and Lawrence Berkeley Laboratory (LBL). The EELS energy shift can be related to the helium atom density. The best estimate of the helium density was $\approx 61 \pm 2.8$ He atoms/nm³ for bubbles with radii of $\approx 1.36 \pm 0.3$ nm. These results are reasonably consistent with a high pressure EOS assuming a simple capillary model and surface energy of 1.8 J/m².

PROGRESS AND STATUS

Introduction

Nanostructured ferritic alloys (NFA) manage helium by trapping it in small bubbles at the interfaces between nano-scale oxide features and the Fe-Cr matrix [1,2]. Thus it is important to know the relation between the bubble size and helium content. Assuming the simple capillary approximation, the gas pressure, p , balances the surface tension as $p = 2g/r$, where g is the surface energy and r is the bubble radius (or radius of curvature). Hence, *very small* high-pressure bubbles can efficiently store helium in a way that prevents its deleterious effects like void nucleation and other manifestations of radiation damage. The pressure, p , is related to the helium atom density, r (here in units of the number of atoms/nm³), by a high-pressure equation of state (EOS). The corresponding number of helium atoms (n_{He}) in a bubble also depends on its morphology and the effects of finite bubble size.

Electron Energy-Loss Spectroscopy (EELS) was carried out using small probe transmission electron microscopy methods (TEM) that can be used to measure the helium density in bubbles [3-5]. There is a blue energy shift for the 1s-2p transition of helium, ΔE , which is related to atom density in the bubbles. Frécharde et al., reported the relationship between r and the blue shift as, $\Delta E = 0.019 r + 1.36$; they also found that all the results in the literature can be fitted by $\Delta E = 0.036 r + 0.39$. Similar relations and theoretical models of the blue energy shift and r are given in [4,5].

The helium bubbles in irradiated NFA are small (typical diameters, $d < 3$ nm) and have a narrow size distribution. The bubble size probed here is about 33% smaller than the smallest previously reported [3].

Experimental Procedure

Dual ion irradiations in the DuET facility at Kyushu University created a population of helium bubbles in NFA MA957 and a developmental 14YWT heat called PM2. Table 1 lists the alloy compositions. Both NFA MA957 and PM2 were irradiated at 650°C. The actual dpa, He and He/dpa vary with ion beam penetration depth into the sample. The areas examined in both alloys were at a depth of $\approx 1.3 \mu\text{m}$ from the surface, corresponding to 118 dpa at a rate of 2.8×10^{-3} dpa/s and 2750 appm He. Lift-out TEM specimens were prepared by using a FEI Helios focused ion beam microscope (FIB). A final lift out cleaning step used a low energy 2 KV, 5.5 pA beams to minimize gallium ion damage. Electron Energy-Loss Spectroscopy (EELS) was carried out on the bubbles using the TEAM 0.5 double aberration corrected TEM at the National Electron Microscopy Center (NCEM) at LBL.

It is difficult to obtain He 1s-2p signals from the bubbles with radius $< 2 \text{ nm}$. However, by using a combination of so-called “spectra image” (SPIM) mode and the “chronospim” approach [3,4], it was possible to increase the signal to noise ratio sufficiently to evaluate ΔE . The chronospim approach involves acquiring, realigning and summing a large number of spectra [3]. We acquired 50-100 spectra from different, but similarly sized ($d < 3 \text{ nm}$) bubbles in the two alloys. The helium 1s-2p peaks were established by Gaussian curve fits that subtracted a fitted plasmon signal from the total EELS spectrum. High angle annular dark field (HAADF), which is superior to bright field through focus imaging for detecting voids, was used to measure the sizes of the bubbles probed.

Table 1. Alloy composition (in wt.%)

Alloy	Cr	Ti	W	Mo	Y	Fe
MA 957	14.0	0.9		0.3	0.25	84.55
PM2	14.0	0.35	3.0		0.30	82.35

Results and Discussion

Figure 1 shows that the helium bubbles are small and quite uniform in size, lying in the range of $d \approx 2\text{-}3 \text{ nm}$. Table 2 compares the bubble size range characterized here to those in previous studies.

As noted above it is difficult to measure the He 1s-2p peak for an individual EELS spectrum, because it overlaps the plasmon peak of the matrix. However, it is possible to realign and sum many peaks as shown in Figure 2 (e.g., the chronospim approach). Figure 2a shows a realigned and summed EELS spectrum with the matrix plasmon signal fitted by a Gaussian curve (red line). Figure 2b shows the helium 1s-2p signals obtained by subtracting the plasmon curve from the total realigned and summed EELS spectrum. The helium signal is also fitted using a Gaussian curve to establish the peak energy. Note the different appearance of the curve in Figure 2a is due to the large number of counts acquired in this case.

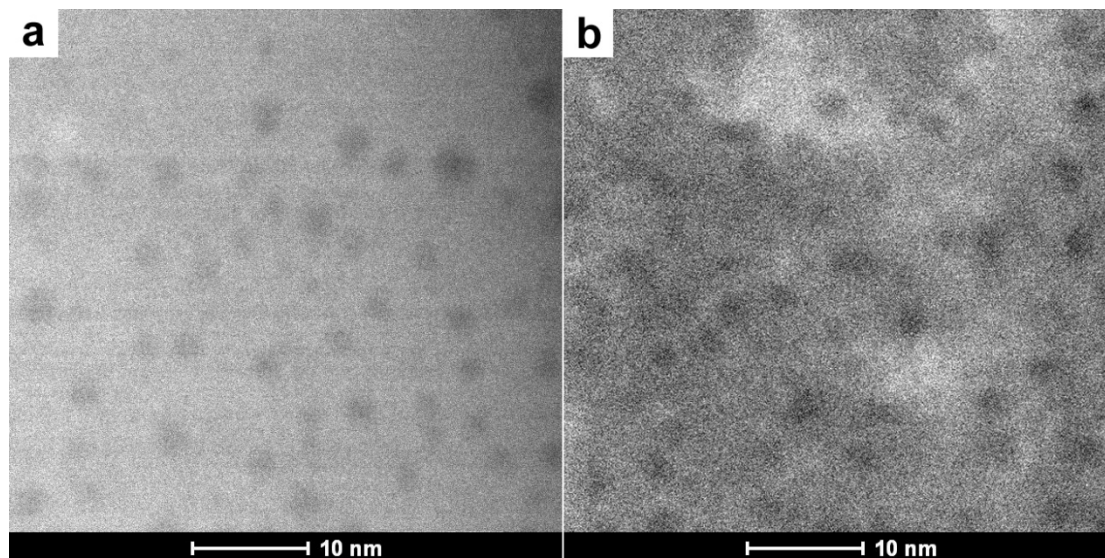


Figure 1. HAADF images of helium bubbles in: a) PM2; and, b) MA957.

Table 2. Comparison of bubble size in the literature measuring He density-using EELS.

	Bubble diameter (nm)
S. Frechard, et al., (Ref. 1)	4-12
D. Taverna, et al., (Ref. 2)	5-24
J. C. Rife, et al., (Ref. 3)	~ 5
This report	< 3

The energy 1s-2p peak energy for a free helium atom is 21.2 eV. The measured $E \approx 23.7$ eV was found for the helium in bubbles in MA957, so $\Delta E = 2.5$ eV. The average radius of the bubbles from which EELS spectra was $\langle r \rangle \approx 1.34$ nm, with r ranging from 1.01 to 1.68 nm. Using the relationship between the energy shift (ΔE) and the helium density ρ as $\Delta E \approx 0.036\rho + 0.39$, yields $\rho = 58.6/\text{nm}^3$. Using $\Delta E = 0.019\rho + 1.36$, yields $\rho \approx 60.0/\text{nm}^3$. The corresponding ΔE for the bubbles in PM2 was 2.6 eV, yielding corresponding $\rho \approx 61.4$ and $65.3/\text{nm}^3$, respectively. The average radius of the bubbles in PM2 was $\langle r \rangle \approx 1.37$ nm, with r ranging from 1.15 to 1.65 nm. The uncertainty of ΔE is estimated to be less than $\approx \pm 0.2$ eV, corresponding to an average maximum variation of ρ of $\approx \pm 11$. The different ρ - ΔE correlations suggest a smaller degree of helium density variability, and the overall average and standard deviation of ρ are $61.3 \pm 2.8/\text{nm}^3$. The average radius of the bubbles from which EELS spectra were obtained was $\langle r \rangle \approx 1.36 \pm 0.3$ nm. This corresponds to a He/vacancy ratio of ≈ 0.72 .

Figure 4 shows the ρ reported in the literature (filled red circles) [3], along the current results, plotted as a function of $1/r$. The Fréchard et al. data is for a 9Cr tempered martensitic steel that was implanted with 5000 appm helium at 550°C. The pseudo error bars show the estimated ranges of ρ and $1/r$ for the bubbles examined in this study. The solid and dashed lines are predictions based on a simple high pressure EOS [6], assuming $p = 2\gamma/r$, using for $\gamma = 1.8$ J/m² for 650 (current study) and 550°C (Fréchard), respectively. The agreement is good for the

current results, but only in more qualitative agreement with the previous measurements on somewhat larger helium bubbles. In this case the capillary EOS model over-predicts and under-predicts the ρ at larger bubble and smaller bubble sizes, respectively. That is the slope of the ρ versus $1/r$ data trend is higher than predicted. In the size range of about $r \approx 2.1 \pm 0.2$ nm, the measured ρ average $\approx 28\%$ higher than the prediction. Extrapolating the model suggests that the He/vacancy ratio approaches 1 at $r < 0.5$ nm.

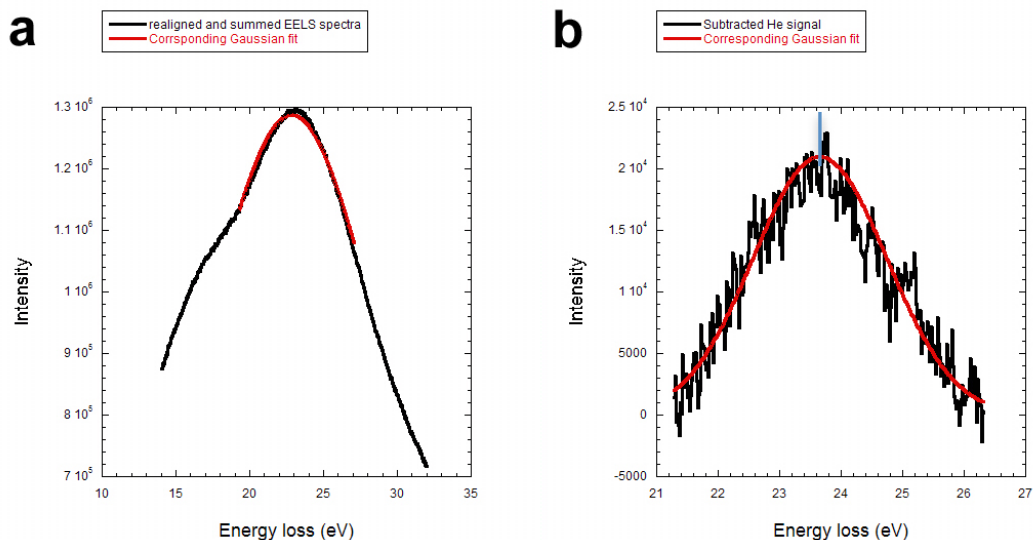


Figure 2. Gaussian fit curves (red) to MA957 EELS spectra data: a) the realigned and summed spectra from many bubbles with similar size and the fit to the plasmon peak; and b) the fitted subtracted helium signal.

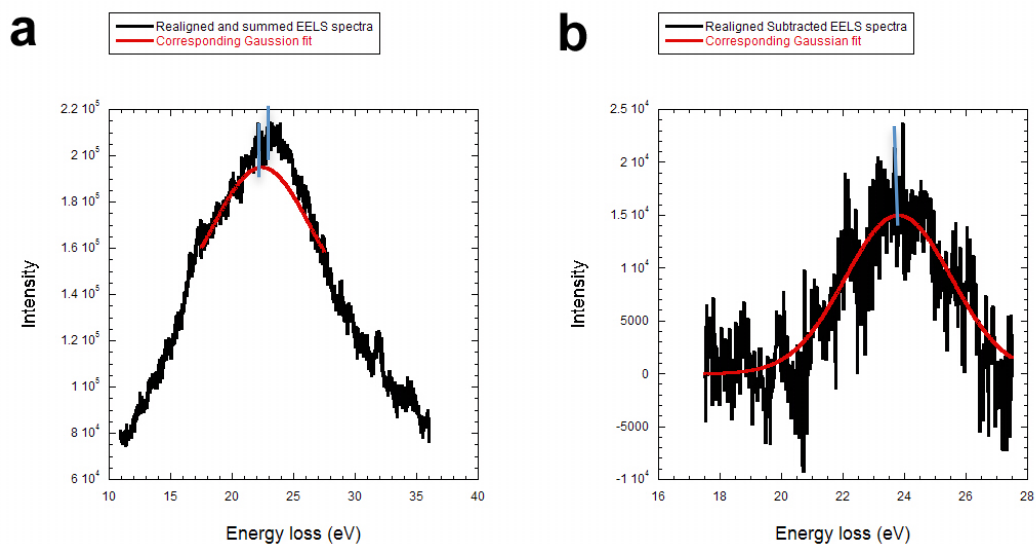


Figure 3. Gaussian fit curves (red) to PM2 EELS spectra data: a) the realigned and summed EELS spectra from many bubbles with similar size and the fit to the plasmon peak; and b) the subtracted helium signal.

More quantitatively, the model predicts $\rho = 57.9 \text{ He/nm}^3$ for $r = 1.36 \text{ nm}$ at 650°C compared to the measured average of 61.3 He/nm^3 . The effect of temperature is modest, with the predicted values of ρ varying from 65.7 He/nm^3 at 300°C to 55.2 He/nm^3 at 800°C . Variations in γ from 1.6 to 2 J/m^2 result in predicted ρ of 55.1 to 60.4 He/nm^3 , respectively.

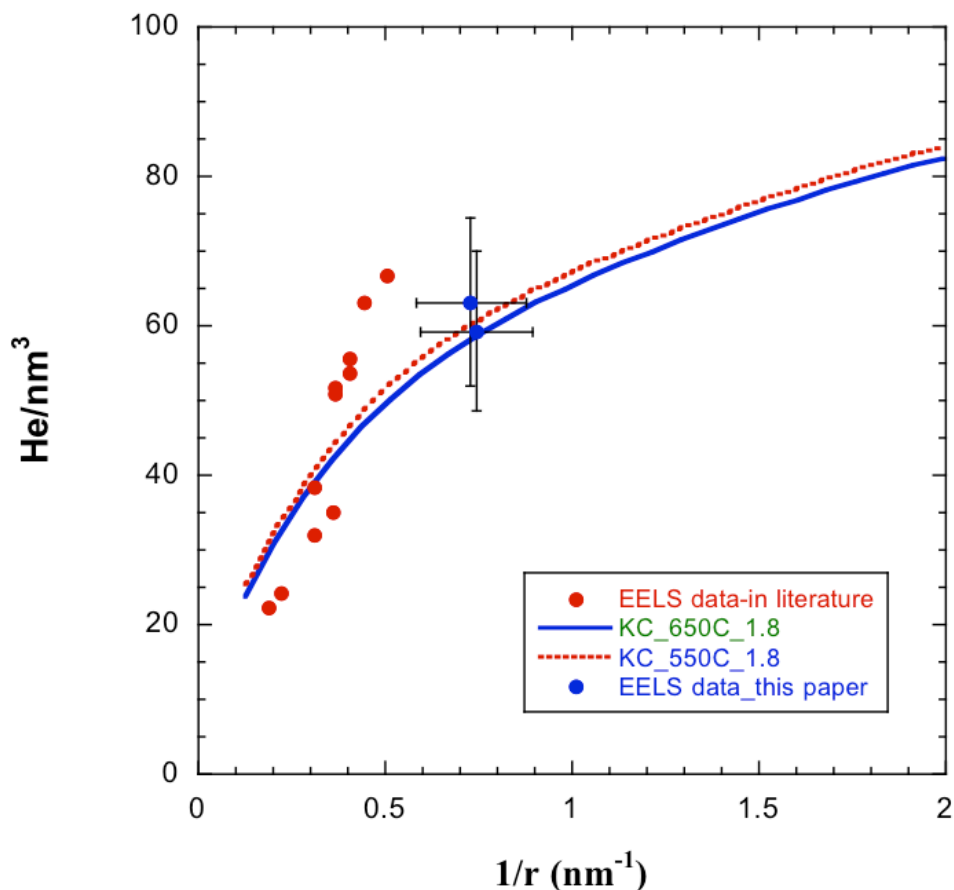


Figure 4. Predicted versus measured helium atom densities as a function of the inverse bubble radius.

DISCUSSION AND FUTURE WORK

The results in this study extend EELS measurements of helium density in bubbles at 650°C down to an average radius of $r \approx 1.36 \pm 0.3$ nm of $r \approx 61.3 \pm 2.8$ He/nm³ are in good agreement with a simple model. The measured r corresponds to helium to vacancy ratio, $\text{He}/V \approx 0.72$ for relative small bubble size. The model under-predicts previously reported r data by about 28% for larger $r = 2 \pm 0.2$ nm bubbles formed during helium implantation at 550°C. In the temperature range from 550 to 650°C, the predicted He/vacancy ratio approaches 1 at $r \approx 0.5$ nm and drops to ≈ 0.24 at $r = 10$ nm.

Through focus series TEM measurements of the helium bubble average size and number density in the implanted regions in this study yielded 2.3 nm and $5.9 \times 10^{23}/\text{m}^3$, respectively. Based on the EELS measurements of ρ , this corresponds to a total amount of helium in spherical bubbles of 2605 appm, in good agreement with the estimate of implanted helium of 2750 appm.

Future work will evaluate other nominally more rigorous equations of state after both Stoller [7] and Caro [8] and co-workers. The objective of quantifying helium partitioning and balances will also be pursued. This will require evaluation of the morphology of bubbles on precipitates and more careful consideration of various sources of experimental and modeling uncertainties.

ACKNOWLEDGEMENT

Electron Microscopy experiments were performed at the National Center for Electron Microscopy, Lawrence Berkeley National Laboratory, which is supported by the DOE BES under Contract # DE-AC02-05CH11231.

REFERENCES

- [1] G. R. Odette, M. J. Alinger, and B. D. Wirth, *Annu. Rev. Mater. Res.* **38** (2008) 471.
- [2] G. R. Odette and D. T. Hoelzer, *JOM* **62** (2010) 84.
- [3] S. Fréchar, M. Walls, M. Kociak, J.P. Chevalier, J. Henry, and D. Gorse, *J. Nucl. Mater.* **393** (2009) 102.
- [4] D. Taverna, M. Kociak, O. Stephan, A. Fabre, E. Finot, B. Decamps, and C. Colliex, *Phys. Rev. Lett.* **100** (2008) 035301.
- [5] J. C. Rife, S. E. Donnelly, A. A. Lucas, J. M. Gilles, and J. J. Ritsko, *Phys. Rev. Lett.* **46** (1981) 1220.
- [6] R. E. Stoller and G. R. Odette, *J. Nucl. Mater.* **131** (1985) 118.
- [7] R. E. Stoller and Y. N. Osetskiy, Fusion Reactor Materials Program, Dec. 31, 2012, DOE/ER-0313/53 (2012) 100.
- [8] A. Caro, J. Hetherly, A. Stukowski, M. Caro, E. Martinez, S. Srivilliputhur, L. Zepeda-Ruiz, and M. Nastasi, *J. Nucl. Mater.* **418** (2011) 261.

8.1 OBJECT KINETIC MONTE CARLO SIMULATIONS OF MICROSTRUCTURE EVOLUTION — G. Nandipati, W. Setyawan, H. L. Heinisch, K. J. Roche, R. J. Kurtz, (Pacific Northwest National Laboratory); and B. D. Wirth (University of Tennessee)

OBJECTIVE

The objective is to report the development of the flexible object kinetic Monte Carlo (OKMC) simulation code **KSOME** (kinetic simulation of microstructure evolution) which can be used to simulate microstructure evolution of complex systems under irradiation. In this report we briefly describe the capabilities of **KSOME** and present preliminary results for short term annealing of single cascades in tungsten at various primary-knock-on atom (PKA) energies and temperatures.

SUMMARY

We have developed a flexible lattice-based object KMC code, **KSOME**, to simulate the evolution of point defects in metals created by particle irradiation. In principle, **KSOME** deals with the migration, emission, creation, transformation and recombination of all types of intrinsic point defects and their complexes. In addition, the interaction of these point defects with sinks such as dislocations, grain boundaries and free surfaces is also treated. **KSOME** is designed such that all the necessary information regarding the properties of defects such as type, size, location, orientation etc., and their diffusion-reaction processes, along with simulation parameters regarding the size, temperature and properties of the simulation cell, are provided via text-based input files. This gives **KSOME** the capability to simulate complex systems involving complex processes that have not been possible with previously developed OKMC codes.

PROGRESS AND STATUS

Description of **KSOME**

KSOME is a flexible and computationally efficient OKMC code written using object-oriented methodologies in C++ to simulate long-time scale evolution of microstructure under irradiation. Patterned after the original FORTRAN code ALSOME [1], **KSOME** is significantly more sophisticated, faster and flexible. Accordingly, in **KSOME** objects of interest are vacancies, self-interstitial atoms (SIA), interstitial impurities and their respective clusters, produced during irradiation. Depending on various properties of these defects, the events these objects can perform are diffusion, dissolution (emission of defects from a cluster) and transformation of defect conformation and diffusion types. The probabilities for these events are calculated in terms of Arrhenius frequencies for thermally activated events, $G_i = n_i \exp(-E_i/k_B T)$, where n_i is the attempt frequency (prefactor) for an event (process) i , E_i is the corresponding activation energy, k_B is Boltzmann's constant and T is the absolute temperature. The interaction between objects is treated as a non-activated or spontaneous event. **KSOME** is based on a rejection-free kMC algorithm also known as the BKL method [1]. The simulation proceeds by the random selection of an event from all possible events, weighted by its rate. The simulation clock is incremented by the time drawn from an exponential distribution. The efficiency of our simulations is improved by using a binary tree algorithm [2, 3] combined with lists.

KSOME keeps track of the locations of lattice defects, impurities and their clusters as a function of simulated elapsed time. Defects and impurities are treated as objects characterized by their

type, size, shape, position, and orientation. These defects (more precisely their centers of mass) are each associated with a specific lattice site, and they migrate by hopping from one lattice site to another in specific crystallographic directions corresponding to the lattice type. If a defect is within the interaction range of another defect, that interaction is performed, and the lists of defects are updated. The present version of *KSOME* can deal with cubic, fcc and bcc lattice types. In addition, *KSOME* allows for user-defined non-crystallographic diffusion directions to be included in the input script file. The present version of *KSOME* has no limit on the size of the simulation cell or the number of type of objects that can be included into the simulation. However, the memory consumption and speed of *KSOME* depends on the number of defects in the simulation cell as well as the size of the diffusion-reaction event databases, which are read at the start of a simulation.

Since *KSOME* simulates microstructure evolution under irradiation, the starting point for these simulations is the primary damage state, i.e., (x,y,z) locations of all defects along with their properties such as type, size and other available properties, obtained from molecular dynamic (MD) simulations of displacement cascades. With *KSOME*, apart from standard properties such as defect type and size we can assign additional properties to a defect if such information is available in the form of parameters. For example, one can differentiate between glissile and sessile SIA clusters or between a vacancy loop and a spherical void. Information about a primary damage state is provided to *KSOME* via a text-based input file; as such, defect information from other simulation tools can also be given as input for these simulations.

Depending on their properties, defects and defect clusters can diffuse randomly in 1-, 2- or 3-dimensions depending on their nature. If an object is a cluster it can also emit one or more defects. *KSOME* allows emission of multiple defects of the same type or different types if the cluster is a “complex”. For example, a vacancy, a SIA or an interstitial impurity atom (IIA) can emit single, or multiple entities of the same object while V+IIA or SIA+IIA can emit basic entities or complexes. We note that emission events can also include loop punching or trap mutation events as well. In addition to a migration and an emission event, another possible event is a transformation event. For example a transformation event includes an activated event like rotation or change of direction of 1D diffusing SIA clusters, or a vacancy loop transforming into a spherical void, or transformation from a glissile to a sessile loop. All thermally activated events a defect or an object can perform are user-defined in an activated-event database.

When two defects come within a given interaction distance, their interaction is modeled as a non-thermally activated event called a “reaction event”. The most common reaction events are the annihilation of a defect after encountering a defect of opposite nature (e.g., a SIA encountering a vacancy), and aggregation by adding a point defect to a cluster. All reaction events are considered diffusion limited, and there is no barrier for a reaction between two defects. Reaction events are considered as spontaneous events and therefore do not contribute to the progression of time. Since the defects are described as point objects, these events are identified on the basis of geometrical considerations (overlap of reaction volumes), and they take place spontaneously whenever two defects come closer than a reaction distance, which is equal to the sum of the capture radii associated with each of the two objects. The capture radius depends on the size and properties of a defect. At each KMC step all possible reaction events in the system are performed before the next KMC step is performed. Possible reaction events and capture radii are user-defined, and they are read from two separate input files at the beginning of a simulation. A reaction event database has a set of rules on how two defects should interact; while the capture radius database stores the sum of capture radii depending on the properties of interacting defects. In *KSOME* defects are considered as spherical objects, and their interactions with other defects are isotropic.

The fact that the possible diffusion-reaction events and capture radii are read from a text-based file at the beginning of a simulation and are not hardwired into the code allows a user to define any type of system. For example, for a *SIA-V-H-He* system it allows inclusion of intrinsic defects (vacancies (V) and self-interstitials (SIA)), He-V, H-V, H-He-V, He-SIA, H-SIA, H-He-SIA and H-He complexes as well as their interactions via reaction events. One new feature of *KSOME* that may not exist in previous or existing codes is its ability to recognize if no information about an active defect is available in the activated-event or in reaction or capture radius databases. For example, at any point during a simulation if no information on the activated event is in the database for a defect, the simulation stops after saving the simulation data (defect information). It is important to note that the user provides the information about activated events as an input; the code itself cannot predict them. It only informs the user that the required information does not exist in the database. *KSOME* is also structured such that additional modification to extend its capability and testing can be done relatively easily.

The basic *KSOME* code has been completed and it has been tested using data for 1MeV Kr⁺ ion irradiation at 80 °C on a 36 nm molybdenum film 4. Fig. [1]1 compares the results from *KSOME* with cluster dynamics calculations of the areal defect density as a function of ion dose.

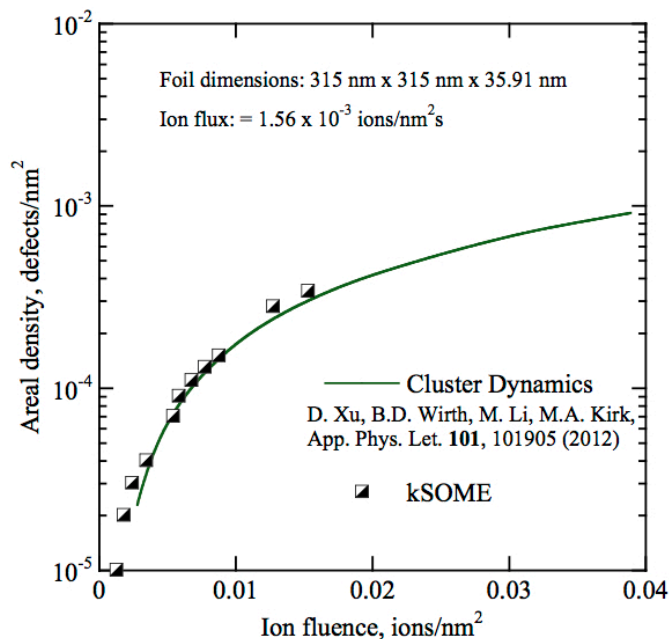


Figure 1. Comparison of cluster dynamics and *KSOME* calculations of the areal defect density dose dependence in a 36 nm molybdenum foil irradiated with 1 MeV Kr ions.

Short term annealing simulations of single cascades in Tungsten

Input data to KMC

A simulation was performed on a cubic block of tungsten atoms of size 162 nm³ with each axis parallel to a <100> direction of the crystal. Each atom hops to a nearest neighbor site at $a/2(111)$. Initial defect distributions of SIA and vacancy defects obtained from MD cascade

damage simulations were placed in the center of the box. Absorbing boundary conditions were adopted in all three directions.

The values of activation energies and pre-factors for diffusion and binding energies of defects used in our annealing simulations are taken from the *ab initio* calculations of Becquart *et al.* [5]. In the present model SIAs of all sizes were constrained to diffuse in 1-D along one of the <111> directions, and only single SIAs were allowed to rotate from one <111> direction to another with an activation barrier of 0.38 eV. Since MD does not provide information on the orientation of SIA diffusion, directions were assigned randomly to SIAs at the start of a simulation. All interstitial clusters are considered to be glissile (mobile), and their migration/diffusion rates decrease with increasing size. For a single vacancy, the activation barrier for diffusion is taken as 1.66 eV, and vacancy clusters larger than a dimer were assumed to be inactive i.e., they neither diffuse nor emit -- although they interact with other defects if they are within the range of interaction. The vacancy (SIA) dissociation rate is given by $G_d = n_d \exp(-(E_m + E_d)/k_B T)$, where E_d is the binding energy of a vacancy (SIA) to a vacancy (SIA) cluster, and E_m is the migration energy of a single vacancy (SIA).

RESULTS

Short-term annealing simulations using KSOME have been used to follow the evolution of cascade damage at an atomic scale beyond MD time scales. For PKA energies ranging from 1keV to 100keV, cascade annealing simulation results were averaged over a set of 20 cascades for larger PKAs (40-100 keV) and 15 cascades for smaller PKAs, generated using MD. Annealing simulations were carried out at temperatures of 300, 1025, and 2050 K for 10 ns. Figure [2] shows total number of defects (SIA + vacancies) in the simulation box initially and after 10 ns of simulation time.

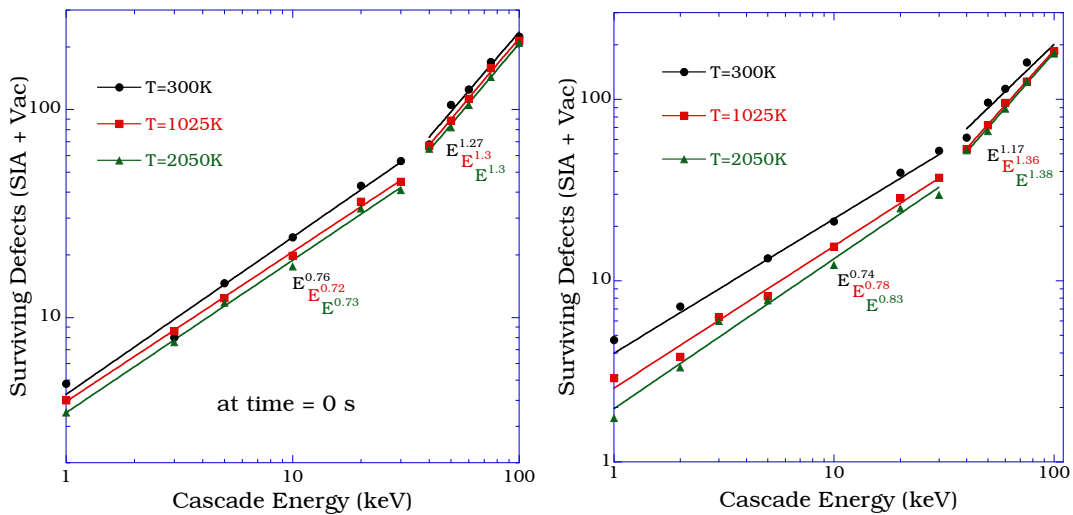


Figure 2. Surviving defects in tungsten before (left) and after (right) annealing for 10 ns.

It can be seen from Fig. [2] that the exponents did not change significantly after 10 ns of annealing. The characteristic slopes shown in Figure [2] are presumably related to different cascade morphologies as a function of PKA energy. The diffusion mechanism of the SIAs has a strong effect on the free interstitial fraction of stable defects. While none of the vacancies left the box due to 1D diffusion, most SIAs escape the cascade region, and they are either near the boundaries of the simulation box or have escaped the simulation box. Any loss in the number of vacancies after 10ns is entirely due to recombination. We find (not shown here) that the amount of recombination after 10ns of annealing depends on the temperature at which the cascade was generated and the PKA energy.

FUTURE WORK

Current knowledge of the diffusion mechanisms of SIA clusters in tungsten comes from MD, and the SIA migration and its activation energy remain a debated question, the sensitivity and effects of which can be studied further with parameter variations in *KSOME* simulations. Moreover due to the uncertainty in the diffusion mechanism of mid-size interstitial clusters, additional simulations will be carried out to illustrate the effects of rotation.

REFERENCES

- [1] H. L. Heinisch, *J. Nucl. Mater.* **117** (1983) 46.
- [2] A. B. Bortz, M. H. Kalos and L. Lebowitz, *J. Comp. Phys.* **17** (1975) 10.
- [3] L. J. Blue, I. Beichl and F. Sullivan, *Phys. Rev. E* **51** (1995) R867.
- [4] G. Nandipati et al., *J. Phys.: Condens. Matter* **21** (2009) 084214.
- [5] D. Xu et al., *App. Phys. Lett.* **101** (2012) 101905.
- [6] C. S. Becquart et al., *J. Nucl. Mater.* **403** (2010) 75.

8.2 Molecular Dynamics Modeling of Atomic Displacement Cascades in 3C-SiC —
 G. D. Samolyuk, Y. N. Osetskiy, and R. E. Stoller (Oak Ridge National Laboratory)

OBJECTIVE

The objective of this research is to investigate the damage induced in 3C-SiC under fusion irradiation conditions and describe the microscopic origin of the experimentally observed phenomena.

SUMMARY

A set of atomic displacement cascades was simulated using the Tersoff and Gao-Weber [1] interatomic potentials for SiC. The types of created defects and their dynamics were analyzed. The validity of existing interatomic potentials was investigated by comparing typical point defect formation energies with first principles results.

PROGRESS

The purpose of this work is to develop a basic understanding of defect formation and evolution SiC. The most popular interatomic potentials used for SiC are the Tersoff and modified embedded atom (MEAM). We have previously shown that these potentials significantly overestimate the vacancy-interstitial recombination barrier. In order to demonstrate an importance of right recombination barrier value to correct description of defects recombination we are planning to simulate cascades with Gao-Weber (GW) potential.

Table 1. The formation energies (in eV) of interstitials (dumbbells $C^+-C<100>$, $C^+-Si<100>$, $Si^+-C<100>$, $Si^+-Si<100>$ and tetrahedral interstitials C_{TC} ...), antisite defects (C_{Si} , Si_C) and vacancies ($C(V)$, $Si(V)$), together with those calculated by *ab initio* methods.

Defects	<i>ab initio</i>	GW[1]	Current report
$C^+-C<100>$	3.16	3.04	3.05
$C^+-Si<100>$	3.59	3.43	3.44
$Si^+-C<100>$	10.05	7.54	7.75
$Si^+-Si<100>$	9.32	5.53	5.51
C_{TC}	6.41	4.65	4.66
C_{TS}	5.84	4.32	4.33
Si_{TC}	6.17	3.97	3.98
Si_{TS}	8.71	6.77	6.79
C_{Si}	1.32	1.69	1.69
Si_C	7.20	7.79	7.94
$C(V)$	5.48	2.76	2.77
$Si(V)$	6.64	3.30	3.30

The GW potential code was introduced into the LAMMPS molecular dynamics (MD) package. The good agreement between MD and first-principles calculated formation energies of twelve most typical defects were demonstrated (Table 1). To improve the weak repulsive of part of the GW potential at short distances, we joined the GW with the well-established Ziegler, Biersack and Littmark (ZBL) potential at 0.95 Å (see Fig. 1).

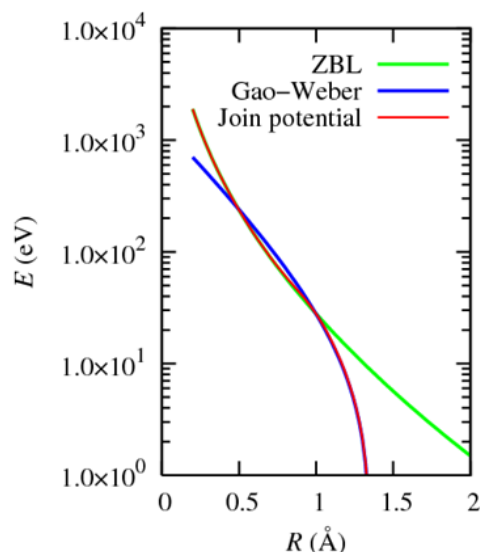


Figure 1. Repulsive Si-C atoms interaction. The GW potential is shown by blue color, the ZBL by green color and the resulting join potential is shown by red color line.

Simulations with 10 keV Si primary knockon atoms have been executed. The simulation cell contains from 80x80x80 unit cells (409600 atoms). Point defects in SiC consist of interstitials (I) and vacancies (V) of both carbon and silicon, as well as antisite defects of C on an Si site (C_{Si}) and Si on a C site (Si_C). The carbon defects predominate as shown by the green and purple symbols in Fig. 1. This result is qualitatively similar to that obtained with Tersoff potential (Fig. 1b). However, in contrast to the simulations with the Tersoff potential, the GW potential (Fig. 1b) produces almost twice as many C vacancies and interstitials at the time of maximum disorder (~ 0.2 ps) but only about 25% more stable defects at the end of the simulation. As a result the ratio of peak-to-stable defects is much higher for the GW potential. This result is more similar to that observed in metals and oxides. Only about 20% of the carbon defects produced with the Tersoff potential recombine during the in-cascade annealing phase, while about 50% recombine with the GW potential. As discussed in our earlier reports, the energy barrier for carbon V-I recombination with the GW potential is much smaller than with the Tersoff potential barrier, and is closer to result of first-principles calculation. On the basis of these result we can conclude that GW potential gives a much more realistic description of cascade dynamics in SiC and we will use this potential in our continuing work.

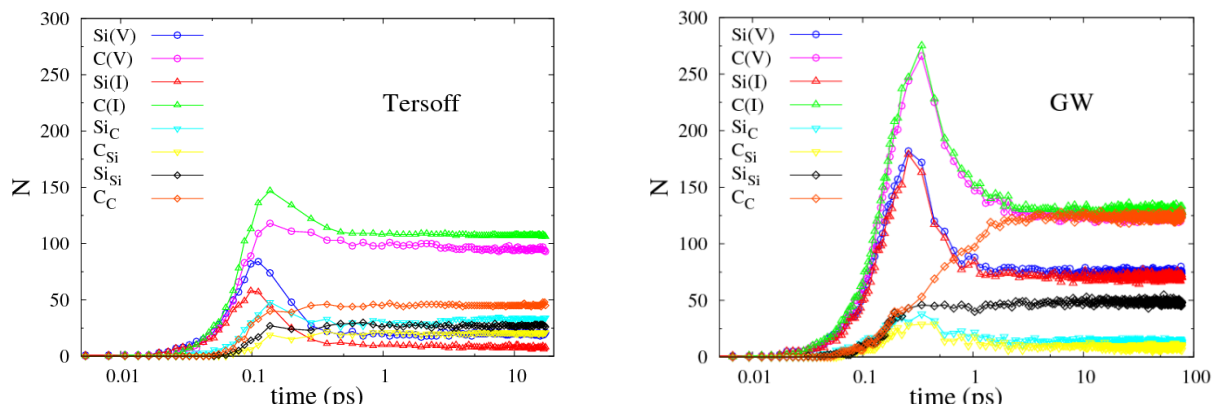


Figure 2. Time dependence of the number of point defects observed in MD displacement cascade simulations 10 keV pka at 300 K: (a) Tersoff potential, (b) GW potential.

The results for cluster size distribution at the end of simulation for both potential are presented in Fig. 3. In our analysis we defined group of point defects as a linked cluster if any of them are connected by the distance less than lattice parameter. Both simulations produce a significant amount of pair clusters and ~ 75 % of these clusters correspond to the same atom type I-V pair. However if in the case of Tersoff potential all I-V pair clusters correspond to carbon atoms, in the case of GW potential the significant part of these clusters corresponds to silicon. Another difference is corresponds to large size clusters distribution. Thus the in the case of Tersoff potential (Fig. 3a) there are only two relatively large clusters containing 19 and 21 defects, in the case of GW potential there are four clusters of size 21, 30, 35 and 51 defects. These large size clusters could be discussed as a potential candidate for amorphisation region. One of these clusters containing 51 defects is presented in Fig. 4. The carbon defects predominate as shown by the green and purple symbols in Fig. 4. The fill analysis of the clusters structure is in progress.

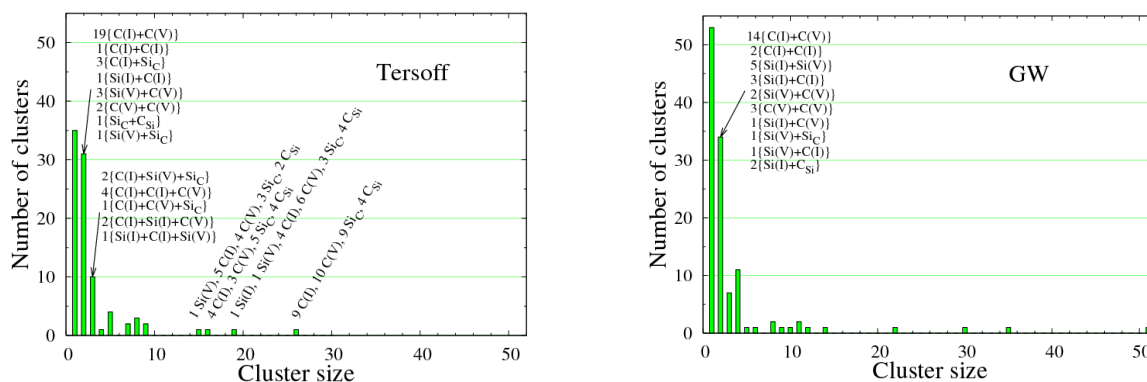


Figure 3. Cluster size distribution at the end of 10 keV Si recoil event in SiC at 300 K: (a) Tersoff potential, (b) GW potential.

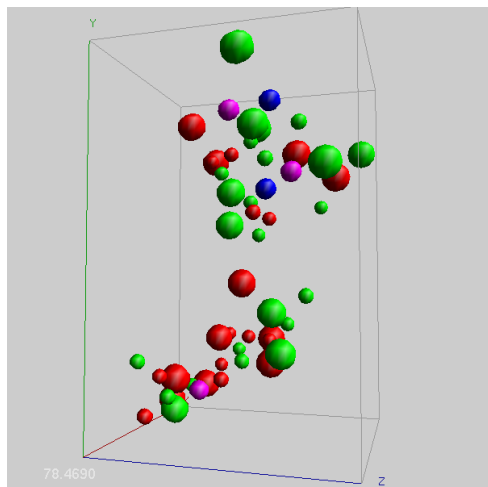


Figure 4. Carbon (green) and silicon (red) interstitials (large spheres) and vacancies (small spheres) at the end of 10 keV Si recoil event in SiC. Blue and purple spheres correspond to Si_C and C_Si antisites, respectively.

FUTURE WORK

During the next reporting period we are planning to increase the statistics on the simulations of the cascades in SiC with GW potential at different temperatures and pka energies in order to further assess the impact of the recombination barrier on stable defect formation. This will provide further insight that can be used to correct the current generation of interatomic potentials for SiC.

LITERATURE

[1] F. Gao and W. J. Weber. *J. Nucl. Instrum. Methods Phys. Res. B* **191** (2002) 504-508.

8.3 FIRST-PRINCIPLES CALCULATIONS OF INTRINSIC DEFECTS AND Mg TRANSMUTANTS IN 3C-SiC — S. Y. Hu, W. Setyawan, R. M. Van Ginhoven, W. Jiang, C. H. Henager, Jr., and R. J. Kurtz (Pacific Northwest National Laboratory)

This is an extended abstract for a paper submitted for publication in the *Journal of Nuclear Materials* [1].

Silicon carbide (SiC) possesses many desirable attributes for applications in high-temperature and neutron radiation environments. These attributes include excellent dimensional and thermodynamic stability, low activation, high strength, and high thermal conductivity. Therefore, SiC based materials draw broad attention as structural materials for the first wall (FW) and blanket in fusion power plants. Under the severe high-energy neutron environment of D-T fusion systems, SiC suffers significant transmutation resulting in both gaseous and metallic transmuted products. Recent calculations by Sawan, *et al.* [2] predict that at a fast neutron dose of ~ 100 dpa, there will be about 0.5 at% Mg generated in SiC through nuclear transmutation. Other transmutation products, including 0.15 at% Al, 0.2 at% Be and 2.2 at% He, also emerge. Formation and migration energies of point defects in 3C-SiC have been widely investigated using density functional theory (DFT). However, the properties of defects associated with transmuted products are currently not well understood. Fundamental understanding of where the transmutation products go and how they affect microstructure evolution of SiC composites will help to predict property evolution and performance of SiC-based materials in fusion reactors.

In this work, the Vienna Ab-initio Simulation Package (VASP) is used to calculate the formation energies of different defects in 3C-SiC-Mg. The convergence and accuracy in terms of pseudopotentials, energy cutoff, supercell size, and k-point mesh used in DFT calculations are first examined by comparing the thermodynamic properties from our calculations with experimental data and existing DFT results, including cohesive energy, lattice constants and elastic constants of perfect crystals {Si(diamond), Mg(fcc), 3C-SiC, Mg₂Si, C(diamond), and Mg(hcp)}, and formation energies of defects and defect clusters in 3C-SiC. Different defect configurations including substitutional, interstitial, and dumbbell are considered in the

calculations. The substitutional and interstitial are described as A_B . A denotes the species and the subscript B denotes the lattice site. There are two interstitial sites in 3C-SiC. One is the tetrahedral center of Si, and the other is the tetrahedral center of C. The two interstitial sites are described as TSi and TC, respectively. A dumbbell is described as $A_1^+ - A_2 - \langle a \rangle$. A_1 and A_2 denote the two species in the dumbbell. Subscript “+” of A_1 denotes that the dumbbell locates at A_1 lattice. $\langle a \rangle$ denotes the direction of the dumbbell. The formation energies of defects and defect complexes in SiC-Mg are

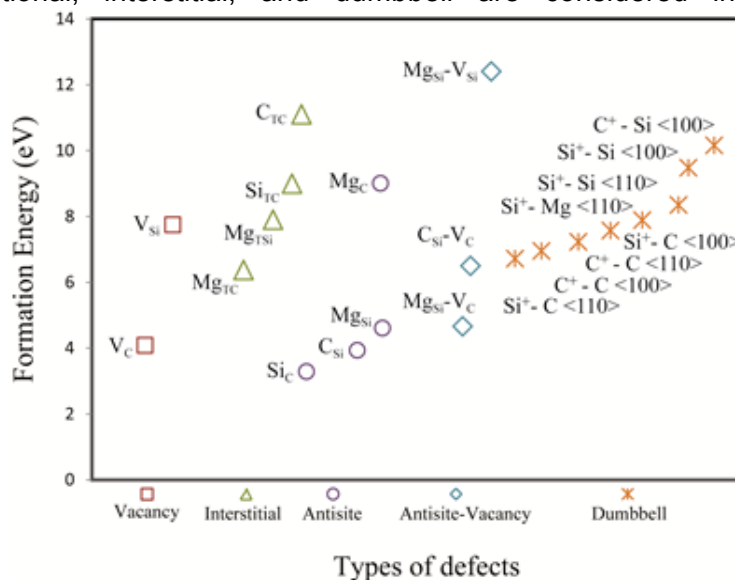


Figure 1. Summary of formation energies of different point defects and defect complexes in 3C-SiC.

presented graphically in Figure 1. The results show that substitutional Mg_{Si} is the most stable defect of Mg, with formation energy 4.61 eV. The complex $Mg_{Si}-V_C$ has a little higher formation energy (4.66 eV). The defect complexes: Mg_C-V_{Si} , $Mg_{TSi}-V_C$, $Mg_{TSi}-V_{Si}$ are unstable. They will transform to $Mg_{Si}-V_C$, Mg_C , and Mg_{Si} without overcoming energy barriers, respectively. The stability of $C^+-Mg\langle 100 \rangle$, $C^+-Mg\langle 110 \rangle$, $Si^+-Mg\langle 100 \rangle$ and $Si^+-Mg\langle 110 \rangle$ dumbbells were carefully checked by relaxing the dumbbell configuration with different initial distances from 0.84 Å to 1.4 Å. It is interesting to find that only $Si^+-Mg\langle 110 \rangle$ dumbbell is stable. The remaining three dumbbells are unstable, and dissociate to form Mg interstitials. The interstitial Mg_{TC} has lower formation energy than that of the interstitial Mg_{TSi} .

The minimum energy paths (MEP) of defect migration and small cluster evolution are determined with a generalized solid-state elastic band (G-SSNEB) method. In the simulations, the first step is to relax the defect configurations of the initial and final states, after that three images are inserted between the initial and final states, and then a search for the MEP using the G-SSNEB method is performed with both atomic motion and the relaxation of the supercell. The MEPs of C, Si, Mg_{Si} migrations to their nearest neighbor vacancies show that the activation energy of Si to V_{Si} is 3.51 eV which is in good agreement with the DFT result 3.4 eV [3]. The activation energy of C to V_{Si} is about 3.33 eV compared to 4.58 eV for C_{Si} to V_C . It is found that the activation energy of Mg_{Si} to V_{Si} (0.97 eV) is much smaller than that of Si to V_{Si} (3.51 eV). The migrations of Mg_{Si} to V_C , Mg_{Si} to V_{TSi} , and Mg_C to V_{TC} are energetically not favored because the process causes an energy increase. Figure 1 shows that the $Si^+-Mg\langle 110 \rangle$ dumbbell is a metastable. It may transform to more stable defect Mg_{TC} via two different processes. One is $Si^+-Mg\langle 110 \rangle$ to Mg_{TC} . The other has two steps, i.e., $Si^+-Mg\langle 110 \rangle$ to Mg_{TSi} and then Mg_{TSi} to Mg_{TC} . The MEPs for these two processes are calculated. The results show that the activation energy of $Si^+-Mg\langle 110 \rangle$ to Mg_{TC} is 0.23 eV. The activation energies of $Si^+-Mg\langle 110 \rangle$ to Mg_{TSi} are 0.3 eV while it is 0.91 eV for Mg_{TSi} to Mg_{TC} migration. The first process $Si^+-Mg\langle 110 \rangle$ to Mg_{TC} has lower activation energy than that of the second process. Interstitial Mg_{TC} has a lower formation energy than that of interstitial Mg_{TSi} . The activation energy from Mg_{TC} to Mg_{TSi} is 2.44 eV. It is small compared with the activation energies of Si and C self-diffusions (3.5 eV). Therefore, the transition from Mg_{Si} to V_{Si} , $Si^+-Mg\langle 110 \rangle$ to Mg_{TC} , and Mg_{TC} to Mg_{TSi} could be Mg diffusion mechanisms during the formation of Mg-related clusters and Mg_2Si nucleus.

ACKNOWLEDGEMENTS

This work was performed by Pacific Northwest National Laboratory, which is operated by Battelle for the United States Department of Energy under Contract DE-AC05-76RL01830. This study was supported by the U.S. Department of Energy, Office of Fusion Energy Sciences.

REFERENCES

- [1] S. Y. Hu, W. Setyawan, R. M. Van Ginhoven, W. Jiang, C. H. Henager, Jr. and R. J. Kurtz, *J. Nucl. Mater.* (submitted 2013).
- [2] M. E. Sawan, Y. Katoh, and L. L. Snead, *J. Nucl. Mater.*, in press (2013).
- [3] M. Bockstedte, A. Mattausch, and O. Pankratov, *Phys. Rev. B* **68** (2003) 205201.

8.4 MOLECULAR DYNAMICS INVESTIGATION OF HELIUM BUBBLE EQUATION OF STATE — Y. N. Osetskiy and R. E. Stoller (Oak Ridge National Laboratory)

OBJECTIVE

The objective of this research is to determine the equation of state of helium in radiation-induced bubbles in iron-based alloys. Properties of He-bubbles significantly affect the evolution of the microstructure and mechanical properties under radiation damage conditions.

SUMMARY

An extensive modeling program was launched earlier to model He-filled bubbles in Fe. We are studying bubbles of radius from 0.25 to 5.0nm with He-to-vacancy ratio from 0.1 to 2.0 over the temperature range 300-1000K. An unexpectedly long simulation time was found to be necessary to accurately determine the equilibrium properties of small bubbles.

PROGRESS AND STATUS

Introduction

An extensive simulation program using molecular dynamics (MD) is in progress to characterize the behavior of helium in small bubbles in iron as representative of Fe-based alloys. The objective is to obtain an accurate, atomistic-based equation of state, which describes the pressure-volume relationship for He in such bubbles as a function of temperature. This information is absolutely necessary for predicting radiation damage evolution in fusion materials where He is generated due to transmutation reactions. The presence of He strongly influences the microstructural processes controlling the formation and evolution of cavities, which in turn can that dramatically change the defect balance and kinetics of microstructural evolution.

Progress

The three-body, angular dependent interatomic potential for Fe-He developed earlier at ORNL [1,2] was used in this study. A special study was made to define the equilibrium state of gas-filled bubbles. We first used the concept of the bubble volume that was defined via the displacement of the surface atoms [3,4]. The general idea is that an equilibrium bubble should not induce additional displacements of the surface atoms, which should be in the same positions as if they were in a perfect lattice. This works well for nearly flat surfaces (large radii) and high concentrations of gas atoms, which permit one to accumulate high statistics of gas-surface interactions over a suitable averaging time. However, we found that this does not work well even for medium size bubbles, < 3-4 nm, because their surface is quite curved and the equilibrium He concentration is relatively low, a He-to-vacancy ratio of 0.25 to 0.5 depending on the temperature. This introduces a significant inaccuracy in definition of the equilibrium state. We then adopted another criterion, which is based on the average pressure in the Fe matrix. Formally, this definition is completely equivalent to the previous one; we define a bubble to be in equilibrium if it does not changes its original volume as defined in reference to the perfect lattice and therefore does not produce an additional pressure contribution in the Fe the matrix. Calculation of the total pressure in the system is fast and the average value converges well because of the large number of atoms used in practical modeling.

Another problem arises in a study such as this related to small bubbles, $<0.5\text{nm}$, due to inaccuracy of the statistical definition of thermodynamic parameters such as gas temperature and pressure in small systems. The smallest bubble we studied may contain as few as only one He atom and estimation of He temperature inside such a bubble becomes indeterminate. A similar but easier to resolve problem also arises for larger bubbles at the lowest temperatures. For example, at 300K the few slowly moving He atoms in bubbles 0.25-0.5nm have too few collisions with the bubble wall per unit time to define pressure easily. A bubble with a 0.25nm radius occupies only 9 lattice sites and with the equilibrium He-to-vacancy ratio of ~ 2 at 300K contains only 18 He atoms. Accumulation of enough collisions between He atoms inside the bubble and Fe atoms on the interface becomes a real statistical problem. On the contrary, a 5nm bubble occupies 44,399 lattice sites and for a He-to-vacancy ratio of 0.35 at 300K contains 15540 He atoms. See Figs.1a and b for a comparison the smallest and largest studied bubbles at the lowest and highest applied temperatures. The statistical differences make the accuracy of the estimated equilibrium pressure inside He bubbles quite strongly dependent on parameters such as bubble size, He content and temperature.

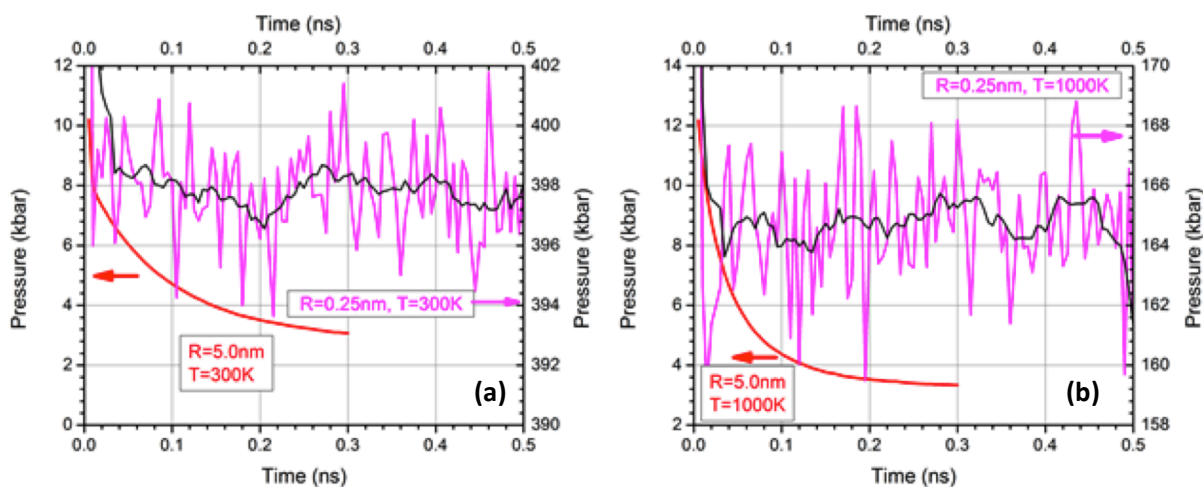


Figure 1. Dependence of the He pressure inside 0.25nm and 5.0nm bubbles during equilibration at a) 300K and b) 1000K. Red and pink lines connect points averaged over 5ps while the black lines average over for 50ps.

We have carried out extensive modeling to identify where the molecular dynamics results are accurate enough. So far we equilibrated large bubbles ($>0.5\text{nm}$) over 6×10^5 time steps and small ones ($<0.5\text{nm}$) over a million steps at each particular set of conditions. This is equivalent to a physical time equal to 0.3ns and 0.5ns, respectively. Examples of the equilibration process, i.e. the He pressure inside the bubble versus time, are presented in Figs 1a and b for small and large bubbles at the low and high temperature respectively. It can be seen that pressure in the large bubble equilibrates smoothly although 0.3ns appears to be too short a time to obtain complete equilibrium. On the contrary, pressure in the small bubble shows very large fluctuations and does not demonstrate convergence to the equilibrium state. Note that the values shown by the red and pink lines connect points averaged over 5ps while the black lines average over for 50ps.

We have concluded that even the relatively long simulation time of 0.5 ns used so far in our modeling is not sufficient for the smallest bubble studied with a radius of 0.25nm to reach stable

pressures. We are the process of extending the simulation time by about a factor of two for all cases. However, we recognize that it may not be computationally practicable to obtain a highly accurate pressure for the smallest bubbles at the lowest temperatures with a large range of He-to-vacancy ratios. In this case we plan to focus on close-to-equilibrium conditions and, by running the simulations for as long as possible, to obtain the maximum possible accuracy in the equilibrium parameters. Values obtained for other He-to-vacancy ratios will be more approximate but the fitting procedure used to obtain the equation of state will average over the data scatter once the fit to equilibrium conditions is obtained.

FUTURE WORK

The simulation component of this program is nearing the stage where we can treat the results to define He gas equation of state, which is now bubble size dependent. This will be done at the next stage of the program.

REFERENCES

- [1] T. Seletskaya, Y. N. Osetsky, R. E. Stoller and G. M. Stocks, "Calculation of Helium Defect Clustering Properties in Iron Using a Multi-Scale Approach," *J. Nucl. Mater.* **351** (2006) 109-118.
- [2] D. M. Stewart, Y. N. Osetsky, R. E. Stoller, S. I. Golubov, T. Seletskaya, and P. J. Kamenski, "Atomistic Studies of Helium Defects Properties in BCC Iron: Comparison of He-Fe Potentials," *Philos. Mag.* **90** (2010) 923.
- [3] D. M. Stewart, Y. N. Osetskiy, and R. E. Stoller, "Atomistic Study of Helium Bubbles in Fe: Equilibrium State," MRS Proceedings (2011), 1298: mrsf10-1298-q08-04, Materials Research Society 2011, DOI: 10.1557/opl.2011.551, Published online by Cambridge University Press: 15 March 2011.
- [4] D. M. Stewart, Y. N. Osetskiy, and R. E. Stoller, "Atomistic Studies of Formation and Diffusion of Helium Clusters and Bubbles in BCC Iron," *J. Nucl. Mater.* **147** (2011) 1110-1114.

8.5 DYNAMICS OF DEFECT-LOADED GRAIN BOUNDARIES UNDER SHEAR DEFORMATION IN α -Fe — L. Yang, F. Gao, H. L. Heinisch, and R. J. Kurtz (Pacific Northwest National Laboratory)

OBJECTIVE

To simulate the dynamics of defect-loaded grain boundaries (GBs) in bcc Fe under shear deformation using molecular dynamics, to study the effects of loaded defects on the motion of grain boundaries, and to explore the interaction of interstitial-loaded GBs with vacancies.

SUMMARY

The defects produced in collision cascades will interact with microstructural features in materials, such as GBs and dislocations. The coupled motion of GBs under stress has been widely observed in simulations and experiments. Two symmetric tilt GBs with a common $\langle 110 \rangle$ tilt axis ($\Sigma 3$ and $\Sigma 11$) in bcc iron are used to investigate the coupled motion of GBs under shear deformation. Also, we have explored the effect of self-interstitial atoms (SIAs) loading on the GB motion, with different concentrations of interstitials randomly inserted around the GB plane. The simulation results show that the interstitial loading reduces the critical stress of the GB coupled motion for the $\Sigma 3$ GB. Furthermore, the interstitials and vacancies are inserted randomly at the GB plane and at a distance of 1 nm away from the GB plane, respectively, to understand the self-healing mechanism of GBs under stress. The behavior of the defect-loaded GBs depends on the GB structure. The loaded interstitials in the $\Sigma 3$ GB easily form $\langle 111 \rangle$ interstitial clusters that do not move along with the GB. The vacancies in the $\Sigma 3$ GB impede the GB motion. However, the interstitials move along with the $\Sigma 11$ GB and annihilate with vacancies when the GB moves into the vacancy-rich region, leading to the self-healing and damage recovery of the $\Sigma 11$ GB.

PROGRESS AND STATUS

Introduction

It is known that grain boundaries (GBs) play a significant role in the microstructure evolution and mechanical properties of materials. In irradiation environments, the defects produced in the collision cascades, such as self-interstitial atoms and vacancies, will interact with microstructural features, such as GBs and dislocation cores [1, 2]. Bai et al. observed that the interstitials produced by nearby collision cascades tend to be absorbed into GBs in copper [1], and Vorovikov et al. proposed a radiation damage healing mechanism due to GB motion under stress in tungsten [2]. In general, four typical motions of GBs, in response to shear stresses, are found in many materials, including 1) normal motion (i.e., the process by which a GB moves in its normal direction), 2) relative translation of the grains parallel to the GB plane coupled to normal GB motion (so called coupled motion of GB), 3) relative rigid body translation of the grains along the GB by sliding, and 4) grain rotations [3]. Ferritic steels and alloys are widely used for structural materials in current nuclear fission reactors, and they are proposed as

This work was supported by the U.S. Department of Energy, Office of Fusion Energy Sciences. PNNL is operated by Battelle Memorial Institute for the U.S. DOE under Contract DE-AC-06-76RLO 1830.

candidate materials for plasma facing first wall structural materials in future fusion energy facilities [4]. Campana et al., simulated the influence of displacement cascades on GB structures and their stability in bcc Fe, and found that a cascade near a GB can significantly reduce the critical stress for shearing or migration of the GB [5]. Here, the coupled motion of two tilt GBs in bcc iron with different concentrations of defects are investigated under a shear deformation that is applied parallel to the GB plane and perpendicular to the tilt axis. Also, we have investigated the detailed mechanism for an interstitial-loaded GB to annihilate with vacancies when the GB moves into a vacancy-rich region.

Simulation Methods

Two symmetric tilt GBs with a common $\langle 110 \rangle$ tilt axis ($\Sigma 3$ and $\Sigma 11$) are used to investigate the coupled motion of GBs under shear deformation. The simulation cell sizes of $\Sigma 3$ and $\Sigma 11$ are $84.20\text{\AA} \times 140.00\text{\AA} \times 80.84\text{\AA}$ with 80,240 Fe atoms and $47.5356\text{\AA} \times 140.00\text{\AA} \times 40.54\text{\AA}$ with 22,600 Fe atoms, respectively. Periodic boundary conditions are imposed along the x and z directions, but fixed boundary conditions are applied along the y direction, where the x, y and z represent the $[1-11]$, $[-112]$ and $[-1-10]$ directions in the $\Sigma 3$ GB model, and $[1-13]$, $[-332]$ and $[-1-10]$ directions in the $\Sigma 11$ GB model.

The NVT (constant number of atoms, volume and temperature) ensemble is applied in the present simulations with a time step of 1 fs. To study the effects of loading self-interstitial atoms (SIAs), different concentrations of interstitials are inserted randomly around the GB plane. After the interstitials are inserted, the configuration is quenched to 0 K, followed by a temperature rescaling to the desired temperature for 50 ps. Then, the system is driven by applying a velocity $V=1.0$ m/s to the atoms in the uppermost region at a given temperature. Temperatures of 0, 100 and 300 K are considered for the $\Sigma 3$ GB. The corresponding shear stress is calculated according to the method in Ref. 6. The orientation and

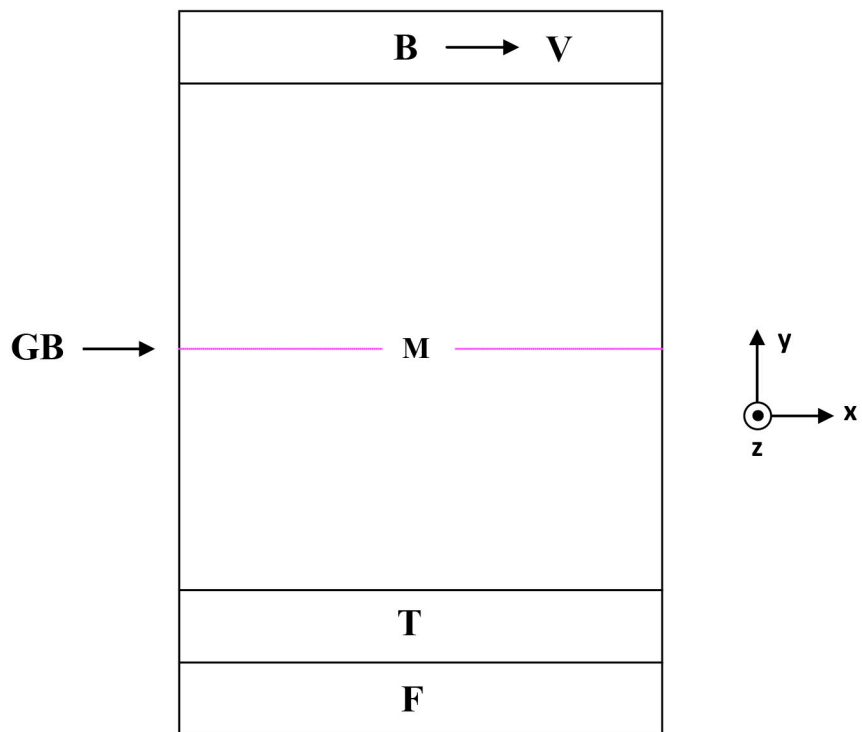


Figure 1. Geometry of the simulation box.

identification of specific regions of the simulation cell are shown in Fig. 1. The upper part B is used to control the deformation of the sample, where the atoms are displaced along the x direction by a constant increment at each time step, but they are free to move in the yz plane. The atoms in region F are rigidly fixed in their original positions, whereas the atoms in region T are used to control temperature by performing a velocity rescaling on the atoms every 100 time steps according to the difference between the current temperature and the desired temperature.

The atoms in the middle region M are free to move. The interstitial concentrations of 10%, 30%, 50%, 70% and 100% are the ratios of the number of interstitial atoms to that of Fe atoms on the GB plane in the $\Sigma 3$ and $\Sigma 11$ GBs. The critical stress is averaged by the each critical stress during the 1.0 ns simulation in the GBs. In order to understand the self-healing mechanism in bcc Fe under stress, the interstitials are inserted randomly around the GB plane, and the same amount of vacancies is introduced synchronously at a distance of 1.0 nm away from the GB plane.

Results and Discussion

The motion of the $\Sigma 3$ and $\Sigma 11$ GBs without defects under shear deformation was simulated at 0, 100 and 300 K. A coupled GB motion is observed in the two GBs when applying shear deformation along the x direction. After adding the shear deformation, the GB becomes mechanically unstable and jumps to a new position at the critical stress. The shear velocity (V) applied to the B region was tested in the $\Sigma 3$ GB at 300 K, and it was determined that the critical stress required for migration of the GB depends only slightly on the velocity when V is varied from 0.1 m/s to 10 m/s, but the GB migration velocity normal to the GB plane is proportional to V . Thus, the velocity of shear deformation of 1.0 m/s was considered in the following studies.

The coupled GB motion is significantly affected by the loaded SIAs. The critical stress at three temperatures for the $\Sigma 3$ GB as a function of SIA concentration is presented in Fig. 2. During application of the shear deformation, the SIAs migrate easily along the $\langle 111 \rangle$ direction, especially at 300 K, and this leads to the formation of $\langle 111 \rangle$ clusters. When the GB migrates along the $-y$ direction, the applied stress enhances the motion of the SIA clusters along the x direction ($\langle 111 \rangle$), but they seldom migrate along with the GB. As expected, the critical stress decreases with increasing temperature for a given interstitial concentration. For the three temperatures studied, the critical stress decreases with the loaded SIAs at the concentrations of 10% and 30%, which is due to the fact that the SIAs enhance the GB motion. The critical stress is the lowest at an SIA concentration of 30%. However, at a concentration of 50% or larger the critical stress increases with increasing SIAs from 30% to 100%. It is found that the SIAs form an extra atomic layer parallel to the GB at a concentration of 100%, although it is not a perfect atomic layer. The critical stress at 100% concentration is lower than the perfect GB, which is due to the fact that the inserted SIAs at this concentration do not form a perfect atomic layer, and some of them are still in interstitial positions. The simulations for the $\Sigma 11$ GB are now in progress.

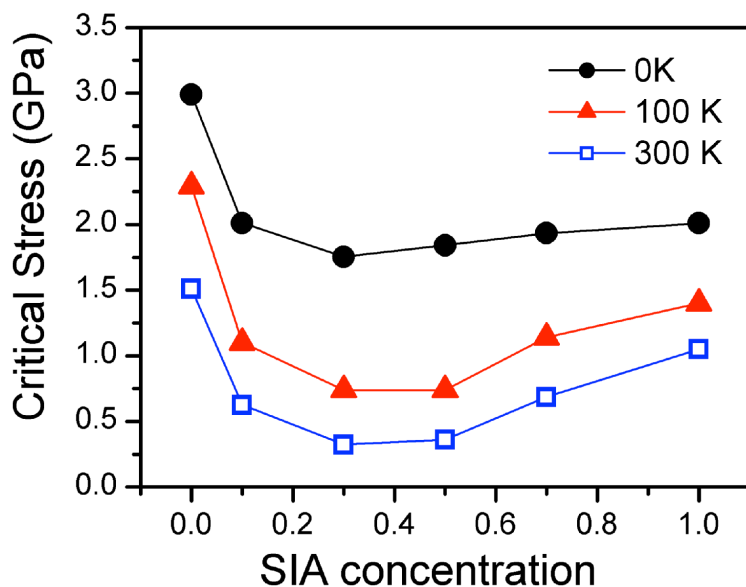


Figure 2. Average critical stress versus the inserted SIA concentration in the $\Sigma 3$ GB at different temperatures.

Under irradiation, many interstitials created during collision cascades can be absorbed by nearby GBs, leaving the slower vacancies behind in the bulk. To understand the interaction of the interstitial loaded GBs with vacancies, a 10 % concentration of interstitials are inserted randomly around the GB plane and the same amount of vacancies is introduced synchronously at 1.0 nm away from the GB plane. Fig. 3 shows several snapshots of the $\Sigma 3$ GB configuration simulated at 300 K. It is of interest to note that most of the inserted interstitial atoms accumulate to form $\langle 111 \rangle$ clusters during the applied shear deformation, and these clusters can migrate along the $\langle 111 \rangle$ direction. When the GB moves toward the vacancy-rich region, only a few Fe atoms migrate to and combine with the vacancies, but the SIA clusters are left behind in the bulk, as shown in the snapshot at 0.6 ns in Fig. 3. Once the GB moves into the vacancy-rich layer, the vacancies are absorbed by the GB, which impedes the GB motion somewhat. Only 8.8% inserted SIAs recombine with vacancies after the GB plane breaks through the layer with vacancies, but the rest of the SIAs form clusters and remain behind in the bulk, as shown in the snapshot at 1.0 ns.

Similar simulations have been performed in the $\Sigma 11$ GB. The interstitial atoms at a concentration of 20% are loaded into the GB at 300 K. The motion of the interstitials is significantly different from that in the $\Sigma 3$ GB. Fig. 4 shows several snapshots of the $\Sigma 11$ GB configuration simulated. It is found that the coupled GB motion in the $\Sigma 11$ GB is more favorable than in the $\Sigma 3$ GB. Moreover, the interstitial atoms migrate along with the GB (see Fig. 4 at 0.2 ns). The snapshot at 0.5 ns illustrates that the interstitial atoms almost recombine with the vacancies when the GB moves into the vacancy-rich layer. After the GB sweeps off vacancies in the layer, the atomic configuration almost recovers to a perfect GB structure, except for a few interstitials at the GB plane. This result exhibits a self-healing mechanism in the $\Sigma 11$ GB under stress, which is different to that in the $\Sigma 3$ GB. The difference response of the two GBs to defects may be attributed to the different GB structures.

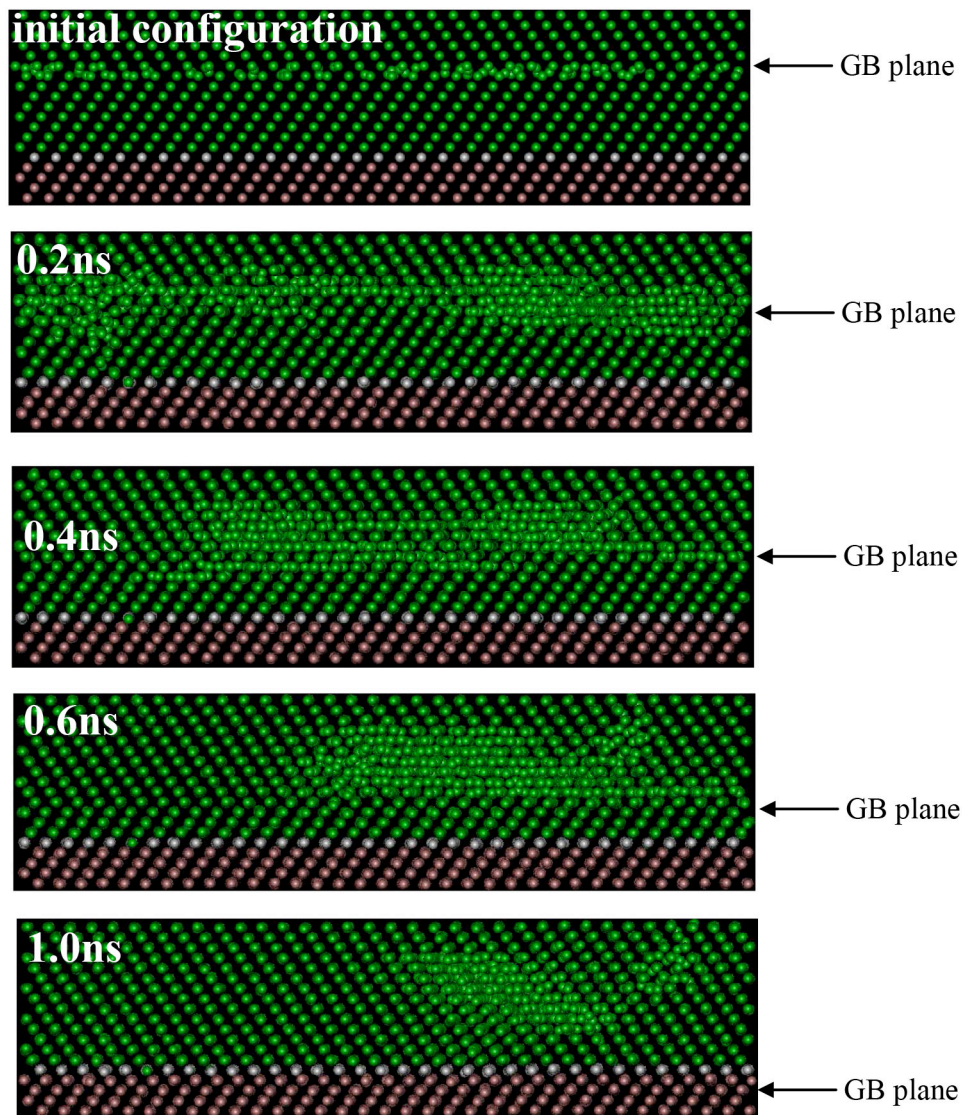


Figure 3. Snapshots of atomic configurations of the $\Sigma 3$ GB with 10% SIAs and 10% vacancies at 300 K, where the SIAs are originally distributed near the GB plane and vacancies are located on the layer with white spheres.

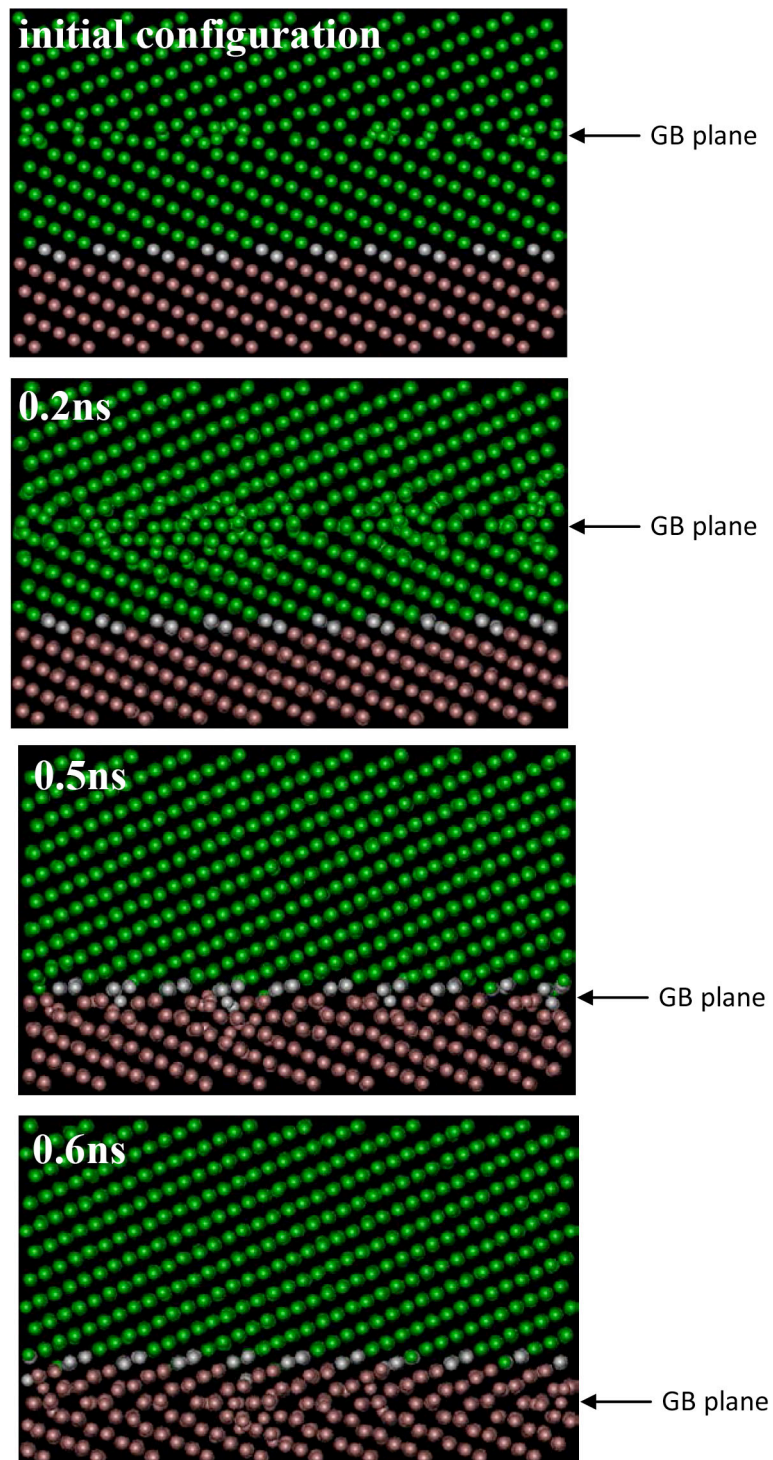


Figure 4. Snapshots of atomic configurations of the $\Sigma 11$ GB with 20% SIAs and 20% vacancies at 300 K, where the SIAs are originally distributed near the GB plane and vacancies are located on the layer with white spheres.

SUMMARY

The interstitial loading reduces the critical stress of the GB coupled motion in the $\Sigma 3$ GB of bcc Fe. The behavior of the defects in the GBs depends on the GB structure. The interstitials loaded into the $\Sigma 3$ GB easily form $\langle 111 \rangle$ clusters that remain behind in the bulk when the GB migrates along the direction perpendicular to the GB plane. The vacancies in the $\Sigma 3$ GB impede the GB coupled motion. However, the loaded interstitials can move along with the $\Sigma 11$ GB and combine with the vacancies, leading to defect recovery and the self-healing of radiation damage. The self-healing phenomenon is observed only in the $\Sigma 11$ GB.

REFERENCES

- [1] X. M. Bai, A. F. Voter, R. G. Hoagland, M. Nastasi and B. P. Uberuaga, *Science* **327** (2010) 1631.
- [2] V. Borovikov, X. Z. Tang, D. Perez, X. M. Bai, B. P. Uberuaga and A. F. Voter, *Nucl. Fusion* **53** (2013) 063001.
- [3] J. W. Cahn, Y. Mishin and A. Suzuki, *Acta Mater.* **54** (2006) 4953.
- [4] J. Marian and B. D. Wirth, *Phys. Rev. Lett.* **88** (2002) 255507.
- [5] C. Campana and K. P. Boyle, *Phys. Rev. B* **78** (2008) 134114.
- [6] Yu. N. Osetsky and D. J. Bacon, *J. Nucl. Mater.* **323** (2003) 268.

8.6 DISPLACEMENT CASCADE SIMULATION IN TUNGSTEN AT 1025 K — W. Setyawan, G. Nandipati, K. Roche, H. Heinisch, R. J. Kurtz, (Pacific Northwest National Laboratory); and B. D. Wirth (University of Tennessee, Knoxville)

OBJECTIVE

The objective of this research is to support the prediction of irradiation damage properties of bulk tungsten-based materials using computational methods.

SUMMARY

Molecular dynamics simulation was employed to investigate the irradiation damage properties of bulk tungsten at 1025 K (0.25 melting temperature). A comprehensive data set of primary cascade damage was generated up to primary knock-on atom (PKA) energies 100 keV. The dependence of the number of surviving Frenkel pairs (N_{FP}) on the PKA energy (E) exhibits three different characteristic domains presumably related to the different cascade morphologies that form. The low-energy regime < 0.2 keV is characterized by a hit-or-miss type of Frenkel pair (FP) production near the displacement threshold energy of 128 eV. The middle regime 0.3 – 30 keV exhibits a sublinear dependence of $\log(N_{FP})$ vs $\log(E)$ associated with compact cascade morphology with a slope of 0.73. Above 30 keV, the cascade morphology consists of complex branches or interconnected damage regions. In this extended morphology, large interstitial clusters form from superposition of interstitials from nearby damage regions. Strong clustering above 30 keV results in a superlinear dependence of $\log(N_{FP})$ vs $\log(E)$ with a slope of 1.365. At 100 keV, an interstitial cluster of size 92 and a vacancy cluster of size 114 were observed.

PROGRESS AND STATUS

Introduction

Tungsten is considered as the primary solid material choice for divertor components in future fusion reactors due to its low sputtering coefficient, excellent thermal conductivity, relatively low neutron activation and good mechanical strength. Bulk tungsten will be exposed to energetic neutrons escaping the plasma. The deuterium-tritium reaction will produce He, through nuclear transmutation reactions, and neutrons with characteristic kinetic energies of 3.5 and 14.1 MeV, respectively. Collisions of 14.1-MeV neutrons with W atoms produce W primary-knock-on atoms (PKAs) with various recoil velocities. The spectrum of the recoil atoms as a function of recoil speed decreases drastically above ~ 250 keV. The purpose of the current work is to generate a comprehensive data set of the cascade damage in pure W produced by PKA up to 100 keV in particular at a temperature of interest ~ 1025 K.

Simulation details

The molecular dynamics (MD) technique was employed to simulate displacement cascades. For the W-W interaction, the Finnis-Sinclair type potential developed by Ackland and Thetford [1] was taken, in which the short-range part was then modified to harden the repulsion [2]. Modification was also done at distances relevant to self-interstitial configurations to improve defect formation energies. The simulations were performed using LAMMPS software [3]. Before a displacement cascade was initiated, the system was thermalized in the *NPT* ensemble for 50 ps with a Nosé-Hoover thermostat to generate a canonical distribution of velocities at 1025 K. A random PKA was then chosen and assigned an initial velocity with a random

direction. Periodic boundary conditions were applied in all axis coordinates. During the simulation, interstitials may cross the simulation cell boundary. While this does not create any issue for counting point defects, it raises a challenge when clusters of point defects need to be recognized and when spatial distribution of the clusters is important for example if the data will be embedded in a larger cell in kinetic Monte Carlo simulations. Therefore, the MD run was discarded when boundary crossing occurred. To minimize the wasted simulations, the PKA was randomly chosen from a region near the center of the cell and a large enough cell was used. All cascades generated in this work have interstitials contained in the cell throughout the simulation without crossing the boundary. At the beginning the collision cascade simulation was performed in the *NVE* ensemble using an adaptive time step allowing a maximum atom displacement of 0.005 Å per step. Cascade events and cooling were followed for ~10 ps, afterwards the system was thermalized to a target temperature in *NVT* and defect migration was followed for a total simulation time of 55 to 60 ps.

Results

The calculated melting temperature T_m using the empirical potential is 4100 ± 50 K [2], compared to experimental value of 3695 K. Hence, 1025 K represents $0.25T_m$ of the potential which is equivalent to an experimental value of ~924 K. The average displacement threshold energy E_t was calculated to be 128 eV with a minimum E_t of 48 eV [2]. Table 1 shows the size of simulation cell as a function of PKA energy ranging from below the average E_t up to 100 keV.

Vacancies (V) and interstitials (I) were determined using Wigner-Seitz cell occupancy. The number of surviving Frenkel pairs (N_{FP}) is plotted in Figure 1. The data points were averaged from 15 to 40 simulations as presented in Table 1. The plot in a log-log scale reveals three regions that can be fit with linear functions exhibiting different slopes. The lines in Figure 1 represent the least-square linear fits of the three domains namely 0.1 – 0.2, 0.3 – 30 and 30 – 100 keV that were determined on a log-log scale. The fitted equations correspond to $N_{FP} = 0.640E_{MD}^{0.334}$, $N_{FP} = 1.795E_{MD}^{0.730}$ and $N_{FP} = 0.209E_{MD}^{1.365}$ respectively where E_{MD} is given in keV. The exponents may change slightly if different fitting boundaries were used. However, the change will not eliminate the fact that the slope in the middle regime is sublinear while that in the high region is superlinear. These characteristic slopes signify a departure from the standard Norgett-Robinson-Torrens (NRT) model which predicts $N_{FP} = 0.4E_{MD}/E_t$. In the low-energy region, one may argue that the low and middle regions can be fitted as a single curve. However, the separation of the low region has a physical significance. It is related to the maximum E_t . When E_{MD} is less than the maximum E_t , the event of creating a stable Frenkel pair is a hit-or-miss process. This kind of process can result in an N_{FP} curve that has a different temperature dependence as compared to that at $E_{MD} > \text{maximum } E_t$. This is because at PKA energies near E_t , increasing temperature decreases the probability of easy replacement events, but, conversely, increased mobility of the temporary interstitial may increase the chance to escape the vacancy created by the PKA or the chance for the vacancy to be occupied by the **Table** surrounding lattice atoms.

1. Simulation cell size as a function of PKA kinetic energy E_{MD} . Cubic cells were used with side length L given in units of the W lattice constant $a = 3.17 \text{ \AA}$.

E_{MD} (keV)	L (a)	#atoms	#simulations
0.1, 0.15, 0.2, 0.3	15	6,750	40
0.5, 0.75	20	16,000	20
1, 1.5, 2, 3	30	54,000	20
5, 7.5	40	128,000	20
10, 15	50	250,000	15
20, 30, 40	64	524,288	15
50, 60	80	1,024,000	15
75	100	2,000,000	15
100	120	3,456,000	20

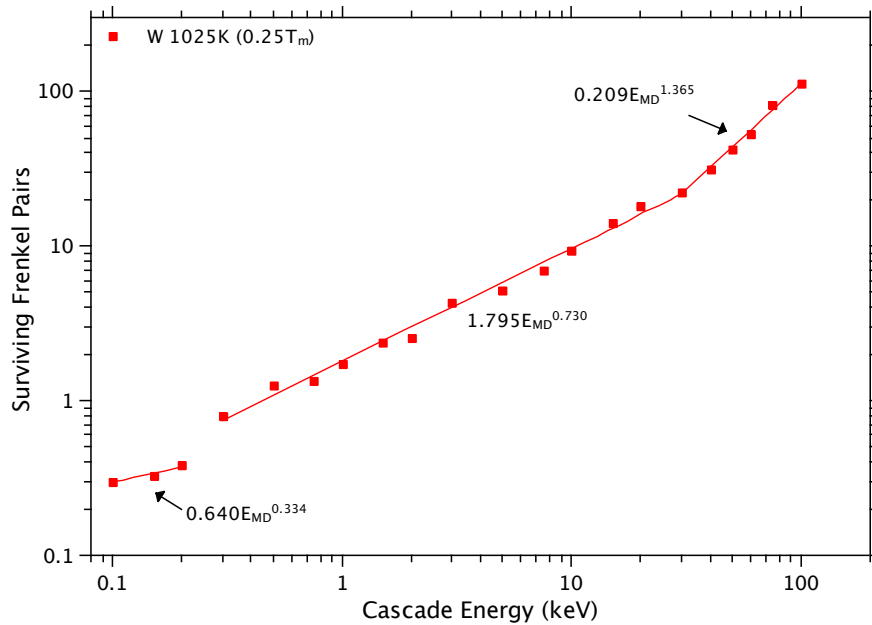


Figure 1. Characteristic curve of the number of surviving Frenkel pairs in tungsten at 1025 K (0.25 melting temperature) as a function of primary-knock-on atom kinetic energy E_{MD} . Straight lines represent least-square linear fits on a log-log scale with E_{MD} in keV.

The characteristic slopes shown in Figure 1 are presumably related to different cascade morphologies as a function of PKA energy. Snapshots of temporary vacancies and interstitials from several typical simulations with a 10-keV PKA are shown in Figure 2a. The snapshots were taken after ~ 0.4 ps when the maximum damage occurred. The morphology consists of a single and compact damage region. Evolution of cascade morphology from a typical simulation with 100-keV is shown in Figure 2b. In this regime, the morphology consists of complex branches or interconnected damage regions. We refer to this as an extended morphology. When a PKA

creates an extended morphology, interstitials are concentrated in the interconnecting regions between the vacancy-concentrated regions. The interstitial pockets produce large interstitial clusters at the end of simulation. It appears that the formation of large interstitial clusters and vacancy clusters mediated by the formation of an extended morphology results in the superlinear behavior of the N_{FP} curve.

Clustering of point defects was analyzed using a cutoff distance of 3.82 Å corresponding to a midpoint between the first and second nearest-neighbor distance in bcc W. Several statistical quantities were computed: dumbbell (or mono-vacancy) fraction, average cluster size $\langle \text{size} \rangle$, maximum cluster size size_{max} , average of maximum cluster size $\langle \text{size}_{\text{max}} \rangle$ and the ratio of $\langle \text{size}_{\text{max}} \rangle / \langle \text{size} \rangle$. The results are presented in Table 2. The clustering trend is evident from the decreasing dumbbell or mono-vacancy fraction and from the increasing ratio of $\langle \text{size}_{\text{max}} \rangle / \langle \text{size} \rangle$ as PKA energy increases. In Table 2, the PKA energy of 30 keV corresponds to the approximate location of the inflection point in the N_{FP} curve separating the region of compact and extended cascade morphology (see Figure 1). This energy is ~ 234 times E_t . From Table 2, one can see that the maximum size of interstitial and also vacancy clusters below 30 keV is less than 10 particles. However, above 30 keV, this value rapidly grows. This indicates strong clustering associated with the extended nature of the cascade morphology as previously discussed.

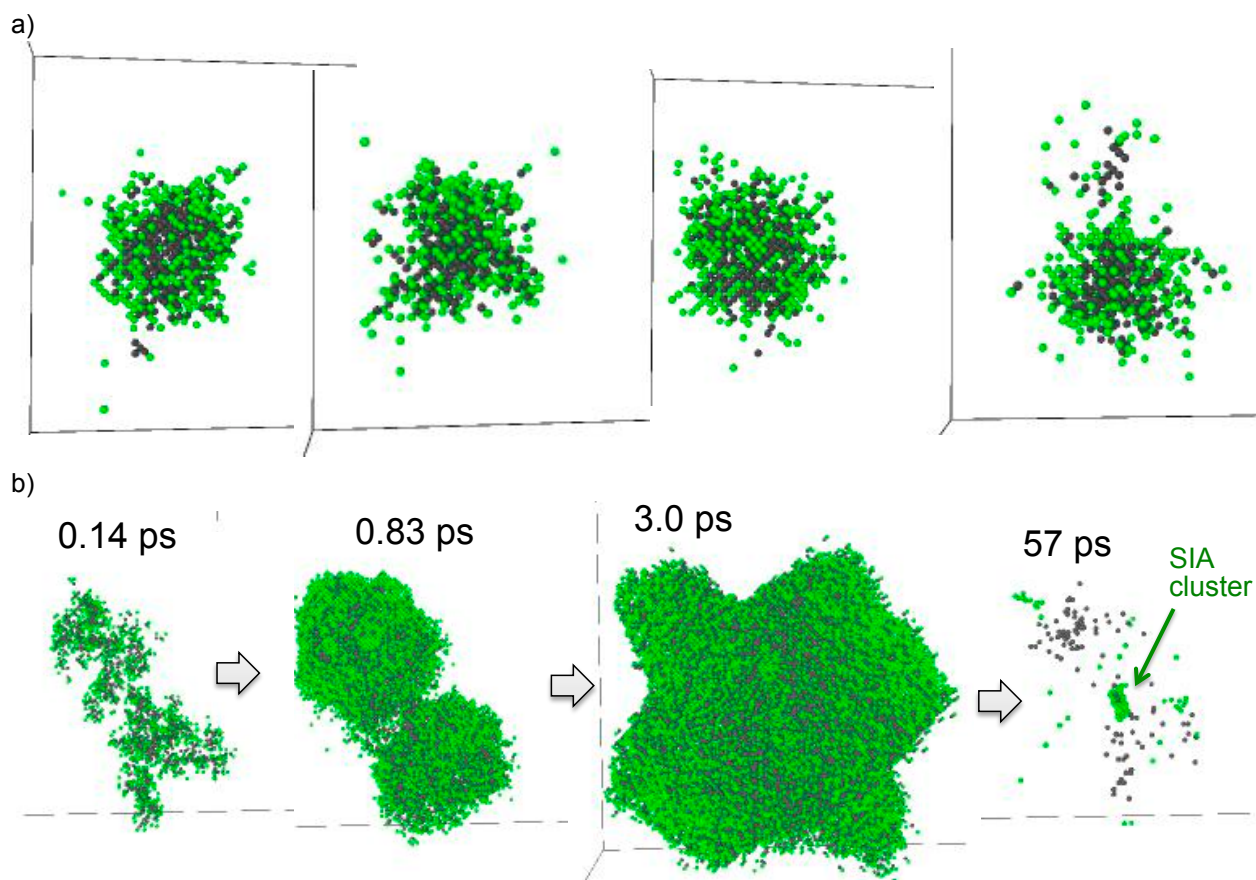


Figure 2. (a) Snapshots of temporary vacancies (black) and interstitials (green) from four different simulations with 10-keV PKA after ~ 0.4 ps showing a compact cascade morphology. (b) Evolution of cascade morphology from a typical run with 100-keV PKA, showing an extended morphology.

Table 2. Statistics of interstitial cluster and vacancy cluster. $\langle \rangle$ denotes the average over simulation runs.

E_{MD} (keV)	Interstitial clusters					Vacancy clusters				
	Dumbbell fraction	$\langle \text{size} \rangle$	size_{max}	$\langle \text{size}_{max} \rangle$	$\frac{\langle \text{size}_{max} \rangle}{\langle \text{size} \rangle}$	Monovac fraction	$\langle \text{size} \rangle$	size_{max}	$\langle \text{size}_{max} \rangle$	$\frac{\langle \text{size}_{max} \rangle}{\langle \text{size} \rangle}$
1	1.00	1.00	1	1.00	1.00	0.67	1.32	3	1.42	1.08
1.5	0.96	1.05	3	1.11	1.05	0.74	1.16	4	1.47	1.27
2	0.98	1.00	2	1.05	1.05	0.70	1.16	2	1.42	1.23
3	0.88	1.25	3	1.50	1.20	0.68	1.15	2	1.70	1.48
5	0.97	1.10	2	1.20	1.09	0.75	1.05	3	1.65	1.57
7.5	0.87	1.30	4	1.65	1.27	0.80	1.15	3	1.70	1.48
10	0.96	1.13	3	1.33	1.18	0.78	1.13	3	1.87	1.65
15	0.76	1.73	8	3.13	1.81	0.70	1.20	6	2.20	1.83
20	0.78	1.67	7	2.87	1.72	0.69	1.47	5	2.60	1.77
30	0.68	2.13	9	4.00	1.88	0.69	1.33	3	2.33	1.75
40	0.63	3.87	23	8.20	2.12	0.73	1.80	10	3.67	2.04
50	0.58	4.73	35	12.13	2.56	0.57	2.53	18	5.93	2.34
60	0.48	6.07	42	16.40	2.70	0.65	3.00	41	7.33	2.44
75	0.48	7.93	74	23.0	2.90	0.51	8.07	117	24.93	3.09
100	0.41	10.35	92	36.80	3.56	0.50	9.8	114	35.5	3.62

ACKNOWLEDGEMENT

Computations were performed partly on Olympus supercomputer (FUSION account) at Pacific Northwest National.

REFERENCES

- [1] G. J. Ackland and T. Thetford, *Phil. Mag. A* **56** (1987) 15.
- [2] N. Juslin and B. D. Wirth, *J. Nucl. Mater.* **432** (2013) 61.
- [3] S. Plimpton, *J. Comp. Phys.* **117** (1995) 1.

8.7 A SEMI-PHENOMENOLOGICAL MODEL FOR DISLOCATION MOBILITY IN TUNGSTEN — D. Rivera, G. Po, T. Crosby, and N. Ghoniem (University of California at Los Angeles, UCLA)

OBJECTIVE

The dependence of dislocation velocity in tungsten on the applied stress and temperature is investigated. First, we give a brief theoretical overview of the mechanisms of kink pair formation and the relationship to dislocation motion under stress. We then discuss the theory of phonon scattering and its influence on damping dislocations that move at stresses higher than values where kink motion controls dislocation mobility. A general phenomenological framework is presented, where semi-empirical equations for the dislocation velocity in tungsten are presented. The objective of this effort is to develop a more general procedure for dislocation velocity in other BCC, FCC and HCP metals on the basis of the phenomenological theory, supported by data collected from experiments and MD simulations.

SUMMARY

Dislocation mobility is a fundamental property of a material that determines many of the characteristics of plastic deformation. It is an essential ingredient in large-scale dislocation dynamics (DD) simulations, as it controls the rates of dislocation-dislocation interaction mechanisms, and thus the way the material hardens or softens with further deformation. The objective of this effort is to develop a consistent description of the dependence of dislocation mobility on the material crystal structure (e.g., BCC, FCC, or HCP), the applied stress and its orientation, the temperature and influence of alloying elements. Such task seems to be daunting at first sight. However, we will use guidance of theory, together with experimental measurements and computer simulations (Molecular Statics, Molecular Dynamics, and First Principles) to establish a semi-phenomenological database for dislocation mobility as a key input to DD simulations. In this first report, we focus on the dislocation mobility in tungsten single crystals.

The approach we will take here is that we will consider two regimes of dislocation motion. The first is at low values of stress and temperature, where dislocations can only move via kink pair nucleation and migration. This regime is characterized by the Peierls Stress (PS) at 0 K, and the thermal component of the Critical Resolved Shear Stress (CRSS) at any given temperature. The values of PS and CRSS are material dependent, and are very low for FCC metals, intermediate for HCP, and significant for BCC metals. At stress levels below the CRSS, dislocation motion is diffusive with a bias driven by the applied stress. If the bias is too high (i.e., high stress), the thermally activated process of kink pair nucleation and migration becomes irrelevant, and the dislocation momentum is reduced as a result of the scattering of elastic phonon waves off of the dislocation as it moves. This mechanism of damping, which was first introduced by Leibfried, becomes the dominant mechanism of motion at relatively high stress values and at high temperatures. As the dislocation velocity approaches the transverse speed of sound, it loses energy by emitting elastic waves, and thus the velocity is limited by the sound speed. In the following, we sketch out the basic theoretical ingredients that explain these mechanisms, and follow that with a semi-phenomenological description for DD simulations.

PROGRESS AND STATUS

Introduction

Peirels introduced the concept of whole-sale motion of a dislocation as a string above a sinusoidal barrier at absolute zero temperature. The dislocation line is assumed to be pushed rigidly over an atomic sinusoidal barrier. We discuss here the theoretical background behind the Peierls stress at absolute zero temperature. At finite temperatures, dislocation lines nucleate kinks and can move easier by kink nucleation and sideways motion.

Following Dorn and Rajnak [1], the energy per unit length of the dislocation can be approximates by a sinusoidal function of the form:

$$\Gamma(y) = \frac{\Gamma_c + \Gamma_0}{2} + \frac{\Gamma_c - \Gamma_0}{2} \left(\frac{\alpha}{2} + \cos \frac{2\pi y}{a} - \frac{\alpha}{4} \cos \frac{4\pi y}{a} \right) \quad (1)$$

where Γ_c and Γ_0 are the energies at the top and bottom of the Peierls hill, α is a factor that controls the shape of the potential, and a the lattice constant, as shown in Fig. 1. The three parameters, Γ_c , Γ_0 , and α , can be readily obtained by fitting MS or First Principles data. Once

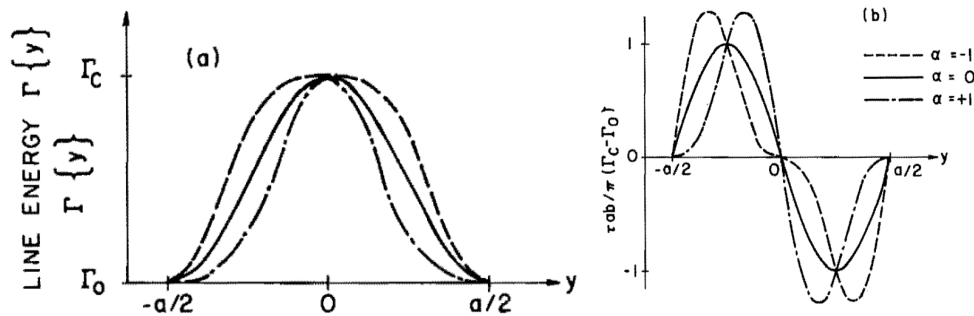


Figure 1. Illustration of Peierls Barrier (after Dorn & Rajnak).

obtained, and taking the derivative of Eq. 1, we obtain the PS as the maximum value of the energy derivative. Thus,

$$\tau_p b = \frac{\Gamma_c - \Gamma_0}{|\alpha| a} \frac{\pi}{16} \left(3 + \sqrt{1 + 8\alpha^2} \right) \sqrt{8\alpha^2 - 2 + 2\sqrt{1 + 8\alpha^2}} \quad (2)$$

In the special case of a sinusoidal energy profile ($\alpha = 0$), and taking the minimum energy $\Gamma_0 = 0$, we obtain a simple relationship between the Peierls stress and the Peierls energy barrier Γ_c :

$$\tau_p = \frac{\pi \Gamma_c}{\sqrt{2}ab} \quad (3)$$

There is some confusion in the literature as to the meaning of the Peierls Stress (PS), the flow stress (or Critical Resolved Shear Stress - CRSS), and how they depend on temperature and strain rate. For the purposes of facilitating DD computer simulations, we adhere to the strict definition of the Peierls Stress as *the stress required to move the dislocation rigidly across an atomic potential barrier at absolute zero*. As the temperature increases, fluctuations cannot be suppressed and dislocation motion will naturally move by the generation and motion of kink pairs. However, if the strain rate is very high (as in MD simulations, for example), the dislocation must generate higher and higher concentrations of kink pairs to keep up with the applied strain rate. Thus, for a given temperature and a high enough strain rate, there will be a stress at which the dislocation appears to move as a whole again (similar to the Peierls concept at absolute zero), and the applied stress will be balanced by phonon drag alone (no short range atomic barrier). This situation coincides with the thermal regime of plastic flow measured experimentally in single crystals. We will refer to this critical stress value as the Kink Saturation Stress (KSS), or $\tau_k(T)$. Finally, the CRSS (or flow stress), is *the stress at which dislocations move so as to keep up with an applied strain rate*. The CRSS is temperature and strain rate dependent, and has a thermal ($\tau^*(T)$), and an athermal, or friction (τ_F) component. At very high temperatures (above $\approx 0.7 T_m$), the CRSS decreases as a result of vacancy diffusion.

Theory of Dislocation Motion

Kink-Pair Formation

Because in the first regime dislocation motion is governed by the motion of kinks, we consider the theoretical background of kink formation and migration under applied stress. We then determine the velocity of kinks and finally express the dislocation velocity in terms of the kink velocity. The kink formation energy is the difference in the dislocation line energy from its straight configuration at the bottom of the Peierls hill (Γ_0), as shown in Fig. 2, thus:

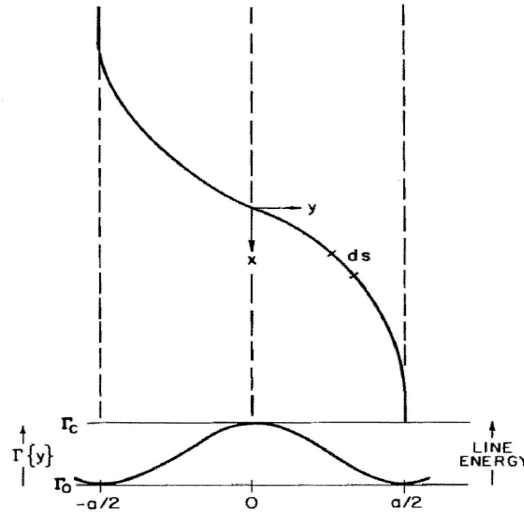


Figure 2. A stable isolated kink (after Dorn & Rajnak [1]).

$$U_k = \int_{-\infty}^{+\infty} \Gamma\{y\} ds - \Gamma_0 dx = \int_{-\infty}^{+\infty} f(y(x)) dx \quad (4)$$

This is a functional of the shape $(y(x))$, that can be minimized using $\delta U_k = 0$, which gives the Euler condition:

$$\frac{\partial f}{\partial y} - \frac{d}{dx} \frac{\partial f}{\partial y'} = 0 \quad (5)$$

The solution of Eq. 5 should result in uniquely determining the shape of the bent dislocation line with a kink on it, but ignores energy differences between the screw one edge components. The kink pair formation energy is given by:

$$U_k = \Gamma_0 \int_{-a/2}^{+a/2} \left(\sqrt{\left(\frac{\Gamma\{y\}}{\Gamma_0} \right) - 1} \right) dy \quad (6)$$

In the special case of $\alpha = 0$, this last equation can be integrated to give a closed form expression for the kink pair formation energy in a parametrized form:

$$U_k = \frac{\Gamma_0 a}{\pi} \left(\sqrt{2(R-1)} + (R+1) \tan^{-1} \sqrt{\frac{R-1}{2}} \right) \quad (7)$$

where $R = \Gamma_c / \Gamma_0$.

The energy required to nucleate a pair of kinks in the presence of an applied shear stress that is smaller than the Peierls stress ($\tau^* < \tau_p$) is given by the excess line energy from the straight configuration less the amount of work done by the shear stress in moving the kink pair across the Peierls barrier, thus:

$$\Delta H = \int_{-\infty}^{+\infty} \left(\Gamma\{y\} \sqrt{1 + \left(\frac{dy}{dx}\right)^2} - \Gamma\{y_0\} - \tau^* b(y - y_0) \right) dx \quad (8)$$

Again, when we minimize the energy functional utilizing Euler's equation, a closed form expression for the line slope $\frac{dy}{dx}$ is obtained as:

$$\frac{dy}{dx} = \pm \sqrt{\left(\frac{\Gamma\{y\}}{\tau^* b(y - y_0) + \Gamma\{y_0\}} \right)^2 - 1} \quad (9)$$

Now, when Eq. 9 is substituted back into Eq. 8, the formation enthalpy of a kink pair is obtained as:

$$\Delta H_k^* = \int_{-\infty}^{+\infty} \left[\frac{(\Gamma\{y\})^2}{\tau^* b(y - y_0) + \Gamma\{y_0\}} - \Gamma\{y_0\} - \tau^* b(y - y_0) \right] dx \quad (10)$$

Dorn and Rajnak performed numerical evaluations of the integral, and the results are shown in Fig. 3.

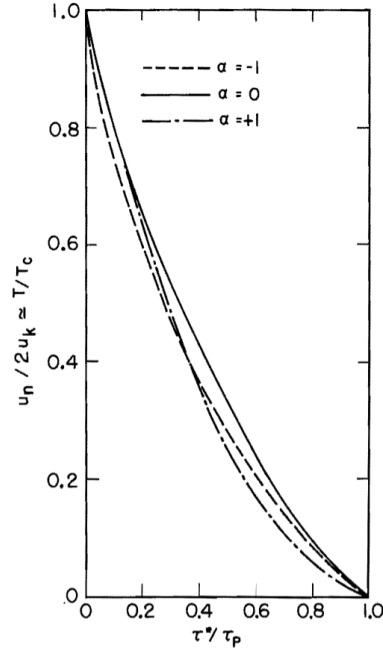


Figure 3. Kink Nucleation Enthalpy as a function of applied shear stress (after Dorn & Rajnak [1]).

The treatment presented above of Dorn and Rajnak assumes that the dislocation takes on a critical configuration to produce a kink pair that is not well-separated. Accurate line energy calculations of such critical configuration are difficult. If the critical configuration involves two well-separated kinks, separated a distance x apart on the dislocation line, the kink pair nucleation energy of this configuration will be:

$$\Delta H_k(x) = 2U_k - \frac{\mu b^2 h^2}{8\pi x} - \sigma b h x \quad (11)$$

This dependence of the formation enthalpy on x has a maximum at $x^* = \left(\frac{\mu b h}{8\pi\sigma}\right)^{1/2}$, which, when substituted back into the previous equation yields:

$$\Delta H_k^* = 2U_k - \left(\frac{\mu\sigma b^3 h^3}{2\pi}\right)^{1/2} \quad (12)$$

If we approximate both b^3 and h^3 as Ω , the atomic volume, the previous equation takes a simple interpretation, as follows. If we define a mean stress $\sigma_m = \sqrt{\sigma\mu}$, then the work done by this stress on an atomic volume is $W_\sigma = \sigma_m \Omega$, and this mean stress decreases the kink pair nucleation energy by this amount of work, i.e.

$$\Delta H_k^* \approx 2U_k - \sigma_m \Omega = 2U_k - \left(\frac{\mu b^3 h^3}{2\pi} \right)^{1/2} \sqrt{\sigma} \quad (13)$$

The result of this last Eq. 13 is in qualitative agreement with the previous numerical estimation, given by Eq. 10. Both are indicative of a cut-off stress above which kink pair nucleation is thermal (The Peierls stress). However, Dorn and Rajnak's treatment expressed by Eq. 10 is more transparent, because of the explicit dependence on the CRSS (Peierls stress), which is itself a function of temperature.

If we take the activation energy for kink migration as E_k^m , then the jump frequency of kinks is:

$$\omega \approx \nu \exp\left(-\frac{E_k^m}{kT}\right) \quad (14)$$

Although ν is the attempt frequency of a kink jump (which depends on how widely separated a kink pair is), it can be roughly taken as the Debye frequency ν_D . The Debye frequency is an indication of how stiff the elastic medium is in propagating sound waves, and is interpreted as the highest frequency of phonons in the solid. This is associated with the shortest phonon wave, on the order of several ($\approx 2a$) lattice constants. It is obtained from the Debye temperature as: $kT_D = h\nu_D$, where T_D is the Debye temperature, and h is Planck's constant.

The diffusion coefficient of kinks is simply $D_k = \beta a^2 \omega$, where β is a numerical factor. Under applied force, the diffusion of kinks becomes biased by the force and the velocity is described by the mobility of a kink in an applied force field, namely:

$$v_k = \frac{D_k}{kT} F = \frac{D_k}{kT} \sigma b h \approx \nu_D b^2 \exp\left(-\frac{E_k^m}{kT}\right) \frac{\sigma b h}{kT} = \exp\left(-\frac{E_k^m}{kT}\right) \frac{\sigma \nu_D b^4}{kT} \quad (15)$$

Here, we took $h \approx b$. Since the transverse sound speed is $C_t \approx \nu_D b$, and since there is evidence that kinks move even at temperatures close to absolute zero, then we will also take the limit that $E_k^m \ll kT$, making the exponential term to be nearly unity. The kink velocity is then:

$$v_k \approx C_t \left(\frac{\sigma \Omega}{kT} \right) \quad (16)$$

where C_t is the transverse sound speed. The same result of Eq. 16 can also be obtained from Leibfried's theory of momentum transfer by elastic wave scattering, which we will outline later. A simpler way of remembering this result is to scale the stress by Ω/kT and the velocity by C_t . Thus, if we define scaled stress and velocity, respectively, as: $\tilde{v}_k = v_k/C_t$, and $\tilde{\sigma} = \sigma\Omega/kT$, we have:

$$\tilde{v}_k = \tilde{\sigma} \quad (17)$$

Dislocation Velocity

If one takes the concentration of positive and negative kinks to be equal, then $C_k = \frac{2}{a} \exp(-\frac{\Delta_k^*}{kT})$. Let's assume that a kink has moved a distance X along the dislocation line till it recombines with another average kink, making the dislocation move forward a distance h at a velocity v . The area swept by the kink lateral motion must be the same as that swept by the motion of the dislocation line, $vX = v_k h$. This simple argument gives the dislocation velocity as a function of the kink velocity;

$$v = \frac{h}{X} v_k \quad (18)$$

The distance X is the inverse of the kink concentration on the dislocation line, C_k . Therefore, we can now develop a simple equation for the velocity of a dislocation:

$$v = \frac{2\sigma b h^2}{a k T} D_k \exp(-\frac{\Delta H_k^*}{kT}) \quad (19)$$

Substituting for the kink diffusivity $D_k \approx v_D a^2$, and ignoring geometric differences between a , h , and b , we obtain the following approximate equation for the dislocation velocity:

$$v = \frac{2\sigma\Omega}{kT} v_D a \exp(-\frac{\Delta H_k^*}{kT}) \quad (20)$$

Because we are looking for a semi-phenomenological description, and because of the numerical uncertainties in the forgoing theoretical treatments, we will re-write Eq. 20 as:

$$v = \zeta \left(\frac{\sigma\Omega}{kT}\right) \exp(-\frac{\Delta H_k^*}{kT}) (v_D a) \quad (21)$$

where ζ is a numerical factor. The last equation (Eq. 21) is written in this form to emphasize the origin of the dislocation velocity being determined by the success of kink jumps at the Debye frequency over an atomic distance, biased forward by the ratio of the work done on an atomic volume to that in thermal vibrations. As we did earlier for the kink velocity, we can also use

scaled variables for the dislocation velocity if we remember that the product of the Debye frequency and the lattice constant is approximately the transverse sound speed, C_t . Thus, in scaled variable form, the scaled dislocation velocity is:

$$\tilde{v} = \xi \tilde{\sigma} \exp\left(-\frac{\Delta H_k^*}{kT}\right) \quad (22)$$

The nucleation theory approach

To complete this theoretical description and put it in perspective, we can also develop the same equation for the dislocation velocity (Eq. 22) from considerations of classical nucleation theory of kinks on the dislocation line. Here we follow the treatment given by Hirth and Lothe.

According to classical nucleation theory, the constrained equilibrium concentration of kink pairs (without mutual interaction) is given by:

$$C_p = C_k^+ C_k^- = \frac{1}{a^2} \exp\left(-\frac{\Delta H_k}{kT}\right) \quad (23)$$

The main result of classical nucleation theory is that the nucleation rate of kinks, J_k is only determined by the kink concentration at the saddle point and the critical size of a kink pair, x_{crit} . This critical size is the size that overcomes thermal fluctuations, i.e., given by:

$$\sigma b h x_{crit} \approx kT \quad (24)$$

The kink nucleation rate is:

$$J_k \approx \frac{2D_k C_p(x^*)}{2x_{crit}} = \frac{\sigma b h}{a^2 kT} D_k \exp\left(-\frac{\Delta H_k^*}{kT}\right) \quad (25)$$

If the average distance travelled on the dislocation line before kinks are annihilated is X , the dislocation velocity is the average distance a dislocation line of unit length advances per unit time. Such average distance is simply the area swept by a kink pair times the rate at which kink pairs are created per unit time, thus:

$$v = hXJ_k \quad (26)$$

However, the distance X is dependent on the average lifetime of a kink pair $X = 2v_k \tau$, and $\tau = 2/J_k X$, which gives:

$$X = 2\left(\frac{v_k}{J_k}\right)^{1/2} \quad (27)$$

Which, when inserted into Eq. 26, gives:

$$v = 2h(J_k v_k)^{1/2} = \xi \left(\frac{\sigma \Omega}{kT}\right) \exp\left(-\frac{\Delta H_k^*}{kT}\right) (v_D a) \quad (28)$$

which is now identical to Eq. 22.

Dislocation Motion Limited by Phonon Interactions

At high stress, the velocity is controlled by dislocation interaction with elastic waves and damping results from momentum loss. We will first consider the thermally-activated regime, where kinks are created on dislocation lines, and the dislocation as a whole moves when these kinks glide and annihilate along the dislocation line itself. At high stresses and temperatures, the dislocation is dragged in a phonon gas, which results in imparting damping properties on dislocation motion by a number of mechanisms.

Leibfried's Phonon Scattering Theory

The theory of Leibfried [2] mimics the idea of momentum loss of electromagnetic waves upon scattering from objects of a finite cross-section. We briefly summarize the idea here. Consider a plane shear wave: $u_z = A \cos(k \cdot r - \omega t)$. The momentum density of the wave is $g = \frac{1}{2} \omega A^2 k$. If we assume that the dislocation has a scattering cross-sectional area of approximately D per unit length, and an elastic wave of energy density $w = \frac{1}{2} \rho_0 \bar{u}^2$. For a wave train of length $L = C_t t$, the transmitted wave train contains less energy after scattering by the amount DLw , and hence less momentum by the amount $DLwt$, where t is the scattering time. Per unit length, the momentum loss in scattering the elastic wave is:

$$\Delta M/L = Dtw \quad (29)$$

and the force imparted to the dislocation during this impulse is simply $F/L = \Delta M/Lt = Dw$. Leibfried found that balancing this scattering radiation force against damping due to thermal vibrations requires that the scattering cross-section D be on the order of $b/10$, and that the elastic energy per unit time ($wC_t D^2$) must be lost to the energy contained in the volume swept by dislocation motion per unit time ($w_T v D^2$), where $w_T = 3kT/\Omega$ is the average thermal energy density. Thus:

$$wC_t = w_T v \quad (30)$$

Therefore, an estimate for the force per unit length of the dislocation under this momentum balance assumption is:

$$F/L = \sigma b = \frac{w_T b}{10} \frac{v}{C_t} \quad (31)$$

or,

$$\tilde{v} = 10\sigma/w_T = 10\sigma\Omega/3kT = \frac{10}{3} \tilde{\sigma} \quad (32)$$

Apart from the numerical factor of $\frac{10}{3}$, this form of Leibfried's equation is essentially the same as the kink velocity equation we showed earlier (Eq. 17).

Phonon Gas Viscosity

In this approach, damping of elastic waves in the solid is considered to result from an effective phonon viscosity. Mason [3] extended this idea to model the damping of a moving dislocation, where the dislocation is assumed to be dragged in a phonon gas. Thus, the classical kinetic theory of gases and the Debye model of the specific heat can be used to construct an equation for dislocation viscosity.

The key results of the kinetic theory of gases are as follows:

$$\lambda = \frac{3K}{C_v \bar{C}_s} \quad (33)$$

$$\eta = \frac{NM\lambda}{3} \quad (34)$$

where λ is the phonon mean free path, K the thermal conductivity, C_v the specific heat at constant volume, \bar{C}_s is an average sound speed ($\bar{C}_s^3 = C_t^3(3/(2 + C_T^3/C_L^3))$), η is the viscosity, N the number of phonons and M their momentum; $M = \hbar\omega/\bar{C}_s$. Using these results of kinetic theory, the dislocation viscosity is found as:

$$\eta = \frac{N\hbar\omega\lambda}{3\bar{C}_s} = \frac{E_0\lambda}{3\bar{C}_s} = \frac{kT\lambda}{3\Omega\bar{C}_s} \quad (35)$$

where $E_0 = kT/\Omega$ is the thermal energy in the phonon gas per unit volume. Since the force on the dragged dislocation, $F = \sigma b$, must be balanced by viscous drag ηv , where v is the dislocation velocity, then we have:

$$v = \frac{\sigma b}{\eta} = \frac{3\sigma b \Omega \bar{C}_s}{kT\lambda} \quad (36)$$

This last equation can again be cast in scaled variables as:

$$\tilde{v} = \frac{3}{\tilde{\lambda}} \tilde{\sigma} \quad (37)$$

where $\tilde{\lambda} = \lambda/b$. The remarkable resemblance of Eq. 37, which is purely based on the kinetic theory of gases, and Leibfried's formula (Eq. 32), which he developed from scattering theory, indicates that the phonon mean free path in Leibfried's theory must be on the order of one lattice constant for the two approaches to be equivalent. Although Leibfried's formula is used in some estimates of dislocation mobility in the literature, Eq. 37 that we developed here based on

Mason's work may be more useful. For example, size effects do not show up in Leibfried's formula, but they can affect the interpretation of MD simulation data, where the mean phonon free path length is dependent on the simulation size. What remains now is a method to determine $\tilde{\lambda}$ from thermodynamic materials data for large crystals, or from MD data for small systems. Following the kinetic theory results above, the phonon mean free path length is determined by knowing the thermal conductivity, the specific heat at constant volume and the average sound speed. However, since in reality we have two interacting gases; the phonon and electron gases, we would need to just consider the contributions of the phonon gas to the conductivity and specific heat. In metals, the thermal conductivity is dominated by electrons, while the specific heat is dominated by the phonons. Mason expressed the specific heat of electrons as $C_{ve} = \beta T$, and showed that when the ratio of the electron to phonon thermal conductivity are used, the phonon mean free path length from thermodynamic data can be found as:

$$\lambda = \frac{3\bar{C}_s K}{bC_{ve}V_F^2} = \frac{3\bar{C}_s K}{b\beta TV_F^2} \quad (38)$$

where V_F is the electron Fermi velocity:

$$V_F = \frac{\hbar(3\pi^2)^{1/3}}{\Omega^{1/3}m} \approx \frac{\hbar(3\pi^2)^{1/3}}{bm} \quad (39)$$

and m is the electron mass. We note that the specific heats are per unit volume. When this is substituted back into the previous equation, we get:

$$\lambda \approx \frac{\bar{C}_s K b^2 m^2}{b\hbar^2 \beta T} \quad (40)$$

In scaled units;

$$\tilde{\lambda} \approx \frac{\bar{C}_s K m^2}{\hbar^2 \beta T} \quad (41)$$

This finally means that we need to use the thermal conductivity, the average sound speed, and the β constant that describes the electronic specific heat in order to determine $\tilde{\lambda}$.

A phenomenological model of dislocation velocity

Our next goal is to utilize the theoretical forms and understanding to represent the dislocation mobility data in DD simulations. We would thus be using a phenomenological approach, where the velocity equations are fitted either from experimental data or from MD simulations, guided by the theoretical understanding presented in the previous section. A similar law was determined by numerical integration by Dorn and Rajnak for a different Peierls potential. For generality we shall use the following fit [4]:

$$\Delta H^* = \Delta H_0 \left[1 - \left(\frac{\sigma}{\tau_p} \right)^p \right]^q \quad (42)$$

We now wish to find the *stress necessary to sustain a given plastic strain rate for a given temperature by the double kink mechanism*. To this end, we consider the plastic strain rate in the thermally-activated regime in the form:

$$\dot{\gamma} = \dot{\gamma}_0 \exp\left(-\frac{\Delta G^*}{kT}\right) = \dot{\gamma}_0 \exp\left(-\frac{\Delta H^* - T\Delta S^*}{kT}\right) \quad (43)$$

where ΔS^* is the activation entropy. Now plug (42) into (43) and solve for σ . This gives:

$$\sigma(T) = \tau_p \left[1 - \left(\frac{T}{T_a} \right)^{\frac{1}{q}} \right]^{\frac{1}{p}} \quad (44)$$

where the "athermal" temperature, T_a is given by:

$$T_a = \frac{\Delta H_0}{\Delta S^* + k \ln \frac{\dot{\gamma}_0}{\dot{\gamma}}} \quad (45)$$

We now note that when $\dot{\gamma}$ is the maximum plastic strain rate allowed by the double kink mechanism ($=\dot{\gamma}_0$), we obtain $T_a = \frac{\Delta H_0}{\Delta S^*}$. Since ΔS^* is related to changes in vibrational frequencies of the crystal during the kink formation process, then T_a must be a function of the Debye temperature. Assuming a linear dependence, we consider $T_0 = mT_D$, where T_D is the Debye temperature and m is approximately 2. However, if we consider entropic effects (Seeger, 1955), we would have to modify the dependence of T_a on strain rate.

The experimental data and MD simulations for dislocation velocity show a consistent behavior that can be modeled in a universal phenomenological law. We will utilize both MD simulations and experimental data on single crystals to determine the dynamic PS, as a function of temperature. Since T_a scales inversely with the logarithm of the strain rate (See Eq. 46), then we may write it phenomenologically as:

$$T_a = \frac{mT_D}{\left(1 + \ln \frac{\dot{\gamma}^{sat}}{\dot{\gamma}} \right)} \quad (46)$$

where T_D is the Debye temperature, and $\dot{\gamma}^{sat}$ is the "kink saturation" strain rate, which can be set at $10^7 s^{-1}$. The MD results (say at $\dot{\gamma} = 10^7 s^{-1}$) can be used with other experimental data in the scaling relationship. Let's now account for thermal activation effects on the stress by introducing a second scaled stress given by:

$$\tilde{\sigma} = \tilde{\sigma} \exp\left(-\frac{\Delta H_k^*}{kT}\right) \quad (47)$$

To reproduce the two velocity regimes, and to account for differences in the mechanisms of kink motion between edge and screw components, we will describe the activation energy for kink nucleation, as follows:

$$\Delta H_k^*(\tau) = [U(0) - U(\tau_p(T))] \Delta H_0(T) \left[1 - \left(\frac{\sigma}{\tau_p(T)} \right)^p \right]^q \quad (48)$$

This last equation is quite universal, because it accounts for transitions between the kink-dominated and phonon-drag dominated velocity regimes through the introduction of the unit step functions: $U(0)$ and $U(\tau_p(T))$. It also accounts for a gradual velocity mechanism transition between screw and edge components through the \cos angle between the tangent and Burgers vectors of the dislocation, b and t , respectively. Once this universal kink nucleation energy is calculated, and to account for acoustic radiation losses that limit dislocation velocities to the average sound wave speed at high stress, the following universal law is proposed:

$$\tilde{v} = 1 - \exp\left(-\frac{3\tilde{\sigma}}{\tilde{\lambda}}\right) \quad (49)$$

It is noted that the fitting parameters that lead to Eq. 49 are here interpreted as a function of the dislocation line orientation (screw or edge), and may also be distinguished for different families of slip systems. The remarkable simplicity of Eq. 49 and its ability to capture the stress and temperature dependence of both screw and edge dislocations in BCC, FCC, and HCP metals makes it a good candidate for inclusion in DD simulation computer programs.

The calculation algorithm for the dislocation velocity would now be simple, and as follows. For a given stress, temperature, crystal structure, slip plane, dislocation orientation, and material, we first calculate the scaled stress, $\tilde{\sigma}$. Next, we find the Peierls and phonon-drag stress (which can be very low for FCC metals). Knowing the kink nucleation energy at absolute zero, ΔH_1 , we can calculate ΔH_k^* , and hence the scaled stress $\tilde{\sigma}$. Then, we determine the scaled phonon m.f.p $\tilde{\lambda}$ from Eq. 41. Finally, we apply the universal velocity equation, given by Eq. 49.

RESULTS

The CRSS [4] for tungsten has been determined by Dorn and Rajnak [1], Lassner [5], and Brunner [6]. The results are obtained at different strain rates, and reflect some strain rate

effects, as shown in Figure (4). In addition, we also determined the CRSS from our MD simulations of pure tungsten by an extrapolation procedure of the dynamics velocity data. The MD results are also consistent with a strain rate shift of the CRSS, as can be seen in Figure (4).

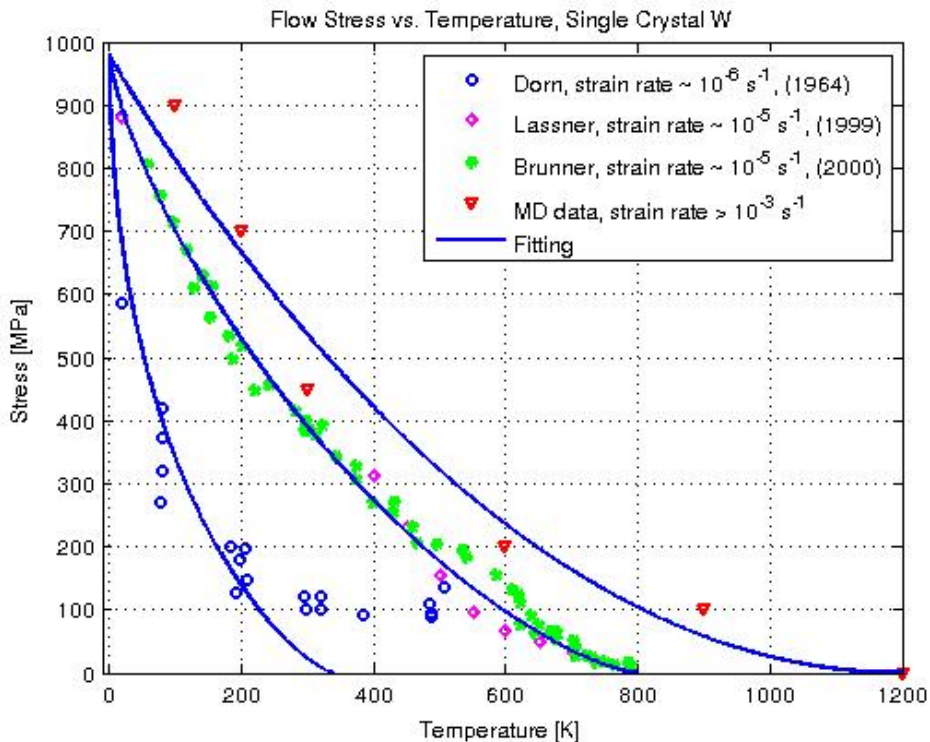


Figure 4. Plot showing flow stress data taken from Dorn 1964 and Lassner 1999, the blue circles correspond to the raw data taken from fig.13 of Dorn 1964, while the magenta squares correspond to data taken from Lassner 1999 book. Red triangles correspond to MD data approaching high strain rate regime. The athermal temperature is defined as that at which the fitted curves intersect the x-axis, being 340K and 800K for Dorn and Lassner respectively. In addition, the fitting parameters p and q are $p = 0.51$, $q = 1.26$ for Dorn, and $p = 1$, $q = 1.69$ for Lassner data.

The data obtained from experimental sources, and those from MD simulations were fitted to Equations (44) for the CRSS, with Equation (46) for the characteristic temperature, T_a . This procedure can produce a universal CRSS versus the scaled temperature T/T_a , as shown in Figure (5). Except for a few data points, the universal fit is consistent with the proposed model.

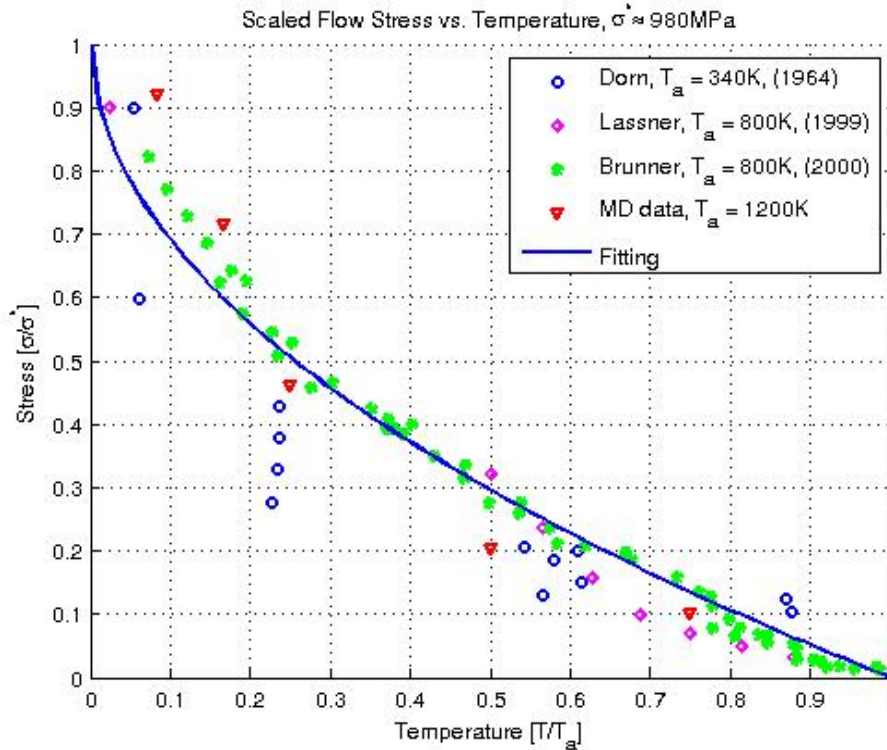


Figure 5. Normalized flow stress vs. Temperature, data in figure 4 is scaled by their respective athermal temperature and Peierl's stress (approx 980 MPa). As can be seen, all the data collapses into one master curve, which can be fitted with the aid of equation 44. The fitting parameters are $q = 2$ and $p = 1$.

Figure (6) shows the results of the model for the screw dislocation velocity in tungsten at any applied stress and temperature. The results indicate that the kink nucleation and motion regime is very limited to low stress and temperature combinations. That may be one of the reasons that MD simulations can best give information on the phonon drag mechanism rather than the kink pair nucleation mechanism.

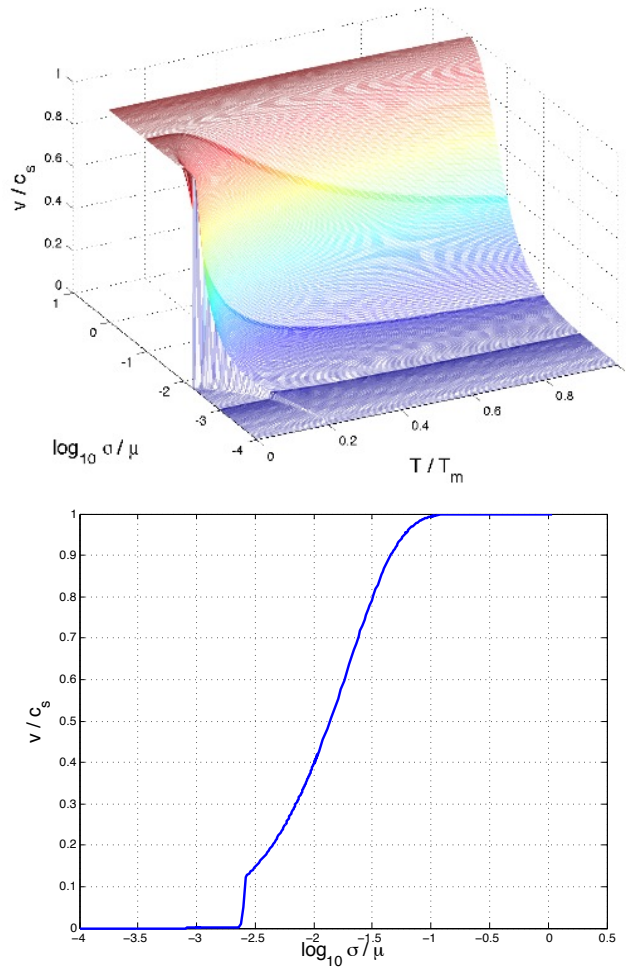


Figure 6. Dislocation velocity (normalized by $c_s = 2890 \text{ m/s}$) of screw dislocations in W. a) Velocity as a function of applied stress and temperature. b) Dislocation velocity at 300K. Three regimes are distinguishable: the kink-pair regime, the phonon drag regime, and the regime characterized by energy radiation.

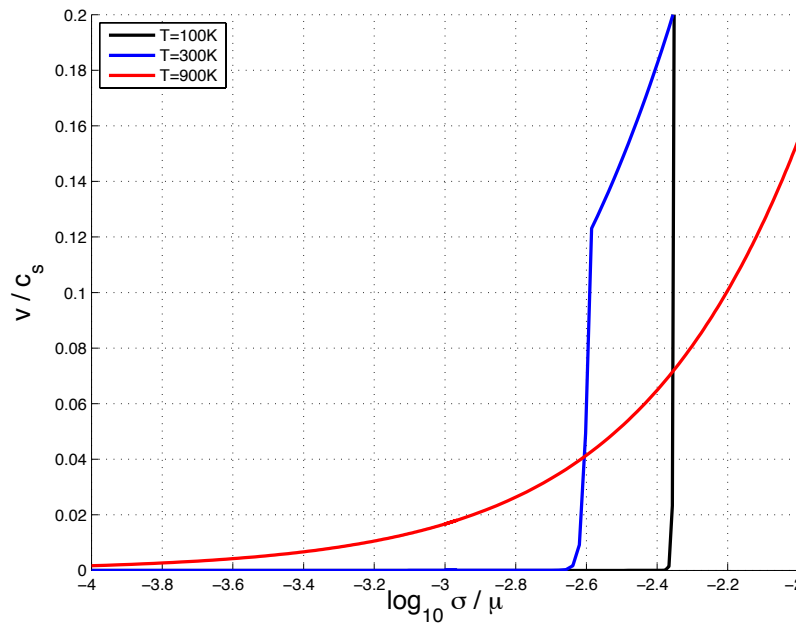


Figure 7. Dislocation velocity in the low stress range, for three different temperatures. At $T=100\text{K}$, dislocations move by the kink mechanism only. At $T=300\text{K}$, the transition between the kink regime and the phonon regime is visible. At $T=900\text{K}$, dislocation motion is by phonon drag only.

Figure (7) shows the dislocation velocity as a function of applied stress for three different temperatures. In the low temperature regime, dislocations clearly move by the generation and motion of kink pairs. At 300 K, the transition between kink dominated motion and phonon drag is evident. At high temperature, dislocation motion is entirely dominated by phonon drag.

REFERENCES

- [1] John Dorn and Stanley Rajnak, "Nucleation of Kink Pairs and the Peierls' Mechanism of Plastic Deformation," *Transactions of the Metallurgical Society of AIME*, 320, 1052-1064, 1964.
- [2] Gunther Leibfried, "Über den Einfluss thermisch angeregter schallwellen auf die plastische deformation, -On the influence of thermally excited sound waves on the plastic deformation," *Zeitschrift fur Physik*, 127, 344-356, 1950.
- [3] Warren Mason, "Phonon viscosity and its effect on acoustic wave attenuation and dislocation motion," *The Journal of the Acoustical Society of America*, 32(4), 458-472, 1960.
- [4] Kocks, U., Argon, A., & Ashby, M. (1975). Thermodynamics and Kinetics of Slip. *Progress in Materials Science*, 19, 1-281.
- [5] Erik Lassner and Wolf-Dieter Schubert, "Tungsten, Properties, Chemistry, Technology of the Element, Alloys, and Chemical Compounds", Kluwer Academic / Plenum Publishers 1999.
- [6] Brunner, Dieter, "Comparison of flow-stress measurements on high-purity tungsten single crystals with the kink-pair theory", *Materials Transactions, JIM(Japan)* 41 1 152-160.

8.8 HELIUM EFFECTS ON DISPLACEMENT CASCADES IN TUNGSTEN — W. Setyawan, G. Nandipati, K. Roche, H. Heinisch, R. J. Kurtz, (Pacific Northwest National Laboratory); and B. D. Wirth (University of Tennessee)

OBJECTIVE

The objective of this research is to support the prediction of helium effects on irradiation damage properties of tungsten-based materials using computational methods.

SUMMARY

Molecular dynamics (MD) simulations were performed to investigate He effects on displacement cascades in W. Helium content, proportion of interstitial and substitutional He and temperature were varied to reveal the various effects. The effect of interstitial He on the number of self-interstitial atoms (SIAs) produced during cascade damage appears to be insignificant. However, interstitial He tends to fill a vacancy (V). Nevertheless, this process is less favorable than SIA-V recombination particularly when excess SIAs are present before a cascade. The efficiency of He filling and SIA-V recombination increases as temperature increases due to increased point defect mobility. Likewise, substitutional He is more susceptible to displacement during a collision cascade than W. This susceptibility increases towards higher temperatures. Consequently, the number of surviving V is governed by the interplay between displaced substitutional He and SIA-V recombination. The temperature dependence of these processes results in a minimum number of V reached at an intermediate temperature.

PROGRESS AND STATUS

Introduction

Tungsten is a primary material choice for divertor components in future fusion reactors due to its low sputtering coefficient, excellent thermal conductivity, relatively low neutron activation and good mechanical strength. Tungsten will be exposed to a flux of He escaping the plasma as well as He produced from transmutation. The presence of He degrades the intended materials properties. Some studies have been done on He diffusion and retention [1-3], bubble formation [4, 5], He-related nano voids formation [6, 7] etc. However, the effects on primary displacement cascade damage have not been explored in detail. An earlier work was done to study the effects on cascade damage at 300 K with relatively low primary-knock-on atom (PKA) energy up to 20 keV [8]. The current work is intended to investigate He effects on cascade damage at higher PKA energies. Different He concentrations and initial proportion of substitutional versus interstitial He, and temperatures up to 2050 K are included.

Formalism

Molecular dynamics (MD) simulations were performed to investigate He effects on displacement cascade evolution in W. A combination of empirical potentials was employed. For the W-W interaction, the Finnis-Sinclair type of potential developed by Ackland and Thetford [9] was taken, in which the short-range part was then modified to harden the repulsion at small interatomic distances [10]. Modification was also done at distances relevant to self-interstitial configurations to improve defect formation energies. A new W-He pair potential from Ref. [10] was used. The potential reproduces simple He defect energetics and structures in excellent agreement with ab initio results. The calculated interstitial He atom migration energy with the

new W-He potential is 0.2 eV. For He-He interaction, the Beck potential [11] with short-range modification by Morishita [12] was used.

The simulations were performed using LAMMPS software [13]. Before He atoms were added, the pure tungsten system was thermalized in the *NPT* ensemble for 30 ps. Then He atoms were placed at random interstitial positions at least 1.6 Å from W or any previously placed He. This is the starting configuration to generate three He compositions, namely 100% interstitial (100I), 50% substitutional (50I50S) and 100% substitutional (100S). To create substitutional He, random interstitial He were swapped with random W. All compositions were further thermalized in *NPT* for 5 ps before displacement cascade was initiated. The short thermalization time was intended to randomize the velocity of He atoms without allowing clustering to occur.

A displacement cascade was simulated using a 75-keV tungsten primary-knock-on atom (PKA) randomly chosen from the central region of the simulation cell. The PKA was given a random initial direction. At the beginning, the cascade was performed in *NVE* using an adaptive time step with maximum displacement of 0.005 Å per step. The cascade events and cooling were followed for ~10 ps, afterwards the system was thermalized to a target temperature in *NVT* and defect migration was followed for a total simulation time of 55 to 60 ps. Periodic boundary conditions were applied to a cubic cell of size $100a \times 100a \times 100a$ containing 2M W atoms in a bcc lattice.

Results

In the absence of a displacement cascade, clustering of He atoms was first investigated. The 100I composition with He content of 134, 460, 2300 and 4600 appm was thermalized at 300, 1025 and 2050 K. Note that 1025 and 2050 K represent 0.25 and 0.5 of tungsten's melting temperature respectively. The clustering was followed for 200 ps. The number of self-interstitial atoms (SIAs) at 50, 100, 150 and 200 ps is summarized in Table 1. Note that the number of SIAs in Table 1 is given in appm for easy comparison with the He content. At room temperature, He clustering of size up to five occurred. However, no SIAs were observed for all concentrations presumably due to limited mobility of the clusters to form large enough clusters to displace W from the lattice sites (kick-out mechanism). At 1025 and 2050 K, large enough clusters formed and produced SIAs. The minimum He cluster size to start a kick-out mechanism is 7 atoms at 1025 K. The minimum size decreases to 5 atoms at 2050 K. Therefore, at lower temperatures, not only that the cluster mobility is more limited, the W atoms themselves are more stable at the lattice sites compared to at elevated temperatures.

Table 1. Number of SIAs in appm due to He clusters (initially interstitial) displacing W from the lattice sites. Each set of four values corresponds to the number of SIAs at 50, 100, 150 and 200 ps simulation time.

	134 appm	460 appm	2300 appm	4600 appm
300 K	0,0,0,0	0,0,0,0	0,0,0,0	0,0,0,0
1025 K	0,0,0,0	0,0,0,0	0,2,8,15	6,36,96,153
2050 K	0,0,0,0	0,0,2,2	21,76,137,181	151,360,507,605

The clustering study is also useful in estimating the number of SIAs produced by kick-out mechanism in addition to those produced during the displacement cascade. In all cases of cascade simulations reported here, there are no kick-out SIAs within the simulation time of ~60 ps. The number of surviving V in pure tungsten was calculated to be 80.9 at 1025 K (Table 2). This number slightly increases at lower temperatures and vice versa. Note that results from all displacement cascades are averaged from 15 simulations. Helium effects on the cascade damage are first studied at 1025 K as a function of He level and composition. The results are summarized in Table 3. Three legends are used to label vacancies for discussion purposes. V_W denotes tungsten-vacant sites that may or may not be occupied by He. Sites that are occupied by neither W nor He are simply denoted as V. Helium-filled vacancies are denoted as V^{He} . Note that there can be more than one He occupying a V^{He} . Therefore, to discuss the He effects on the vacancy and SIA production, V^{He} is used instead of the number of substitutional He.

The effects of interstitial He are the following (see the top portion of Table 3). At 134 appm, the number of SIAs is only +2 compared to pure W. This value increases to 87.7 (+7 from pure case) with 460 appm. However, at 2300 appm, the number decreases to 81.7, which is only +1 from pure case. Therefore, it appears that the small variation in the number of SIAs is a statistical effect and that interstitial He has insignificant effect on SIA production. On the other hand, the effect on the number of vacancies is significant. Up to 460 appm, the number of V is 81.3 (approximately the same as in pure case) with 134 appm and 80.1 (-1 from pure case) with 460 appm, and decreases to 47.1 (-34 from pure case) with 2300 appm. Clearly, interstitial He atoms start to fill some of the vacancies produced during the cascade. The corresponding V^{He} are 1.7, 7.6 and 34.6 with 134, 460 and 2300 appm.

The effects of substitutional He can be seen from the 460 appm data in Table 3. The number of new V^{He} (additional number relative to the initial number before cascade) decreases from 7.6 to -44.5 (with 50I50S) and to -157.3 (with 100S). This indicates that some of the initial V^{He} are now occupied by initial SIAs. However, it is unclear to what proportion that this process occurs during the cascade compared to during the SIA migration after the cooling stage. Further analysis is needed. On the other hand, the number new SIAs are 87.7, 20.1 and -91.1 with 100I, 50I50S and 100S respectively. This indicates that there is a critical composition where the number of new SIAs would be zero, i.e., the number of SIAs produced by cascade is balanced by the number of initial SIAs filling the vacancies created by the cascade. Note that at the critical composition, the number of vacancies is not necessarily zero even though there are no new SIAs created. The number of V is 80.1, 64.7 and 66.3 with 100I, 50I50S and 100S respectively. These surviving vacancies may come from the initial V^{He} where the He atoms get displaced during the collision cascade. It is also interesting to note that the number of surviving V saturates at ~65 as the proportion of substitutional He is increased. The critical composition and the minimum number of surviving vacancies are expected to depend on factors such as PKA energy (damage volume), He content and temperature.

Table 2. Number of surviving vacancies (V) in pure tungsten after damage from 75-keV PKA as a function of temperature.

	300 K	1025 K	2050 K
V	81.5	80.9	77.1

Table 3. Number of point defects after damage from 75-keV PKA at 1025 K as a function of He content and initial He composition, i.e., substitutional (S) and interstitial (I). V_W denotes the number of sites that are not occupied by W. V^{He} denotes the number of vacancies (V) occupied by He.

appm	He(S) _{init}	He(I) _{init}	SIA _{init}	V	V_W	SIA _{new}	V^{He}_{new}
134	0	268	0	81.3	82.9	82.9	1.7
460	0	918	0	80.1	87.7	87.7	7.6
2300	0	4590	0	47.1	81.7	81.7	34.6
134	134	134	134	74.6	203.0	69.0	-5.6
460	459	459	459	64.7	479.1	20.1	-44.5
2300	2295	2295	2295	65.1	1784.0	-511.0	-576.1
460	918	0	918	66.3	826.9	-91.1	-157.3

The effects of temperature are studied using 460 appm He. The results for different He compositions are presented in Table 4. First, the number of new V^{He} with 100I increases with temperature due to increased He mobility. The increase is from 6.8 at 300 K to 7.6 at 1025 K and to 15.3 at 2050 K. However, when initial SIAs are present, the number of new V^{He} decreases with temperature. This decrease is more significant compared to the increase in the 100I case indicating the more dominant process of SIA filling vacancies than He filling vacancies. The SIA-V recombination is enhanced towards higher temperature. The consequence on the critical composition in which no new SIAs created is that as the temperature increases, it requires a smaller proportion of interstitial He in the initial composition to balance the damage-produced SIAs.

Next is temperature effect on the minimum number of vacancies. At 300 K, increasing the proportion of substitutional He does not change the number of surviving V which is ~86. At 1025 K, the number of surviving V decreases from ~80 at 100I composition to (and saturates at) ~65 towards 100S as previously discussed. At 2050 K, a reverse trend occurs, i.e., the number of V increases: 67, 73 and 79 for 100I, 50I50S and 100S respectively. The results show that the number of surviving vacancies in the presence of substitutional He reaches a minimum at an intermediate temperature (in this study is 1025 K). This can be understood from the following. When initial V^{He} are present, the substitutional He atoms are more susceptible to displacement during collision cascade than W. Some of the initial V^{He} are then filled by initial SIAs. Hence the number of surviving V is determined by the interplay between the increased number of damage-created vacancies from V^{He} and the increased SIA-V recombination. At low temperatures, SIA-V recombination is not as effective, while at high temperatures the instability of initial substitutional He is more than the increased SIA-V recombination, resulting in a minimum number of V at an intermediate temperature.

Table 4. Number of point defects after damage from 75-keV PKA with 460 appm He as a function of temperature (T) and initial He composition, i.e., substitutional (S) and interstitial (I). V_W denotes the number of sites that are not occupied by W. V^{He} denotes the number of vacancies (V) occupied by He.

T (K)	He(S) _{init}	He(I) _{init}	SIA _{init}	V	V_W	SIA _{new}	V^{He}_{new}
300	0	918	0	86.3	93.1	93.1	6.8
1025	0	918	0	80.1	87.7	87.7	7.6
2050	0	918	0	65.9	81.2	81.2	15.3
300	459	459	459	87.4	516.5	57.5	-29.9
1025	459	459	459	64.7	479.1	20.1	-44.5
2050	459	459	459	73.0	458.5	-0.5	-73.5
300	918	0	918	85.9	895.1	-22.9	-108.8
1025	918	0	918	66.3	826.9	-91.1	-157.3
2050	918	0	918	79.3	758.0	-160.0	-239.3

ACKNOWLEDGEMENT

Computations were performed partly on Olympus supercomputer (FUSION account) at Pacific Northwest National.

REFERENCES

- [1] A. Wagner and D. Seidman, *Phys. Rev. Lett.* **42** (1979) 515.
- [2] J. Amano and D. Seidman, *J. Appl. Phys.* **56** (1984) 983.
- [3] S. B. Gilliam, et al., *Nucl. Instr. Meth. Phys. Res. B* **241** (2005) 491.
- [4] K. O. E. Henriksson, et al., *Appl. Phys. Lett.* **87** (2005) 163113.
- [5] K. O. E. Henriksson, et al., *Nucl. Instrum. Methods Phys. Res. B* **244** (2005) 377.
- [6] A. Debelle, M. F. Barthe and T. Sauvage, *J. Nucl. Mater.* **376** (2008) 216.
- [7] A. Debacker, et al., *J. Nucl. Mater.* **429** (2012) 78.
- [8] N. Juslin, V. Jansson and K. Nordlund, *Philos. Mag.* **90** (2010) 3581.
- [9] G. J. Ackland and T. Thetford, *Philos. Mag. A* **56** (1987) 15.
- [10] N. Juslin and B. D. Wirth, *J. Nucl. Mater.* **432** (2013) 61.
- [11] D. E. Beck, *Mol. Phys.* **14** (1968) 311.
- [12] K. Morishita, et al., *Nucl. Instrum. Methods Phys. Res. B* **202** (2003) 76.
- [13] S. Plimpton, *J. Comp. Phys.* **117** (1995) 1.

9.1 HFIR IRRADIATION EXPERIMENTS – July 31, 2013

Summary of Recent, Current and Planned Fusion Materials Program Experiments

Experiment Designation	Primary Materials	Specimen Types*	Irradiation Temperature (°C)	Max Exposure (dpa)	Number of Reactor Cycles	Irradiation Period (month/year)		
<i>Beryllium reflector (RB) irradiation positions</i>								
RB-15J	F82H	T, F, FT	300, 400	6	10	6/08	–	12/09
<i>Target zone full-length capsules</i>								
JP-25	F82H	T, FT	300, 500	20	10	2/99	–	1/01
JP-26	F82H	T, FT	300,400,500	9	5	12/03	–	11/04
JP-27	F82H	T, FT	300, 400	21	13	12/03	–	1/08
JP-28	F82H	T, FT	300,400,500	80	46	4/05	–	7/13
JP-29	F82H	T, FT	300,400,500	80	46	1/05	–	7/13
12-DCT	F82H	DCT	50	1.6	1	8/11	–	8/11
JP-30	F82H	T, FT	300,400,650	20	~10	11/11	–	
JP-31	F82H	T, FT	300,400,650	20	~10	11/11	–	
<i>Target zone rabbit capsules (DOE-JAEA)</i>								
F8A1	F82H	T, FT	300	50	29	2/09	–	7/13
F8A2	“	“	“	“	“	“	–	“
F8B1	“	“	“	“	“	“	–	“
F8B2	“	“	“	“	“	“	–	“
JCR-1	SiC/SiC	Bend bars	800	30	15	10/04	–	1/09
JCR-2	“	“	“	“	“	“	–	“
JCR-3	“	“	“	“	“	“	–	“
JCR-4	“	“	“	“	“	“	–	“
JCR-5	“	“	“	>50	>25	10/04	–	2/11
JCR-6	“	“	“	“	“	“	–	“
JCR-7	“	“	“	“	“	“	–	“
JCR-8	“	“	“	“	“	“	–	“
JCR-9	“	“	500	30	15	10/04	–	1/09
JCR-10	“	“	“	“	“	“	–	“
JCR-11	“	“	“	“	“	“	–	“
JCR-12	“	“	“	“	“	“	–	“
F11A3	F82H	T, FT	300	20	12	5/11	–	2/13
F11A4	“	“	“	“	“	“	–	“
F11B3	“	“	“	“	“	“	–	“

M4-TEN	F82H	DCT	50	1.6	1	8/11	–	8/11
JCR11-01	SiC/SiC	Bend bars	950	50	25	11/12	–	
JCR11-02	SiC/SiC	Bend bars	950	10	5	10/12	–	
JCR11-03	SiC/SiC	Bend bars	950	30	15	5/13	–	
JCR11-04	SiC/SiC	Bend bars	950	30	15	5/13	–	
JCR11-05	SiC/SiC	Bend bars	950	50	25	10/12	–	
JCR11-06	SiC/SiC	Bend bars	950	10	5	10/12	–	7/13
JCR11-07	SiC/SiC	Bend bars	950	100	50	10/12	–	
JCR11-08	SiC/SiC	Bend bars	950	100	50	10/12	–	
JCR11-09	SiC/SiC	UDMC	950	4	2	6/13	–	
JCR11-10	SiC/SiC	UDMC	950	10	5	6/13	–	
JCR11-11	SiC/SiC	UDMC	950	30	15	6/13	–	
JCR11-12	SiC/SiC	UDMC	950	100	50	6/13	–	
Target zone rabbit capsules (TITAN)								
T8A1	SiC	BSR	300	0.01	HT**	10/09	–	10/09
T8A2	SiC	BSR	300	0.1	HT	10/09	–	10/09
T8B1	SiC	BSR	500	0.01	HT	10/09	–	10/09
T8B2	SiC	BSR	500	0.1	HT	10/09	–	10/09
T8C1	SiC	BSR	500	~1	1	5/09	–	6/09
T8D1	SiC	BSR	800	0.1	HT	3/11	–	10/09
T8E1	SiC	BSR	800	~1	1	8/09	–	8/09
T8F1	SiC	BSR	1200	~1	1	8/09	–	8/09
T9A1	W, Ni	Discs	90	0.1	HT	1/09	–	10/09
T9A2	W, Ni	Discs	90	1.2	1	1/09	–	1/09
T9C1	Steels	T, MC	500	5.5	3	11/09	–	2/10
T9C2	Steels	T, MC	500	9.6	5	11/09	–	6/10
T9G1	Steels	T, MC	300	1.2	1	6/09	–	8/09
T9G2	Steels	T, MC	300	9.6	8	6/09	–	8/11
MTTN01	Steels	T, MC	300	4.8	4	1/12	–	8/11
300-LD-1	Steels	SSJ, MC	300	2	1	5/12	–	6/12
300-HD-1	Steels	SSJ, MC	300	12	6	5/12	–	2/13
500-LD-1	Steels	SSJ, MC	500	2	1	5/12	–	6/12
500-HD-1	Steels	SSJ, MC	500	12	6	5/12	–	2/13
500-HD-2	Steels	SSJ, MC	500	12	6	5/12	–	2/13
500-HD-3	Steels	SSJ, MC	500	12	6	5/12	–	2/13
650-LD-1	Steels	SSJ, MC	650	2	1	5/12	–	6/12
650-LD-2	Steels	SSJ, MC	650	2	1	5/12	–	6/12
650-HD-1	Steels	SSJ, MC	650	12	6	5/12	–	2/13
650-HD-2	Steels	SSJ, MC	650	12	6	5/12	–	2/13
300-LD-2	Steels, W	SSJ, MC	300	2	2	7/12	–	8/12
300-MD-1	Steels, W	SSJ, MC	300	7	4	7/12	–	2/13
500-LD-2	Steels, W	SSJ, MC	500	2	2	1/13	–	7/13
300-LD-3	Steels, W	SSJ, MC	300	2	2	7/12	–	11/12
300-HD-2	Steels, W	SSJ, MC	300	12	8	7/12	–	
500-LD-3	Steels, W	SSJ, MC	500	2	1	7/12	–	8/12

500-HD-4	Steels, W	SSJ, MC	500	12	6	7/12	–	7/13
650-LD-3	Steels, W	SSJ, MC	650	2	2	10/12	–	7/13
650-HD-3	Steels, W	SSJ, MC	650	12	8	7/12	–	
PC1	Various	SSJ, MC	80/100	0.02	HT	6/12	–	6/12
PC1A	Various	SSJ, MC	80/100	0.02	HT	6/12	–	6/12
PC2	Various	SSJ, MC	80/100	0.1	HT	6/12	–	6/12
PC2A	Various	SSJ, MC	80/100	0.1	HT	6/12	–	6/12
PC3	Various	SSJ, MC	80/100	0.5	HT	6/12	–	7/12
PC3A	Various	SSJ, MC	80/100	0.5	HT	6/12	–	7/12
PC4	Various	SSJ, MC	80/100	2	1	6/12	–	7/12
PC4A	Various	SSJ, MC	80/100	2	1	6/12	–	7/12
PC5	Various	SSJ, MC	80/100	20	9	6/12	–	
TB-300-1	Steels, W	SSJ, MC	300	0.02	HT	8/12	–	8/12
TB-300-2	Steels, W	SSJ, MC	300	0.1	HT	8/12	–	8/12
TB-300-3	Steels, W	SSJ, MC	300	0.5	HT	8/12	–	8/12
TB-300-4	Steels, W	SSJ, MC	300	7	5	7/12	–	6/13
TB-500-1	Steels, W	SSJ, MC	500	0.1	HT	8/12	–	8/12
TB-500-2	Steels, W	SSJ, MC	500	0.5	HT	8/12	–	8/12
TB-500-3	Steels, W	SSJ, MC	500	7	4	7/12	–	2/13
TB-650-1	Steels, W	SSJ, MC	650	0.1	HT	8/12	–	8/12
TB-650-2	Steels, W	SSJ, MC	650	0.5	HT	8/12	–	8/12
TB-650-3	Steels, W	SSJ, MC	650	7	5	7/12	–	6/13
TB-650-4	Steels, W	SSJ, MC	650	20	11	7/12	–	
TTN09	SiC	Joint	500	3.4	2	8/11	–	11/11
TTN10	SiC	Joint	500	4.1	2	8/11	–	11/11
TTN11	SiC	Joint	800	4	2	3/12	–	5/12
TTN01	SiC	BSR	300	1	1	2/11	–	3/11
TTN02	SiC	BSR	300	10	6	2/11	–	12/11
TTN03	SiC	BSR	300	20	11	2/11	–	
TTN04	SiC	BSR	500	10	6	5/11	–	4/12
TTN05	SiC	BSR	500	20	11	5/11	–	
TTN06	SiC	BSR	800	10	6	5/11	–	4/12
TTN07	SiC	BSR	800	20	11	5/11	–	
TTN08	SiC	BSR	1200	10	6	5/11	–	8/12
TTN16	SiC	Fiber BSR	500	1	1	11/11	–	12/11
TTN17	SiC	Fiber BSR	500	10	6	8/11	–	6/12
TTN18	SiC	Fiber BSR	500	20	11	8/11	–	
TTN19	SiC	Fiber BSR	1200	1	1	3/12	–	4/12
TTN20	SiC	Fiber BSR	1200	10	6	3/12	–	11/12
Target zone rabbit capsules (US-TITAN-JAEA)								
T11-01J	V-4Cr-4Ti	BTC	425	2	1	11/12	–	12/12
T11-02J	V-4Cr-4Ti	BTC	425	6	3	1/13	–	7/13
T11-03J	V-4Cr-4Ti	BTC	425	2	1	11/12	–	12/12
T11-04J	V-4Cr-4Ti	BTC	425	6	3	1/13	–	7/13
T11-05J	SiC	BTC	600	2	1	11/12	–	12/12

T11-06J	SiC	BTC	600	6	3	1/13	–	7/13
T11-08J	SiC	BTC	600	6	3	1/13	–	7/13
T11-09J	SiC	BTC	600	2	1	11/12	–	12/12
T11-11J	SiC	BTC	600	2	1	11/12	–	12/12
T11-13J	Graphite	BTC	600	2	1	11/12	–	12/12
T11-14J	Graphite	BTC	600	6	3	1/13	–	7/13
J12-01	F82H	BTC	300	1.5	1	1/13	–	2/13
J12-02	F82H	BTC	300	6	3	5/13	–	7/13
J12-03	F82H	BTC	300	1.5	1	5/13	–	2/13
J12-04	F82H	BTC	300	6	3	1/13	–	6/13
J12-05	F82H	BTC	300	1.5	1	1/13	–	2/13
J12-06	F82H	BTC	300	6	3	5/13	–	6/13
<i>Target zone rabbit capsules (US-IMR)</i>								
MX-1	Ceramics	Various	400	2	1	7/13	–	
MX-2	Ceramics	Various	400	TBD	TBD	7/13	–	
MX-3	Ceramics	Various	400	10	6	7/13	–	
MX-4	Ceramics	Various	700	2	1	7/13	–	
MX-5	Ceramics	Various	700	TBD	TBD	7/13	–	
MX-6	Ceramics	Various	700	10	5	7/13	–	
MX-7	Ceramics	Various	1000	2	1	7/13	–	
MX-8	Ceramics	Various	1000	TBD	TBD	7/13	–	
MX-9	Ceramics	Various	1000	10	5	7/13	–	

*T = Tensile, F = Fatigue, FT = Fracture Toughness, MC = Multipurpose Coupon, BSR = Bend Stress Relaxation Creep, DCT = Disc Compact Tension, BTC: Bellows-loaded Tensile Creep, UDMC: Uni-directional Mini-composite. Most experiments also contain TEM disks, other special purpose specimens, and monitors occupying small spaces.

**Hydraulic tube – fractional cycle exposures.